Numerical and Experimental Investigation of a Hall Thruster Operating with Air

Matteo Ciolini

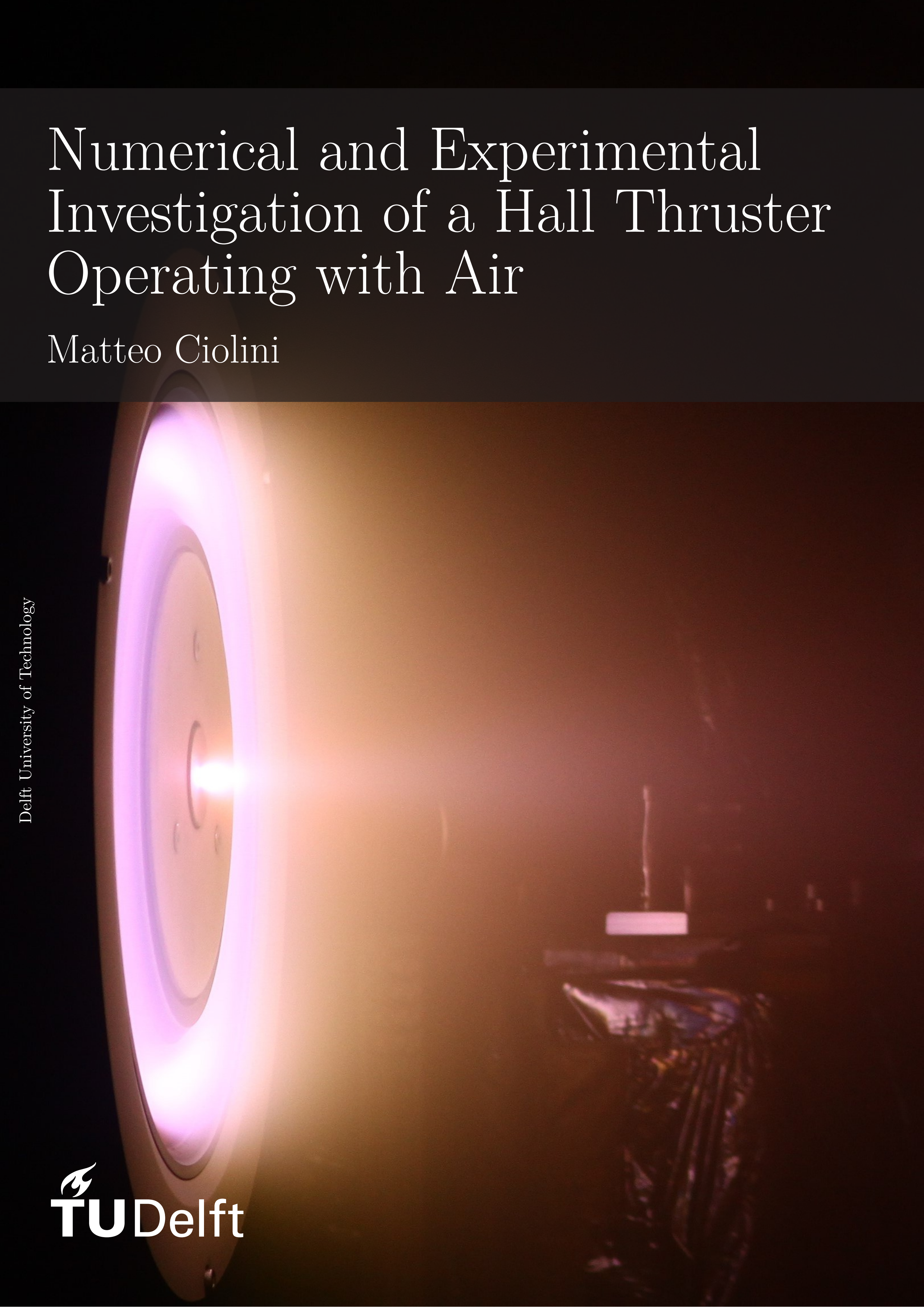

Delft University of Technology

Numerical and Experimental Investigation of a Hall Thruster Operating with Air

by

Matteo Ciolini

to obtain the degree of Master of Science
at the Delft University of Technology,
to be defended publicly on Thursday, 24 February 2022 at 14:00.

Student Number:	5006929	
Project Duration:	March, 2021 - February, 2022	
Thesis Supervisors:	Dr. Angelo Cervone	TU Delft (supervisor)
	Dr. Tommaso Misuri	SITAEL (co-supervisor)
	Vittorio Giannetti, MSc	SITAEL (co-supervisor)
	Eugenio Ferrato, MSc	SITAEL (co-supervisor)
Examination Committee:	Dr. Angelo Cervone	TU Delft (supervisor)
	Dr. Jian Guo	TU Delft (chair)
	ir. Marc C. Naeije	TU Delft (external member)
	Dr. Tommaso Misuri	SITAEL (co-supervisor)
Institution:	Delft University of Technology	
Place:	Faculty of Aerospace Engineering, Delft	

Cover Image:
SITAEL HT5k Hall thruster operating with air. (Reproduced with permission of SITAEL).

Alla mia famiglia.

Preface

This thesis contains the research I have conducted about Hall thrusters operating with air, in fulfilment of the MSc programme in Aerospace Engineering at TU Delft. Over a period of almost a year of fulltime work at SITAEL S.p.A. (Pisa, Italy), I have extensively expanded my knowledge (and passion) about electric propulsion and plasma physics. At SITAEL I have managed to see with my own eyes the development and testing of Hall thrusters, delving with great enthusiasm into this fascinating research field.

First and foremost I want to thank my academic supervisor Dr. Angelo Cervone for his guidance and valuable insights. I have also really appreciated his critical attitude and efficiency in dealing with any kind of doubt, which have proved extremely helpful.

Additionally, I want to express my sincere gratitude to my company supervisors Dr. Tommaso Misuri, Vittorio Giannetti and Eugenio Ferrato for their invaluable support in my everyday work at SITAEL. Their precious advices and the constant discussions together have been crucial for the accomplishment of the objectives of this research. A special thanks also goes to Dr. Tommaso Andreussi for his helpful technical suggestions.

Overall, I want to thank all my colleagues and friends at SITAEL, with whom I have been lucky enough to share knowledge and everyday experiences. Moreover, I am very grateful for the opportunity I have been given to participate in the company research programme about air-breathing electric propulsion and to publish, in the following months, the outcomes of this work.

Finally, the most significant and heartfelt thank you goes to my family for having always supported me throughout my studies and in life.

Matteo Ciolini
Delft, February 2022

Summary

In this work it is investigated the plasma behaviour in an air-propelled Hall thruster by means of numerical modelling and experimental measurements. The device considered is a 5 kW-class magnetically shielded Hall thruster developed by SITAEL (i.e. HT5k [1]) and it has been experimentally characterized during operation with a nitrogen/oxygen mixture representing the air composition found in the Earth thermosphere. The ultimate goal of this experimental campaign (not addressed in this work) is that of assessing whether the HT5k plume produced can be considered a representative atmospheric flow, to allow on-ground testing of Air-Breathing Electric Propulsion (ABEP) devices [1, 2].

While xenon or krypton plasmas, for instance, can be generally modelled by considering only singly charged ions, a species of neutral atoms and electrons, a nitrogen/oxygen plasma represents a much more complex case. Indeed, both its molecular nature and the presence of two distinct chemical species (i.e. nitrogen and oxygen) determine a wider range of products to be considered. In such multispecies plasma, the main modelling challenges concern the interactions between particles and their effects on the thruster plasma behaviour. In order to address these phenomena, the first part of this work delves into the kinetic theory of electropositive multispecies plasmas and also into an accurate chemical modelling of the reactions relevant for a Hall thruster operating with air.

At first, after an introductory discussion about Hall thrusters and basic plasma physics, the generalized Bohm sheath criterion in multispecies plasmas is presented, highlighting the related uncertainties in the correct definition of the ion velocities at the sheath edge. In order to solve them, it is then explored the theory of instability-enhanced friction in the presheath which, through a kinetic description of ion-ion streaming instabilities, is known to accurately predict these velocities in a plasma with two ion species [3, 4]. In particular, this theory suggests that ion species characterized by different masses (and thus velocities) mutually interact along their acceleration in the plasma presheath. Under certain conditions, this interaction may cause instabilities, which determine a significant kinetic friction among them, effectively blocking their differential velocities. Otherwise, the ions accelerate undisturbed, thus reaching their individual sound velocities at the sheath edge. The theoretical discussion about plasma sheaths is then concluded by presenting a comprehensive sheath model with N ion species, posing the bases for the successive modelling activities.

Next, by means of an atmospheric model it is defined the air encountered in the Earth thermosphere as a nitrogen/oxygen mixture [5]. Then, this is investigated chemically, so as to determine the most significant plasma species to be considered in the thruster numerical model. The analysis is restricted to electron-impact processes only due to their predominant influence on plasma dynamics, thus excluding mixed reactions involving both nitrogen and oxygen species, which result much less frequent. Then, by evaluating the reaction cross-sections of all possible electron-impact processes through literature results, it is concluded that only singly charged positive ion species must be considered. This brings to nine the total number of species needed to model the air plasma of a Hall thruster by means of a fluid numerical approach: four neutral species (N_2, N, O_2, O), four positive ion species (N_2^+, N^+, O_2^+, O^+) and electrons. To the author's knowledge, this work is the first-ever to model a Hall thruster plasma composed of so many species. Actually, not even Hall thruster models dealing with mixed plasmas (i.e. composed of different chemical species) are known from literature. Generally,

these limit to pure xenon or krypton plasmas, which rarely include up to thirdly charged ions (e.g. Xe^{+}, Xe^{++} and Xe^{+++}) [6, 7, 8, 9, 10].

Successively, the knowledge of number and type of ion species considered is used to solve the sheath model of a representative air plasma, also including the kinetic description of instability-enhanced friction in the presheath. The solutions are then thoroughly investigated to understand the effects of ion-ion streaming instabilities on the sheath description. It is then concluded that this theory determines variations in the ion velocities at the sheath edge up to 20% of the corresponding sound speeds, for electron temperatures ranging between 10 eV and 50 eV. In particular, different combinations of these instabilities and the secondary-electron emission (SEE) from the thruster channel wall are studied, showing comparable variations which become increasingly significant going toward higher electron temperatures.

Additionally, it is also evaluated the sheath model solution sensitivity to the two main assumptions considered: constant and equal temperatures for all four ions and fixed plasma composition. The former appears to significantly affect the instability threshold, which generally shifts toward the sheath edge as the ion temperatures increase. This is due to thermal agitation, which acts against the instability-enhanced friction. Regarding the other assumption, the sensitivity analysis highlights the species-specific role of each ion considered, coherently with the general rule that lighter particles accelerate the others more strongly and heavier ones slow them down with increasing intensity.

In the second part of this work, it is presented a non-stationary one-dimensional model of the air-propelled HT5k plasma and the related experimental campaign conducted at SITAEL. Then, the model results are analyzed and partially validated against the experimental measurements.

At first, it is described the numerical model, which is being actively developed by a research group of the University of Pisa (in collaboration with SITAEL) for studying oscillations in Hall thruster [10] and modified in this work to account for a nitrogen/oxygen mixture instead of xenon. Particular focus is placed on the steps performed to adapt it to this particular propellant and to the thruster characteristics (e.g. magnetic shielding configuration, centrally mounted cathode, chamfered channel). These include the implementation of the relevant chemical processes as well as the multispecies sheath model, so as to consistently solve the plasma-wall interactions in the thruster channel depending on the local temperature and density conditions, also including the effect of ion-ion streaming instabilities. In addition, it is also implemented a plume expansion description for each ion and neutral species considered which, together with an extension of the domain length in the near-plume, aims at a better model representativeness in this region.

Successively, it is presented the experimental campaign, posing particular attention on the diagnostics employed, namely Faraday probes, RPA probe, fast-diving triple Langmuir probe and spectrometers. For each of them (spectrometers excluded[1]), the main data acquisition and analysis techniques are presented and extended to the case of a multispecies nitrogen/oxygen plasma. However, the presence of several ion species (and so of as many different contributions mixed) generally makes them underdetermined, thus not allowing to resolve the individual measurements without combining the results of different diagnostics. While this approach could not be investigated further due to time limitations of the project, the analysis models relative to each diagnostic device are outlined for future work, especially highlighting the required cross-contributions between them.

The work then proceeds with the thruster model calibration, which consists in tuning

---

[1] In order to analyse the emission spectra measurements acquired by the spectrometers, it is required a collisional-radiative model of the mixture. These models are very complex and are generally developed and used by the research groups providing the instruments, which thus are also responsible for data analysis.

a set of unknown quantities to let the predicted discharge current match the experimental one. The ones considered in this work are: the neutral velocities, the intensity of plasma-wall interactions (scaled by means of a coefficient) and the anomalous electron diffusion profile. In order to define them uniquely, it is generally required an oscillatory discharge current signal to be used as reference, as the amplitude, frequency and mean value of the current represent very specific features to match.

During the experimental campaign the thruster was successfully characterized at $\phi_d = 225\,\mathrm{V}$, $\dot{m}_a = 6\,\mathrm{mg/s}$, $\dot{m}_c = 0.63\,\mathrm{mg/s}$ and, by scaling down the magnetic field intensity from the nominal $B_{max} = B^*$ to a configuration in which $B_{max} = 0.57B^*$, it was possible to establish a low-frequency oscillatory behaviour of the plasma (i.e. breathing mode). The corresponding discharge current signal exhibited a well-defined and relatively noise-free behaviour, although not constantly sustained in time. Therefore, this operating point was selected as a reference for model calibration and validation.

Successively, the results of model calibration in absence of ion-ion streaming instability are presented, showing a predicted discharge current accurately reproducing the major features of the reference experimental signal. Specifically, breathing mode low-frequency oscillations at $f_{BM} = 16.36\,\mathrm{kHz}$ appear reliably replicated, while high-frequency components predicted in the 0.9-1.7 MHz frequency range cannot not be experimentally resolved due to background noise. However, the spatiotemporal analysis of the model results suggests a very tight relationship of the latter with the ion transit instability observed in literature [11, 12, 13].

After having assessed the successful model calibration, the predicted space-time plasma properties are thoroughly investigated. These allow to identify all the dynamic mechanisms responsible for breathing mode ionization instability, thus confirming the physical validity of the current formulation in reproducing these oscillations, even in complex multispecies plasmas.

Then, in order to proceed with model validation, the triple Langmuir probe measurements are presented and analysed, so as to retrieve the probed plasma parameters. These however show strong perturbations even outside the channel due to the thruster magnetic shielding configuration and the strong azimuthal electron current present. As a consequence, it is concluded that the probe measurements can be considered reliable only from 13.4 mm downstream the channel exit, thus preventing the experimental validation of the model results in the most critical regions.

In the following, the predicted plasma properties are compared with the results obtained from the triple Langmuir probe measurements. Apart from the high-frequency oscillations, which cannot not be experimentally validated due to the probe signal filtering, the comparison results satisfactory, even if significantly limited due to the probe perturbation to the plasma. In particular, all the properties compared (i.e. species densities, electron temperature and plasma potential) are reproduced at the correct order of magnitude, although the model fails in shifting outside the channel the thruster acceleration region, as it typically happens in magnetically shielded devices. As a consequence, both the plasma potential and the density profiles are predicted too upstream. In addition, the latter also appears underestimated by 2-4 times with respect to the probe results. Regarding the electron temperature, the agreement is remarkable, with both magnitude and inclination tightly matching.

Overall, the (limited) comparison do not allow a complete experimental validation of the model, as the conditions inside the channel cannot be even explored with the triple Langmuir probe. However, the remarkable agreement with the discharge current signal undoubtedly confirms the physical validity of the numerical description implemented.

Regarding the model results obtained while accounting for ion-ion streaming instability, these appear barely distinguishable from the ones neglecting it. The reason is attributed to the model calibration, which has required a significantly low value for the plasma-wall interactions to comply with the magnetic-shielding configuration of the thruster. Although in the particular case studied this kinetic instability does not play a significant role, simulations of non-shielded thrusters are expected to show an higher sensitivity to it, in line with the variations observed while testing the sheath model alone for a representative air plasma.

Contents

Nomenclature

Symbols

The following list describes the symbols, both in Latin and Greek letters, used throughout this work.

Latin Symbols

A	Plasma cross-sectional area
	or energy advection term (energy conservation equation)
A_c	Geometric area of the collector plate of a plasma probe
$A_{c,eff}$	Effective area of the collector plate of a plasma probe, taking into account all the uncertainties related to probe design and internal particle interactions
AF	Neutral velocity accommodation factor
a, b	Fitting coefficients used for describing SEE from a generic material
a, b, c	Fitting coefficients used for describing Mausbach's normalized probe current
$\mathbf{B}$	Magnetic field vector
B	Scalar magnetic field. If no subscript is used it refers to the magnitude, otherwise to a component (e.g. B_r for the radial component)
C	Collision operator
	or Courant number
c_s	Common system sonic speed
$c_{s,i}$	Ion sonic speed (Bohm velocity) for the generic ion species i
$\mathbf{D}$	Vector of measured data in Bayesian analysis
D_T	Diameter of the thruster outer channel wall
$\mathbf{E}$	Electric field vector
E	Scalar electric field. If no subscript is used it refers to the magnitude, otherwise to a component (e.g. E_z for the axial component)
	or ion energy
e	Electron charge
$\hat{e}$	Unit vector
F	Thrust
F_0	Electron energy distribution function (EEDF)
f	Particle distribution function (PDF)
$f(...)$	General function of some quantity
$f(u)$	Ion velocity distribution function (IVDF)
$f(\chi)$	Normalized probe (electrode) current in Langmuir probes

f_{BM}	Breathing mode frequency
g	Ion energy distribution function (IEDF)
I	Electric current
I_{axial}	Axial component of the thruster beam current
I_{BC}	Bias-common current in Langmuir probes
I_{beam}	Thruster beam current
I_{MA}	Current through an electrode immersed in a plasma using the Mausbach's parametrization
I_{TS}	Current through an electrode immersed in a plasma using the thin sheath theory
i	Imaginary unit
j	Current density
K	Energy exchange coefficient for a generic chemical reaction
$\mathbf{k}$	Wave vector
k	Angular wavenumber
	or reaction rate for a generic chemical reaction
k_B	Boltzmann constant
L_{ch}	Thruster channel length
l_A	Angular correction factor on the φ-plane, in the analysis of Faraday probes
l_D	Distance correction factor on the φ-plane, in the analysis of Faraday probes
m	Particle mass (depending on the subscript)
N	General number of particles
n	Number density of a given particle population (depending on the subscript)
$\mathcal{P}$	Particle pressure tensor
p	Probability distribution
$\mathcal{Q}$	Tensor kernel of the collision operator C
Q	Energy conduction term (energy conservation equation)
q	Particle charge
$\mathbf{R}$	Frictional force density vector
R	Frictional force density
	or distance between the Faraday probes and the thruster
R_{in}	Thruster channel inner radius
	or plasma inner boundary radial location
R_{out}	Thruster channel outer radius
	or plasma outer boundary radial location
R_{pr}	Radius of a Langmuir probe electrode
r	Spatial coordinate along the thruster radial direction
r_L	Larmor radius
S_e	Particle collisions source/sink term (energy conservation equation)
S_c	Particle collisions source/sink term (continuity equation)
S_m	Particle collisions source/sink term (momentum conservation equation)
S_{pl}	Electron energy source/sink term in the plume

S_w	Electron energy sink term at the thruster channel walls
s	Generic plasma species
T	Temperature of a given particle population (depending on the subscript)
T_{eV}	Electron temperature (in eV)
T_g	Grid optical transmissivity, in the context of plasma probes
T_{iV}	Ion temperature (in eV)
t	Time
u	Velocity of a given particle population (depending on the subscript)
V	Electric voltage
V_{acc}	Ion acceleration voltage
V_{BC}	Bias-common voltage in Langmuir probes
V_{gC}	Ground-common voltage in Langmuir probes
V_{gp}	Ground-plasma voltage in Langmuir probes
V_{grid}	Voltage swept on the IRE grid (RPA probe)
$\mathbf{v}$	Three-dimensional velocity vector
$\mathbf{v}_r$	Three-dimensional flow-shifted velocity vector
v_T	Thermal drift velocity (most probable velocity in three-dimensions)
v_{th}	Thermal drift velocity (mean magnitude of the velocity in any single direction)
W	Power
w	Thruster channel width
$\mathbf{x}$	Three-dimensional space vector
x	Spatial coordinate along the presheath/sheath domain
$\mathbf{Y}$	Forward model of the expected **D** given a certain $\boldsymbol{\Theta}$ in Bayesian analysis
Z	Plasma dispersion function
	or assumed wave growth length
Z_i	Ion charge number (e.g. +1 for singly charge ions, +2 for doubly charged ions)
z	Spatial coordinate along the thruster axial direction
z_f	Axial location of the thruster numerical model virtual boundary in the near-plume

Greek Symbols

α	Calibration parameter for wall interaction phenomena
	or generic angle on the θ-plane, in the analysis of Faraday probes
β	Calibration parameter for ν_{anom}
	or generic angle on the φ-plane, in the analysis of Faraday probes
Γ	Particle flux
	or empirical function used for describing SEE from a generic material
γ	Adiabatic coefficient

	or plasma growth rate
	or ion-impact secondary electron emission (SEE) yield coefficient
ΔR	Thruster channel width
	or plasma width
Δt	Time step
Δu	Velocity difference
Δu_c	Ion-ion streaming instability threshold
Δz	Distance between mesh elements
$\Delta \phi$	Plasma potential difference between the numerical model boundaries (i.e. anode sheath edge and cathode orifice)
δ	Dirac delta
	or general angle, in the analysis of Faraday probes
$\delta V_1, \delta V_2$	Correction parameters in Bayesian analysis accounting for mutual interactions between triple Langmuir probe electrodes in presence of plasma inhomogeneities
ϵ	Maxwellian electron energy (in eV)
ε_0	Dielectric constant in vacuum
ϵ_{th}	Threshold electron energy for a generic chemical reaction
$\hat{\varepsilon}$	Normalized plasma dielectric function
ζ	Generic argument of the plasma dispersion function $Z(\zeta)$
$\mathbf{\Theta}$	Vector of investigated plasma properties in Bayesian analysis
θ	Normalized electron temperature (i.e. ratio between electron and ion temperatures)
	or angular coordinate along the thruster azimuthal direction
	or angular coordinate along the movement of the movable rack in the IV10 vacuum chamber
θ_1, θ_2	General parameters in Bayesian analysis
κ_A	Angular correction factor on the θ-plane, in the analysis of Faraday probes
κ_D	Distance correction factor on the θ-plane, in the analysis of Faraday probes
κ_G	Factor accounting for ions collected at the collector sidewalls in plasma probes
κ_P	Factor accounting for internal particle interactions in plasma probes
κ_{SEE}	Factor accounting for SEE in plasma probes
λ	Half-divergence angle of the thruster plume
λ_{De}	Debye length
μ	Normalized ion mass (i.e. ratio between ion and electron masses)
$\mu_{\parallel}$	Electron mobility along **B** field lines
$\mu_{\perp}$	Electron mobility across **B** field lines
μ_{eff}	Effective electron mobility enhanced by azimuthal instabilities
ν	Collision frequency
ν_{anom}	Anomalous collision frequency
ξ	Normalized spatial coordinate along the presheath/sheath

Π	Stress tensor
ρ	Charge density
Σ	Covariance matrix of the experimental data in Bayesian analysis
σ	Electron-impact secondary electron emission (SEE) yield coefficient or collision cross-section for a generic reaction
σ_{SCS}	SEE yield coefficient at space-charge saturation (SCS) condition
ϕ	Plasma potential
ϕ_w	Plasma potential drop over the sheath
φ	Normalized plasma potential or angular coordinate along the movable rack in the IV10 vacuum chamber
χ	Normalized probe potential in Langmuir probes
Ω	Complex parameter in the context of plasma kinetic theory or Hall parameter
Ω_i	Ion current fraction
ω	Dispersion relation or complex angular wave frequency
ω_e	Electron gyrofrequency
ω_p	Plasma frequency of a given particle population p

Subscripts and Superscripts

The following list describes the subscripts and the superscripts used throughout this work. Different subscripts can be found in the same symbol separated by commas. Superscripts can also be found on subscripts.

Subscripts

0	Referring to the sheath edge location
	or referring to an initial time instant
1	Referring to ion species 1 (the numbering is done in order of increasing mass)
2	Referring to ion species 2 (the numbering is done in order of increasing mass)
3	Referring to ion species 3 (the numbering is done in order of increasing mass)
4	Referring to ion species 4 (the numbering is done in order of increasing mass)
a	Referring to the thruster anode
avg	Referring to the average value of a quantity
B	Referring to the *bias* (B) electrode in Langmuir probes
$bulk$	Referring to the plasma bulk location (i.e. away from boundaries)
C	Referring to the *common* (C) electrode in Langmuir probes
c	Referring to the critical value of a quantity at the ion-ion streaming instability threshold
	or referring to the thruster cathode
	or referring to the collector plate of a plasma probe
DI	Referring to a dissociative-ionization reaction
d	Referring to the thruster discharge (i.e. discharge current and voltage)
$diss$	Referring to a dissociation reaction
e	Referring to electrons
el	Referring to an elastic momentum transfer reaction
exc	Referring to an excitation reaction
F	Referring to the farthest channel centerline, in the analysis of Faraday probes
	or referring to the *float* (F) electrode in Langmuir probes
I	Referring to the imaginary component of a quantity
IE	Referring to instability-enhanced contribution, in the context of plasma kinetic theory
i	Referring to ion species
ion	Referring to a ionization reaction
j	Referring to a plasma wave mode
	or referring to a generic plasma species j
k	Referring to a generic plasma species k
LB	Referring to Lenard-Balescu contribution, in the context of plasma kinetic theory

max	Referring to the maximum value of a quantity
min	Referring to the minimum value of a quantity
N	Referring to atomic nitrogen (N)
	or to the nearest channel centerline, in the analysis of Faraday probes
N_2	Referring to molecular nitrogen ($\mathrm{N_2}$)
O	Referring to atomic oxygen (O)
O_2	Referring to molecular oxygen ($\mathrm{O_2}$)
pl	Referring to the thruster plume
pr	Referring to a plasma probe
R	Referring to the real component of a quantity
s	Referring to a generic plasma species s
	or referring to secondary electrons
th	Referring to particle thermal agitation
	or referring to a threshold value
tot	Referring to a total quantity (by summation of partial quantities)
w	Referring to the thruster channel walls location

Superscripts

k	Referring to a specific time instant k
$s{-}s'$	Referring to an interaction between two generic plasma species s and s'

Accents

The following list describes the accents used throughout this work.

$\dot{X}$	Indicating the time derivative of the quantity X
X'	Indicating another generic quantity X or indicating the derivative of the quantity X
X^*	Indicating the reference value of the quantity X
$\bar{X}$	Indicating a generic normalized quantity X (the normalization magnitude is specified within the text)

Acronyms

The following list describes the acronyms used throughout this work.

ABEP	Air-Breathing Electric Propulsion
BPT	Bayesian Probability Theory
CEX	Charge-exchange (collisions)
CFL	Courant-Friedrichs-Lewy (stability condition)
CNR	Consiglio Nazionale di Ricerca (Italian National research Council)
DM	Development Model
EEDF	Electron Energy Distribution Function
EP	Electric Propulsion
ESE	External Shielding Electrode
FVS	Flux Vector Splitting
HET	Hall Effect Thruster
IEDF	Ion Energy Distribution Function
IRE	Ion Retarding Electrode
ISA	International Standard Atmosphere
IVDF	Ion Velocity Distribution Function
LIF	Laser-induced Fluorescence
MFFP	Magnetically Filtered Faraday Probe
PDE	Partial Differential Equation
PERE	Primary Electron Retarding Electrode
PFG	Particle Flow Generator
PIC	Particle-In-Cell
PSD	Power Spectral Density
RPA	Retarding Potential Analyzer probe
RPT	reference Performance Test
SCS	Space-charge Saturation
SEE	Secondary Electron Emission
SERE	Secondary Electron Suppressor Electrode
SR	Schumann-Runge (continuum)
STP	Standard Temperature and Pressure
TU	Test Unit
VKI	Von Karman Institute for Fluid Dynamics
VLEO	Very-Low Earth Orbit

List of Figures

List of Tables

1

Introduction

In recent years, the concept of Air-Breathing Electric Propulsion (ABEP) has gained great popularity among companies and research groups [14, 15]. In particular, the need for such technology is driven by the aim of extending the operative lifetime of VLEO satellites without requiring increasingly higher amounts of propellant [16]. Indeed, spacecrafts at these very low orbits (below 250 km altitude) greatly suffer from the drag exerted by the upper layers of the Earth atmosphere, which require them to continuously sustain their orbit with the propulsion system. Once the propellant is consumed, the satellite readily starts deorbiting. To overcome this limitation, electric propulsion systems capable of collecting and using the rarefied air present at these altitudes are currently being developed.

One of the few air-breathing electric propulsion (EP) devices currently existing is called RAM-EP and is produced by SITAEL.[1] In 2017, a RAM-EP prototype became the world-first ABEP system experimentally tested, confirming the concept feasibility [17]. To test the RAM-EP prototype in a representative environment, a Sitael HT5k Hall effect thruster (HET) was simultaneously propelled with a nitrogen/oxygen mixture (i.e. N_2/O_2) in front of the RAM-EP intake [1]. In this way, the plume of this Hall thruster, acting as a Particle Flow Generator (PFG), reproduced the high-velocity stream conditions that the RAM-EP would encounter in the upper atmosphere. However, at that time the HT5k propelled with such alternative propellant mixture had not been previously experimentally characterized and so the PFG plume representativeness could not be assessed. This aspect, which not only concerns the velocities of the accelerated particles but also their chemical species, charge and densities at the intake location, needs to be precisely investigated in order to allow an accurate RAM-EP testing. For this reason, a stand-alone experimental campaign of the PFG was carried out in the past months at the SITAEL facility in Ospedaletto (Pisa), with the aim of completely characterize its behaviour by means of a variety of plasma diagnostics. This activity represents the first step toward another future combined test of an improved RAM-EP device and the HT5K thruster acting as PFG [2].

This thesis develops around this PFG experimental campaign, by precisely focusing on the study of nitrogen/oxygen plasmas and their behaviour in Hall thrusters. Indeed, in addition to the ultimate goal of assessing the thruster representativeness as PFG, this test offered the unique opportunity of conducting an extensive experimental investigation on an air-propelled HET. To the author's knowledge, similar testing has been only performed by Gurciullo et al. [18] world-wide and, although the PFG is not intended as a thruster, this campaign may still

---

[1] The RAM-EP development is the goal of the SITAEL-led AETHER project, currently funded by the European Union's Horizon 2020 research and innovation programme.

substantially contribute to the current understanding of ABEP devices and to the development of future HETs in general. In order to investigate the air plasma produced in the PFG, in this work a one-dimensional (axial) time-dependent numerical model developed by the University of Pisa and SITAEL for studying breathing mode oscillations in HETs [10] is modified to account for a nitrogen/oxygen mixture instead of xenon. To do so, the main physical and chemical characteristics of the propellant are extensively studied and, regarding the sheath description in multispecies plasmas, even numerically modelled. In addition, the data collected during the experimental campaign are investigated and compared with the model results to evaluate its capabilities. Upon a successful implementation, the model would become one of the first-ever to simulate a Hall thruster operating with air, and it is expected to provide valuable information about the plasma behaviour in these devices.

1.1. HETs Characteristics

Hall effect thrusters are electric devices essentially formed by two components: an annular discharge chamber (also referred as thruster channel) and a hollow cathode (also acting as a neutralizer). In Figure 1.1 it is shown a schematic illustrating the basic geometry and functioning of such devices.

Because of the cathode-emitted plasma outside the thruster channel, an axial electrostatic field **E** is established between the anode plate, at the channel bottom, and this electron plasma. Near the annular chamber exit a static radial magnetic field **B** is applied to prevent the external electrons from reaching the anode (that is positively biased). Indeed, the magnetic field blocks them in a spiral motion around its field lines, as it is shown in Figure 1.1. In addition, due to the combined presence of the axial electric field, the electrons also experience an $\mathbf{E} \times \mathbf{B}$ azimuthal motion around the channel. This electric current is known as Hall current and it gives its name to the device. In this setting, the propellant (usually xenon) is fed into the cylindrical insulated chamber from the anode plate. Then, the neutral atoms moving through the trapped electrons get firstly ionized and consequently accelerated by the electric discharge potential to form the thruster beam. Once outside in the plume, part of the electrons emitted from the cathode neutralizes the beam ions in order to prevent charge accumulation on the spacecraft surfaces.

1.2. Basic Plasma Physics

In general, as the propellant gas injected into the thruster gets ionized, both ions and electrons are created, then forming what it is referred as *plasma*. In particular, a plasma is a set of charged particles, freely reacting to both internally generated and externally applied electromagnetic fields, and it is globally neutral. For this reason, as plasma modelling is concerned, ion and electron densities are considered nearly equal, i.e. $n_i \approx n_e$, determining a condition referred as *quasi-neutrality*. This assumption well applies to the bulk of plasma volume, while it does not hold for its boundaries, as it is discussed in the following. More specifically, quasi-neutrality is valid whenever the spatial scale length of the plasma is much larger than the Debye length. This distance represents the characteristic length over which significant charge separation occurs, that is when mobile charges electrically shield the electric fields in the plasma, either from charge distributions or from boundaries.

The boundaries of a plasma represent the surface interfacing with the external, through which both energy, momentum and particles get transferred. In general, depending on the conditions outside, the plasma will adapt to them by establishing potential and density variations at the boundaries. This is the case, for instance, of Hall effect thrusters, where specific electrical conditions or particle balances have to be satisfied at the walls. In general, this plasma boundary region, in which such modifications happen, is called *sheath*.

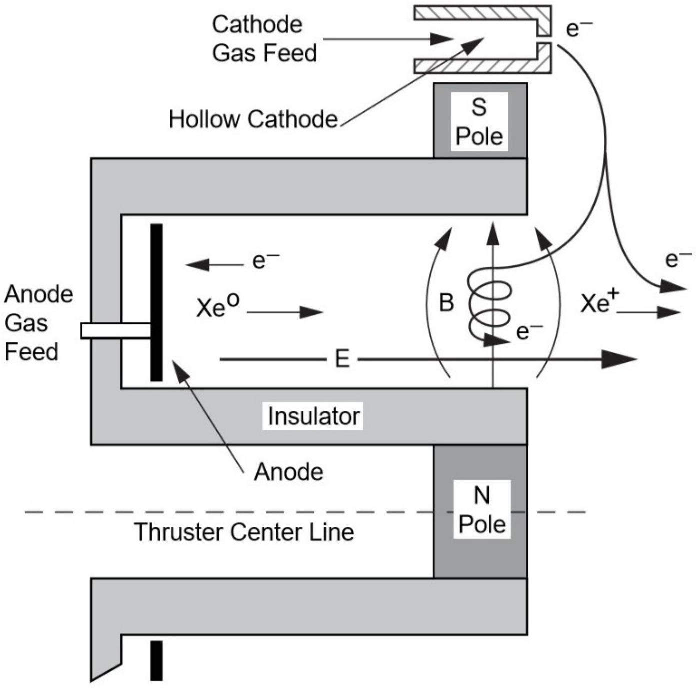

Figure 1.1: Hall effect thruster cross-section schematic illustrating the main components and features. (Source: Ref. [19])

In a generic plasma of isothermal electrons and singly charged ions, the ratio between their current densities j to the boundary is

$$\frac{j_e}{j_i} = \frac{n_e e u_e}{n_i e u_i} = \frac{u_e}{u_i} \tag{1.1}$$

where u_e and u_i represent the electron and ion velocities, respectively.

From energy conservation, in absence of an electric field, it also results

$$\begin{aligned} \frac{1}{2} m_e u_e^2 &= \frac{k_B T_e}{e} \\ \frac{1}{2} m_i u_i^2 &= \frac{k_B T_i}{e} \end{aligned} \tag{1.2}$$

where T_e and T_i are the electron and ion temperatures in kelvin, respectively. These, inserted into Eq. 1.1, give

$$\frac{j_e}{j_i} = \frac{u_e}{u_i} = \sqrt{\frac{m_i}{m_e}\frac{T_e}{T_i}} \tag{1.3}$$

which, due to the fact that in electrostatic thrusters $T_e \gg T_i$, states very clearly that electron velocities to the boundary wall are much greater than the ion ones. This result may make one wonder how the plasma would then be able to maintain quasi-neutrality. The explanation is that, at the beginning of plasma formation, the faster electrons indeed more rapidly leave the plasma bulk than the ions, and by doing so they negatively charge the boundaries. This separation forms an initial sheath, characterized by the negative potential difference generated, thus called *sheath potential*. As the sheath potential increases (negatively), increasingly more electrons get reflected back, up to a point in which equilibrium is reached and the plasma sheath results stable. Therefore, by generating a stable negative sheath that acts as an interface with the external boundaries, this self-sustained equilibrium maintains the plasma quasi-neutral.

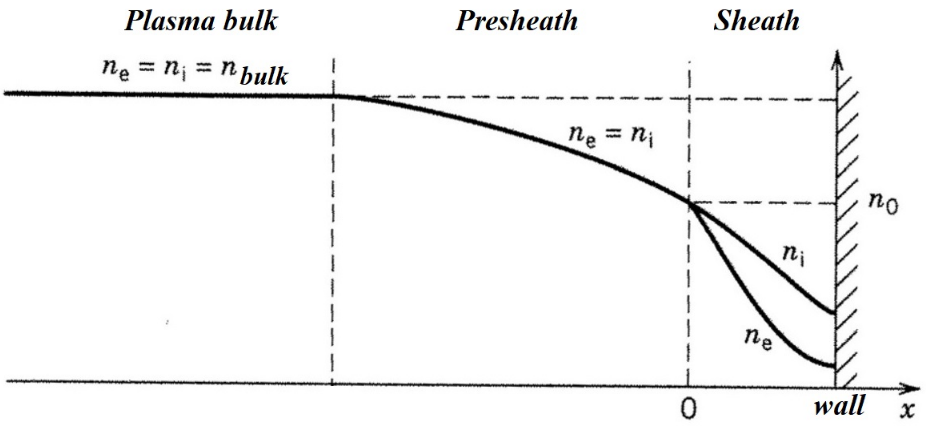

Figure 1.2: Ion and electron density profiles from the plasma bulk to the wall. (Modified from source: Ref. [20])

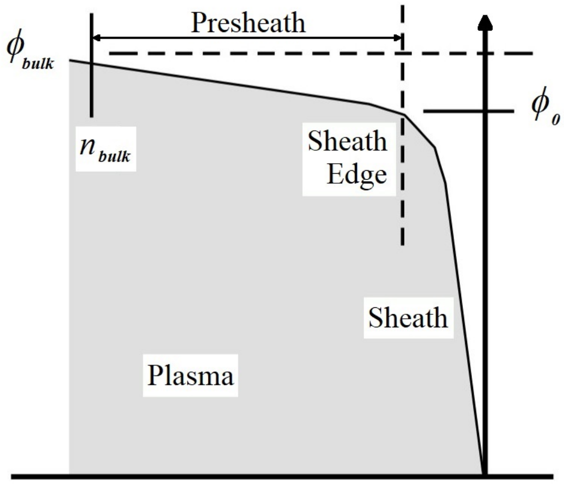

Figure 1.3: Plasma potential profile from the plasma bulk to the wall. (Modified from source: Ref. [19])

Needless to say, due to the various conditions that may be imposed by the boundaries, inside the sheath quasi-neutrality does not generally hold.

The plasma bulk is characterized by a globally constant potential and thus also by particles that can be assumed stationary and in equilibrium. In order for these conditions to match the ones at the sheath edge, it is generally identified an intermediate region called *presheath*. Along the presheath, which is much thicker than the sheath, quasi-neutrality is maintained (see Figure 1.2) but the ions are assumed to be subjected to a net potential drop ϕ_0, called *presheath potential*, which thus corresponds to the sheath edge potential relative to the plasma bulk potential ϕ_{bulk} (see Figure 1.3). This accelerates the ions which, in case they are singly charged, arrive at the sheath edge with an energy

$$\frac{1}{2} m_i u_{i,0}^2 = e\phi_0 \tag{1.4}$$

where the subscript 0 indicates the sheath edge location.

Note that the value of ϕ_0 is self-adjusted by the plasma to make the sheath stable. For a plasma composed of a unique singly charged species of positive (cold) ions and electrons only, in its well-known article, Bohm [21] analytically derived the equations governing a stable sheath. In particular, starting from Poisson's equation (see Eq. 2.37) he obtained that, in order to allow the formation of a monotonically decreasing sheath potential (thus fully ion-attracting, avoiding any non-physical oscillating characteristic), the potential drop ϕ_0 through the quasi-neutral plasma presheath needs to verify

$$\phi_0 \geq \frac{k_B T_e}{2e} \tag{1.5}$$

which is known as Bohm sheath criterion. Consequently, since the ion velocity at the sheath edge is $u_{i,0} = \sqrt{2e\phi_0/m_i}$, Eq. 1.5 gives

$$u_{i,0} \geq \sqrt{\frac{k_B T_e}{m_i}} = c_{s,i} \tag{1.6}$$

meaning that, for a stable sheath to form, the cold ion i has to enter the sheath with at least its sound (acoustic) speed $c_{s,i}$. In case a finite ion temperature T_i is considered, its sound speed results

$$c_{s,i} = \sqrt{\frac{\gamma_i k_B T_i + k_B T_e}{m_i}} \tag{1.7}$$

where γ_i is a coefficient depending on the flow conditions (e.g. $\gamma_i = 1$ for an isothermal ion flow, $\gamma_i = 5/3$ for an adiabatic flow with isotropic pressure, $\gamma_i = 3$ for a 1-D adiabatic flow [22, 23]). However, note that the ion temperature contribution is often safely neglected while dealing with electrostatic thrusters as $T_e \gg T_i$.

As a final remark, note that, while in modelling Hall effect thrusters the sheath theory mainly concerns interactions with the channel internal walls, in general it is relevant to all surfaces in contact with a plasma, thus including plasma diagnostics.

1.3. Objectives and Research Questions

The main research objective of this thesis is:

> "To investigate the plasma behaviour in an air-propelled Hall thruster by means of numerical modelling and experimental measurements".

In particular, in order to achieve such objective, several secondary goals need to be accomplished. These are now presented along with the respective research questions.

The first one is to characterize a multispecies nitrogen/oxygen plasma in terms of its internal particle interactions. These phenomena govern the plasma behaviour and thus require an accurate modelling to realize a representative simulation. Therefore, the first research question, with its two sub-questions, is formulated as:

- **Q1**: *Which are the characteristics of a multispecies nitrogen/oxygen plasma in terms of internal particle interactions and how can these be modelled?*
  - **Q1.1**: *How does the Bohm sheath criterion modify in a nitrogen/oxygen plasma?*
  - **Q1.2**: *Which chemical reactions should be considered for accurately describing the nitrogen/oxygen plasma of a Hall thruster?*

Then, the next secondary goal consists in modifying the existing thruster numerical model to simulate the PFG air plasma. To do so, the results of the previous characterization of a general nitrogen/oxygen plasma has to be properly implemented in the numerical description, together with the particular thruster features. Indeed the HT5k used as PFG for this experimental campaign implements a magnetic shielding configuration and a centrally mounted cathode which are novel characteristics not present in the version tested by Giannetti et al. [10]. These are not trivially implementable in a one-dimensional model and require a careful investigation. In addition, the numerical scheme originally employed has to be proven effective in such a complex multispecies case. Therefore, the second research question and its two sub-questions are formulated as:

- **Q2**: *How can the existing time-dependent 1D model be modified to simulate the SITAEL HT5k thruster operating with air?*
    - **Q2.1**: *Which are the model calibration parameters needed in the new formulation?*
    - **Q2.2**: *Can the originally employed numerical scheme effectively describe the behaviour of a multispecies nitrogen/oxygen plasma?*

Next, the third secondary goal concerns the experimental results. Upon a successful testing of the thruster, it will be necessary to understand how to elaborate and analyse the multitude of data collected, to depict the most insightful view of the thruster functioning. Indeed, the employment of several advanced diagnostics (i.e. Faraday probes, fast-diving triple Langmuir probe, RPA and spectrometers) will require a great effort in the data analysis phase, in which all the information will be merged in a wider scheme aiming at a thorough characterization of the thruster plasma. It is then formulated another research question which, together with its sub-question, reads as:

- **Q3**: *How can the data collected during the PFG experimental campaign be analysed and merged to completely characterize the thruster functioning?*
    - **Q3.1**: *Which are the limits encountered in the testing phase and how do they affect the thruster experimental characterization?*

Successively, by using the experimental results collected, the model has to be firstly calibrated (generally with the discharge current signal) in order to identify the correct values for the calibration parameters employed. Then, upon a successful calibration, its capabilities in reproducing the plasma behaviour will be investigated and, through comparison with the experimental data analysed, the model validation can be assessed. Therefore, the last main research question and its sub-question are formulated as:

- **Q4**: *Can the developed model successfully reproduce the plasma dynamics experimentally captured in an HT5k Hall thruster operating with air?*
    - **Q4.1**: *Which are the model limits in reproducing the thruster behaviour?*

Lastly, as a side note it is mentioned that initially also a complete data analysis of the experimental results was planned. By means of this activity, it was expected to fully characterize the PFG behaviour, so as to determine its plume representativeness for the RAM-EP thruster. However, due to time limitations of this work, such task could not be undergone.

1.4. Methodology

The methodology used to approach and solve the aforementioned objectives is now briefly outlined.

At first, it has been investigated the state-of-the-art in kinetic modelling of electropositive multispecies plasmas, so as to identify which particle interactions and instabilities could result relevant for an air-propelled HET. After having identified the ion-ion streaming instabilities in plasma presheath as a possibly relevant phenomenon, its modelling has been thoroughly studied, reproduced and then extended to the case under analysis. In parallel, also the chemical interactions in a nitrogen/oxygen plasma have been catalogued from the literature. Then, the collision frequencies relative to each one have been collected, often with the aid of LXCat databases [24], and translated in reaction rates with Bolsig+ solver [25].

Regarding the numerical model (implemented in MATLAB), the existing version, developed for xenon operations, has been updated with the previously determined particle interactions as well as the new thruster characteristics. The implementation of the latter, in particular, has required special attention in ensuring the numerical description correctness. In addition, other potentially beneficial improvements to the model have been evaluated and tested, aiming at a better representativeness and self-consistency. In this preliminary phase the model has been adjusted to just produce a meaningful plasma behaviour, as a detailed calibration of the parameters has been performed only after the experimental campaign. Specifically, by means of the collected discharge current signal, the model has been ultimately correctly calibrated. Finally, experimental measurements of the triple Langmuir probe have been used to assess its validation.

As the experimental campaign is concerned, at first the main data acquisition and analysis techniques for each employed diagnostics (spectrometers excluded[2]) have been investigated in literature. Then, these have been adapted and extended to the case of a multispecies nitrogen/oxygen plasma. However, the presence of several ion species (and so of as many different contributions mixed) has soon highlighted the need of merging together the results of several diagnostics. While this approach could not be investigated further due to time limitations of the project, the analysis models relative to each diagnostic device have been outlined for future work, especially highlighting the required cross-contributions between them.

1.5. Organization

The work is organized as follows.

In Chapter 2 is presented the general theory of instability-enhanced friction in plasma presheaths with multiple ion species. Then, the classical sheath model for an electropositive plasma is extended to a general multispecies case.

Chapter 3 discusses all the aspects related to an air plasma, starting from the definition of air used in this work. Next, the relative chemical reactions interesting a Hall thruster plasma are identified and discussed. Finally, it is developed and analysed a presheath/sheath model for a nitrogen/oxygen plasma including the effects of ion-ion streaming instabilities.

In Chapter 4 is detailed the numerical model description, modified to account for a nitrogen/oxygen plasma. Assumptions, equations and numerical scheme are presented.

Next, Chapter 5 presents an overview of the PFG experimental campaign and outlines an analysis approach for the results collected. Data processing relative to each of the diagnostic employed is detailed, with special attention to the role of a multispecies air plasma on the measurements.

Then, Chapter 6 discusses model calibration and the analysed experimental results. Successively, the plasma behaviour predicted by the model is thoroughly investigated, also in comparison with the triple Langmuir probe data.

Finally, the conclusions are presented in Chapter 7, together with the recommendation for future work. Appendices A and B respectively define the error function and the plasma dispersion function. Appendix C presents the general theory surrounding the electronic terms for atoms and molecules. Appendix D lists a complete collection of the numerical model results.

---

[2] In order to analyse the emission spectra measurements acquired by the spectrometers, it is required a collisional-radiative model of the mixture. These models are very complex and are generally developed and used by the research groups providing the instruments, which thus are also responsible for data analysis.

2

Multispecies Plasmas

With the term *multispecies plasmas* are generally referred all plasmas containing different species of ions and neutrals. While also electrons can be distinguished in different populations depending on their energy distributions, for instance, this concept is more subtle and not so sharply defined as for heavy plasma particles. These indeed can be distinguished based on their chemical nature (i.e. which element or molecule they are) or, for ions, even based on their charge state (e.g. N^-, N^+, N^{2+}). In general, regardless of the application, all plasmas are multispecies to some extent, although often the presence of multiply charged ions is safely neglected because of their very low relative concentrations.

In this work, dealing with a Hall effect thruster propelled with a mixture of atmospheric gases representing air, the presence of multiple species is critical and has to be approached thoroughly. In particular, in order to effectively model such a complex plasma, the interactions between the species and their effects on the plasma characteristics need to be clearly identified and understood. Among these, the sheath description represents one of the major unknowns, as the Bohm criterion (Eq. 1.5) in a multispecies plasma is generally underdetermined. Therefore, in this chapter it is introduced the general theory of plasma sheaths with multiple positive ion species,[1] with special focus on ion-ion streaming instabilities in the presheath, which have been shown, in literature [3], to insightfully solve the Bohm criterion uncertainties in these plasmas. The results of the theoretical models presented here are then applied to the particular case of an air plasma in Chapter 3, after having clearly defined its chemical composition.

Overall, this chapter develops as follows. At first, it is introduced the generalized Bohm sheath criterion, highlighting its limitations. Then, it is discussed the theory of ion-ion streaming instabilities in electropositive multispecies plasmas. Finally, a general sheath model in case of N ion species is developed.

2.1. Generalized Bohm Sheath Criterion

An extension of the classical model of Bohm [21] (Eqs. 1.5 and 1.6) to a case with multiple ion species was firstly derived by Riemann [23],[2] which generalized the Bohm sheath criterion for N ion species in the form

$$\sum_{i=1}^{N} \frac{n_{i,0}}{n_{e,0}} \frac{Z_i^2 c_{s,i}^2}{u_{i,0}^2 - \dfrac{v_{T,i}^2}{2}} \leq 1 \tag{2.1}$$

---

[1] As it is shown in Chapter 3, negative ion species can be neglected for the nitrogen/oxygen plasma mixture under analysis.

[2] The same formulation has been also obtained by the coeval works of Valentini [26] and Benilov [27].

where $n_{i,0}/n_{e,0}$ and $v_{T,i} = \sqrt{2\gamma_i k_B T_i/m_i}$ are, respectively, the density ratio and the thermal drift velocity of the i-th ion species. For the limit case of a unique singly charged ion species, Eq. 2.1 gives exactly $u_{i,0} \geq c_{s,i}$ with $c_{s,i}$ from Eq. 1.7, or Eq. 1.6 in case $v_{T,i}$ is neglected. This is justified by the fact that generally, in plasmas of interest $u_{i,0} \approx c_{s,i} \gg v_{T,i}$, and thus the ion thermal contribution can be safely omitted at the sheath edge.

The inequality in the Bohm criterion indicates a minimum energetic condition needed for sheath formation, which has been shown to be in general marginally verified (i.e. with the equality sign) [23, 28]. This result has been also experimentally demonstrated for quiescent weakly collisional plasmas [29, 30].

Mathematically, Eq. 2.1 alone is underdetermined and thus it can be satisfied by an infinite number of ion velocities $u_{i,0}$. In practice, two extreme cases are usually considered in studies concerning multispecies electropositive plasmas. The first is to assume that all the ion species reach the sheath edge with their individual sound velocities, i.e.

$$u_{i,0} = c_{s,i} \tag{2.2}$$

This case, implicitly neglecting any type of ion-ion interaction that may possibly arise in the plasma, considers the ion species completely independent and has been safely used for decades. Indeed, plasma kinetic theory for Coulomb collisions in low temperature plasmas generally predicts ion-ion and ion-neutral collision mean free paths in the order of few cm, which is approximately the length of the entire presheath [31]. This consideration led to conclude that the ion-ion friction is generally weak in all the plasma, presheath included. Also, theoretical works by Franklin on multispecies plasmas [32, 33, 34, 35] predicted the same result, providing an expected confirmation. However, later experimental tests with laser-induced fluorescence (LIF) in both He-Ar [36] and Ar-Xe plasmas [37, 38] unexpectedly obtained a different answer: the sheath edge velocities of the different ion species were much closer to a common system sound velocity

$$u_{i,0} = c_s = \sqrt{\sum_{i=1}^{N} \frac{n_{i,0}}{n_{e,0}} c_{s,i}^2} \tag{2.3}$$

This result, which has then become the second extreme case usually considered, has been also confirmed by later ion-acoustic wave measurements in an Ar-Xe plasma by Lee et al. [39, 40]. Specifically, they measured that the ion-acoustic wave speed at the sheath edge was approximately two times its plasma bulk speed. This was shown to imply that each ion species entered the sheath with the common sound speed c_s. However, at that time it was not identified any physical mechanism responsible for this behaviour.

2.2. Instability-Enhanced Friction

A formal explanation for the unexpected ion species velocities at the sheath edge was found only years later by Baalrud et al. [3], which demonstrated for a two-ion-species plasma that, under certain conditions, ion-ion streaming instabilities can enhance a significant collisional friction in the plasma. By taking into account this instability-enhanced friction it is possible to solve the discrepancy between theoretical models and experimental results.

In order to investigate the instability properties of a cold plasma, Baalrud et al. [3] started from the Lenard-Balescu kinetic equation [41, 42], which they generalized to account for convectively or absolutely unstable plasmas [43]. This equation, for a generic plasma species s of interest (electrons included) in an unmagnetized plasma, is [31]

$$\frac{df_s}{dt} = \frac{\partial f_s}{\partial t} + \mathbf{v} \cdot \frac{\partial f_s}{\partial \mathbf{x}} + \frac{q_s}{m_s} \mathbf{E} \cdot \frac{\partial f_s}{\partial \mathbf{v}} = C(f_s) \tag{2.4}$$

where df_s/dt is the convective derivative of the particle distribution function f_s of the species s in the six-dimensional phase space $(\mathbf{x},\mathbf{v})$, and $C(f_s)$ is the total collision operator. In presence of many plasma species s', $C(f_s)$ is equal to the sum of all the component collision operators $C(f_s, f_{s'})$ describing collisions between species s and each species s', including $s' = s$, i.e.

$$C(f_s) = \sum_{s'} C(f_s, f_{s'}) \tag{2.5}$$

Although the generalization to unstable plasmas, each component collision operator $C(f_s, f_{s'})$ can still be expressed in *Landau form*[3], thus resulting

$$C(f_s, f_{s'}) \equiv -\nabla_{\mathbf{v}} \cdot \int d^3v' \mathcal{Q}^{s-s'} \cdot \left(\frac{\nabla_{\mathbf{v}'}}{m_{s'}} - \frac{\nabla_{\mathbf{v}}}{m_s} \right) f_s(\mathbf{v}) f_{s'}(\mathbf{v}') \tag{2.6}$$

where $\nabla_{\mathbf{v}} = \partial/\partial\mathbf{v}$ is a velocity-space gradient and $\mathcal{Q}^{s-s'} = \mathcal{Q}_{LB}^{s-s'} + \mathcal{Q}_{IE}^{s-s'}$ is the tensor kernel. This formulation of $\mathcal{Q}^{s-s'}$, with the addition of an instability-enhanced component $\mathcal{Q}_{IE}^{s-s'}$ to the conventional Lenard-Balescu kernel $\mathcal{Q}_{LB}^{s-s'}$, represents the novelty of the generalization developed by Baalrud et al. [43]. In particular, $\mathcal{Q}_{LB}^{s-s'}$ refers to the stable plasma, characterized by Debye-shielded Coulomb interactions due to local plasma polarization, i.e.

$$\mathcal{Q}_{LB}^{s-s'} = \frac{2q_s^2 q_{s'}^2}{m_s} \int d^3k \frac{\mathbf{kk}}{k^4} \frac{\delta\left[\mathbf{k}\cdot(\mathbf{v}-\mathbf{v}')\right]}{\left|\hat{\varepsilon}\left(\mathbf{k},\mathbf{k}\cdot\mathbf{v}\right)\right|^2} \tag{2.7}$$

while $\mathcal{Q}_{IE}^{s-s'}$ describes instability-enhanced collective interactions, i.e.

$$\mathcal{Q}_{IE}^{s-s'} = \frac{2q_s^2 q_{s'}^2}{m_s} \int d^3k \frac{\mathbf{kk}}{k^4} \sum_j \frac{\gamma_j}{(\omega_{R,j} - \mathbf{k}\cdot\mathbf{v})^2 + \gamma_j^2} \times \frac{e^{2\gamma_j t}}{\left[(\omega_{R,j} - \mathbf{k}\cdot\mathbf{v}')^2 + \gamma_j^2\right] \left|\frac{\partial\hat{\varepsilon}(\mathbf{k},\omega)}{\partial\omega}\right|^2_{\omega_j}} \tag{2.8}$$

where j indicates each (stable or unstable) plasma wave mode. In these equations, $\mathbf{k}$ is the three-dimensional wave vector, k is its magnitude, $\hat{\varepsilon}(\mathbf{k},\omega)$ is the plasma dielectric function (discussed in the following) and $\omega_{R,j}$ and γ_j are respectively the real and imaginary parts of the dispersion relation $\omega_j(\mathbf{k})$ for the j-th mode [22], i.e.

$$\omega_j(\mathbf{k}) = \omega_{R,j}(\mathbf{k}) + i\gamma_j(\mathbf{k}) \tag{2.9}$$

which is one of the roots of $\hat{\varepsilon}(\mathbf{k},\omega) = 0$. The sign of the imaginary part γ_j, also called *growth rate*, describes the respective mode stability: a positive value indicates an unstable response while a negative or zero value stands for a damped or null response, respectively. Therefore, as it can be inferred directly for Eq. 2.8, stable plasma wave modes ($\gamma_j \leq 0$) result in a rapid decay of the wave-particle interaction term $\mathcal{Q}_{IE}^{s-s'}$, leaving essentially only the conventional Lenard-Balescu term $\mathcal{Q}_{LB}^{s-s'}$. On the contrary, unstable modes rapidly increases $\mathcal{Q}_{IE}^{s-s'}$, making it the dominant contribution [3, 31].

Regarding the plasma dielectric function $\hat{\varepsilon}(\mathbf{k},\omega)$ for electrostatic fluctuations in an unmagnetized plasma, this is defined as [31, 45]

$$\hat{\varepsilon}(\mathbf{k},\omega) = 1 + \sum_s \frac{q_s^2}{k^2\varepsilon_0 m_s} \int d^3v \frac{\mathbf{k}\cdot\nabla_{\mathbf{v}} f_s}{\omega - \mathbf{k}\cdot\mathbf{v}} \tag{2.10}$$

---

[3] *Landau form* refers to the collision operator integrand being written as the product between a tensor kernel $\mathcal{Q}$ and an asymmetric term for the velocity derivatives of the distribution functions. This form is the one originally used by Landau in its work [44]. Consequently, the formulations of Landau [44], Lenard and Balescu [41, 42] and Baalrud et al. [43] only differ in the tensor kernel $\mathcal{Q}$.

Note that here the plasma species s also comprehend electrons, as the dielectric characteristic of a plasma is affected by the complete set of particles present. Assuming a flow-shifted Maxwellian distribution for the ion species (thermal speed $\ll$ flow speed) and a normal Maxwellian distribution for the electrons (thermal speed $\gg$ flow speed) [46, 47], i.e.

$$f_i(\mathbf{v}) = \frac{n_i}{\left(\pi^{3/2} v_{T,i}^3\right)} \exp\left(-\frac{(\mathbf{v}-\mathbf{u_i})^2}{v_{T,i}^2}\right) \tag{2.11}$$

$$f_e(\mathbf{v}) = \frac{n_e}{\left(\pi^{3/2} v_{T,e}^3\right)} \exp\left(-\frac{\mathbf{v}^2}{v_{T,e}^2}\right) \tag{2.12}$$

the plasma dielectric function becomes

$$\hat{\varepsilon}(\mathbf{k},\omega) = 1 - \sum_{i=1}^{N} \frac{\omega_{p,i}^2}{k^2 v_{T,i}^2} Z'\left(\frac{\omega - \mathbf{k}\cdot\mathbf{u_i}}{k v_{T,i}}\right) - \frac{\omega_{p,e}^2}{k^2 v_{T,e}^2} Z'\left(\frac{\omega}{k v_{T,e}}\right) \tag{2.13}$$

where

$$\omega_{p,s} = \sqrt{\frac{q_s^2 n_s}{\varepsilon_0 m_s}} \tag{2.14}$$

$$v_{T,s} = \sqrt{\frac{2 k_B T_s}{m_s}} \tag{2.15}$$

are respectively the plasma frequency and the thermal velocity of species s and $Z(\zeta)$ is the plasma dispersion function [48]. This can be written as

$$Z(\zeta) = 2ie^{-\zeta^2} \int_{-i\zeta}^{\infty} e^{-t^2} dt = i\sqrt{\pi} e^{-\zeta^2} \operatorname{erfc}(-i\zeta) \tag{2.16}$$

in which erfc represents the complementary (complex) error function. The derivative of $Z(\zeta)$, appearing in Eq. 2.13, is defined as

$$Z'(\zeta) = \frac{dZ(\zeta)}{d\zeta} = -2\left[1 + \zeta Z(\zeta)\right] \tag{2.17}$$

All the properties and characteristics of both error function and plasma dispersion function are discussed in detail in Appendices A and B, respectively.

Considering that ion-ion streaming instabilities have a phase speed ω in the order of the ion sound speed $v_{T,i}$ and that electrons are much hotter than ions ($T_e \gg T_i$), it is assumed

$$\frac{\omega}{k v_{T,e}} \approx \sqrt{\frac{T_i m_e}{T_e m_i}} \ll 1 \tag{2.18}$$

also effectively excluding ion-acoustic instability, that is generally much weaker (i.e. lower growth rate) than ion-ion instability [47]. As a consequence, it is obtained

$$\hat{\varepsilon}(\mathbf{k},\omega) = 1 + \frac{1}{k^2 \lambda_{De}^2} \sum_{i=1}^{N} \left[1 - \frac{Z_i^2}{2} \frac{T_e}{T_i} \frac{n_i}{n_e} Z'\left(\frac{\omega - \mathbf{k}\cdot\mathbf{u_i}}{k v_{T,i}}\right)\right] \tag{2.19}$$

where λ_{De} is the Debye length, defined as

$$\lambda_{De} = \sqrt{\frac{\varepsilon_0 k_B T_e}{e^2 n_e}} \tag{2.20}$$

Note that in Eq. 2.19, the density ratio n_i/n_e refers to any plasma location at which the instability is investigated. Having assumed a quasi-neutral plasma everywhere except from the sheath and considering that ion-ion streaming instabilities can only arise in the presheath, $n_i/n_e = n_{i,bulk}/n_{e,bulk} = n_{i,0}/n_{e,0}$ is always constant in the plasma of interest.

Having introduced the theory behind ion-ion streaming instabilities, it is now discussed the instability-enhanced friction and its effects on the ion species flowing in the presheath. Starting from the plasma kinetic equation (Eq. 2.4), by taking the lowest order velocity-space moments, namely density moment ($\int d^3v \dots$) and momentum moment ($\int d^3v m_s \mathbf{v} \dots$), it can be derived, respectively, the fluid continuity equation

$$\frac{\partial n_s}{\partial t} + \nabla \cdot (n_s \mathbf{u_s}) = 0 \tag{2.21}$$

and the momentum conservation equation

$$m_s n_s \left(\frac{\partial \mathbf{u_s}}{\partial t} + \mathbf{u_s} \cdot \nabla \mathbf{u_s} \right) = n_s q_s \mathbf{E} - \nabla \cdot \mathcal{P}_s - \nabla \cdot \Pi_s + \mathbf{R_s} \tag{2.22}$$

In particular, all the fluid variables appearing have been defined in terms of the velocity-space moments of the distribution function f_s, so that $n_s \equiv \int d^3v f_s$ is the density, $\mathbf{u_s} \equiv \int d^3v \mathbf{v} f_s / n_s$ is the fluid flow velocity, the pressure tensor is $\mathcal{P} \equiv \int d^3v m_s \mathbf{v_r} \mathbf{v_r} f_s$ where $\mathbf{v_r} \equiv \mathbf{v} - \mathbf{u_s}$ is a flow-shifted phase-space variable, $\Pi_s \equiv \int d^3v m_s (\mathbf{v_r}\mathbf{v_r} - v_r^2 I/3) f_s$ is the stress tensor and $\mathbf{R_s} \equiv \sum_{s'} \int d^3v m_s \mathbf{v} C(f_s, f_{s'})$ is the frictional force density.

Since each component collision operator $C(f_s, f_{s'})$ is defined as the sum of two terms (i.e. Lenard-Balescu and instability-enhanced) also the frictional force density $\mathbf{R_s}$ for each species s can be written as

$$\mathbf{R_s} = \mathbf{R_{LB,s}} + \mathbf{R_{IE,s}} \quad \Rightarrow \quad \mathbf{R_s} = \sum_{s'} \mathbf{R^{s-s'}} = \sum_{s'} \mathbf{R_{LB}^{s-s'}} + \mathbf{R_{IE}^{s-s'}} \tag{2.23}$$

Moreover, since the collision operator conserves momentum (the proof is available in Ref. [49]), the frictional force density exerted between any two species s and s' is equal and opposite, i.e.

$$\mathbf{R^{s-s'}} = -\mathbf{R^{s'-s}} \tag{2.24}$$

Consequently, the frictional force accelerates the slower species while it slows down the faster one.

By theoretically calculating $\mathbf{R_{LB}^{1-2}}$ and $\mathbf{R_{IE}^{1-2}}$ for the two singly charged ions of a 50% Ar + 50% Xe plasma (i.e. Ar^+ and Xe^+, indicated as $s = 1$ and $s' = 2$), Baalrud et al. [31] were able to compare the stable plasma frictional contribution with the developed instability-enhanced friction. The results, shown in Figure 2.1, represent the stable plasma contribution $\mathbf{R_{LB}^{1-2}}$ and the instability-enhanced one (i.e. $\mathbf{R_{IE}^{1-2}}$) for ion-ion two-stream instabilities after three different wave growth lengths, namely $Z = 10\lambda_{De}, 15\lambda_{De}$ and $20\lambda_{De}$. For the plasma investigated by the authors (see Ref. [38]), the presheath length is $\approx 5\,\mathrm{cm}$ and $\lambda_{De} \approx 6 \times 10^{-3}\,\mathrm{cm}$, so that a wave growth of $20\lambda_{De}$ represents only $\approx 2.4\%$ of the presheath. Nevertheless, the figure shows clearly that even within such a tiny length span the instability-enhanced friction grows enormously to over 10^4 times the stable plasma contribution, thus dominating the momentum conservation equation. Such friction is so strong that, in view of the equal and opposite interaction between the ion species (Eq. 2.24), the authors safely claimed that the differential flow effectively locks when instability arises [31]. In other words, the friction prevents the ion species from freely accelerating toward the sheath and forces them to maintain the constant velocity difference Δu_c, which corresponds to the threshold at which instability arises. Figure 2.2 depicts these predicted velocity profiles.

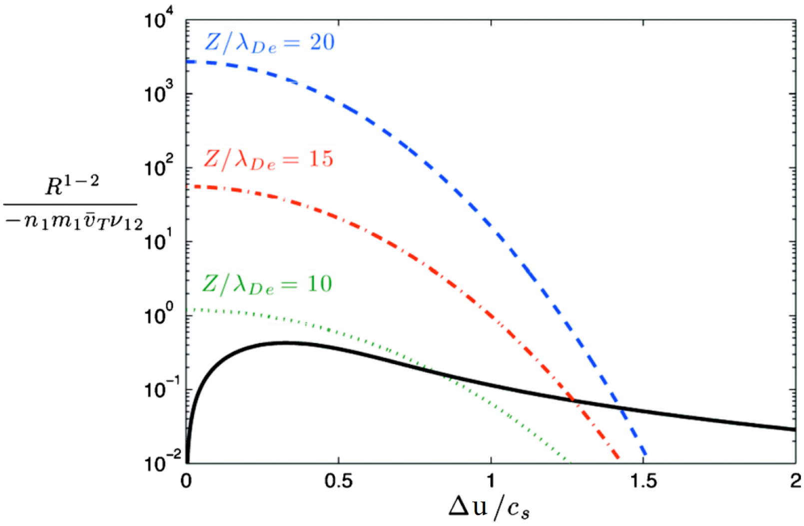

Figure 2.1: Normalized collisional friction force density in a 50/50 Ar-Xe plasma (parameters taken from Ref. [38]) for varying normalized flow difference. The black solid line represents the stable plasma (Lenard-Balescu) contribution. The coloured lines represent the instability-enhanced contribution after three different wave growth lengths. (Modified from source: Ref. [31])

In the limit case of cold ions (i.e. $T_i = 0$), it results $\Delta u_c = 0$ and the instability directly appears at the beginning of the presheath where ions are assumed stationary. In this case, the ion species arrive at the sheath edge with the common system sound speed c_s.

In a general case with finite ion temperatures, the instability onset occurs at $\Delta u_{12} = u_{1,0} - u_{2,0} \geq \Delta u_c \approx \mathcal{O}(v_{T,i})$, where the value of Δu_c in principle can be any, depending on plasma parameters (e.g. electron and ion temperatures) and composition. Clearly, in case $\Delta u_c \geq c_{s,1} - c_{s,2}$ the ion species reach the sheath edge before the condition for the instability onset is fulfilled, thus verifying the Bohm sheath criterion with the individual sound speed of the species. Therefore, it can be stated that, for two generic ion species "1" and "2", the velocity difference at the sheath edge is

$$\Delta u = \min(|c_{s,1} - c_{s,2}|, \Delta u_c) \tag{2.25}$$

For a plasma with only two ion species, this condition allows to uniquely solve the generalized Bohm criterion (Eq. 2.1) for each ion species velocity $u_{i,0}$. The resulting solutions for a two ion species plasma have been validated by both experimental measurements [4] and Particle-In-Cell (PIC) simulations [50], confirming the theory validity. Moreover, ion-ion two-stream instability has been also measured in an He-Ar plasma with similar concentrations, showing oscillations in the MHz order [51].

Regarding the conditions necessary for the ion-ion streaming instability to onset, intimately related to a sufficiently large Δu, also the electron and ion temperatures play a crucial role. In particular, the temperature ratios T_e/T_i must be larger than some corresponding threshold ratios $(T_e/T_i)_c$ for the instability to arise before the ion species reach their sound speeds at the sheath edge [50]. Therefore, the conditions required are

$$\begin{cases} \Delta u > \Delta u_c \\ \dfrac{T_e}{T_i} > \left(\dfrac{T_e}{T_i}\right)_c \qquad \text{for every } i \end{cases} \tag{2.26}$$

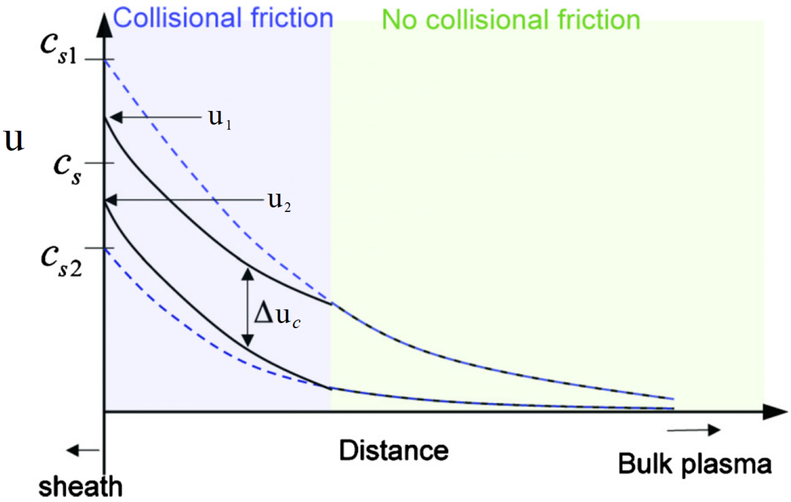

Figure 2.2: Sketch of the predicted velocity profiles for two ion species in case of ion-ion two-stream instability. Two distinct regions form: one with no collisional friction (before the instability onset) and one with collisional friction. In the former, the ion species acceleration is free and independent. In the latter, the differential flow is locked on the threshold value Δu_c. (Modified from source: Ref. [31])

Note that these thresholds are not independent as the ion temperatures T_i directly affect the onset of instability. Indeed, in the simplified case in which all ion temperatures are equal, a higher T_i determines a more intense thermal motion of ions, which acts more strongly against the instability-enhanced friction, thus increasing Δu_c.[4] Instead, the electron temperature T_e does not influence the value of Δu_c but rather the presheath location at which this threshold is reached: higher T_e means higher velocities and thus a threshold encountered nearer the plasma bulk. Therefore, the relation between Δu_c and $(T_e/T_i)_c$ is univocal and they can only be verified together.

Finally, as the plasma composition influence on Δu_c is concerned, it has been demonstrated that, in a plasma with two ion species, extreme density ratios (i.e. nearly single-species plasma) determine the absence of instability [4, 50]. The reason is that these very unbalanced compositions strongly limit the mutual interaction between the two species, as one is greatly underrepresented, thus requiring very high Δu_c.

In conclusion, this theoretical approach involving ion-ion streaming instabilities has been shown capable of explaining the previously unclear discrepancy seen in experimental results (recall Section 2.1), expanding the understanding of multispecies plasmas.

2.3. Sheath Model

It is now derived a general model for a collisionless sheath in presence of secondary electron emission (SEE) from an insulated wall in contact with a multispecies plasma composed of N ion species. This allows to resolve the plasma boundary conditions at the channel walls of a HET. In particular, once the ion velocities at the sheath edge are defined (by the kinetic approach just presented, for instance), by modelling the sheath it is possible to define the particle, momentum and energy exchanges happening at this interface.

Before starting the derivation, in Figure 2.3 is defined the reference system used for the spatial coordinate x and the sheath potential ϕ. Note that, in a plasma forming an ion sheath (the one here considered), the potential monotonically decreases going toward the wall along the

---

[4] Note that in case the ion temperatures vary independently, this cause-effect relation is not always valid. An example can be found in Subsection 3.3.4.

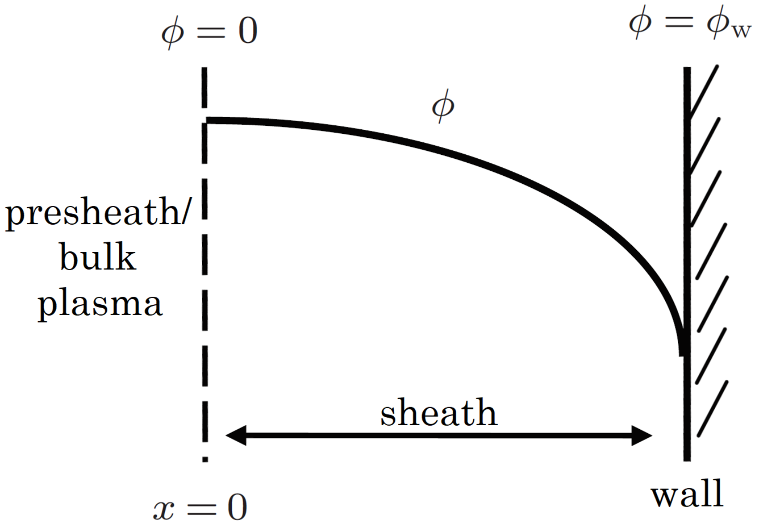

Figure 2.3: Sketch of the potential profile in a general plasma ion sheath. Going toward the wall, ϕ grows negatively with respect to the sheath edge potential and x increases. (Modified from source: Ref. [52])

presheath/sheath. Therefore, the sheath potential ϕ is here considered negative with respect to the sheath edge at which $\phi_0 = 0$. Concerning x, it is assumed $x > 0$ in the sheath and $x < 0$ in the presheath. It is worth mentioning that, from now on in this chapter, the subscript s will be used to indicate the population of secondary electrons, and not a generic plasma species as done previously.

2.3.1. Basic Equations

Assuming a Maxwellian distribution of electrons (i.e. thermodynamic equilibrium) the primary electron density in the sheath is governed by the Boltzmann relationship

$$n_e = n_{e,0} \exp\left(\frac{e\phi}{k_B T_e}\right) \tag{2.27}$$

In a steady-state collisionless sheath, continuity and momentum conservation equations for each ion population with constant temperature T_i are

$$\frac{d}{dx}(n_i u_i) = 0 \tag{2.28}$$

$$m_i u_i \frac{du_i}{dx} = -Z_i e \frac{d\phi}{dx} - \frac{\gamma_i k_B T_i}{n_i}\frac{dn_i}{dx} \tag{2.29}$$

where the ion pressure is given by $\mathcal{P}_i = \gamma_i n_i k_B T_i$. Note that this expression should be more rigorously written as a stress tensor since $\mathcal{P}_i$ can, in general, be anisotropic.

In the following, the ion pressure contribution in Eq. 2.29 (second term of the right-hand side) will be neglected, even if a cold ion model is not formally considered in this derivation. The reason is that, as previously explained for the ion sound speed (see Eqs. 1.7 and 2.1), the electron temperature T_e is generally much higher than the (although finite) ion temperature T_i. As a consequence the influence of this term on the sheath characteristics results minimal. Instead, the advantage of this simplification is that it allows to express in a closed form the ion density n_i, thus enabling an analytical manipulation of the expressions.

The wall bombardment from the plasma (highly energetic) primary electrons determines an emission of low-energy secondary electrons (i.e. few eV [53, 54]), in a ratio defined by the material-dependent SEE yield coefficient σ (see Eq. 2.35). By assuming that in the sheath this population of secondary electrons follows the conservation laws [55], the continuity and momentum conservation equations result

$$\frac{d}{dx}(n_s u_s) = 0 \quad \Rightarrow \quad n_{s,0}u_{s,0} = n_s u_s = n_{s,w}u_{s,w} \tag{2.30}$$

$$m_e u_s \frac{du_s}{dx} = e\frac{d\phi}{dx} - \frac{\gamma_s k_B T_s}{n_s}\frac{dn_s}{dx} \tag{2.31}$$

where the subscripts 0 and w indicate the sheath edge and the wall locations, respectively.

As for the ion case, also the (constant) secondary electron temperature T_s is generally much lower than that of the impinging primary electrons. Therefore, it will be neglected as well in the following.

In case the walls are insulated, as in Hall thrusters, the wall potential ϕ_w is floating and it adjusts itself so as to ensure that a zero net current enters the wall. This current balance at the wall, in steady-state, writes as

$$j_e = \sum_{i=1}^{N} j_i + j_s \tag{2.32}$$

where

$$j_e = \frac{1}{4} e n_{e,0}\sqrt{\frac{8k_B T_e}{\pi m_e}} \exp\left(\frac{e\phi_w}{k_B T_e}\right) \tag{2.33}$$

$$j_i = Z_i e n_{i,0} u_{i,0} \tag{2.34}$$

$$j_s = \sigma j_e \tag{2.35}$$

are the current densities for primary electrons, ions and secondary electrons, respectively.

Moreover, since the plasma is assumed quasi-neutral everywhere apart from the sheath, charge neutrality holds at the sheath edge, i.e.

$$\sum_{i=1}^{N} Z_i n_{i,0} = n_{e,0} + n_{s,0} \tag{2.36}$$

Regarding the electrostatic sheath potential ϕ, this is governed by Poisson's equation

$$\frac{d^2\phi(x)}{dx^2} = -\frac{e}{\varepsilon_0}\left(\sum_{i=1}^{N} Z_i n_i - n_e - n_s\right) = -\frac{\rho}{\varepsilon_0} \tag{2.37}$$

in which the primary electron density n_e has been defined in Eq. 2.27. The ion density n_i can be determined by firstly integrating Eq. 2.29 and then using Eq. 2.28, so as to obtain

$$n_i = \frac{n_{i,0}}{\sqrt{1 - \dfrac{2Z_i e\phi}{m_i u_{i,0}}}} \tag{2.38}$$

Similarly, the secondary electron density n_s can be obtained from Eqs. 2.30 and 2.31, thus resulting

$$n_s = \frac{n_{s,0}u_{s,0}}{\sqrt{\dfrac{2e(\phi - \phi_w)}{m_e} + u_{s,w}^2}} \tag{2.39}$$

Finally, the condition necessary for the formation of a stable sheath (i.e. monotonically decreasing potential) can be expressed in the form [22, 23]

$$\left.\frac{d\rho}{d\phi}\right|_{\phi=0} \leq 0 \tag{2.40}$$

Its derivation starts by linearizing Eq. 2.37 near the sheath edge ($\phi = \phi_0 = 0$), assuming that the charge density ρ is a function of the potential ϕ. This gives

$$\varepsilon_0 \frac{d^2\phi}{dx^2} = -\left.\frac{d\rho}{d\phi}\right|_{\phi=0} \phi \tag{2.41}$$

Then, multiplying by the electric field $E = -d\phi/dx$ and then integrating over dx results in

$$\frac{\varepsilon_0 E^2}{2} = -\left.\frac{d\rho}{d\phi}\right|_{\phi=0} \frac{\phi^2}{2} \tag{2.42}$$

which implies the condition of Eq. 2.40.

Nondimensionalization

In order to make the sheath model dimensionless, the following arbitrary variables are defined

$$\begin{cases} \xi = \dfrac{x}{\lambda_{De}} \\ \varphi = \dfrac{e\phi}{k_B T_e} \\ \bar{n}_j = \dfrac{n_j}{n_{e,0}} \quad \text{for} \quad j = e, i, s \\ \bar{u}_i = \dfrac{u_i}{v_{T,1}} \\ \bar{u}_{s,w} = \dfrac{u_{s,w}}{v_{T,1}} \\ \mu = \dfrac{m_1}{m_e} \\ \theta = \dfrac{T_e}{T_1} \end{cases} \tag{2.43}$$

Consequently, Poisson's equation (Eq. 2.37) becomes

$$\frac{d^2\varphi}{d\xi^2} = \sum_{i=1}^{N} -Z_i \bar{n}_i + \bar{n}_e + \bar{n}_s \tag{2.44}$$

with

$$\bar{n}_i = \frac{\bar{n}_{i,0}}{\sqrt{1 - \theta \dfrac{m_1}{m_i} \dfrac{Z_i \varphi}{\bar{u}_{i,0}^2}}} \tag{2.45}$$

$$\bar{n}_e = \exp(\varphi) \tag{2.46}$$

$$\bar{n}_s = \frac{\sigma}{1-\sigma} \frac{\sum_{i=1}^{N} Z_i \bar{n}_{i,0} \bar{u}_{i,0}}{\sqrt{\theta\mu(\varphi - \varphi_w) + \bar{u}_{s,w}^2}} \tag{2.47}$$

Also, the zero current condition at the wall (Eq. 2.32) results

$$\sum_{i=1}^{N} Z_i \bar{n}_{i,0} \bar{u}_{i,0} = (1-\sigma)\sqrt{\frac{\theta\mu}{4\pi}} \exp\left(\varphi_w\right) \tag{2.48}$$

and the charge neutrality condition at the sheath edge becomes

$$\sum_{i=1}^{N} Z_i \bar{n}_{i,0} = 1 + \bar{n}_{s,0} \tag{2.49}$$

where

$$\bar{n}_{s,0} = \frac{\sigma}{1-\sigma} \frac{\sum_{i=1}^{N} Z_i \bar{n}_{i,0} \bar{u}_{i,0}}{\sqrt{-\theta\mu\varphi_w + \bar{u}_{s,w}^2}} \tag{2.50}$$

Finally, the condition for a stable sheath formation defined in Eq. 2.40 results

$$\frac{d}{d\varphi}\left(\sum_{i=1}^{N} -Z_i \bar{n}_i + \bar{n}_e + \bar{n}_s\right)\Bigg|_{\varphi=0} \leq 0 \tag{2.51}$$

which, by substitution of Eqs. 2.45 to 2.47, gives the generalized Bohm sheath criterion for a plasma with N ion species in presence of SEE, i.e.

$$\sum_{i=1}^{N} \frac{1}{2}\theta \frac{m_1}{m_i} \frac{Z_i^2 \bar{n}_{i,0}}{\bar{u}_{i,0}^2} + \frac{1}{2}\frac{\theta\mu\sigma}{1-\sigma} \frac{\sum_{i=1}^{N} Z_i \bar{n}_{i,0} \bar{u}_{i,0}}{\sqrt{\left(-\theta\mu\varphi_w + \bar{u}_{s,w}^2\right)^3}} \leq 1 \tag{2.52}$$

2.3.2. Space-Charge Saturation Regime

While the SEE yield coefficient σ for a particular material can in principle assume even values higher than one, in plasma sheaths the secondary electron emission is space charge limited, as determined by Hobbs and Wesson [56] in their renowned work. In particular, above a certain electron temperature, the sheath enters in a space-charge saturation regime characterized by a fixed coefficient σ_{SCS}. A general expression for σ is then [19]

$$\sigma = \min(\Gamma(2+b)a\ T_{eV}^b, \sigma_{SCS}) \tag{2.53}$$

where T_{eV} is the electron temperature in eV, $\Gamma(x)$ is the gamma function and a and b are coefficients usually obtained from experimental data fits.[5] However, in multispecies plasmas σ_{SCS} is not generally known and needs to be self-consistently computed from the sheath solution. In particular, during emission saturation the electric field at the wall reaches zero and so, by integrating Poisson's equation (Eq. 2.44) over the potential ϕ using this condition, it is obtained

$$\begin{aligned}
&\sum_{i=1}^{N} 2\frac{m_i}{m_1}\frac{\bar{n}_{i,0}\bar{u}_{i,0}^2}{\theta}\left(\sqrt{1-\theta\frac{m_1}{m_i}\frac{Z_i\varphi_w}{\bar{u}_{i,0}^2}}-1\right) + \exp(\varphi_w) - 1 \\
&+ \frac{2\sigma_{SCS}}{1-\sigma_{SCS}}\frac{\sum_{i=1}^{N} Z_i\bar{n}_{i,0}\bar{u}_{i,0}}{\sqrt{\theta\mu}}\left(\frac{\bar{u}_{s,w}}{\sqrt{\theta\mu}} - \sqrt{-\varphi_w + \frac{\bar{u}_{s,w}^2}{\theta\mu}}\right) \\
&+ \frac{1}{2}\left(\frac{d\varphi}{d\xi}\right)^2\Bigg|_{\varphi=0} = 0
\end{aligned} \tag{2.54}$$

---

[5] More information can be found in Ref. [19]

which allows to solve for σ_{SCS}. Note that in this expression it also appears the electric field at the sheath edge $\bar{E}_0 = (-d\varphi/d\xi)|_{\varphi=0}$, which is generally equal to 0. Indeed, in plasmas of interest the potential variation along the presheath is negligibly small with respect to that characterizing the sheath, as a comparable potential drop is spread over a length orders of magnitude greater. Therefore, $(d\varphi/d\xi)|_{\varphi=0} \approx 0$. In practice, for the model numerical stability it is used a value of 0.01, which does not affect the solution validity.

2.3.3. Electron Power Loss

The average power lost by a Maxwellian distribution of electrons on the channel walls (characterized by a negative-going sheath potential) is defined as [19]

$$W = \nu_{e,w}\left[2k_BT_e + (1-\sigma)e|\phi_w|\right] \tag{2.55}$$

where $\nu_{e,w}$ is the electron-wall collision frequency. In this expression, the first term $2k_BT_e$ represents the mean energy deposited on the wall by a Maxwellian distribution of electron with energy k_BT_e. The second one instead is the net energy lost by the electron flow (also accounting for secondary electrons emitted from the wall) to traverse the negative-going sheath.

The average power of Eq. 2.55 can be made adimensional by defining the following arbitrary variables

$$\begin{cases} \bar{\nu}_{j,w} = \dfrac{\nu_{j,w}\Delta R}{v_{T,1}} \quad \text{for} \quad j = e,i \\ \bar{W} = \dfrac{W\Delta R}{v_{T,1}k_BT_e} \end{cases} \tag{2.56}$$

where $\Delta R = R_{out} - R_{in}$ is the difference between channel outer and inner radii. The reason for not using λ_{De} here as the reference length (as it has been done in System 2.43) is the very different length scale considered. Indeed, the variable x refers to distances in the presheath, which are in the order of λ_{De}, while W is related to processes happening in the whole channel radial dimension. Consequently, it is obtained

$$\bar{W} = \bar{\nu}_{e,w}\left[2 + (1-\sigma)|\varphi_w|\right] \tag{2.57}$$

where φ_w can be explicitly obtained from the zero current condition at wall (Eq. 2.48), so as

$$\varphi_w = -\ln\left[\frac{(1-\sigma)\sqrt{\dfrac{\theta\mu}{4\pi}}}{\displaystyle\sum_{i=1}^{N} Z_i\bar{n}_{i,0}\bar{u}_{i,0}}\right] \tag{2.58}$$

In order to determine $\bar{\nu}_{e,w}$, it is first written the balance between ions and electron fluxes at the wall, i.e.

$$\sum_{i=1}^{N}\Gamma_{i,w} = (1-\sigma)\Gamma_{e,w} \tag{2.59}$$

where the ion flux to the walls of the species i in a channel control volume of width dz results

$$\Gamma_{i,w} = n_{i,0}u_{i,0}2\pi(R_{out} + R_{in})dz \tag{2.60}$$

Then, the ion-wall collision frequency $\nu_{i,w}$ is obtained by calculating $\Gamma_{i,w}$ per unit density and unit volume, thus obtaining

$$\nu_{i,w} = \bar{n}_{i,0}u_{i,0}\frac{2}{\Delta R} \tag{2.61}$$

Consequently, by doing the same for $\Gamma_{e,w}$ and then bringing all in adimensional form, from Eq. 2.59 it results

$$\bar{\nu}_{e,w} = \frac{2\sum_{i=1}^{N} \bar{n}_{i,0}\bar{u}_{i,0}}{(1-\sigma)} \tag{2.62}$$

2.4. Summary

To conclude the theoretical discussion about multispecies plasmas, it is here proposed a brief summary.

At first, starting from the introductory discussion of Section 1.2, the generalized Bohm sheath criterion in multispecies plasmas was presented, highlighting the related uncertainties in the correct definition of the ion velocities at the sheath edge. In order to solve them, it was then explored the theory of instability-enhanced friction in the presheath which, through a kinetic description of ion-ion streaming instabilities, is known to accurately predict these velocities in a plasma with two ion species [4]. This kinetic model will be extended to the case of an nitrogen/oxygen plasma in Chapter 3, where the type and number of ion species considered will be defined.

Next, a comprehensive sheath model with N ion species was presented, thus posing the theoretical bases for the modelling activities carried out in the following chapters. In particular, in Chapter 3, by exploiting the ion velocities at the sheath edge obtained from the kinetic instability analysis, the model will be solved for the case of an nitrogen/oxygen plasma.

3

Air Plasma

In this chapter, it is discussed the particular case study of an air plasma.

At first, it is defined what it is meant by *air*. Indeed, air is a mixture of several different molecular and atomic species of gases, which composition varies greatly throughout the atmosphere. Then, thanks to a simplified atmospheric model of the thermosphere, it is justified the choice of using a N_2/O_2 mixture for both the numerical modelling of the PFG and its experimental characterization. Contextually, as the thruster numerical model (described in Chapter 4) requires a detailed knowledge of the plasma chemical interactions, these are thoroughly investigated and defined based on the available literature data. Indeed, propellant type and composition have an enormous impact on the plasma dynamics (and so on the thruster performance) and an accurate modelling of its internal interactions is key to aim for the most representative results.

Finally, after having identified the ion species to be considered, the general sheath model proposed in Chapter 2 is applied to the nitrogen/oxygen case and solved for some representative conditions. In particular, the effect of ion-ion streaming instabilities is investigated both in case SEE is considered and in case it is not. Then, with the aim of further characterizing how these instabilities affect the sheath of this plasma, it is presented a detailed sensitivity analysis exploring different plasma compositions and parametric ranges.

3.1. Atmospheric Model

The Particle Flow Generator (PFG) has the objective of generating a particle flow as representative as possible of the one encountered by the RAM-EP orbiting in the upper atmosphere layers (i.e. thermosphere). In order to achieve this goal, the composition of the air used as propellant in the PFG must be carefully selected, also in relation to the thruster performance, which determines how effectively the propellant gets dissociated and/or ionized. However, this effort suffers from many limitations.

The first is that the atmosphere composition is subjected to wide variations with altitude, orbit, diurnal and seasonal cycles, as well as solar and geomagnetic activity. Consequently, unless a precise mission is selected, only a mean composition can be obtained from any atmospheric model. In particular, during the conceptual design of the RAM-EP thruster [5], SITAEL researchers defined this mean composition by means of the NRLMSISE-00 atmospheric model [57] according to the ECSS-E-ST-10-04C standard [58]. Figure 3.1 shows the resulting mean number density variation with altitude for each of the species present in the 150 km to 250 km range. Among them, the figure indicates that on average H, He and Ar are

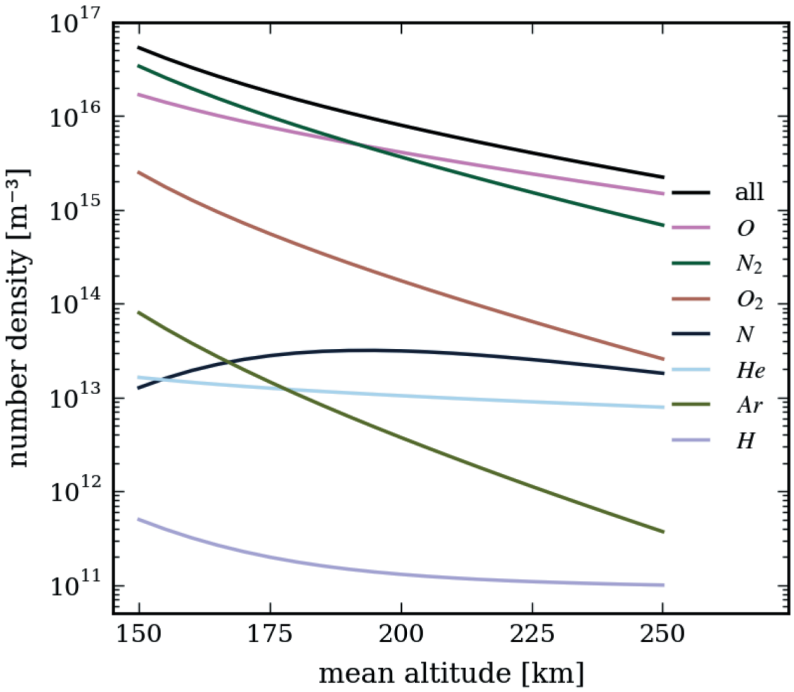

Figure 3.1: Mean thermosphere composition calculated by means of the NRLMSISE-00 model ($F_{10.7} = F_{10.7avg} = 140, A_p = 15$). For the calculation the authors assumed circular dusk-dawn sun-synchronous orbits averaged over orbital, diurnal and seasonal cycles, for moderate (as defined in the ISO 14222:2013 standard [59]) solar and geomagnetic activity. (Source: Ref. [5])

significantly less abundant than N_2, N, O_2 and O.[1] As a consequence, a nitrogen/oxygen mixture has been selected as the PFG propellant. However, the precise N_2/O_2 ratio required to obtain in the thruster plume representative densities for all four target species, if any, is highly dependent on the thruster performance. This dependency represents another great limitation in the process of selecting the appropriate propellant composition, as both dissociation and ionization efficiencies of the PFG are not known a priori. While in general only modelling the complex plasma behaviour of such mixture could provide a precise correlation between propellant composition and plume composition, just knowing these two efficiencies would allow a better guess. However, this not being the case, the propellant composition was assumed only starting from the target densities in Figure 3.1. In particular, by considering all the atomic nitrogen and oxygen to have dissociated from N_2 and O_2, respectively, an average N_2/O_2 ratio of 1.27 was obtained [5].

Note that variations in the assumptions made to derive this ratio may affect the applicability of the results obtained in Section 3.3 and in the following chapters. However, without even knowing the ratio sensitivity, this cannot be assessed. To do so, it would be required an accurate analysis of the NRLMSISE-00 atmospheric model, which however goes beyond the scope of this work.

3.2. Chemical Model

While the atmospheric model only provides details about the target PFG plume composition, an accurate modelling of the chemical reactions between the plasma species is crucial to track

---

[1] By looking at the results plotted in Figure 3.1, N shows a relatively low density comparable to He over the entire altitude range. Nevertheless, the reason that led to the inclusion of N and not of He is that the former is directly related to N_2, which is instead highly abundant.

their evolution. In general, to do so by means of any fluid numerical model, it is necessary to define the mass, momentum and energy source (or sink) terms in the respective conservation equations for each species. These are intimately related not only to the species chemical reactions, but also to the interactions with the thruster channel wall, for instance. Knowing and modelling these processes (based on statistical data) then results crucial to reproduce how each species is formed or recombined, as well as how it exchanges momentum and energy in the plasma.

The modelling task results even more delicate when multispecies plasma are considered, extending the standard electron-neutral-ion system to multiple neutrals and ions. Indeed, in principle all the species interact with each other (even in ways difficult to predict, as for ion-ion streaming instabilities seen in Chapter 2) greatly increasing the complexity of an already strongly coupled and non-linear system. However, as it is usually the case in HETs, only the electron-impact collisions with heavy species (i.e. neutrals and ions) are of interest for the general plasma behaviour, being all the others (i.e. electron-electron, ion-ion, ion-neutral and neutral-neutral) largely negligible in comparison. The reason is that, especially in such devices, these collisions are characterized by much lower cross-sections with respect to the electron-impact ones (see for instance Ref. [19]). It is stressed that this also concerns mixed nitrogen/oxygen reactions which, apart from the expected low cross-sections [60], are even scarcely supported by literature data.

It is worth mentioning that also charge-exchange (CEX) collisions figure in the plasma interactions between heavy species. They describe a resonant exchange of charge in which no kinetic energy is generally transferred. Due to their particular nature, these processes happen even at large distances and are thus characterized by very large cross-sections. However, in view of the constant neutral velocities and temperatures considered in the numerical model (see Section 4.1) including them would not be possible. Indeed, these assumptions do not allow to track the fast and hot neutrals that would be generated by CEX collisions. Therefore, these are neglected in this analysis.

Regarding the considered interactions, throughout this section all the possible electron-impact reactions in a nitrogen/oxygen plasma are evaluated by means of their respective cross-sections, in order to define which are the main ones to be included in the model and which one, if any, can be instead safely neglected.

Following from the cross-sectional data, for each reaction it is also presented the respective reaction rate k, which is necessary to compute the aforementioned source terms in the conservation equations.[2]

In general, all the reaction rates presented have been calculated as a function of the electron temperature T_{eV} for a Maxwellian energy distribution by means of the Boltzmann equation solver Bolsig+ [25]. In particular, for any input cross-section $\sigma(\epsilon)$, where ϵ is the Maxwellian electron energy (in eV), the reaction rate $k(\epsilon)$ is defined as

$$k(\epsilon) = \sqrt{\frac{2e}{m_e}} \int_0^\infty \epsilon\sigma(\epsilon) F_0 d\epsilon \tag{3.1}$$

where F_0 is the electron energy distribution function (EEDF), which is in general non-Maxwellian. Also note that, for a Maxwellian electron distribution, it holds that

$$\epsilon = \frac{3}{2} T_{eV} = \frac{3}{2} \frac{k_B T_e}{e} \tag{3.2}$$

While the generic reaction rate k defines the occurrence frequency of a particular process, the energy exchanged (per unit time) during the reaction is given by the energy exchange

---

[2] A detailed discussion about this topic is presented in Chapter 4, where the model equations are thoroughly illustrated.

coefficient K, which is defined as

$$K = \epsilon_{th} k \tag{3.3}$$

where ϵ_{th} is the reaction threshold energy. Depending of whether energy is lost or gained by the considered particle, ϵ_{th} has to be taken with a positive or negative sign, respectively. This sign convention is in accordance with the formulation of the energy conservation equation used in the numerical model (Eq. 4.36). As this equation is only solved for electrons due to the model assumptions (see Section 4.1), in this work the coefficients K always describe electron power losses.

As a final remark, due to the generally low residence time of the plasma species in the thruster channel, inverse reactions (e.g. superelastic collisions, which are the inverse processes of excitation collisions) are not considered.

3.2.1. Nitrogen

Nitrogen (N) is the chemical element with atomic number 7. A single nitrogen atom has a mass of 14 amu, but in nature, at standard temperature and pressure (STP), it is generally found in its diatomic (molecular) form N_2, with a mass of 28 amu.

The nitrogen component of the air mixture used in the PFG device is pure molecular nitrogen. The interaction between the injected molecular nitrogen and the electron plasma confined into the thruster magnetic field produces a high number of products. These can be divided into neutral products (i.e. N_2 and N) and ionized ones (e.g. N_2^+, N^+, N_2^{2+}, $N^{2+}\dots$). In addition, all these products can be found in either their electronic ground state or in one among the possible excited states characterizing the spectrum of that particular particle. Indeed, the Maxwellian distribution of the electron population results in a continuum of electrons with different energies that, upon impacting with any of the nitrogen products (in this case), will produce a well defined variety of different states. In general, it is also noted that molecules, due to their two-dimensional/ three-dimensional structure (i.e. spatial orientation of the atomic bounds), are subjected to both rotational and vibrational excitation, in addition to the common excitation to electronic states. This topic is discussed in detail for nitrogen in the paragraph relative to its excitation reactions.

In order to describe the electronic state of an atom or a molecule, a special notation is conventionally used. This is composed of a so called *term symbol*, which describes the orbital characteristics of the particle, and, for molecules only, of an additional letter which labels the specific energy level. Due to their importance in the following discussion, these electronic terms are more rigorously defined in Appendix C.

Finally, it is here clarified that the chemical analysis carried out in this section is purposely developed in great detail to provide an accurate picture of the occurring phenomena. However, the fluid nature of the thruster model cannot effectively exploit such level of detail, as in order to track different electronic states it would need to consider them as separate additional species. This would clearly result impractical, computationally expensive and, above all, of little utility as the individual impact of different electronic states on the thruster general behaviour is safely negligible. Rather, Boltzmann equation solvers are a suitable tool for tracking the evolution of several species and even electronic states in plasma. Nevertheless, the detailed analysis presented here is instead fundamental for what concerns the reaction energy thresholds ϵ_{th}. Indeed, these values are directly employed in the computation of the electron energy loss coefficients K associated with each reaction. Therefore, a greater understanding of the plasma chemical processes surely allows to better interpret and use the statistical reaction cross-sections presented in literature, with great advantage for the model representativeness.

Dissociation

The first chemical reaction considered for molecular nitrogen is dissociation from the ground state $N_2(X\,^1\Sigma_g^+)$, i.e.

$$N_2(X\,^1\Sigma_g^+) + e^- \longrightarrow 2\,N + e^- \tag{3.4}$$

Depending on the energy exchanged between the impacting electron and N_2, this reaction may produce couples of nitrogen atoms at different electronic states. The first and most common energy thresholds (called *dissociation limits* in this case) are shown in Table 3.1 with the respective atomic products.

Table 3.1: Dissociation levels of N_2 with the respective products and threshold energies. (Source: Ref. [61])

Reagent state	Threshold energy (eV)	Dissociation products	Dissociation level
$N_2(X\,^1\Sigma_g^+)$	9.7537 ± 0.0011	$N(^4S^o) + N(^4S^o)$	I
	12.1373	$N(^4S^o) + N(^2D^o)$	II
	13.329	$N(^4S^o) + N(^2P^o)$	III

As claimed in the article of Cosby [61], dissociation to $N(^4S^o) + N(^2D^o)$ is the primary dissociation mechanism for N_2. Therefore, in this work it is used the threshold energy of 12.1373 eV for this reaction. Concerning the cross-section, in the same experimental effort Cosby presented some recommended absolute cross-section values that are still taken as a reference nowadays (see for instance the work of Itikawa [62]) and are here depicted in Figure 3.2a. This recommended cross-section is the result of an average between the experimental results of Cosby and those of Winters [63] (corrected for dissociative ionization), which showed to be consistent within their combined uncertainties (±30% for Cosby and ±20% for Winters).[3]

Also, in Figure 3.2b it is shown the respective reaction rate $k_{N_2,diss}$.

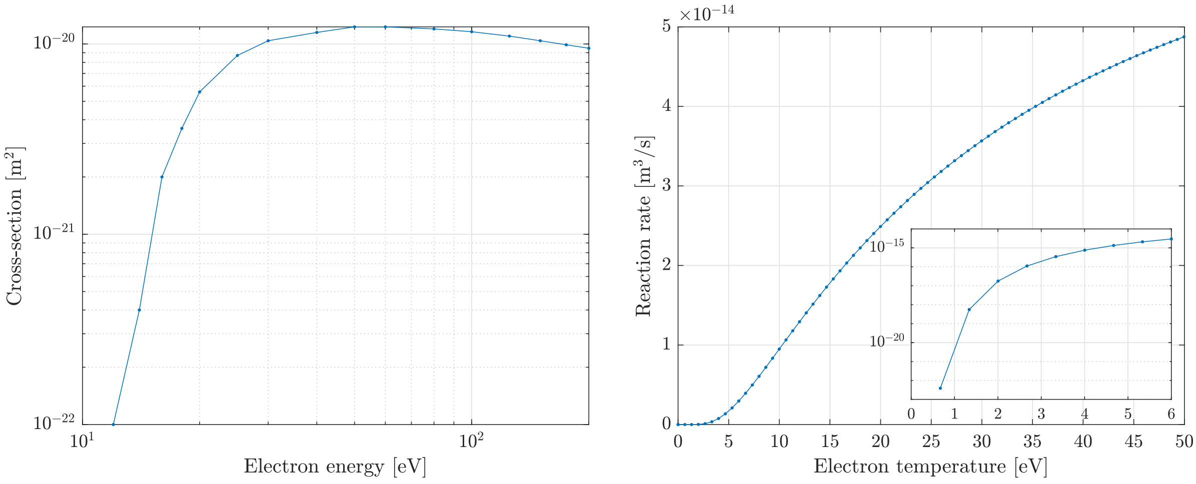

(a) **(b)**

Figure 3.2: (a) Total dissociation cross-section for electron collisions with N_2. (Source: Ref. [61]) (b) Corresponding total dissociation rate for electron temperatures up to 50 eV. The values at small temperatures are resolved in the inset plot.

To complete the discussion about N_2 dissociation, Figure 3.3 reports the potential energy curves of the most important N_2 excited states (which are discussed in the following) as a

---

[3] More details can be found in Ref. [61].

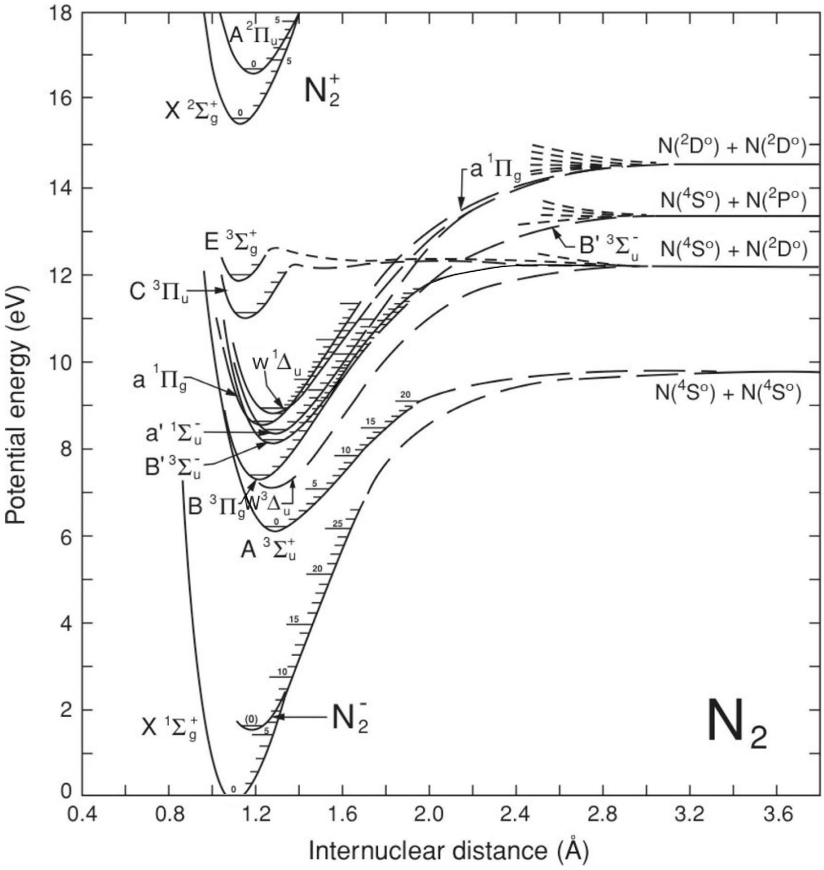

Figure 3.3: Potential energy curves of the major N_2 excited states, as a function of the internuclear distance between the nitrogen atoms. On the right (at high internuclear distances) are shown the respective dissociation limits. The potential energy scale is relative to the ground state $N_2(X\,^1\Sigma_g^+)$ bond energy. A more complete set of potential curves can be found in Ref. [64]. (Corrected from source: Ref. [65])

function of the internuclear distance between the nitrogen atoms. In particular, in a potential energy scale relative to the ground state $N_2(X\,^1\Sigma_g^+)$ bond energy, the couples of dissociation products appear on the right side, each at its own threshold energy. Each of the excited states of N_2 tends toward a particular dissociation level, as the internuclear distance increases. For each state, the depth of the potential energy well below the respective dissociation level represents the bond strength.

This figure is particularly useful in partly clarifying the complex dynamical nature of dissociation, which is often intimately related to excitation and does not always simply result from a single electron collision. Instead, it may happen that, upon electron impact, the molecule transitions to a stable excited state (i.e. a *metastable state*) with a higher dissociation limit. At this point, another electron collision may provide enough energy to dissociate it, or again to reach another higher excited state. A third alternative is a process called *predissociation* in which, without any additional energy, the molecule internally transitions between its current metastable state to an unstable one, which then decays toward its lower dissociation limit. While these phenomena would require a detailed discussion to be fully understood and characterized, this is not provided here, as it goes beyond the scope of this work. However, this simplified explanation is meant to highlight the limitations experienced in dealing with complex chemical interactions, such as dissociation, by means of a model not independently tracking the electronic states.

Ionization

At the basis of electric propulsion devices stands the phenomenon of ionization. For both N_2 and N the ionization reactions respectively write as

$$\mathrm{N_2(X\,^1\Sigma_g^+) + e^- \longrightarrow N_2^+ + 2\,e^-} \tag{3.5}$$

$$\mathrm{N(^4S^o) + e^- \longrightarrow N^+ + 2\,e^-} \tag{3.6}$$

Note that, because of the unfeasibility of simulating non-ground state species with fluid models, both N_2 and N are considered at the ground state (i.e. $\mathrm{N_2(X\,^1\Sigma_g^+)}$ and $\mathrm{N(^4S^o)}$), even if, for instance, in the previous paragraph it was shown that both $\mathrm{N(^4S^o)}$ and $\mathrm{N(^2D^o)}$ are produced with dissociation.

Regarding N_2 ionization, the data used in this work has been retrieved from the extensive study of Itikawa [62], which compared over a hundred of references to highlight the most reliable cross-sectional values for electron collisions with molecular nitrogen. In particular, the best ionization energy results 15.58 eV and the suggested cross-sectional data are those obtained by Lindsay and Mangan [66], which merged the experimental data sets of Straub et al. [67][4] and Rapp and Englander-Golden [68]. This partial cross-section has an estimated absolute uncertainty of ±5% and it is shown in Figure 3.4 together with the respective ionization rate $k_{N_2,ion}$.

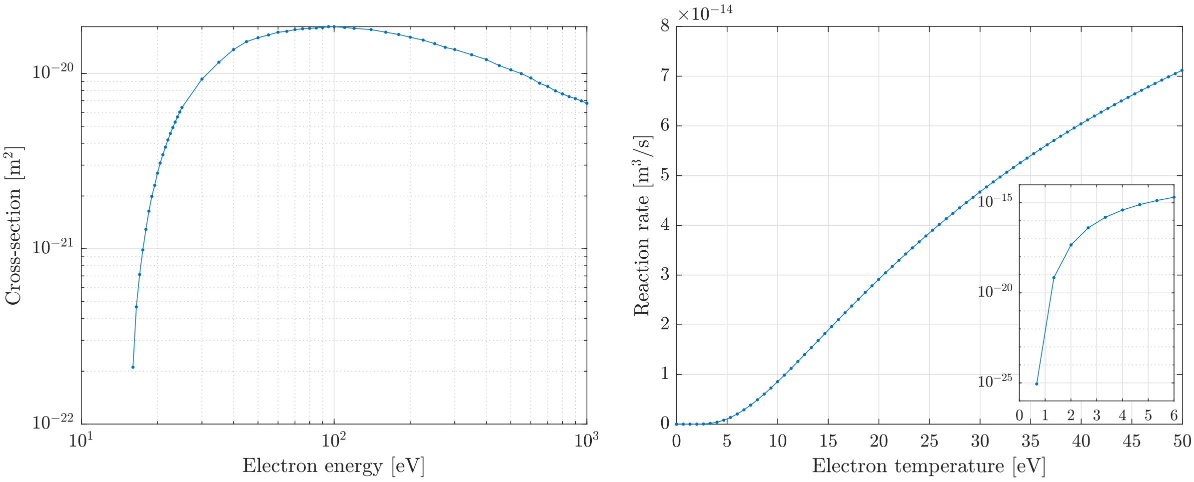

(a) **(b)**

Figure 3.4: (a) Partial ionization cross-section of N_2 for the production of N_2^+. (Source: Ref. [66]) (b) Corresponding ionization rate for electron temperatures up to 50 eV. The values at small temperatures are resolved in the inset plot.

As N ionization is concerned, the cross-sectional values used in this work come directly from the IST-Lisbon database on LXCat [69] and specifically from the work of Wang et al. [70], which numerically calculated them by means of their B-spline R-matrix (BSR) code. Figure 3.5 shows both this cross-section and the respective ionization rate $k_{N,ion}$. The ionization energy of atomic nitrogen is 14.54 eV.

While until now only neutral ionization has been analyzed, it may be the case for the products N_2^+ and N^+ to experience other electron impacts along their flows. This may lead to another step in ionization, with the formation of doubly ionized ion species. The corresponding

---

[4] These data have been slightly adjusted in the review of Lindsay and Mangan [66] to reflect a later recalibration of the experimental apparatus.

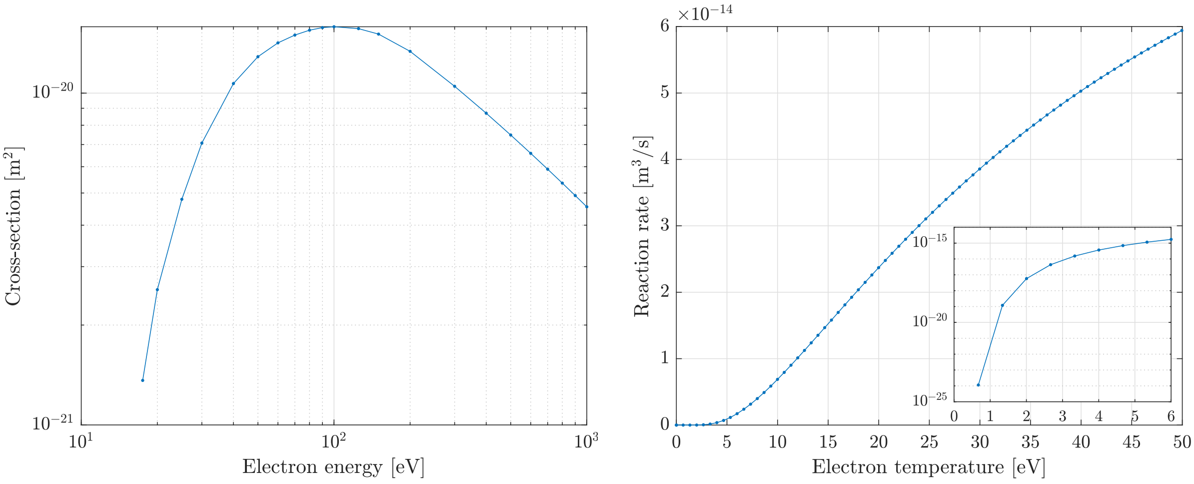

(a) **(b)**

Figure 3.5: (a) Partial ionization cross-section of N for the production of N^+. (Source: Ref. [69]) (b) Corresponding ionization rate for electron temperatures up to 50 eV. The values at small temperatures are resolved in the inset plot.

reactions are

$$N_2^+ + e^- \longrightarrow N_2^{2+} + 2\,e^- \tag{3.7}$$

$$N^+ + e^- \longrightarrow N^{2+} + 2\,e^- \tag{3.8}$$

However, the cross-sectional data for such specific ion-to-ion reactions are not common in literature, probably due to the elusive nature of the phenomena involved, which makes difficult to accurately isolate one or the other reaction. Rather, what it has been usually done in experiments is to look at the overall products of N_2 ionization (in this case), which not only comprehend N_2^+, but also N^+ (for instance from dissociative ionization, see the next paragraph), N_2^{2+}, N^{2+} and surely many others generally too scarce to be even detected. Accordingly, the complete results of the work of Lindsay and Mangan [66] are analyzed. In particular, the experimental data reviewed were obtained by means of a mass spectrometer which managed to detect N_2^+, N^+/N_2^{2+} and N^{2+}, whose cross-sections are shown in Figure 3.6. The absolute uncertainty of these cross-sections is ±5% for N_2^+ and N^+/N_2^{2+} and ±6% for N^{2+}. Note that, as they have the same mass to charge ratio, N^+ and N_2^{2+} could not be distinguished. This poses an obstacle in evaluating their individual ionization cross-sections. However, the problem has been bypassed by looking at the electron-impact ionization of another molecule: CO [71]. Indeed, as CO is isoelectronic to N_2, by comparing the individual cross-sections for the production of CO^{2+} and CO^+ it is possible to obtain an estimate also for N_2. In particular, for CO the ratio between doubly and singly charged ion productions (at 100 eV, near the cross-section curves peaks) results less than 0.5%. Thus, by assuming this to be valid also for N_2, the production of N_2^{2+} can be safely neglected, as it locates within the uncertainty of N^+ cross-section.

Concerning N^{2+}, as it is shown in Figure 3.6 its cross-section is about two orders of magnitude smaller than that of N_2^+. Nevertheless, the key characteristic that allows to safely neglect the presence also of this ionic species is the appearance energy (i.e. the best ionization energy) which locates at about 70 eV, definitely too high for Hall thrusters with the power and size of the HT5k.

In conclusion, the only positive ion species that result relevant in the HET air plasma under analysis are N_2^+ and N^+.

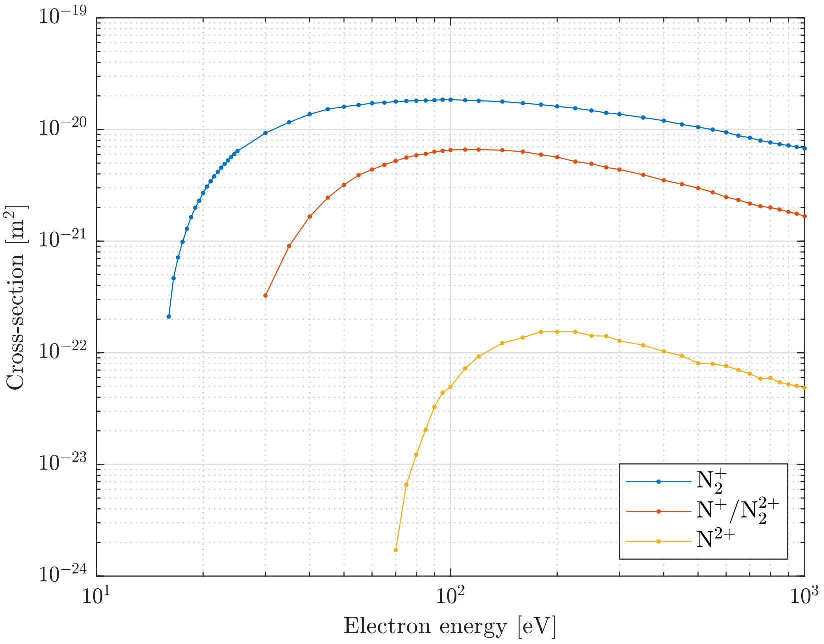

Figure 3.6: Partial ionization cross-sections of N_2 for the production of N_2^+, N^+/N_2^{2+} and N^{2+}. (Source: Ref. [66])

Dissociative Ionization

As briefly introduced in the previous paragraph, N_2 can directly dissociate and ionize upon a single electron impact. This phenomenon is called *dissociative ionization* and the corresponding reaction is

$$N_2(X\,^1\Sigma_g^+) + e^- \longrightarrow N + N^+ + 2\,e^- \tag{3.9}$$

The threshold impact energy of this reaction is generally considered the appearance energy of N^+ in N_2 ionization, which corresponds to 24.34 eV [62]. Concerning the cross-section, even if Lindsay and Mangan [66] did not explicitly define one based on their data, Itikawa [62] considered it to be equal to $\sigma(N^+) + 2\sigma(N^{2+})$. Similarly, Rapp et al. [72] experimentally calculated the absolute cross-section for N_2 dissociative ionization as the total ionization cross-section of non-N_2^+ ions (data uncertainty was not provided). Being N^+ the main of these ions (see Figure 3.6), this assumption is considered reasonably valid.

Finally, both the cross-sections proposed by Itikawa and Rapp et al. are reported in Figure 3.7a, confirming the expected agreement. In this work it is used the data set of Rapp et al., which has been employed to obtain the reaction rate $k_{N_2,DI}$, shown in Figure 3.7b.

Electron Attachment/ Dissociative Attachment

The next group of reactions investigated determines the formation of negative ions of either N_2 or N. It can be divided in electron attachment reactions, i.e.

$$N_2(X\,^1\Sigma_g^+) + e^- \longrightarrow N_2^- \tag{3.10}$$

$$N(^4S^o) + e^- \longrightarrow N^- \tag{3.11}$$

and dissociative attachment reactions, i.e.

$$N_2(X\,^1\Sigma_g^+) + e^- \longrightarrow N + N^- \tag{3.12}$$

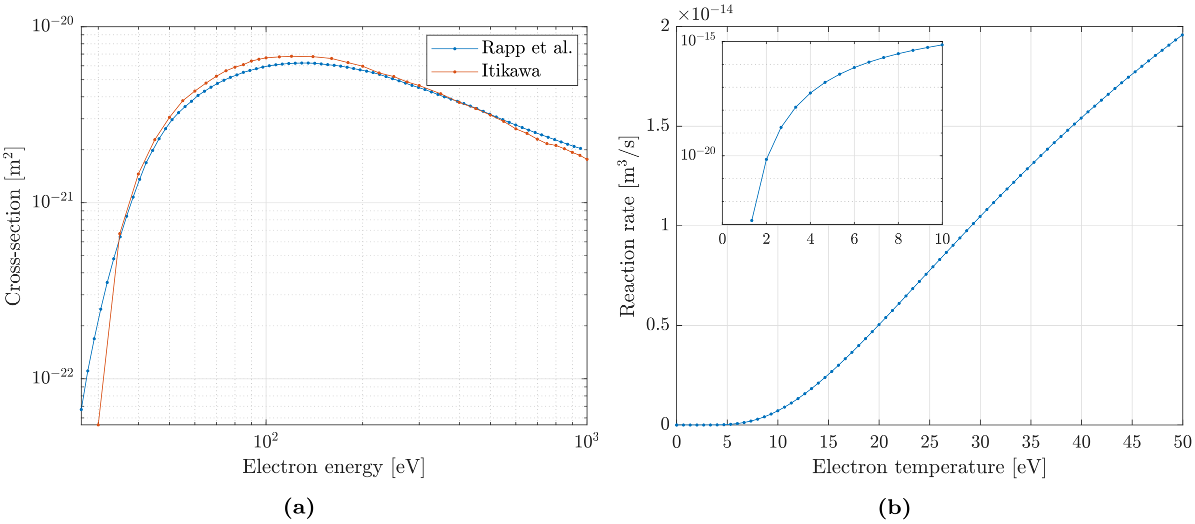

Figure 3.7: (a) Total dissociative ionization cross-section for electron collisions with N_2. The values of Rapp et al. [72] and Itikawa [62] are compared showing a good agreement. (b) Corresponding total dissociative ionization rate for electron temperatures up to 50 eV obtained from the data of Rapp et al. [72]. The values at small temperatures are resolved in the inset plot.

While such interactions are generally expected due to the electronegative nature of nitrogen (as it is the case of iodine, for instance), to the knowledge of the author, data about formation of N_2^- from N_2 are not available in literature. Rather, a three-body attachment reaction involving N_2 has been effectively studied for nitrogen/oxygen mixtures but only indicating the production of negative oxygen ions and not nitrogen ones (i.e. $e^- + O_2 + N_2 \longrightarrow {O_2}^- + N_2$, see for instance the review of Phelps [60]). Although such mixed reactions are not considered in this work because of their minimal effects (as for ion-ion and ion-neutral collisions), this fact, together with the scarcity of N_2^- data, may suggest the negligible nature of the N_2^- production process, especially in nitrogen/oxygen mixtures. Similarly, even if some studies have been conducted on N^- ions, a stable state has never been observed [70, 73].

Consequently, it is safely assumed that negative nitrogen ions are not present in the air plasma under analysis.

Excitation

In this paragraph it is thoroughly investigated molecular and atomic nitrogen excitation upon electron-impact from their respective ground states. The corresponding reactions are

$$N_2(X\,^1\Sigma_g^+) + e^- \longrightarrow N_2^* + e^- \tag{3.13}$$

$$N(^4S^o) + e^- \longrightarrow N^* + e^- \tag{3.14}$$

where the asterisk indicates a generic excited state.

Regarding N_2 excitation, the main excited electronic states are listed in Table 3.2 together with their respective reaction threshold energies. The states have been retrieved from the Biagi database on LXCat [74] and then properly compiled by means of the reviews of Itikawa et al. [62, 75]. Note that the majority of the states have also indicated the vibrational level, or a range of levels in case their difference is negligibly small.[5] Conversely, rotational excitation is always neglected in this work, as it involves too small threshold electron energies. Indeed, the

---

[5] In case the vibrational level is not indicated, the threshold energy is the energy of the lowest vibrational state relative to $N_2(X^1\Sigma_g^+, v = 0)$.

Table 3.2: Excitation of N_2. (Sources: Ref. [62, 74, 75])

Excited state	Vibrational level	Threshold energy (eV)	Excited state	Vibrational level	Threshold energy (eV)
$X\ ^1\Sigma_g^+$	1	0.2889	$a\ ^1\Pi_g$	0-3	8.95
$X\ ^1\Sigma_g^+$	2	0.5742	$B'\ ^3\Sigma_u^-$	0-6	8.974
$X\ ^1\Sigma_g^+$	3	0.8559	$a'\ ^1\Sigma_u^-$	0-6	9.191
$X\ ^1\Sigma_g^+$	4	1.1342	$W\ ^3\Delta_u$	11-19	9.562
$X\ ^1\Sigma_g^+$	5	1.4088	$w\ ^1\Delta_u$	0-5	9.59
$X\ ^1\Sigma_g^+$	6	1.6801	$a\ ^1\Pi_g$	4-15	9.665
$X\ ^1\Sigma_g^+$	7	1.9475	$B'\ ^3\Sigma_u^-$	7-18	9.933
$X\ ^1\Sigma_g^+$	8	2.2115	$a'\ ^1\Sigma_u^-$	7-19	10.174
$X\ ^1\Sigma_g^+$	9	2.4718	$w\ ^1\Delta_u$	6-18	10.536
$X\ ^1\Sigma_g^+$	10	2.7284	$C\ ^3\Pi_u$	0-4	11.188
$X\ ^1\Sigma_g^+$	11	2.9815	$E\ ^3\Sigma_g^+$		11.875
$X\ ^1\Sigma_g^+$	12	3.231	$a''\ ^1\Sigma_g^+$	0-1	12.289
$X\ ^1\Sigma_g^+$	13	3.4769	$b\ ^1\Pi_u$	0-6	12.771
$X\ ^1\Sigma_g^+$	14	3.7191	$c_4'\ ^1\Sigma_u^+$	0-3	12.95
$X\ ^1\Sigma_g^+$	15	3.9576	$G\ ^3\Pi_u$	0-3	13.001
$A\ ^3\Sigma_u^+$	0-4	6.725	$c_3\ ^1\Pi_u$	0-3	13.093
$A\ ^3\Sigma_u^+$	5-9	7.36	$F\ ^3\Pi_u$	0-3	13.174
$B\ ^3\Pi_g$	0-3	7.744	$b'\ ^1\Sigma_u^+$	0-10	13.371
$W\ ^3\Delta_u$	0-5	8.05	$b\ ^1\Pi_u$	7-14	13.382
$A\ ^3\Sigma_u^+$	10-21	8.217	$o_3\ ^1\Pi_u$	0-3	13.564
$B\ ^3\Pi_g$	4-16	8.451	$b'\ ^1\Sigma_u^+$	≥10	14.00
$W\ ^3\Delta_u$	6-10	8.729			

role of excitation reactions in the thruster model employed is solely that of contributing to the overall electron energy lost. In particular, the energy loss terms K (recall Eq. 3.3) relative to each excitation reaction need to be computed and then summed together to define a total excitation energy loss term (e.g. $K_{N_2,exc}$ for N_2). Therefore, due to their minimal ϵ_{th}, the contribution of rotational excitation processes to this term result minimal.

Figures 3.8a-i show the cross-sections relative to all the excited states listed in Table 3.2. Also, in Figure 3.8j is shown the total reaction rate $k_{N_2,exc}$, obtained by summing up the excitation rates relative to all the considered cross-sections.

By comparing Tables 3.1 and 3.2 it is noticed that many electronic states lie above the first dissociation limit (i.e. $N(^4S^o)$ + $N(^4S^o)$ at 9.7537 ± 0.001eV) and even the second one (i.e. $N(^4S^o)$ + $N(^2D^o)$ at 12.1373eV) or the third one (i.e. $N(^4S^o)$ + $N(^2P^o)$ at 13.329eV). Consequently, it is expected that a percentage of each of these excitation processes would then result in a predissociation transition. As the total dissociation cross-section reported in Figure 3.2a already comprehends all possible contributions to dissociation (as it has been obtained by looking at the final products only, for a certain electron energy, regardless of the intermediate processes of excitation/ de-excitation), by including in the model excitation processes that, completely or in part, ultimately lead to dissociation would result in an overestimation of the electron energy losses. However, it is not certain from literature which may be the value of these percentages. To the author's knowledge, the most recent reference about this specific issue is the work of Cosby [61], which reports the predissociation branching ratios (i.e. predissociation/excitation rate) of some electronic states above the lower dissociation level. In

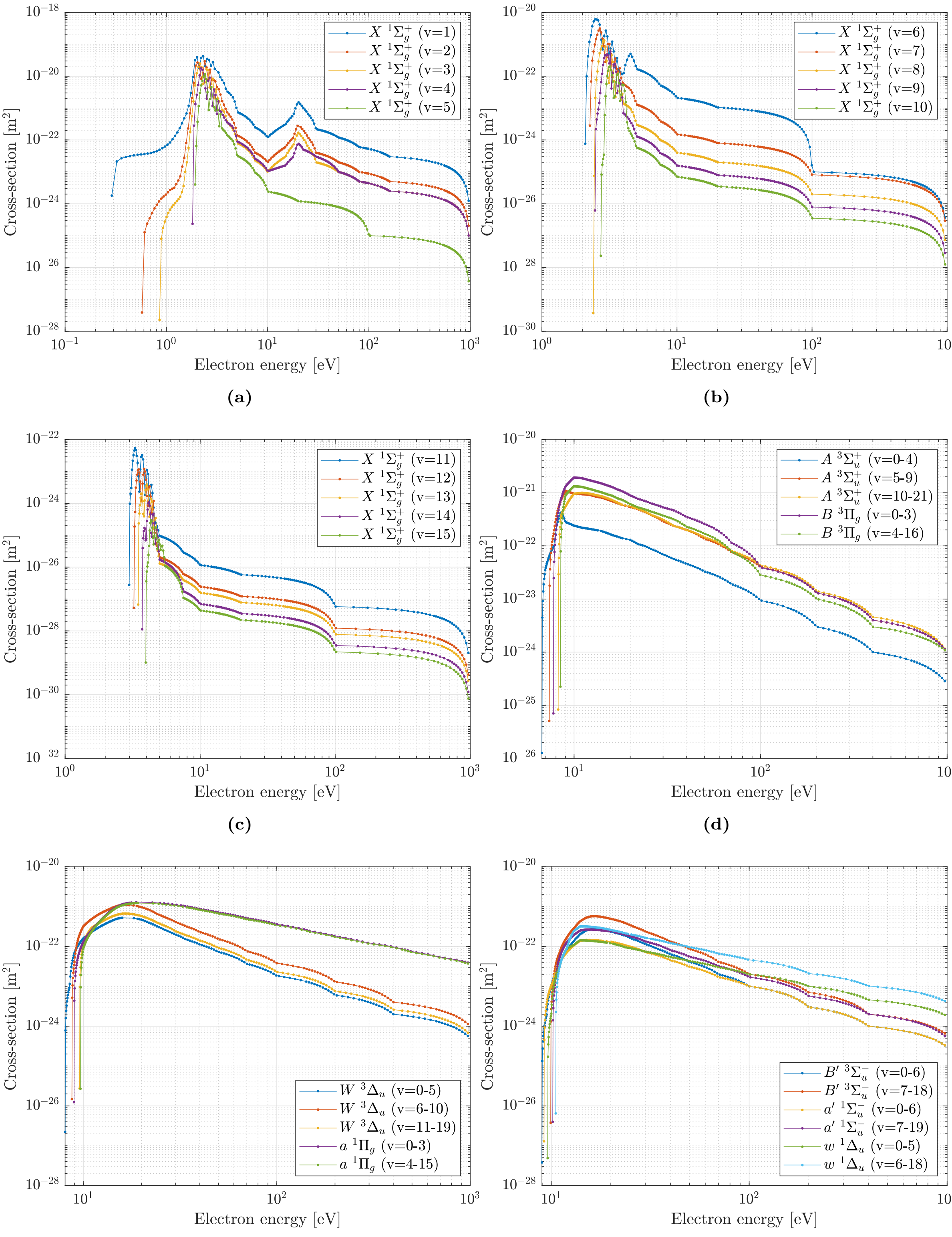

Figure 3.8: (a)-(f) Excitation cross-sections for electron collisions with N_2. The electronic states refer to Table 3.2. (Source: Ref. [74])

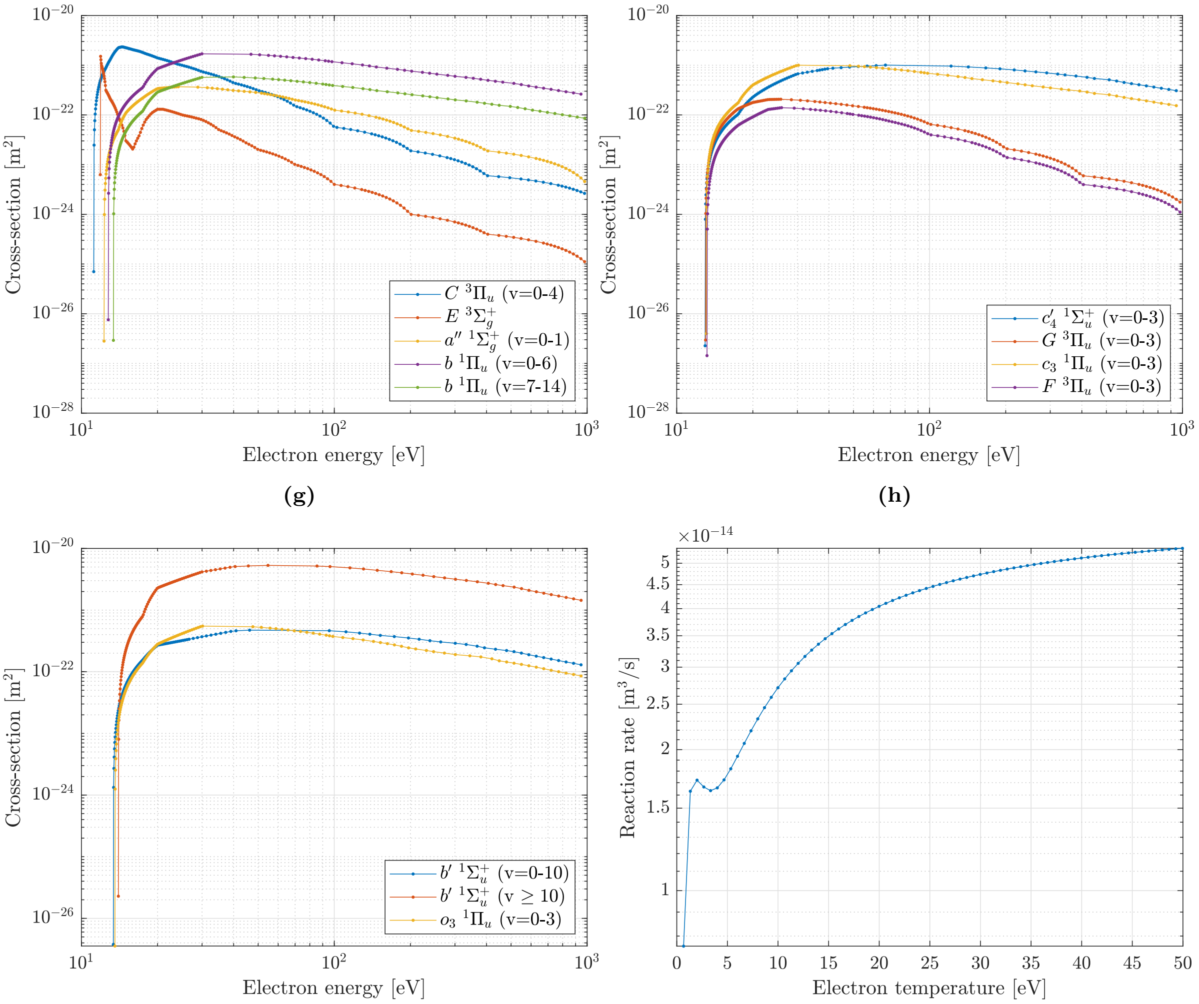

(g) **(h)**

(i) **(j)**

Figure 3.8 (cont.): (g)-(i) Excitation cross-sections for electron collisions with N_2. The electronic states refer to Table 3.2. (Source: Ref. [74]) (j) Total excitation rate of N_2 for electron temperatures up to 50 eV.

particular, for the $b\ ^1\Pi_u$, $b'\ ^1\Sigma_u^+$, $c_4'\ ^1\Sigma_u^+$ (see Ref. [76]) states (and probably also for the $c_3\ ^1\Pi_u$, $o_3\ ^1\Pi_u$, $G\ ^3\Pi_u$, $F\ ^3\Pi_u$ states) ratios near 1 are suggested for both 100 eV and 200 eV electron energies. However, as the typical electron energies observed in Hall thrusters are generally much lower (i.e. not greater than 30/40 eV) these data are not sufficient to estimate the predissociation branching ratios for such low-energy levels. Therefore, it is assumed that for the electron energies of the model all the excitation states listed in Table 3.2 only lead to energy losses, without producing dissociation. While in principle this assumption may result useful to compensate for the electron temperature overestimation expected from the employed numerical model (see the work of Giannetti et al. [10]), the cross-sections involved are so small, if compared to the other processes discussed, that the difference is expected to be negligible anyway.

Concerning N excitation from its ground state $(2s^2 2p^3)^4S^o$, the main excited states with their electronic configuration and threshold energy are listed in Table 3.3. As the available experimental data about atomic nitrogen excitation are very scarce in literature, these states (and the respective cross-sections) have been obtained from the numerical results of the BSR database on LXCat [77], which for atomic nitrogen again base on the work of Wang et al.

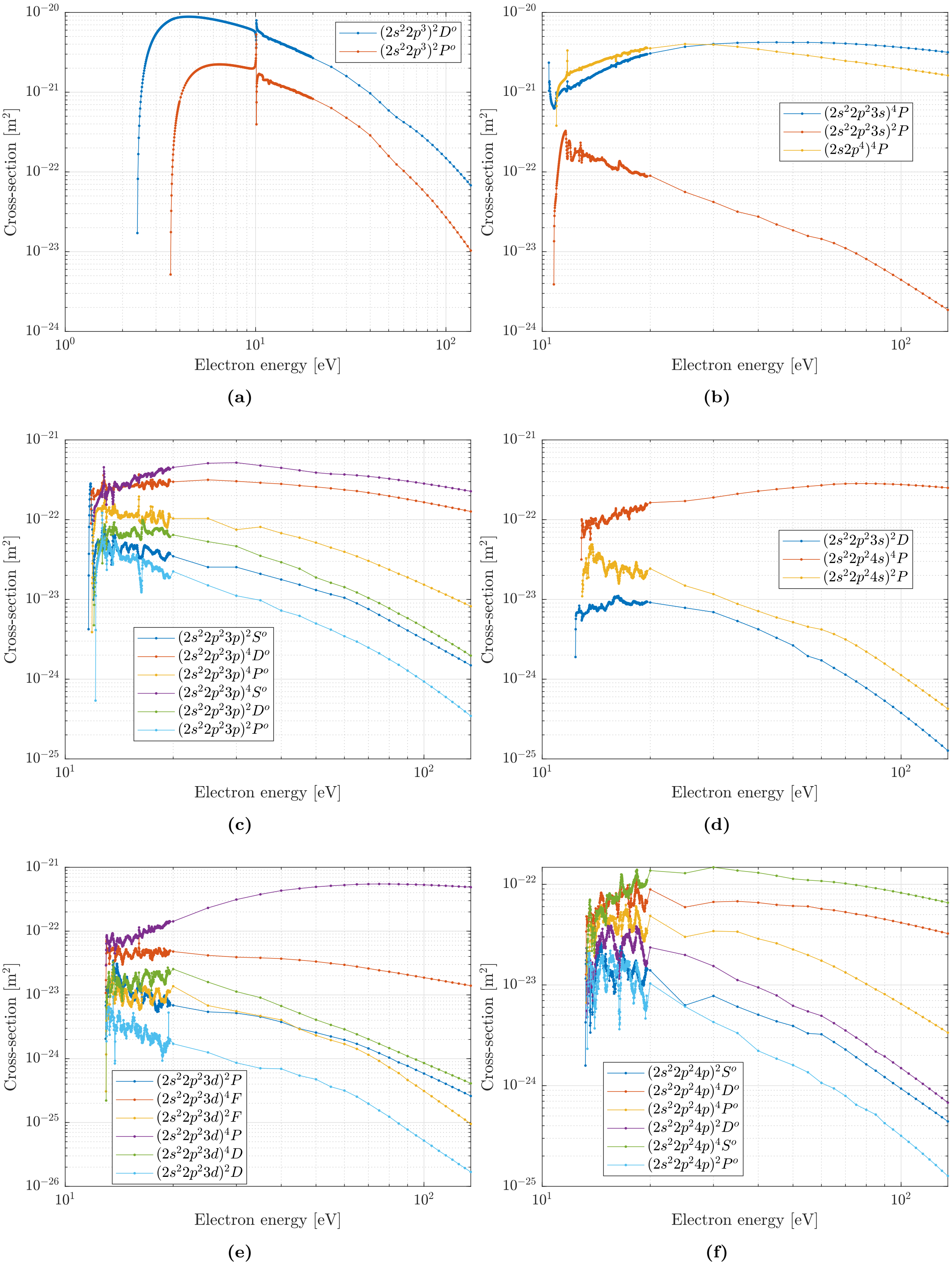

(a) **(b)**

(c) **(d)**

(e) **(f)**

Figure 3.9: (a)-(f) Excitation cross-sections for electron collisions with N. The electronic states refer to Table 3.3. (Source: Ref. [77])

Table 3.3: Excitation of N. (Sources: Ref. [70, 77])

Excited state	Term	Threshold energy (eV)	Excited state	Term	Threshold energy (eV)
$2s^22p^3$	$^2D^o$	2.391	$2s^22p^2(^3P)4s$	^2P	12.918
$2s^22p^3$	$^2P^o$	3.568	$2s^22p^2(^3P)3d$	^2P	12.963
$2s^22p^2(^3P)3s$	^4P	10.422	$2s^22p^2(^3P)3d$	^4F	12.971
$2s^22p^2(^3P)3s$	^2P	10.774	$2s^22p^2(^3P)3d$	^2F	12.983
$2s2p^4$	^4P	10.948	$2s^22p^2(^3P)3d$	^4P	12.986
$2s^22p^2(^3P)3p$	$^2S^o$	11.618	$2s^22p^2(^3P)3d$	^4D	13.005
$2s^22p^2(^3P)3p$	$^4D^o$	11.785	$2s^22p^2(^3P)3d$	^2D	13.021
$2s^22p^2(^3P)3p$	$^4P^o$	11.871	$2s^22p^2(^3P)4p$	$^2S^o$	13.193
$2s^22p^2(^3P)3p$	$^4S^o$	12.003	$2s^22p^2(^3P)4p$	$^4D^o$	13.242
$2s^22p^2(^3P)3p$	$^2D^o$	12.027	$2s^22p^2(^3P)4p$	$^4P^o$	13.268
$2s^22p^2(^3P)3p$	$^2P^o$	12.145	$2s^22p^2(^3P)4p$	$^2D^o$	13.292
$2s^22p^2(^1D)3s$	^2D	12.373	$2s^22p^2(^3P)4p$	$^4S^o$	13.32
$2s^22p^2(^3P)4s$	^4P	12.853	$2s^22p^2(^3P)4p$	$^2P^o$	13.348

[70]. These cross-sections, shown in Figure 3.9, already consider the fact that, as it usually happens in reality, ground state nitrogen has to go through one of its two metastable states (i.e. $(2s^22p^3)^2D^o$ and $(2s^22p^3)^2P^o$) in order to reach the excited states listed in the table.[6] Also, as previously mentioned, dissociation and dissociative ionization processes do not always produce nitrogen atoms in the ground state. Therefore, by considering all excitation processes taking place from the ground state, electron energy losses are again very slightly overestimated.

Finally, in Figure 3.10 is shown the total reaction rate $k_{N,exc}$, obtained by summing up the excitation rates relative to all the considered cross-sections.

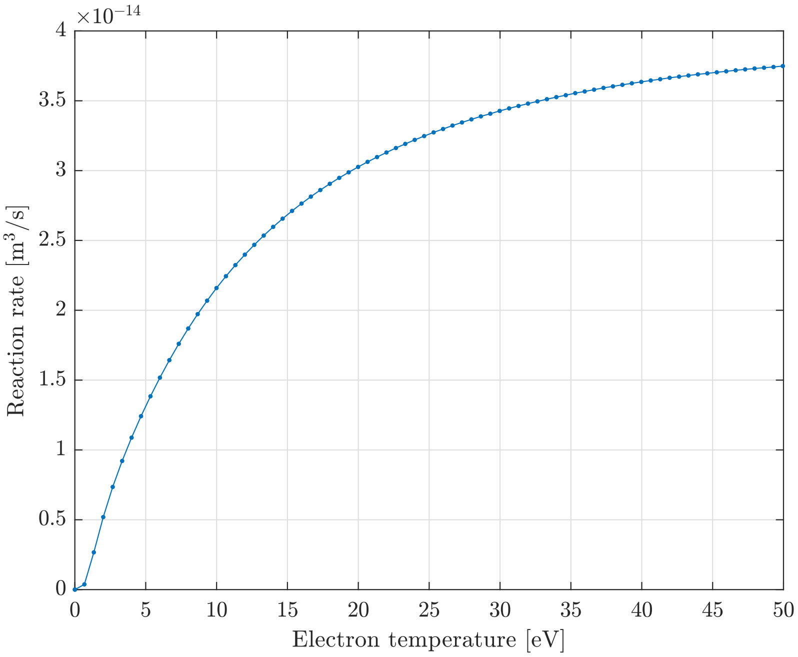

Figure 3.10: Total excitation rate of N for electron temperatures up to 50 eV.

---

[6] More details can be found in Ref. [70].

Elastic Momentum Transfer

Finally, the last process considered for nitrogen is the momentum transfer due to elastic collisions. Together with inelastic collisions between electrons and neutrals (e.g. ionization, excitation, dissociation) also elastic collisions contribute to the total electron collision frequency ν_e. However, the latter do not affect the electron energy distribution as no energy is exchanged (i.e. electrons only lose directional momentum as a consequence of the impact with the much heavier neutrals).

Figure 3.11 reports the elastic momentum transfer cross-section of N_2 together with the corresponding reaction rate $k_{N_2,el}$. The cross-section values are taken from the review of Itikawa [62], where three sets of experimental data have been merged to cover the full electron energy range from 0.001 eV to 100 eV. The reason is that N_2 is characterized by a $^2\Pi_g$ shape resonance in the region around 2.3 eV, which causes the high cross-section peak shown in Figure 3.11a.[7] There, between 0.5 eV and 3.5 eV, only a broad envelope of the cross-section is provided, while in both the 0.001-0.5 eV region (±5% uncertainty) and the 3.5-100 eV one (±20% uncertainty) the data are precisely defined. Note that an uncertainty cannot be defined in the resonance region.

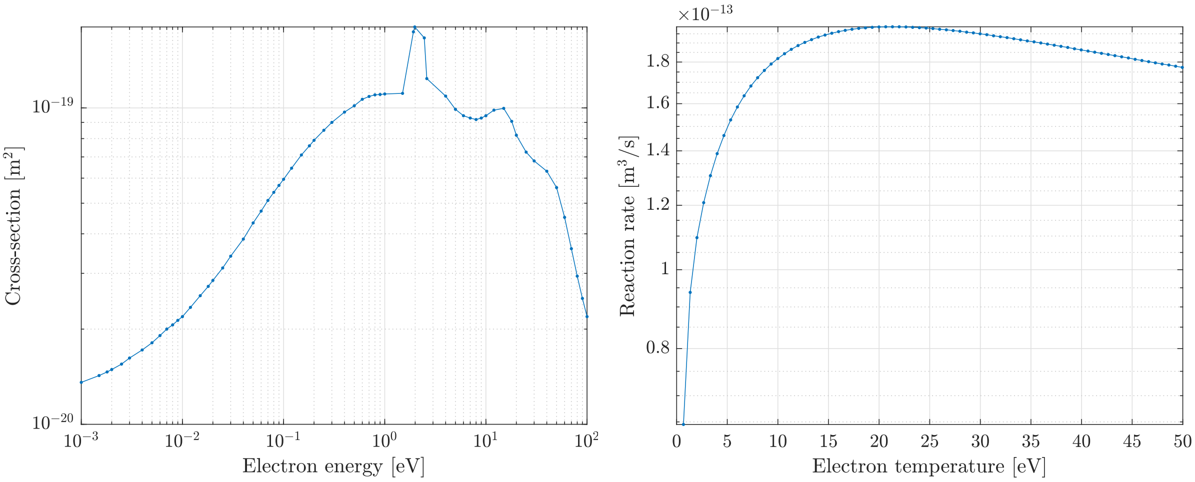

(a) **(b)**

Figure 3.11: (a) Elastic momentum transfer cross-section for electron collisions with N_2. (Source: Ref. [62]) (b) Corresponding reaction rate for electron temperatures up to 50 eV.

Similarly, in Figure 3.12 are shown the cross-section and the reaction rate $k_{N,el}$ relative to N. The cross-section is taken from the IST-Lisbon database [69] and in particular from the work of Wang et al. [70]. It is noticed that the data exhibit a prominent peak at very low electron energies (i.e. <0.1 eV), which is again due to a shape resonance. Precisely, this resonance is related to the lowest $(2s^2 2p^4)^3P$ term of an unstable N^- negative-ion state.[8]

3.2.2. Oxygen

Oxygen (O) is the chemical element with atomic number 8. A single oxygen atom has a mass of 16 amu, but in nature, at standard temperature and pressure (STP), it is generally found in its diatomic (molecular) form O_2, with a mass of 32 amu, exactly as in the case of nitrogen. Through this subsection the great chemical similarities between oxygen and nitrogen will become apparent, not only concerning the characterizing reactions and ion species produced, but

---

[7] More details can be found in Ref. [78].

[8] More details can be found in Ref. [70].

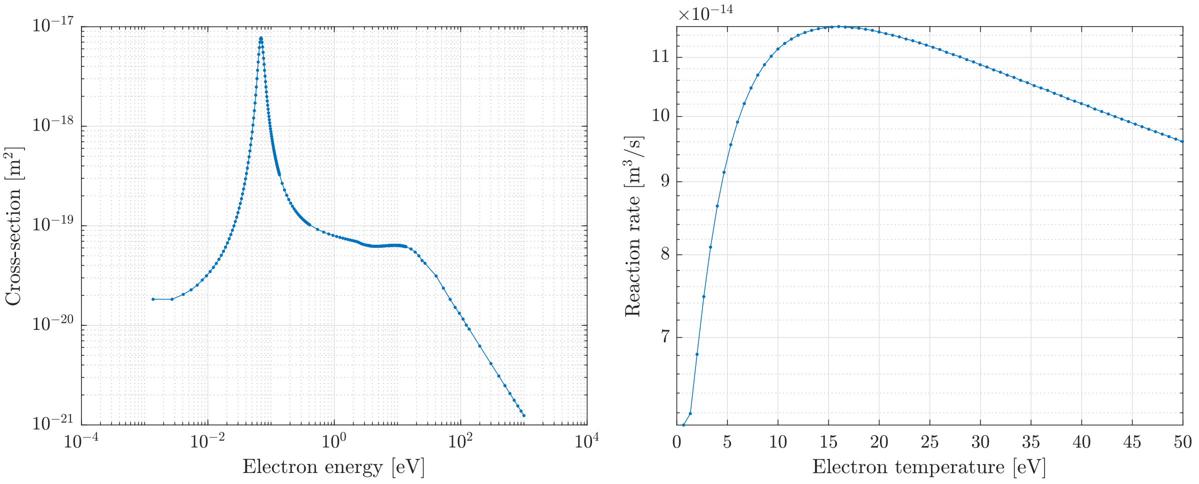

(a) **(b)**

Figure 3.12: (a) Elastic momentum transfer cross-section for electron collisions with N. (Source: Ref. [69]) (b) Corresponding reaction rate for electron temperatures up to 50 eV.

also regarding the cross-sectional data. For this reason, the discussion is often kept brief and concise, with common cross-references to the nitrogen case.

The oxygen component of the air mixture used in the PFG device is pure molecular oxygen. As for nitrogen, the interaction between the injected molecular oxygen and the electron plasma confined into the thruster magnetic field produces a high number of products. These can be divided into neutral products (i.e. O_2 and O) and ionized ones (e.g. O_2^+, O^+, O_2^{2+}, $O^{2+}\dots$). In addition, all these products can be found as well in either their electronic ground state or in one among the possible excited states characterizing the spectrum of that particular particle. However, for the same reasons explained for nitrogen, only particles at the ground state can be eventually considered in the numerical model.

Dissociation

At first, it is presented the dissociation reaction of molecular oxygen from its ground state $O_2(X\,^3\Sigma_g^-)$, i.e.

$$O_2(X\,^3\Sigma_g{}^-) + e^- \longrightarrow 2\,O + e^- \tag{3.15}$$

As for nitrogen, also oxygen dissociation may lead to couples of oxygen atoms at different electronic states. The main dissociation levels considered are two and they are shown in Table 3.4, together with their respective threshold energies and dissociation products.

Table 3.4: Dissociation levels of O_2 with the respective products and threshold energies.

Reagent state	Threshold energy (eV)	Dissociation products	Dissociation level
$O_2(X\,^3\Sigma_g^-)$	$\approx 5.116^a$	$O(^3P) + O(^3P)$	I
	7.083^b	$O(^3P) + O(^1D)$	II

[a] Ref. [79].
[b] Ref. [80].

The mechanisms leading to oxygen dissociation are generally much clearer than the nitrogen ones, due to the fact that, above the first dissociation level energy (i.e. 5.116 eV), the majority of oxygen electronic states excited from $O_2(X\ ^3\Sigma_g^-)$ appear to dissociate [80]. Precisely, in its work Cosby [80] claimed that the main dissociation mechanism consists in the rapid predissociation to $O(^3P) + O(^1D)$ of the $B\ ^3\Sigma_u^-$ electronic state. Also, the excitation of this state causes the so called *Schumann-Runge (SR) continuum*, which is a broad peak between 7.5 eV and 9 eV in the O_2 electron energy loss spectrum [81].

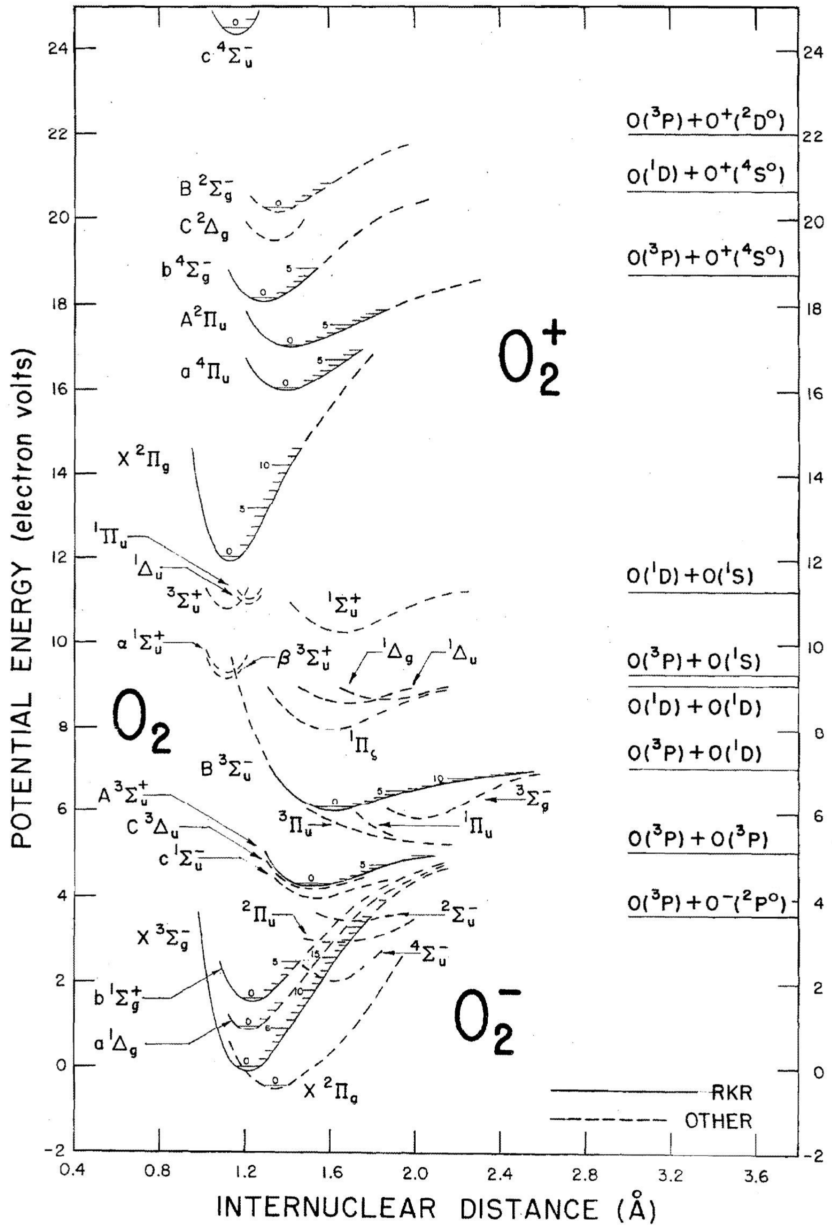

Figure 3.13: Potential energy curves of the major O_2 excited states, as a function of the internuclear distance between the oxygen atoms. On the right (at high internuclear distances) are shown the respective dissociation limits. The potential energy scale is relative to the ground state $O_2(X\ ^3\Sigma_g^-)$ bond energy. (Corrected from source: Ref. [82])

Another small contribution to dissociation is given by a group of three electronic states that have excitation energies so close to often result in overlapped energy loss peaks [79, 81]. These are $c\ ^1\Sigma_u^-$, A' (C) $^3\Delta_u$ [9] and $A\ ^3\Sigma_u^+$ and they all dissociate to $O(^3P) + O(^3P)$. Because

---

[9] The C designation is sometimes found in literature instead of A'. See Ref. [81] for more details.

Table 3.5: Electronic states of O_2 which determine dissociation.

Excited state	Thr. energy (eV) Ref. [79]	Thr. energy (eV) Ref. [80]	Thr. energy (eV) Ref. [74]	Diss. products
$c\ ^1\Sigma_u^-$	4.050^a+1.066^b	?	/	O(^{3}P) + O(^{3}P)
$A'\ (C)\ ^3\Delta_u$	4.262^a+0.861^b	?	/	
$A\ ^3\Sigma_u^+$	4.340^a+0.775^b	?	6.1	
$B\ ^3\Sigma_u^-$	6.120^a+0.963^b	7.083	8.4	O(^{3}P) + O(^{1}D)

[a] Energy of the lowest vibrational state with respect to O_2(X $^3\Sigma_g^-, v = 0$).
[b] Dissociation energy.

of their excitation energies they are often referred as the *6eV states*.

All the electronic states discussed, together with the respective excitation energies, are listed in Table 3.5. Note that the energies are not uniquely defined and vary depending on the author. In particular, Itikawa et al. [79] reported, for each state, the energy of the lowest vibrational level with respect to O_2(X $^3\Sigma_g^-, v = 0$) and the additional energy needed to dissociate from there. The resulting total threshold for the $B\ ^3\Sigma_u^-$ state is identical to the value of Cosby [80], while a comparison with the other states cannot be made as Cosby did not provide explicit energies for the 6 eV states. In general, the dissociation threshold energies of Table 3.4 are considered nominal, as it can be inferred from Figure 3.13, where the potential energy curves of the major O_2 excited states are depicted, together with the corresponding dissociation limits. Also, note that in this figure are reported the vibrational levels of the states, indicated by ticks over the curves. In particular, the lowest ones (i.e. 0 ticks, near the curves minima) confirm the values of Itikawa et al.

On the other hand, in the Biagi database on LXCat [74] are reported slightly higher dissociation energies for both levels, with the first one only determined by the $A\ ^3\Sigma_u^+$ state. Although the origin of these differences is not certain, it is speculated that the threshold energies provided correspond to those required for exciting the two states, which would then autonomously predissociate (at least in the case of $B\ ^3\Sigma_u^-$). In this way, the Biagi database values may more accurately represent the known predissociation process involved, which requires a higher energy than the nominal dissociation limit associated. Regarding the choice of considering only dissociation from $A\ ^3\Sigma_u^+$ rather than all three states, it may just be arbitrary. Indeed, it is worth mentioning that in the Biagi database the states $c\ ^1\Sigma_u^-$ and $A'\ (C)\ ^3\Delta_u$ are considered together in an excitation-only reaction, probably including in the $A\ ^3\Sigma_u^+$ dissociative excitation cross-section even their contribution to O(^{3}P) + O(^{3}P) dissociation.

Concerning the cross-sections, in Figure 3.14a are compared the values of Cosby with those of the Biagi database. Note that the cross-sections reported by Itikawa et al. [79] are not considered here as Itikawa himself, in his most recent review [81], recommended the data set of Cosby. In particular, Cosby experimentally determined a single total dissociation cross-section for O_2 (i.e. comprising contributions to both levels) with a claimed absolute uncertainty of ±34%. In contrast, in the Biagi database are separately reported the numerically determined cross-sections relative to $A\ ^3\Sigma_u^+$ and $B\ ^3\Sigma_u^-$. It is observed that dissociation from $A\ ^3\Sigma_u^+$ is generally much lower than $B\ ^3\Sigma_u^-$, except for energies below $\approx$ 9 eV, which is coherent with the $B\ ^3\Sigma_u^-$ threshold energy of 8.4 eV. Also, although the values of Cosby are more scarce, an agreement in the order of magnitude is seen with the $B\ ^3\Sigma_u^-$ cross-section. While in general an experimental data set is preferred, in this work are chosen the values of the Biagi database, mainly to maintain coherence with the excitation cross-sections of O_2 (discussed in the following), which are also taken from it.

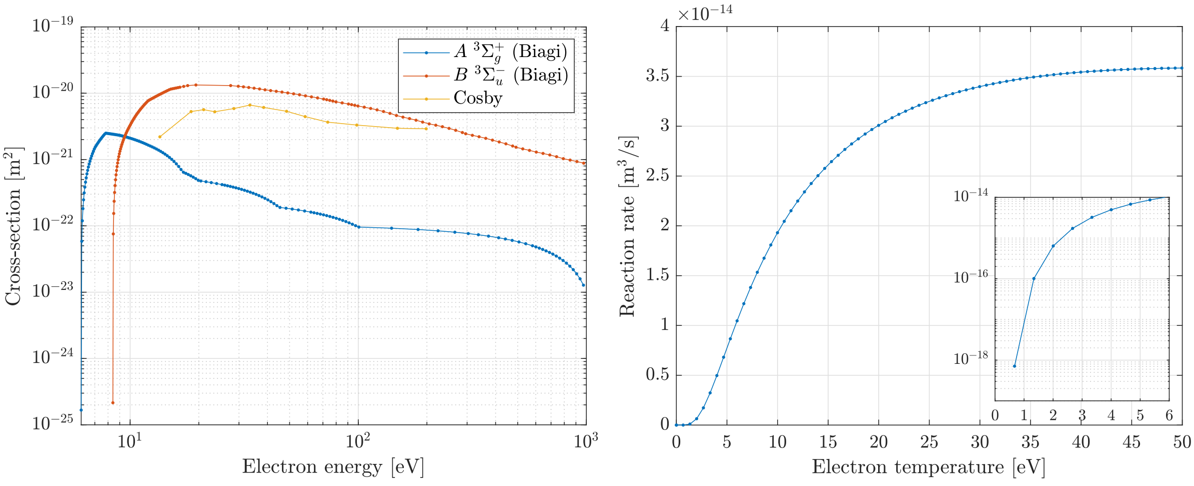

(a) **(b)**

Figure 3.14: (a) Total dissociation cross-section for electron collisions with O_2. The dissociative excitation cross-sections relative to the electronic states $A\ ^3\Sigma_u^+$ and $B\ ^3\Sigma_u^-$ from the Biagi database [74] are compared with the values of Cosby [80]. (b) Corresponding total dissociation rate for electron temperatures up to 50 eV obtained from the data of the Biagi database [74]. The values at small temperatures are resolved in the inset plot.

Finally, in Figure 3.14b is shown the total dissociation rate $k_{O_2,diss}$, obtained by summing up the reaction rates of the two cross-sections selected.

Ionization

It is now investigated ionization. Specifically, ionization reactions for O_2 and O write as

$$O_2(X\,{}^3\Sigma_g{}^-) + e^- \longrightarrow O_2^+ + 2\,e^- \tag{3.16}$$

$$O({}^3P) + e^- \longrightarrow O^+ + 2\,e^- \tag{3.17}$$

where $O({}^3P)$ is the ground state of atomic oxygen.

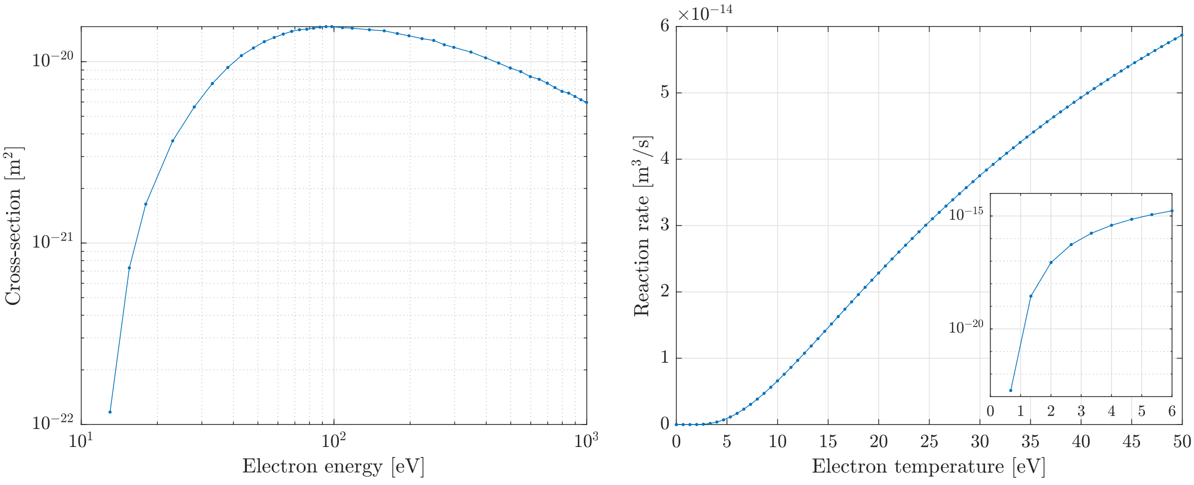

(a) **(b)**

Figure 3.15: (a) Partial ionization cross-section of O_2 for the production of O_2^+. (Source: Ref. [66]) (b) Corresponding ionization rate for electron temperatures up to 50 eV. The values at small temperatures are resolved in the inset plot.

With a threshold energy of 12.06 eV, ionization of O_2 into O_2^+ is considered in the model by means of the experimental cross-section of Lindsay and Mangan [66],[10] also recommended by Itikawa in his review [81]. This partial cross-section, with a claimed absolute uncertainty of ±5%, is shown in Figure 3.15 together with the respective ionization rate $k_{O_2,ion}$.

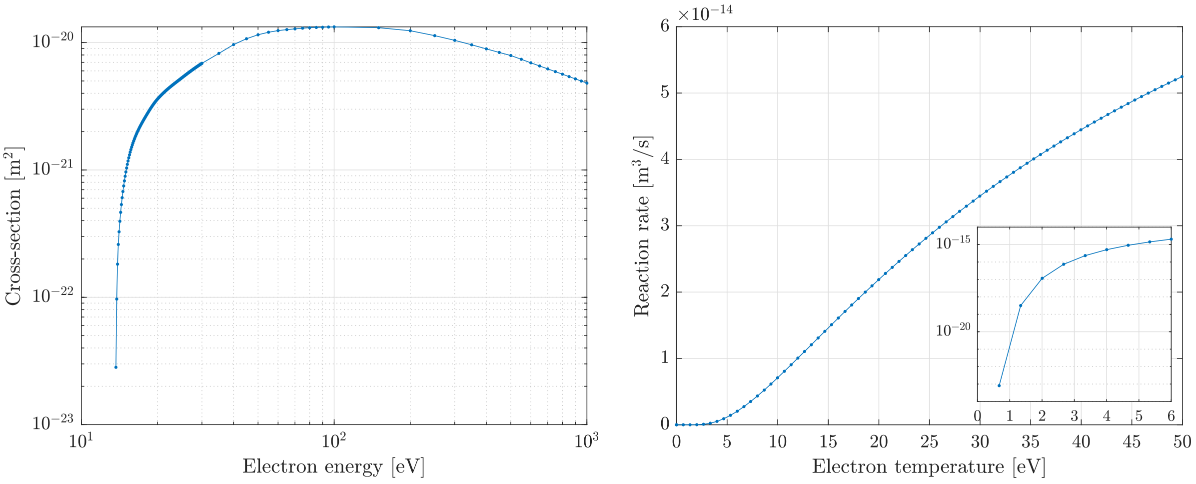

(a) **(b)**

Figure 3.16: (a) Partial ionization cross-section of O for the production of O^+. (Source: Ref. [69]) (b) Corresponding ionization rate for electron temperatures up to 50 eV. The values at small temperatures are resolved in the inset plot.

As in the case of N ionization, also the cross-section values for O ionization in O^+ are retrieved from the IST-Lisbon database on LXCat [69]. However, for this reaction, with ionization energy threshold of 13.6 eV, the original source is the review of Laher and Gilmore [83], which merged two sets of experimental results. The partial cross-section has a claimed accuracy in the ±5-10% range and it is shown in Figure 3.16 with the respective ionization rate $k_{O,ion}$.

Finally, it is analyzed the possibility of other notable products being formed from ionization of O_2^+ and O^+. The respective reactions are

$$O_2^+ + e^- \longrightarrow O_2^{2+} + 2\,e^- \tag{3.18}$$

$$O^+ + e^- \longrightarrow O^{2+} + 2\,e^- \tag{3.19}$$

Again, as for nitrogen, these processes are investigated by looking at the overall products of O_2 ionization. Accordingly, the complete results of the work of Lindsay and Mangan [66] are analyzed. Indeed, these comprise the experimental ionization cross-sections of O_2^+, O^+/O_2^{2+} and O^{2+}, which have been measured by means of a mass spectrometer (thus preventing O^+ and O_2^{2+} from being distinguished). Figure 3.17 reports their values, which are characterized by absolute uncertainties of ±5%, ±5% and ±6%, respectively. In order to solve the uncertainty surrounding the individual cross-sections of O^+ and O_2^{2+}, the results of Sigaud et al. [84] are here reported. Specifically, they managed to experimentally distinguish the two species, showing a difference of about two orders of magnitude between O_2^{2+} and O^+ productions. These cross-sections, with a claimed absolute uncertainty of ±15% for O_2^{2+} and ±5% for O^+, are also shown in Figure 3.17, together with the one they contextually obtained for O_2^+ (±5% absolute uncertainty). As the agreement between the two O_2^+ cross-sections results very good,

---

[10] The experimental data reported in their review are those obtained by Straub et al. [67], later adjusted to reflect a recalibration of the experimental apparatus.

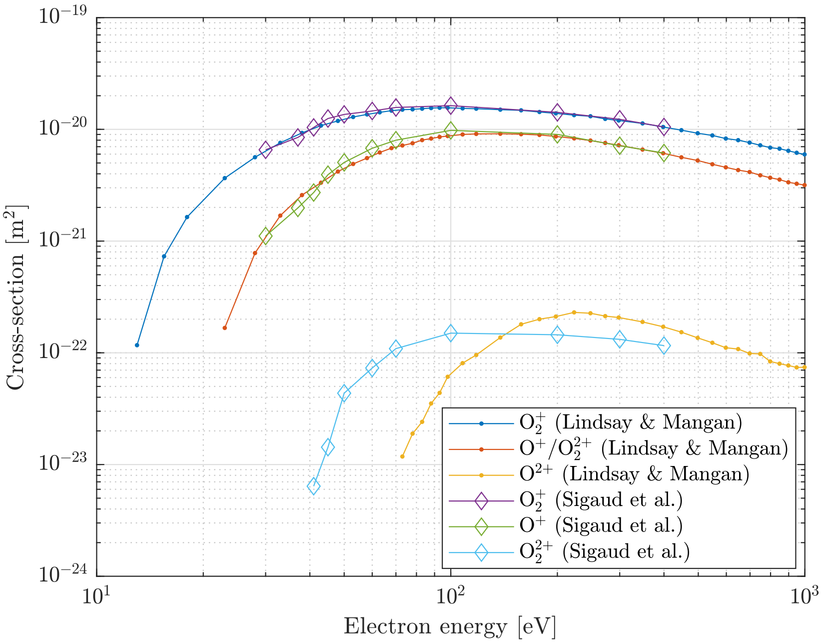

Figure 3.17: Partial ionization cross-sections of O_2 for the production of O_2^+, O^+, O_2^{2+} and O^{2+}. The data of Lindsay and Mangan [66] are compared with those of Sigaud et al. [84], showing a very good agreement.

also the other species data are expected to be comparable. Therefore, the production of O_2^{2+} is safely assumed negligible. Similarly, O^{2+} is neglected too, as its cross-section has the same magnitude of O_2^{2+} with an even higher appearance potential of about 70 eV, which is definitely too high for Hall thrusters with the power and size of the HT5k.

In conclusion, the only positive ion species that result relevant in the HET air plasma under analysis are O_2^+ and O^+.

Dissociative Ionization

Dissociative ionization of O_2 molecules in now briefly presented. The corresponding reaction for O_2 at ground state is

$$O_2(X\,^3\Sigma_g{}^-) + e^- \longrightarrow O + O^+ + 2\,e^- \tag{3.20}$$

Figure 3.18a reports the cross-section from the experimental work of Rapp et al. [72], the same used also for N_2 dissociative ionization. Although the values precisely refer to all non-O_2^+ ions and not only to O^+ production, in the previous paragraph this difference was demonstrated to be negligible (see Figure 3.17). Regarding the appearance potential of O^+ in O_2 dissociative ionization, this is not precisely defined by neither Rapp et al. nor Lindsay and Mangan [66] for their O^+ cross-section. Therefore it is taken the energy of 19.5 eV used for the same reaction in the TRINITI database on LXCat [85].

Lastly, in Figure 3.18b is shown the obtained dissociative ionization rate $k_{O_2,DI}$.

Electron Attachment/ Dissociative Attachment

In this paragraph are investigated the reactions involved in negative ions formation. In particular these can be divided in electron attachment reactions, i.e.

$$O_2(X\,^3\Sigma_g{}^-) + e^- \longrightarrow O_2^- \tag{3.21}$$

$$O(^3P) + e^- \longrightarrow O^- \tag{3.22}$$

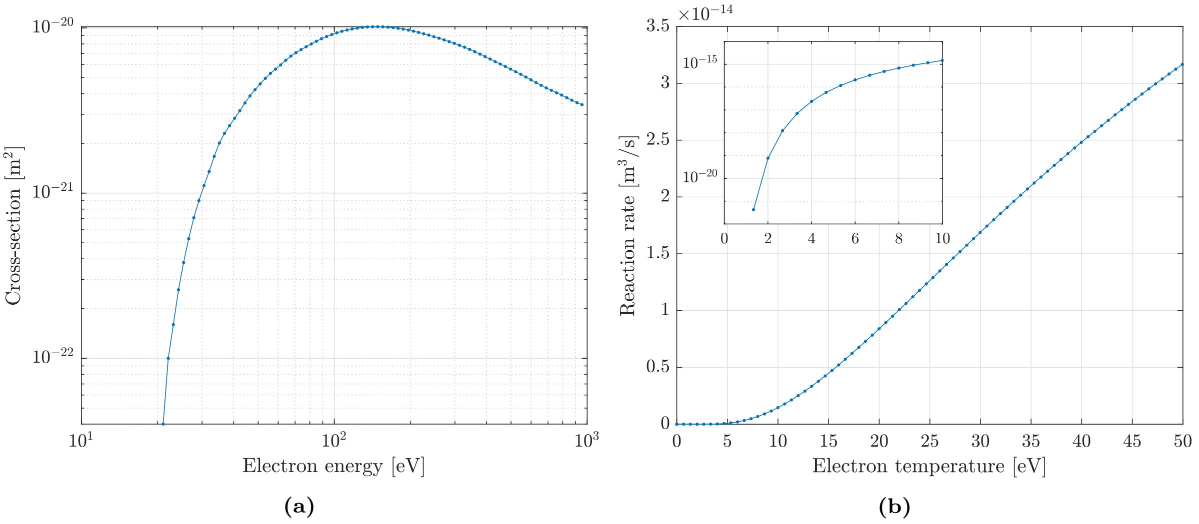

(a) **(b)**

Figure 3.18: (a) Total dissociative ionization cross-section for electron collisions with O_2. (Source: Ref. [72]) (b) Corresponding total dissociative ionization rate for electron temperatures up to 50 eV. The values at small temperatures are resolved in the inset plot.

and dissociative attachment reactions, i.e.

$$O_2(X\,^3\Sigma_g{}^-) + e^- \longrightarrow O + O^- \tag{3.23}$$

Contrarily to the nitrogen case, cross-sectional data about production of negative oxygen ions are available in literature. In particular, starting from electron attachment on O_2, Figure 3.19a shows the values from both Biagi [74] and Phelps [86] databases on LXCat. Similarly, regarding dissociative attachment, Figure 3.19b reports the cross-sections taken from the work of Rapp et al. [87] (also recommeded by Itikawa in his review [81]), and again from both Biagi [74] and Phelps [86] databases. Overall, the data sets appear in very good agreement, thus endorsing the values accuracy. Therefore, due to the extremely low cross-sections characterizing these reactions, it is possible to safely neglect both, together with their products O_2^- and O^-.

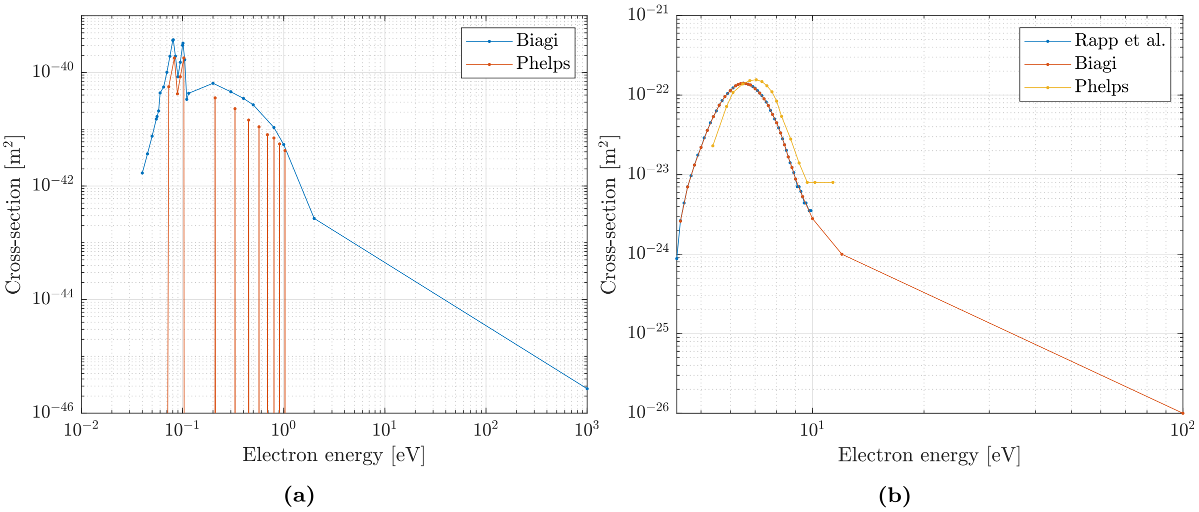

(a) **(b)**

Figure 3.19: (a) Electron attachment cross-section for electron collisions with O_2. The data of Biagi [74] and Phelps [86] databases are compared showing a good agreement. (b) Dissociative attachment cross-section for electron collisions with O_2. The data of Rapp et al. [87] are compared with those of Biagi [74] and Phelps [86] databases, showing a very good agreement.

Regarding electron attachment on O, the only information that could be found in literature is a constant reaction rate in the review of Phelps [60]. However, regardless of the assumed temperature range of validity (i.e. 150-500 K) its constant value of $(1.3 \pm 0.1) \times 10^{-21}\,\mathrm{m^3/s}$ is too low to be considered in the model.

Consequently, as a result of these data it is safely assumed that negative oxygen ions are not present in the air plasma under analysis.

Excitation

It is now discussed electron-impact excitation of both molecular and atomic oxygen from their ground states. The respective reactions write in general form as

$$\mathrm{O_2(X\,^3\Sigma_g{}^-) + e^- \longrightarrow O_2^* + e^-} \tag{3.24}$$

$$\mathrm{O(^3P) + e^- \longrightarrow O^* + e^-} \tag{3.25}$$

As it was introduced in the paragraph about oxygen dissociation, the cross-sectional data for O_2 excitation are taken from the Biagi database [74]. In particular, the excited states considered are listed in Table 3.6 together with the respective excitation energies in eV and, when available, also the vibrational level.[11] It is recalled that, following the data of the Biagi database, only states $B\ {}^3\Sigma_u^-$ and $A\ {}^3\Sigma_u^+$ are assumed responsible for O_2 dissociation. These are therefore excluded from the current discussion and have been greyed out in Table 3.6 for greater clarity. What remains are the two 6 eV states not considered for dissociation (i.e. $c\ {}^1\Sigma_u^-$ and $A'\ (C)\ {}^3\Delta_u$), four vibrational levels of the ground state and the states $a\ {}^1\Delta_g$ and $b\ {}^1\Sigma_g^+$, which are too close to the ground state to dissociate [80]. The respective cross-sections are reported in Figures 3.20a-c, while in Figure 3.20d is shown the total excitation rate $k_{O_2,exc}$, obtained by summing up the reaction rates relative to each cross-section.

Table 3.6: Excitation of O_2. The greyed out states are those responsible for O_2 dissociation, thus being excluded from the computation of $k_{O_2,exc}$. (Source: Ref. [74])

Excited state	Vibrational level	Threshold energy (eV)
$X\ {}^3\Sigma_g^-$	1	0.193
$X\ {}^3\Sigma_g^-$	2	0.386
$X\ {}^3\Sigma_g^-$	3	0.579
$X\ {}^3\Sigma_g^-$	4	0.772
$a\ {}^1\Delta_g$		0.977
$b\ {}^1\Sigma_g^+$		1.627
$c\ {}^1\Sigma_u^-$ $A'\ (C)\ {}^3\Delta_u$		4.5
$A\ {}^3\Sigma_u^+$		6.1
$B\ {}^3\Sigma_u^-$		8.4

Excitation of ground state oxygen (i.e. $\mathrm{O}(2s^2 2p^4\ {}^3P)$ or simply $\mathrm{O(^3P)}$) is accounted for by means of the electronic states listed in Table 3.7. These have been retrieved from the IST-Lisbon database [69] and in particular from the work of Alves et al. [88], which selected the most important ones from the extensive review of Laher and Gilmore [83]. Overall, 17 electronic states were chosen, among which 14 are Rydberg states which were divided in three

---

[11] In case the vibrational level is not indicated, the threshold energy is the energy of the lowest vibrational state relative to $\mathrm{O_2}(X^3\Sigma_g^-, v = 0)$.

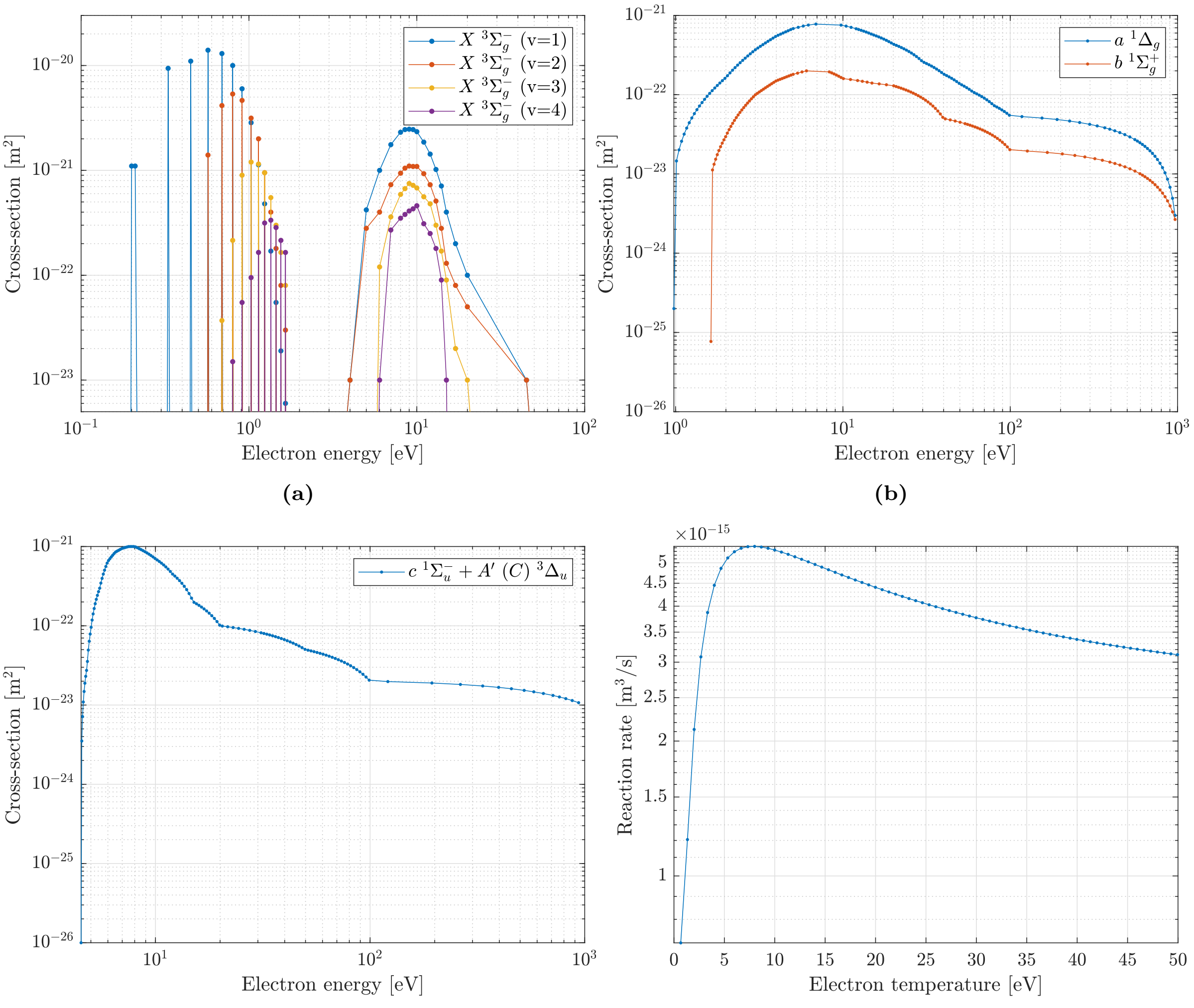

(a)

(b)

(c)

(d)

Figure 3.20: (a)-(c) Excitation cross-sections for electron collisions with O_2. The electronic states refer to Table 3.6. (Source: Ref. [74]) (d) Total excitation rate of O_2 for electron temperatures up to 50 eV.

groups depending on their respective ionic cores.[12] Alves et al. proposed a single averaged cross-section for each ionic core group rather than one for every excited state. This choice has been here preferred in order to keep the discussion compact while still taking into account the contributions of all the major states. These cross-sections are shown in Figure 3.21a-c, while the corresponding overall excitation rate $k_{O,exc}$ in presented in Figure 3.21d.

It is worth mentioning that, in the IST-Lisbon database, all the excitation processes reported are characterized by a very high de-excitation (i.e. low statistical weight between reagents and products, see Ref. [90]). While de-excitation reactions are not considered in this work (mainly because of the low residence time of the propellant in the channel), it remains uncertain the extent to which the O excitation reactions included contribute to electron energy losses. However, by taking into account the presence of many minor excited states not selected

---

[12] An atom in a Rydberg state is characterized by one or more valence electrons located in a very large orbit (i.e. with a high quantum number n), far from the atomic (ionic) core. The distance is such that the outer electron experiences a Coulomb potential from the far and compact ionic core (comprising nucleus and inner electrons) similar to that experienced by the electron in a hydrogen atom. In addition, Rydberg atoms have some other peculiar properties, whose treatment however goes beyond the scope of this work. More information can be found in Ref. [89].

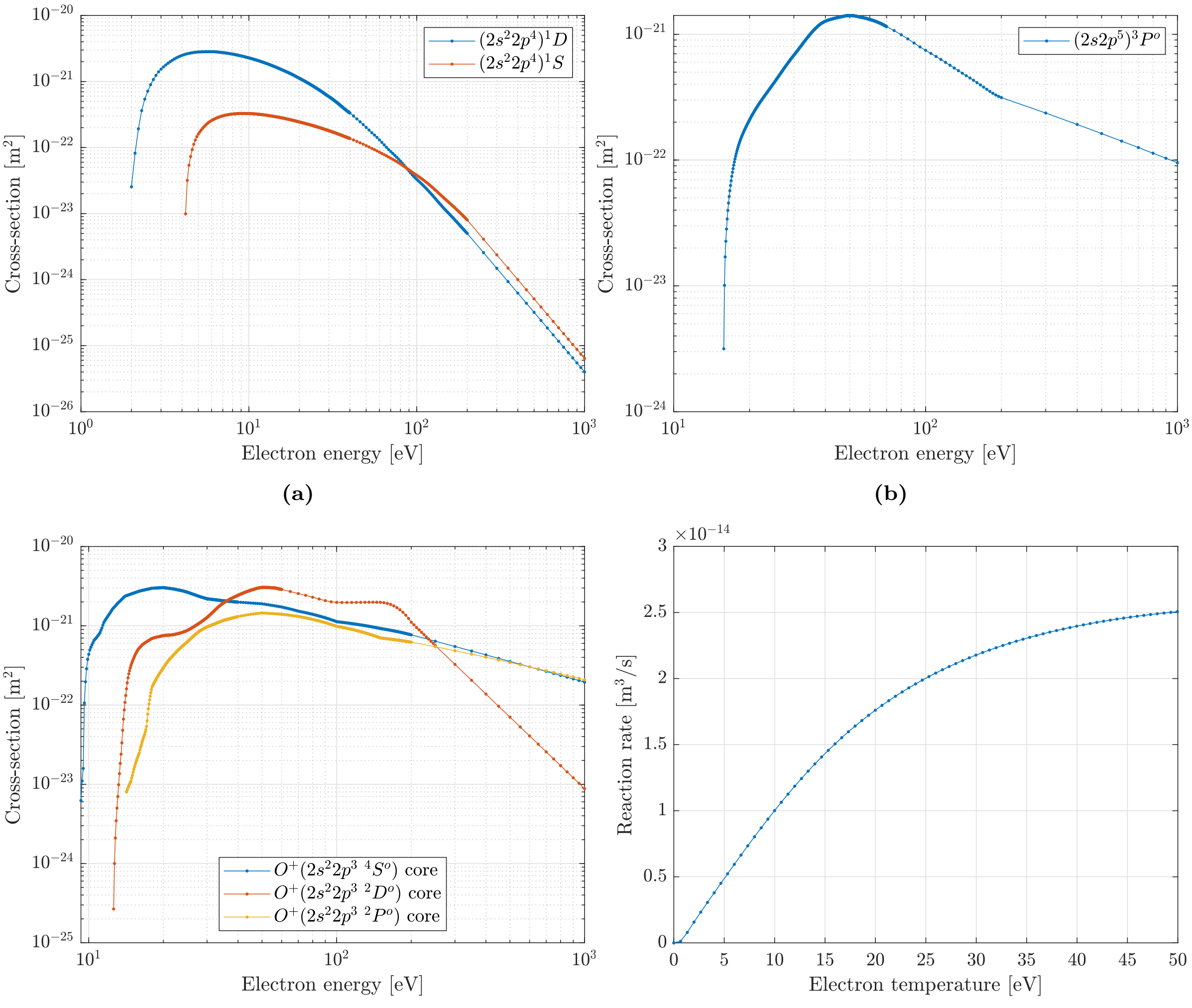

(a) **(b)**

(c) **(d)**

Figure 3.21: (a)-(c) Excitation cross-sections for electron collisions with O. The electronic states refer to Table 3.7. (Source: Ref. [69]) (d) Total excitation rate of O for electron temperatures up to 50 eV.

by Alves et al., together with the possible electron temperature overestimation expected from the numerical model [10], it is speculated that the presented reaction rate is sufficiently reliable in describing electron energy losses in O excitation processes, or at the most slightly overestimating them.

Elastic Momentum Transfer

The last process considered for oxygen is the elastic momentum transfer.

Figure 3.22 shows the relative cross-section for the case of O_2 together with the corresponding reaction rate $k_{O_2,el}$. The cross-section values are taken from the review of Itikawa [81], with an estimated uncertainty within 20%. Contrarily to the case of nitrogen, even if a shape resonance is present in the region below 1 eV, no resonance effect has ever been experimentally reported [81].

Lastly, the cross-section relative to elastic momentum transfer of atomic oxygen is shown in Figure 3.23 together with the respective reaction rate $k_{O,el}$. The data set is taken from the IST-Lisbon database [69] and in particular from the work of Alves et al. [88], as for the case of O excitation. Similarly to O_2, also O does not show any resonance effect in the cross-section.

Table 3.7: Excitation of O. The states follow the notation of Laher and Gilmore, in which unprimed, primed and doubly primed orbitals refer respectively to the $^4S^o$, $^2D^o$ and $^2P^o$ ion cores. Also, the notation $O(4d'^3SPD^o)$ stands for the set of $O(4d'^3S^o)$, $O(4d'^3P^o)$ and $O(4d'^3D^o)$ states, which have been grouped together due to similar electron configurations and energy thresholds. (Sources: Ref. [83, 88])

Excited state	Term	Threshold energy (eV)	Ionic core	Group threshold energy (eV)
$2s^22p^4$	^1D	1.96	/	/
$2s^22p^4$	^1S	4.18	/	/
$2s2p^5$	$^3P^o$	15.65	/	/
$2s^22p^3(^4S^o)3s$	$^5S^o$	9.14	$2s^22p^3\ ^4S^o$	9.2
$2s^22p^3(^4S^o)3p$	^5P	10.73		
$2s^22p^3(^4S^o)4s$	$^3S^o$	11.92		
$2s^22p^3(^4S^o)3d$	$^3D^o$	12.08		
$2s^22p^3(^4S^o)4p$	^3P	12.35		
$2s^22p^3(^4S^o)4d$	$^3D^o$	12.75		
$2s^22p^3(^2D^o)3d'$	$^3S^o$	15.36	$2s^22p^3\ ^2D^o$	12.5
$2s^22p^3(^2D^o)3d'$	$^3P^o$	15.36		
$2s^22p^3(^2D^o)3d'$	$^3D^o$	15.36		
$2s^22p^3(^2D^o)4s'$	$^3D^o$	15.17		
$2s^22p^3(^2D^o)4d'$	$^3SPD^o$	16.08		
$2s^22p^3(^2P^o)3s''$	$^3P^o$	14.11	$2s^22p^3\ ^2P^o$	14.1
$2s^22p^3(^2P^o)3d''$	$^3P^o$	17.09		
$2s^22p^3(^2P^o)4s''$	$^3P^o$	16.81		

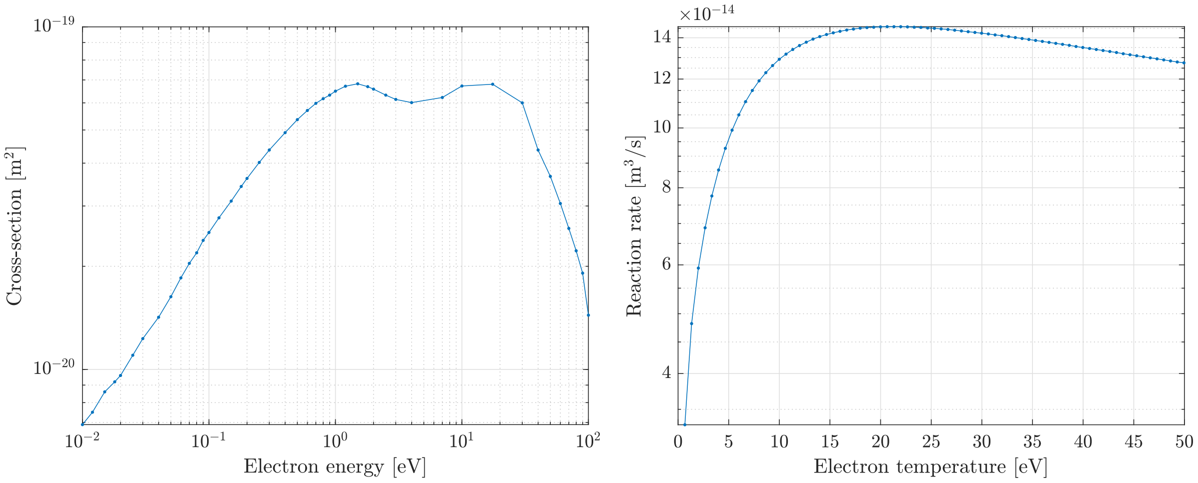

(a) **(b)**

Figure 3.22: (a) Elastic momentum transfer cross-section for electron collisions with O_2. (Source: Ref. [81]) (b) Corresponding reaction rate for electron temperatures up to 50 eV.

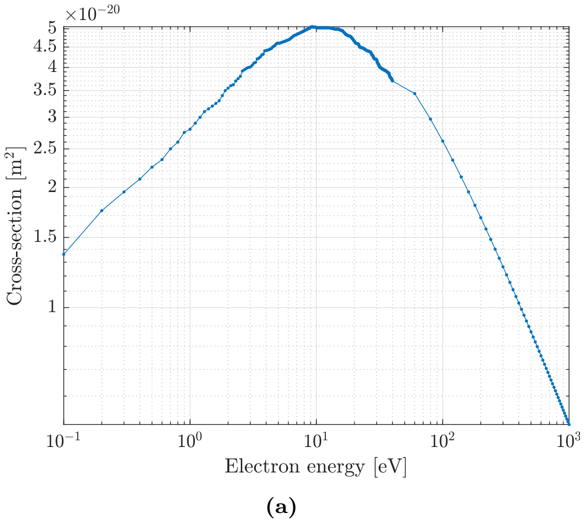

Figure 3.23: (a) Elastic momentum transfer cross-section for electron collisions with O. (Source: Ref. [69]) (b) Corresponding reaction rate for electron temperatures up to 50 eV.

3.2.3. Summary

To conclude the discussion about chemical modelling of nitrogen/oxygen plasmas, it is here presented a brief summary.

At first, the analysis was restricted to electron-impact processes only, due to their predominant influence on plasma dynamics. Consequently, mixed reaction involving both nitrogen and oxygen were excluded as well. Then, by evaluating the reaction cross-sections of all possible electron-impact processes through literature results, it was concluded that only singly charged positive ion species result relevant. This brings to nine the total number of species needed to model an air plasma by means of a fluid numerical approach: four neutral species (N_2, N, O_2, O), four positive ion species (N_2^+, N^+, O_2^+, O^+) and electrons. To the author's knowledge, this work is the first-ever to model a HET plasma composed of so many species. Actually, not even Hall thruster models dealing with mixed plasmas (i.e. composed of different chemical species) are known from literature. Generally, these are limited to pure xenon or krypton plasmas, which rarely include up to thirdly charged ions (e.g. Xe^+, Xe^{++} and Xe^{+++}) [6, 7, 8, 9, 10].

Finally, Table 3.8 reports all the reactions considered in the numerical model, together with their threshold energies (when present) and the corresponding reaction rates.

Table 3.8: Summary of the chemical reactions considered for the modelling of nitrogen/oxygen plasmas. For those reactions whose rates are obtained as a sum of several contributions, both minimum and maximum threshold energies are reported.

Reaction	Threshold energy (eV)	Reaction rate	References
$N_2 + e^- \longrightarrow 2\,N + e^-$	12.1373	$k_{N_2,diss}$	[61]
$N_2 + e^- \longrightarrow N_2^+ + 2\,e^-$	15.58	$k_{N_2,ion}$	[66]
$N + e^- \longrightarrow N^+ + 2\,e^-$	14.54	$k_{N,ion}$	[69, 70]
$N_2 + e^- \longrightarrow N + N^+ + 2\,e^-$	24.34	$k_{N_2,DI}$	[72]
$N_2 + e^- \longrightarrow N_2^* + e^-$	0.2889-14	$k_{N_2,exc}$	[62, 74, 75]
$N + e^- \longrightarrow N^* + e^-$	2.391-13.348	$k_{N,exc}$	[70, 77]
N_2 elastic momentum transfer	/	$k_{N_2,el}$	[62]
N elastic momentum transfer	/	$k_{N,el}$	[69, 70]
$O_2 + e^- \longrightarrow 2\,O + e^-$	6.1-8.4	$k_{O_2,diss}$	[74]
$O_2 + e^- \longrightarrow O_2^+ + 2\,e^-$	12.06	$k_{O_2,ion}$	[66]
$O + e^- \longrightarrow O^+ + 2\,e^-$	13.6	$k_{O,ion}$	[69, 83]
$O_2 + e^- \longrightarrow O + O^+ + 2\,e^-$	19.5	$k_{O_2,DI}$	[72, 85]
$O_2 + e^- \longrightarrow O_2^* + e^-$	0.193-4.5	$k_{O_2,exc}$	[74]
$O + e^- \longrightarrow O^* + e^-$	1.96-15.65	$k_{O,exc}$	[69, 83, 88]
O_2 elastic momentum transfer	/	$k_{O_2,el}$	[81]
O elastic momentum transfer	/	$k_{O,el}$	[69, 88]

3.3. Presheath/Sheath Model

In this section, building on the discussion of Chapter 2 about instabilities in multispecies plasmas, it is presented a presheath/sheath model including ion-ion streaming instabilities for an air plasma containing the four positive ion species determined in the previous section: N_2^+, N^+, O_2^+ and O^+. In particular, for $N = 4$ Eq. 2.19 becomes

$$\hat{\varepsilon}(\mathbf{k}, \omega) = 1 + \frac{1}{k^2 \lambda_{De}^2} \sum_{i=1}^{4} \left[1 - \frac{Z_i^2}{2} \frac{T_e}{T_i} \frac{n_i}{n_e} Z'(\zeta_i) \right] \tag{3.26}$$

where

$$\zeta_i = \frac{\omega(\mathbf{k}) - \mathbf{k} \cdot \mathbf{u_i}}{k v_{T,i}} \qquad \text{for} \quad i = 1, 2, 3, 4 \tag{3.27}$$

represents the four dimensionless arguments of the plasma dispersion function derivative.

By introducing the complex parameter $\Omega = \Omega_R + i\Omega_I$, following the approach used by Severn et al. [91], the dispersion relation $\omega(\mathbf{k})$ (i.e. complex angular wave function) is defined as

$$\omega(\mathbf{k}) = \frac{1}{2} \mathbf{k} \cdot (\mathbf{u_1} + \mathbf{u_4}) + \mathbf{k} \cdot \Delta \mathbf{u_{14}} \Omega \tag{3.28}$$

where the species velocities $\mathbf{u_i}$ through the presheath are ordered from the fastest one to the slowest one. As all the species are considered to be stationary in the plasma bulk (i.e. $\mathbf{u_{i,bulk}} = 0$) and they are accelerated toward the wall by the same presheath potential ϕ_0, lighter species are always faster than heavier ones throughout the presheath. Therefore, the indices $i = 1, 2, 3, 4$ respectively refer to N, O, N_2 and O_2. Thanks to this characteristic, the species velocities diverge one with respect to the other while moving toward the sheath edge. Consequently, contrarily to the two-ion stream case, multiple velocity differences Δu affect the eventual instability onset.

As each ion species has an influence on all the others through the plasma dielectric function (Eq. 3.26), the instability threshold does not correspond to the smallest Δu_c among those characteristic of all two-species plasma combinations alone. Rather, as experimentally observed for the case of various third species (i.e. Kr or Ne) added to a Ar/Xe plasma, the additional species strongly influences the instability onset profile [91, 92]. In particular, the effect varies depending on both its atomic mass and density ratio. Although ion velocity measurements at the sheath edge in plasmas with more than three species are not present in literature to the author's knowledge, similar interactions are expected also in the case here under study.

By recalling that, for the j-th (unstable) mode, $\omega_j = \omega_{R,j} + i\gamma_j$ (see Eq. 2.9), the real and imaginary components of $\omega(\mathbf{k})$ respectively result

$$\omega_R = \frac{1}{2} \mathbf{k} \cdot (\mathbf{u_1} + \mathbf{u_4}) + \mathbf{k} \cdot \Delta \mathbf{u_{14}} \Omega_R \tag{3.29}$$

$$\gamma = \mathbf{k} \cdot \Delta \mathbf{u_{14}} \Omega_I \tag{3.30}$$

where the subscript j is omitted for conciseness. Indeed, as explained in Section 2.2, the study of ion-ion streaming instabilities solely concerns plasma unstable modes (i.e. $\gamma > 0$), which are the only ones responsible for the increase in ion-ion friction that blocks the ion differential flow. Regarding the growth rate γ expression in Eq. 3.30, note that the introduction of Ω highlights both its dependence on $\Delta \mathbf{u_{14}}$ and the fact that the most unstable wavenumber is parallel to $\Delta \mathbf{u_{14}}$.

Overall, the purpose of Ω is that of substituting the unknown $\omega(\mathbf{k})$ in the expression of the plasma dielectric function $\hat{\varepsilon}(\mathbf{k}, \omega)$, thus greatly simplifying the search for its roots. Indeed, by means of Eq. 3.28, $\hat{\varepsilon}(\mathbf{k}, \omega)$ can be expressed as a function of differential flow speeds only, rather than the individual ion velocities, thus reducing by one the number of unknowns. In particular, by putting together Eqs. 3.27 and 3.28 for all ion species, the respective arguments ζ_i read

$$\zeta_1 = \hat{k} \cdot \Delta\bar{\mathbf{u}}_{\mathbf{14}} \left(\Omega - \frac{1}{2}\right) \tag{3.31}$$

$$\zeta_2 = \sqrt{\frac{T_1}{T_2}\frac{m_2}{m_1}}\ \hat{k} \cdot \left(\Delta\bar{\mathbf{u}}_{\mathbf{12}} + \Delta\bar{\mathbf{u}}_{\mathbf{14}} \left(\Omega - \frac{1}{2}\right)\right) \tag{3.32}$$

$$\zeta_3 = \sqrt{\frac{T_1}{T_3}\frac{m_3}{m_1}}\ \hat{k} \cdot \left(\Delta\bar{\mathbf{u}}_{\mathbf{13}} + \Delta\bar{\mathbf{u}}_{\mathbf{14}} \left(\Omega - \frac{1}{2}\right)\right) \tag{3.33}$$

$$\zeta_4 = \sqrt{\frac{T_1}{T_4}\frac{m_4}{m_1}}\ \hat{k} \cdot \Delta\bar{\mathbf{u}}_{\mathbf{14}} \left(\Omega + \frac{1}{2}\right) \tag{3.34}$$

where $\Delta\bar{\mathbf{u}} = \Delta\mathbf{u}/v_{T,1}$.

Before proceeding further with the introduction of all the equations necessary to solve the sheath model, it is now set up a step-by-step analysis that will progress with the discussion. Its aim is that of better illustrating the concepts surrounding ion-ion streaming instabilities as well as the influence of some parameters (e.g. wavenumber, electron temperature), thus allowing important considerations.

In order to find the roots of $\hat{\varepsilon}(\mathbf{k}, \omega)$ some assumptions are needed. The first one concerns the unknown species density ratios n_i/n_e. While some accurate local values of these quantities will be only available from the numerical model, for the current analysis it is assumed a uniformly ionizing plasma composed of a $1.27\mathrm{N_2}$+$\mathrm{O_2}$ mixture (recall Section 3.1).

The advantage of dealing with ratios only is that the individual quantities are not needed. Indeed, as suggested by the Boltzmann equation for electrons (Eq. 2.27), the individual densities greatly vary between plasma bulk and sheath edge (i.e. ≈ 0.6 factor), while their ratios, being the plasma quasi-neutral, remain constant throughout the presheath (see Section 2.2). Also, quasi-neutrality implies that all the ratios sum up to 1. Therefore, by arbitrarily assuming that the densities of $\mathrm{N_2^+}$ and $\mathrm{O_2^+}$ are double than those of $\mathrm{N^+}$ and $\mathrm{O^+}$, respectively, it is obtained the system

$$\begin{cases} \bar{n}_1 + \bar{n}_2 + \bar{n}_3 + \bar{n}_4 = 1 \\ (\bar{n}_1 + \bar{n}_3) = 1.27(\bar{n}_2 + \bar{n}_4) \\ \bar{n}_3 = 2\bar{n}_1 \\ \bar{n}_4 = 2\bar{n}_2 \end{cases} \tag{3.35}$$

where $\bar{n}_i = n_i/n_e$ and the ordering is always N, O, $\mathrm{N_2}$ and $\mathrm{O_2}$ for $i = 1, 2, 3, 4$. By solving it, the density ratios can be uniquely determined as

$$\bar{n}_1 = 0.1865 \qquad \bar{n}_2 = 0.1468 \qquad \bar{n}_3 = 0.3730 \qquad \bar{n}_4 = 0.2937 \tag{3.36}$$

The next assumption concerns the ion temperatures T_i, which in numerical models are generally neglected in comparison to the much higher electron temperature. However, it is recalled that, for the study of ion-ion streaming instabilities, ion temperatures must be considered and also need to be finite in order to have non-null instability differential velocity thresholds Δu_c [31]. Consequently, to a first approximation they are assumed to be all the same (i.e. $T_i = T_1 = T_2 = T_3 = T_4$) and, following the reference values considered by Hara and Mikellides [6], $T_{iV} = 0.2\,\mathrm{eV}$ is employed. In order to make a more precise assumption it would be required either to experimentally measure the individual ion temperatures or to numerically

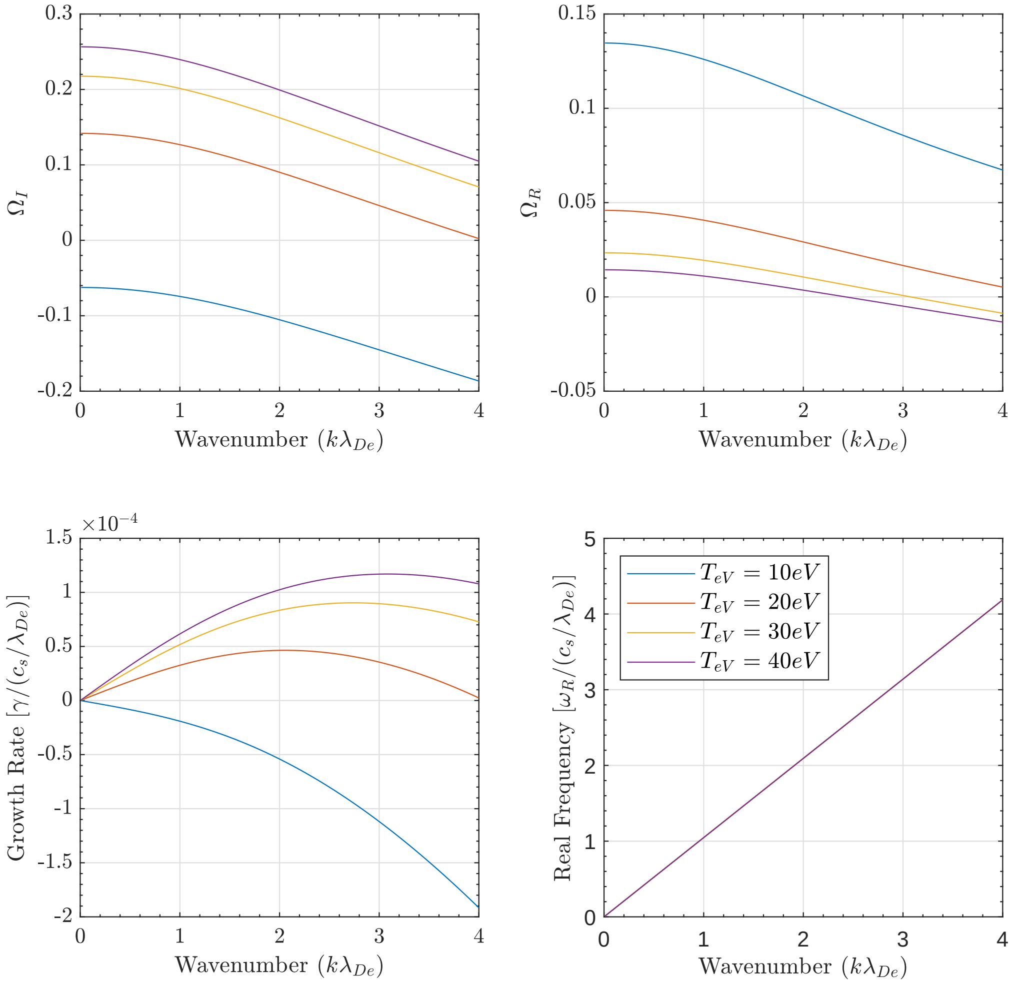

Figure 3.24: Real and imaginary components of both Ω and ω as a function of the wavenumber $k\lambda_{De}$ for $T_{eV} = 10, 20, 30, 40\,\text{eV}$. The solution refers to the only unstable mode (root) present. The plasma characteristics are: 1.27N_2+O_2 mixture with $\bar{n}_3 = 2\bar{n}_1$ and $\bar{n}_4 = 2\bar{n}_2$, $\Delta\bar{u} = \Delta\bar{u}_{max}$ (Eq. 3.37), $T_{iV} = 0.2\,\text{eV}$.

determine them by iteratively solving the ion energy conservation equation for each ion species with this presheath/sheath model. However, both these methods go beyond the scope and possibilities of this work and have not been pursued. Nevertheless, note that the impact of the value selected for T_{iV}, as well as the assumption of considering all ion temperatures equal, is investigated in the sensitivity analysis of Section 3.3.4.

Finally, it is considered the limit case in which the differential velocities $\mathbf{\Delta\bar{u}}$ have their maximum possible values (in absence of SEE), meaning that the ion species have reached, at the sheath edge, their individual sound speeds. For two generic ion species j and k, this condition reads as

$$\Delta\bar{u}_{jk,max} = \frac{c_{s,j} - c_{s,k}}{v_{T,1}} \tag{3.37}$$

Note that this condition may not be achievable for some electron temperatures T_{eV}, as in reality instability may arise at some point before in the presheath, preventing the classical Bohm criterion at the sheath edge from being verified. However, only by looking at such limit case it can be visually determined the threshold (critical) temperature ratio for instability. This is confirmed by Figure 3.24, in which is shown one unstable root of $\hat{\varepsilon}(\mathbf{k}, \omega)$ for four different electron temperatures T_{eV} and for varying wavenumber k. Note that, for the case study here analyzed, this unstable mode (root) is also the only one setting before the sheath edge, while the others arise beyond it, thus never leading to any physical instability. The presented solution, which does not suffer from any analytical approximation as it has been determined by numerically solving Eq. 3.26, shows the real and imaginary parts of both Ω and ω. The latter have been obtained by substitution in Eq. 3.28.

By looking at the growth rate graph in the figure, it clearly appears that at the sheath edge, for this limit condition, only $T_{eV} = 10\,\mathrm{eV}$ causes γ to assume negative values, which means that the plasma is still stable and no instability would have arisen. Contrarily, γ is positive for higher electron temperatures, thus implying an unstable condition which, in a real plasma, would have caused the instability to onset somewhere before in the presheath. In other words, as the electron temperature increases (for fixed ion temperatures), the location where the differential flow velocities frozen due to instability-enhanced friction moves from infinity to the plasma bulk. The temperature at which this location reaches the sheath edge is the threshold and only successive increases cause the instability to effectively arise in the presheath.

The precise value of the temperature threshold can be located numerically by solving Eq. 3.26 with incremental values of T_{eV} and then finding the maximum Ω_I that first crosses 0 (i.e. the first encountered unstable mode). Also, as it can be inferred from Figure 3.24, $\max(\Omega_I(k))$ always locates at $k = 0$. While in general the growth rate γ is not maximum at $k = 0$, this is always true approaching the instability threshold from a stable condition (i.e. from negative values). Therefore, with the goal of investigating the onset of instability, $\hat{\varepsilon}(\mathbf{k}, \omega) = 0$ can be generally solved for $k = 0$, thus resulting

$$Z_1^2 \bar{n}_{1,0} Z'(\zeta_1) + Z_2^2 \bar{n}_{2,0} Z'(\zeta_2) + Z_3^2 \bar{n}_{3,0} Z'(\zeta_3) + Z_4^2 \bar{n}_{4,0} Z'(\zeta_4) = \frac{2}{\theta} \tag{3.38}$$

where $\theta = T_e/T_i$, as defined in Section 2.3.

As a consequence, still assuming the condition of Eq. 3.37, the threshold temperature ratio for this case study is

$$\left(\frac{T_e}{T_i}\right)_c \approx 60 \tag{3.39}$$

Once this threshold is obtained, the other critical parameter Δu_c can be readily determined. Indeed, this corresponds to the difference between ion sound velocities calculated for the threshold electron temperature. More precisely, for the case of four ion species, these thresholds Δu_c are three (i.e. $\Delta u_{12,c}$, $\Delta u_{13,c}$ and $\Delta u_{14,c}$), and they are all mutually constrained by the fact that the ion species arrive at the edge of instability by falling freely under the effect of the same presheath potential ϕ_0. Therefore, in the region before instability (if any) the velocity difference between ion species 1 and a generic ion species j can be written as

$$\Delta u_{1j} = \sqrt{\frac{2e\phi_0}{m_1}} - \sqrt{\frac{2e\phi_0}{m_j}} \quad \Rightarrow \quad \Delta \bar{u}_{1j} = \sqrt{\frac{e\phi_0}{T_1}} \left(1 - \sqrt{\frac{m_1}{m_j}}\right) \tag{3.40}$$

thus leading to the conditions

$$\Delta \bar{u}_{12} = \Delta \bar{u}_{14} \frac{1 - \sqrt{\dfrac{m_1}{m_2}}}{1 - \sqrt{\dfrac{m_1}{m_4}}} \tag{3.41}$$

$$\Delta \bar{u}_{13} = \Delta \bar{u}_{14} \frac{1 - \sqrt{\dfrac{m_1}{m_3}}}{1 - \sqrt{\dfrac{m_1}{m_4}}} \tag{3.42}$$

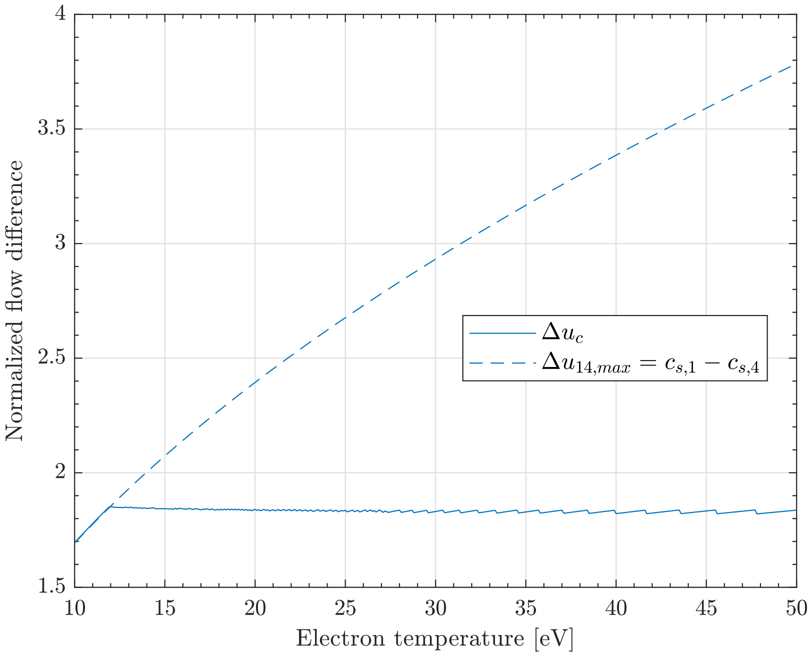

Figure 3.25: Comparison between the critical flow difference Δu_c and the maximum value $\Delta u_{14,max}$ as a function of T_{eV}. This case does not include SEE. The plasma characteristics are: $1.27N_2+O_2$ mixture with $\bar{n}_3 = 2\bar{n}_1$ and $\bar{n}_4 = 2\bar{n}_2$, $T_{iV} = 0.2\,\text{eV}$.

Thanks to these equations, from a single velocity threshold (which in this work, from now on, is assumed to be $\Delta u_{14,c}$) all the others can be obtained. In particular, for the critical temperature ratio of ≈ 60, which implies $T_{eV,c} \approx 12\,\text{eV}$, Δu_c results

$$\Delta u_c \equiv \Delta u_{14,c} \approx 1.8\; v_{T,1} = 2988.6\,\text{m/s} \tag{3.43}$$

Clearly this threshold remains the same for all the electron temperatures greater than $\approx 12\,\text{eV}$, as in these cases it would be only reached before in the presheath rather than at the sheath edge. This is confirmed by Figure 3.25, which has been obtained by solving Eq. 3.38 for a range of T_{eV} while increasing $\Delta\bar{u}_{14}$ (up to $\Delta\bar{u}_{14,max}$, see Eq. 3.37), until for each T_{eV} either instability arises or the sheath edge is reached. Note that the wobbling behaviour seen in the figure for Δu_c is due to numerical instabilities.

Although instability thresholds provide important information about the plasma behaviour in the presheath, the main objective of this kinetic approach remains that of determining the differential flow at the sheath edge (i.e. $\Delta u_{12,0}$, $\Delta u_{13,0}$ and $\Delta u_{14,0}$). Indeed, this information will be then used to calculate the individual ion velocities there by means of the generalized Bohm criterion. However, contrarily to the case of a plasma with only two ion species, it is not certain that upon instability onset the ion differential velocities will lock until the sheath edge. Indeed, to the author's knowledge, velocity measurements in sheaths with more that two ion species have never been achieved. This problem was also pointed out in the experimental studies of Severn et al. [91] dealing with three ion species. Therefore, although neither theoretical nor experimental confirmations of this phenomenon exist, it is here assumed, following the approach of Severn et al., that all ion species effectively keep the velocity differences possessed upon instability onset. Consequently, Eqs. 3.41 and 3.42 result satisfied in the entire presheath, thus also including the region with instability.

Having determined the differential flow at the sheath edge by means of Eqs. 3.38, 3.41 and 3.42, it is now necessary to close the system of equations so as to find the ion velocities. This is achieved by using the same governing equations introduced in the sheath model of Section 2.3. Depending on the presence of secondary electron emission from the wall, two cases are distinguished.

3.3.1. SEE Neglected

In case SEE is not considered, the Bohm sheath criterion for a plasma with $N = 4$ ion species (Eq. 2.52 with $\sigma = 0$) becomes

$$\frac{\bar{n}_{1,0}}{\bar{u}_{1,0}^2} + \frac{m_1}{m_2}\frac{\bar{n}_{2,0}}{\bar{u}_{2,0}^2} + \frac{m_1}{m_3}\frac{\bar{n}_{3,0}}{\bar{u}_{3,0}^2} + \frac{m_1}{m_4}\frac{\bar{n}_{4,0}}{\bar{u}_{4,0}^2} \leq \frac{2}{\theta} \tag{3.44}$$

where all the velocities can be written in terms of a single unknown one (i.e. $\bar{u}_{2,0}$ here) and the three differential velocities, such that

$$\bar{u}_{1,0} = \Delta\bar{u}_{12,0} + \bar{u}_{2,0} \tag{3.45}$$

$$\bar{u}_{3,0} = \Delta\bar{u}_{12,0} + \bar{u}_{2,0} - \Delta\bar{u}_{13,0} \tag{3.46}$$

$$\bar{u}_{4,0} = \Delta\bar{u}_{12,0} + \bar{u}_{2,0} - \Delta\bar{u}_{14,0} \tag{3.47}$$

In this way, the system composed of Eqs. 3.38, 3.41, 3.42 and 3.44 can be solved for the four unknowns ($\Delta\bar{u}_{12,0}$, $\Delta\bar{u}_{13,0}$, Ω, $\bar{u}_{2,0}$). The resulting individual ion velocities at the sheath edge are shown in Figure 3.26a (in solid lines), in comparison with the corresponding sound speeds (in dashed lines). Also, a black dashed line indicates the common system sound speed c_s. The figure shows that, after $\approx 12\,\text{eV}$ ion-ion instability arises and the differential flow effectively freezes, thus preventing the ion velocities from following their sound speeds. As expected, these instead track c_s, due to the fact that Δu_c remains constant and that the frozen flow actually behaves as a whole *system* freely accelerated by ϕ_0.

The two lightest species (i.e. N^+ and O^+) result slowed down by the two heaviest ones (i.e. N_2^+ and O_2+), which conversely are speeded up above their sound speeds. Due to their higher densities (recall the assumption in System 3.35), the latter are less subjected to this effect, showing respectively 3.4-5.1% and 6.2-9% increments for T_{eV} between 30 eV and 50 eV (Figure 3.26b), while the former respectively experience 8.5-11.5% and 6.5-8.7% decrements.

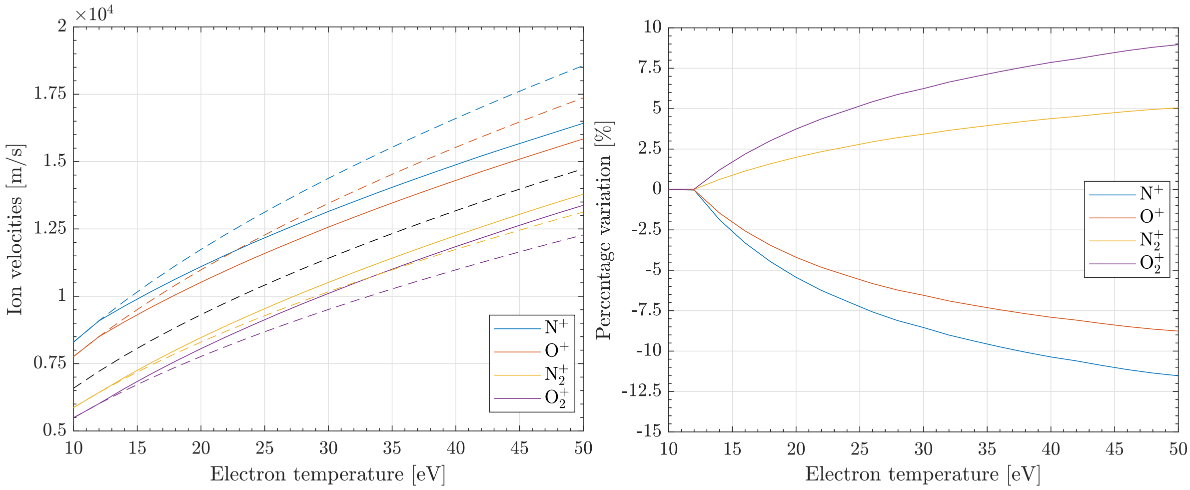

(a) **(b)**

Figure 3.26: (a) Comparison between the individual ion velocities $u_{i,0}$ reached in case of ion-ion streaming instability (solid lines) and the corresponding sound speeds $c_{s,i}$ (dashed lines) as a function of T_{eV}. The black dashed line indicates the common system sound speed c_s (see Eq. 2.3). (b) Corresponding percentage variations. This case does not include SEE. The plasma characteristics are: $1.27\text{N}_2\text{+O}_2$ mixture with $\bar{n}_3 = 2\bar{n}_1$ and $\bar{n}_4 = 2\bar{n}_2$, $T_{iV} = 0.2\,\text{eV}$.

As a final remark, as it can be inferred from the figures, for $T_{eV} > 50\,\mathrm{eV}$ the divergence from the $c_{s,i}$ values continuously increases. However, such electron temperatures are surely above the maximum achievable in HETs with characteristics similar to the PFG. Therefore, such parametric range is not considered in this work.

3.3.2. SEE Considered

In case SEE is taken into account, the model substantially increases in complexity.

At first, the Bohm sheath criterion for a plasma with $N = 4$ ion species in presence of SEE (Eq. 2.52) becomes

$$\frac{\bar{n}_{1,0}}{\bar{u}_{1,0}^2} + \frac{m_1}{m_2}\frac{\bar{n}_{2,0}}{\bar{u}_{2,0}^2} + \frac{m_1}{m_3}\frac{\bar{n}_{3,0}}{\bar{u}_{3,0}^2} + \frac{m_1}{m_4}\frac{\bar{n}_{4,0}}{\bar{u}_{4,0}^2} + \frac{\mu\sigma}{1-\sigma}\frac{\bar{n}_{1,0}\bar{u}_{1,0} + \bar{n}_{2,0}\bar{u}_{2,0} + \bar{n}_{3,0}\bar{u}_{3,0} + \bar{n}_{4,0}\bar{u}_{4,0}}{\sqrt{\left(-\theta\mu\varphi_w + \bar{u}_{s,w}^2\right)^3}} \leq \frac{2}{\theta} \tag{3.48}$$

where Eqs. 3.45 to 3.47 still hold and it is assumed $\bar{u}_{s,w} = 0.16\sqrt{\theta/2}$ as the normalized value for the secondary electrons emission velocity. This value has been taken from the work of Gyergyek et al. [55] which considered this velocity a thousandth of the electron thermal velocity $\sqrt{k_B T_e/m_e}$. However, it has been successively confirmed with this sheath model that even wide variations of this parameter (i.e. between 0 and $10\sqrt{\theta/2}$) produce very little or no effects at all.

Still regarding Eq. 3.48, the unknown adimensional sheath potential drop φ_w is also introduced. As this variable needs to be solved for, another equation is needed. This is the zero current condition at the wall (Eq. 2.48), which for $N = 4$ becomes

$$\bar{n}_{1,0}\bar{u}_{1,0} + \bar{n}_{2,0}\bar{u}_{2,0} + \bar{n}_{3,0}\bar{u}_{3,0} + \bar{n}_{4,0}\bar{u}_{4,0} = (1-\sigma)\sqrt{\frac{\theta\mu}{4\pi}}\exp\left(\varphi_w\right) \tag{3.49}$$

Also, it is recalled that in presence of secondary electrons emitted from the wall, the charge neutrality condition at the sheath edge has to be modified accordingly, assuming the form already derived in Section 2.3 (see Eq. 2.49), i.e.

$$\bar{n}_{1,0} + \bar{n}_{2,0} + \bar{n}_{3,0} + \bar{n}_{4,0} = 1 + \frac{\sigma}{1-\sigma}\frac{\bar{n}_{1,0}\bar{u}_{1,0} + \bar{n}_{2,0}\bar{u}_{2,0} + \bar{n}_{3,0}\bar{u}_{3,0} + \bar{n}_{4,0}\bar{u}_{4,0}}{\sqrt{-\theta\mu\varphi_w + \bar{u}_{s,w}^2}} \tag{3.50}$$

This relation also implies that the assumed ion species densities (Eq. 3.36) are not valid any more. Rather, these are now derived from the sheath model in relation to the SEE. However, for this analysis the other three aforementioned assumptions about plasma composition (see System 3.35) are still necessary.

Finally, depending on the SEE yield coefficient σ, two different systems of equations are defined. Indeed, secondary electron emission is space charge limited and, for a BNSiO$_2$ wall such as the one used in the PFG, σ results [19]

$$\sigma = \min(1.36 \cdot 0.123\ T_{eV}^{0.528}, \sigma_{SCS}) \tag{3.51}$$

Therefore, for the electron temperature range below emission saturation, σ results known and the system composed of Eqs. 3.38, 3.41, 3.42, 3.48, 3.49, 3.50 together with the last three equations of System 3.35 can be solved for the nine unknowns ($\bar{n}_1$, $\bar{n}_2$, $\bar{n}_3$, $\bar{n}_4$, $\Delta\bar{u}_{12,0}$, $\Delta\bar{u}_{13,0}$, Ω, $\bar{u}_{2,0}$, φ_w).

However, as the electron temperature range below emission saturation cannot be defined a priori, it is first required to solve also for σ_{SCS}. In particular, the addition of this tenth unknown requires adding another equation to the system just discussed. This is precisely the zero electric field condition at the wall (Eq. 2.54), which for $N = 4$ becomes

$$
\begin{aligned}
&2\frac{\bar{n}_{1,0}\bar{u}_{1,0}^2}{\theta}\left(\sqrt{1-\theta\frac{\varphi_w}{\bar{u}_{1,0}^2}}-1\right)+2\frac{m_2}{m_1}\frac{\bar{n}_{2,0}\bar{u}_{2,0}^2}{\theta}\left(\sqrt{1-\theta\frac{m_1}{m_2}\frac{\varphi_w}{\bar{u}_{2,0}^2}}-1\right)\\
&+2\frac{m_3}{m_1}\frac{\bar{n}_{3,0}\bar{u}_{3,0}^2}{\theta}\left(\sqrt{1-\theta\frac{m_1}{m_3}\frac{\varphi_w}{\bar{u}_{3,0}^2}}-1\right)+2\frac{m_4}{m_1}\frac{\bar{n}_{4,0}\bar{u}_{4,0}^2}{\theta}\left(\sqrt{1-\theta\frac{m_1}{m_4}\frac{\varphi_w}{\bar{u}_{4,0}^2}}-1\right)\\
&+\exp(\varphi_w)-1 \qquad\qquad (3.52)\\
&+\frac{2\sigma_{SCS}}{1-\sigma_{SCS}}\frac{\bar{n}_{1,0}\bar{u}_{1,0}+\bar{n}_{2,0}\bar{u}_{2,0}+\bar{n}_{3,0}\bar{u}_{3,0}+\bar{n}_{4,0}\bar{u}_{4,0}}{\sqrt{\theta\mu}}\left(\frac{\bar{u}_{s,w}}{\sqrt{\theta\mu}}-\sqrt{-\varphi_w+\frac{\bar{u}_{s,w}^2}{\theta\mu}}\right)\\
&+\frac{1}{2}\left(\frac{d\varphi}{d\xi}\right)^2\Bigg|_{\varphi=0}=0
\end{aligned}
$$

Summarizing, in order to solve this sheath model in case of SEE, for each T_{eV} it is first solved the SCS case. Then, once σ_{SCS} is known, by means of Eq. 3.51 it is defined the correct regime for that T_{eV}. In case this does not correspond to the SCS one, the model is solved again using the material-dependent σ.

Regarding the numerical solution procedure, it is worth mentioning that, while in absence of SEE it is sufficient to solve for $\Delta\bar{u}_{14}$ values up to $\Delta\bar{u}_{14,max}$ (Eq. 3.37), the same does not apply to the SEE case. Indeed, the emission of secondary electrons requires the ions to arrive at the sheath edge with increased velocities in order to maintain charge neutrality (still in accordance with the Bohm criterion though). Therefore, $\Delta\bar{u}_{14,max}$ has to be modified accordingly, so as to span the whole range of differential velocities. Its correct value for each T_e is found by solving once the sheath model without instabilities (which would prevent $\Delta\bar{u}_{14,max}$ from being reached) with the condition

$$\frac{\bar{u}_{1,0}}{c_{s,1}}=\frac{\bar{u}_{2,0}}{c_{s,2}}=\frac{\bar{u}_{3,0}}{c_{s,3}}=\frac{\bar{u}_{4,0}}{c_{s,4}} \tag{3.53}$$

Indeed, it can be easily shown that the velocity increase due to SEE has to be proportionally the same for each ion species, regardless of the plasma composition and number of species. In particular, for two constant k_1 and k_2 that are different in general, it can be written

$$\bar{u}_{1,0}=k_1c_{s,1} \qquad \bar{u}_{2,0}=k_2c_{s,2}$$

$$\Downarrow$$

$$\sqrt{\frac{2e\phi_0}{m_1}}=k_1\sqrt{\frac{k_BT_e}{m_1}} \qquad \sqrt{\frac{2e\phi_0}{m_2}}=k_2\sqrt{\frac{k_BT_e}{m_2}}$$

which is true only if $k_1 = k_2$, thus confirming Eq. 3.53. Consequently, the correct $\Delta\bar{u}_{14,max}$ in case of SEE is shown in Figure 3.27 for a range of T_{eV}, in comparison with the one of Eq. 3.37. In particular, for the plasma and wall material here considered, the space-charge saturation regime is entered at 27.4 eV. In this region, the maximum flow difference is suddenly blocked at $k_1 \cdot (c_{s,1} - c_{s,4})$, after having experienced an exponential increase governed by the material-dependent SEE coefficient $\sigma = 1.36 \cdot 0.123\ T_{eV}^{0.528}$. The figure also shows the critical flow difference Δu_c, which plateaus at the same value seen in case of no SEE (Figure 3.25). This is indeed expected as SEE has not any influence on the instability-enhanced friction blocking the differential flow.

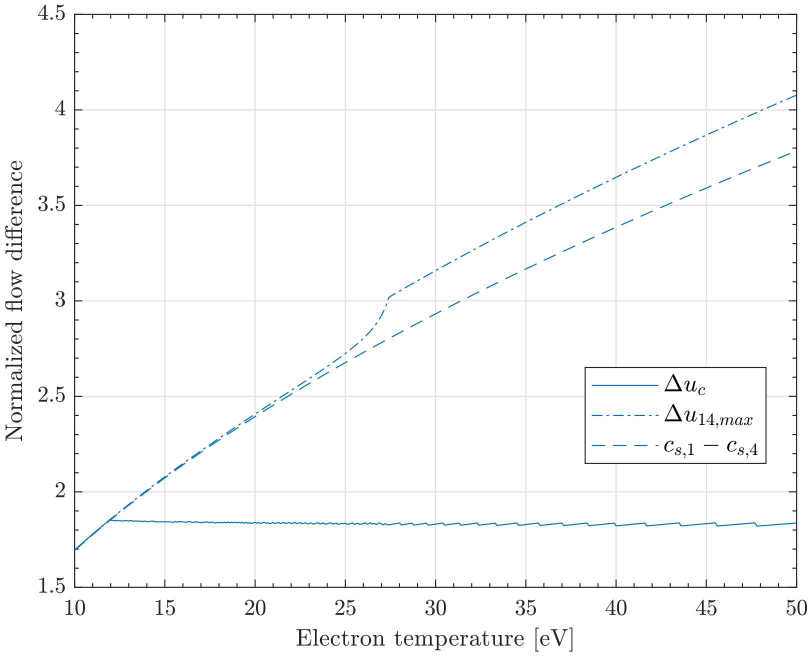

Figure 3.27: Comparison between Δu_c and the maximum flow difference values in case SEE is present (i.e. $\Delta u_{14,max}$) or not (i.e. $c_{s,1} - c_{s,4}$) as a function of T_{eV}. SEE coefficient is $\sigma = \min(1.36 \cdot 0.123\ T_{eV}^{0.528}, \sigma_{SCS})$. The plasma characteristics are: $1.27\mathrm{N_2}+\mathrm{O_2}$ mixture with $\bar{n}_3 = 2\bar{n}_1$ and $\bar{n}_4 = 2\bar{n}_2$, $T_{iV} = 0.2\,\mathrm{eV}$.

Finally, the complete results obtained from the model solution in case of SEE are here presented. At first, Figure 3.28a reports the ion velocities $u_{i,0}$ reached in case ion-ion instability is considered (solid lines) or not (dash-dot lines). As expected, the inclusion of SEE effectively increases all velocities, both at low T_{eV} and in the space-charge saturation regime, with an effect more pronounced in the latter (coherently with Figure 3.27). Overall, the percentage variations obtained (Figure 3.28b) remain very similar to those reported for the case without SEE (Figure 3.26b), showing only slight differences which increase with the electron temperature.

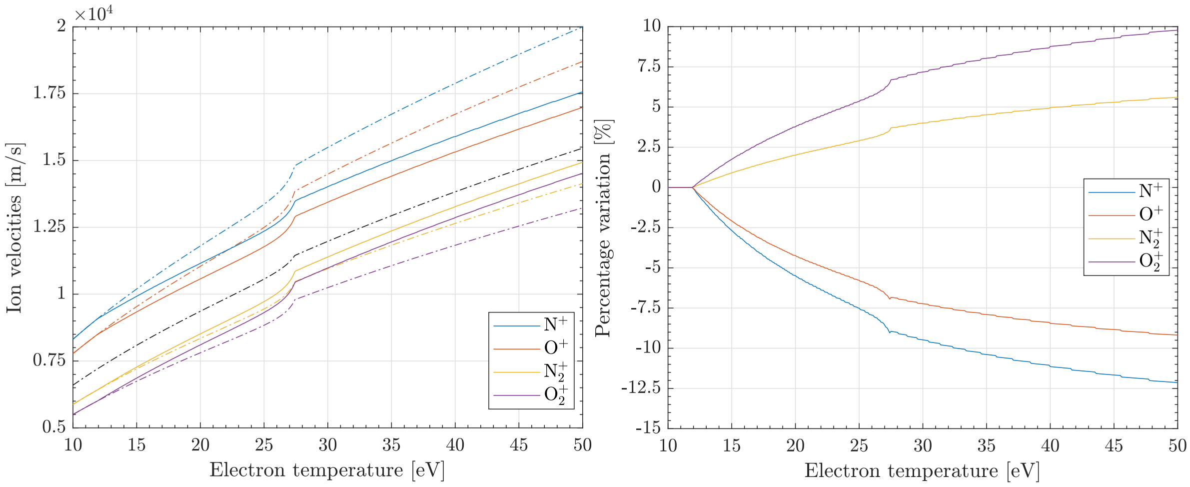

(a) **(b)**

Figure 3.28: (a) Comparison in case of SEE between the individual ion velocities $u_{i,0}$ reached when ion-ion streaming instability is considered (solid lines) and when it is not (dash-dot lines) as a function of T_{eV}. The black dash-dote line indicates the common system sound speed c_s. (b) Corresponding percentage variations. SEE coefficient is $\sigma = \min(1.36 \cdot 0.123\ T_{eV}^{0.528}, \sigma_{SCS})$. The plasma characteristics are: $1.27\mathrm{N_2}+\mathrm{O_2}$ mixture with $\bar{n}_3 = 2\bar{n}_1$ and $\bar{n}_4 = 2\bar{n}_2$, $T_{iV} = 0.2\,\mathrm{eV}$.

Another interesting comparison is that between the same ion velocities $u_{i,0}$ and the corresponding sound speeds $c_{s,i}$ (Figure 3.29). Although these two data sets refer to two inherently different cases (i.e presence of SEE and absence of it, respectively), a comparison may however result very insightful from a practical point of view. Indeed, even if in plasma numerical models SEE is formally considered, only its effects on electron energy and momentum are taken into account, while the related $u_{i,0}$ increase is generally neglected for simplicity [8]. Therefore, it is reasonable to compare the alternative more complex description investigated in the present work with this commonly used approach. The results obtained show an opposite trend with respect to the previous comparisons (Figures 3.26 and 3.28), in which the two lightest species are now those least affected by the modified description. In particular, the decrements of N^+ and O^+ always remain below 5.9% and 4.3%, respectively. On the other hand, moving from the common Bohm criterion to this novel approach would result in $u_{i,0}$ increments well over 10% for both N_2^+ and O_2+ in the SCS regime.

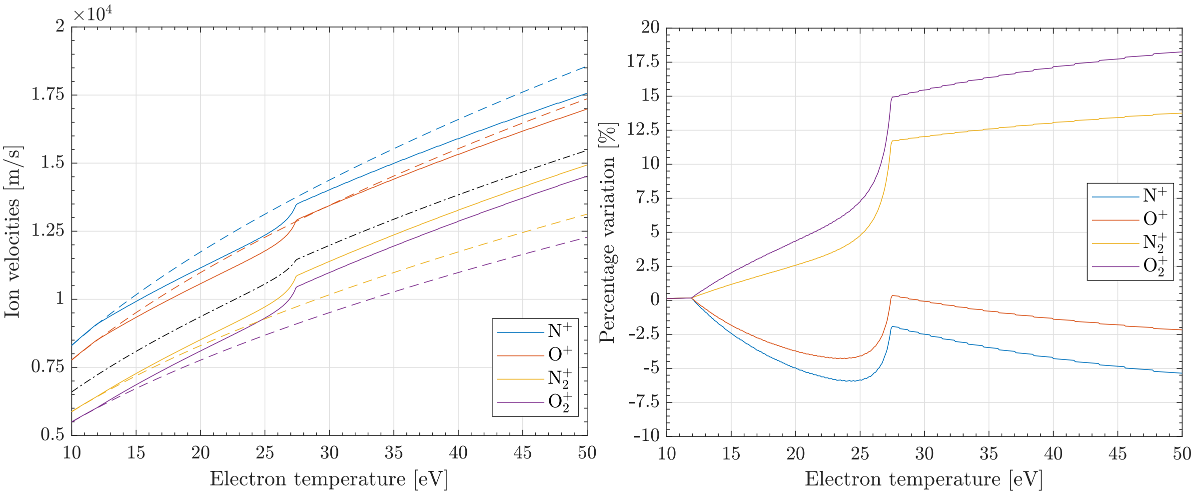

(a) **(b)**

Figure 3.29: (a) Comparison between the individual ion velocities $u_{i,0}$ reached in case of SEE when ion-ion streaming instability is considered (solid lines) and the corresponding sound speeds $c_{s,i}$ (dashed lines) as a function of T_{eV}. The black dash-dot line indicates the common system sound speed c_s. (b) Corresponding percentage variations. SEE coefficient is $\sigma = \min(1.36 \cdot 0.123\ T_{eV}^{0.528}, \sigma_{SCS})$. The plasma characteristics are: $1.27N_2$+O_2 mixture with $\bar{n}_3 = 2\bar{n}_1$ and $\bar{n}_4 = 2\bar{n}_2$, $T_{iV} = 0.2\,\mathrm{eV}$.

As the other resolved variables are concerned, Figures 3.30 to 3.32 show the values of ϕ_w, σ and $\bar{n}_s$, respectively, both in case ion-ion instability is considered and in case it is not. What can be immediately noted is that for each variable the two cases result barely distinguishable. Precisely, for both σ and $\bar{n}_s$ the graphs are coincident where secondary emission has not saturated yet. Indeed, under this regime σ is a material-dependent function of T_{eV} and thus cannot be affected by the sheath edge plasma conditions. Similarly, this also extends to the secondary electrons density ratio $\bar{n}_s$, which is proportional to σ. However, the same does not apply to ϕ_w which, regardless of σ, always depends on the ion velocities (see Eq. 3.49). This is indeed reasonable as the sheath itself exists only to match the plasma boundary conditions with those imposed by the outside surface (i.e. the wall in this case). In particular, in this non-SCS regime the presence of instability leads to a $|\phi_w|$ slightly higher toward the graphs minimum, which is due to the combined effect of the variations depicted in Figure 3.29b at that particular T_{eV}, for the particular plasma composition considered.[13] In the same way, it can be demonstrated the opposite result seen for ϕ_w in the saturation regime. Coherently, as a higher

---

[13] This can be readily understood by applying Eq. 3.49.

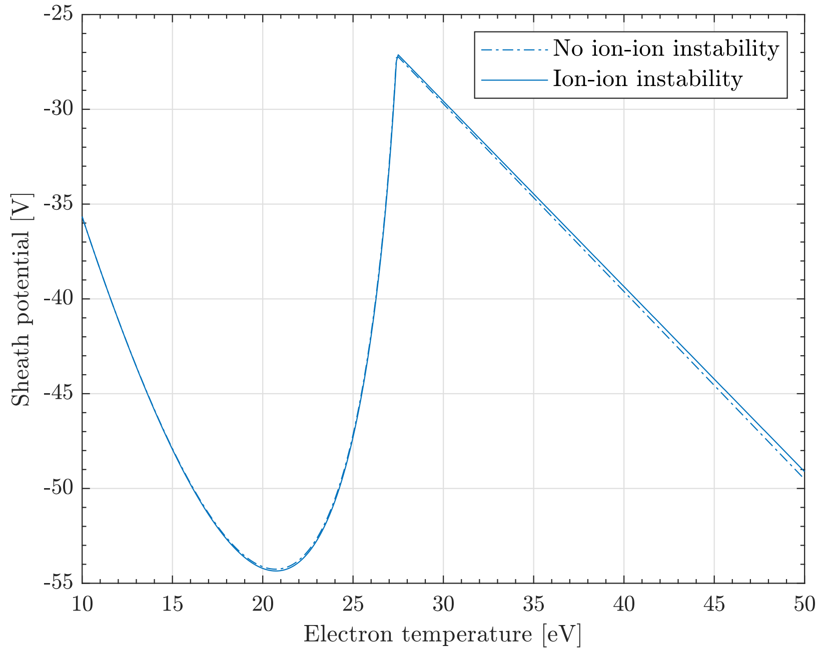

Figure 3.30: Comparison in case of SEE between the sheath potential ϕ_w obtained when ion-ion streaming instability is considered (solid lines) and when it is not (dash-dot lines) as a function of T_{eV}. SEE coefficient is $\sigma = \min(1.36 \cdot 0.123\, T_{eV}^{0.528}, \sigma_{SCS})$. The plasma characteristics are: 1.27N$_2$+O$_2$ mixture with $\bar{n}_3 = 2\bar{n}_1$ and $\bar{n}_4 = 2\bar{n}_2$, $T_{iV} = 0.2\,$eV.

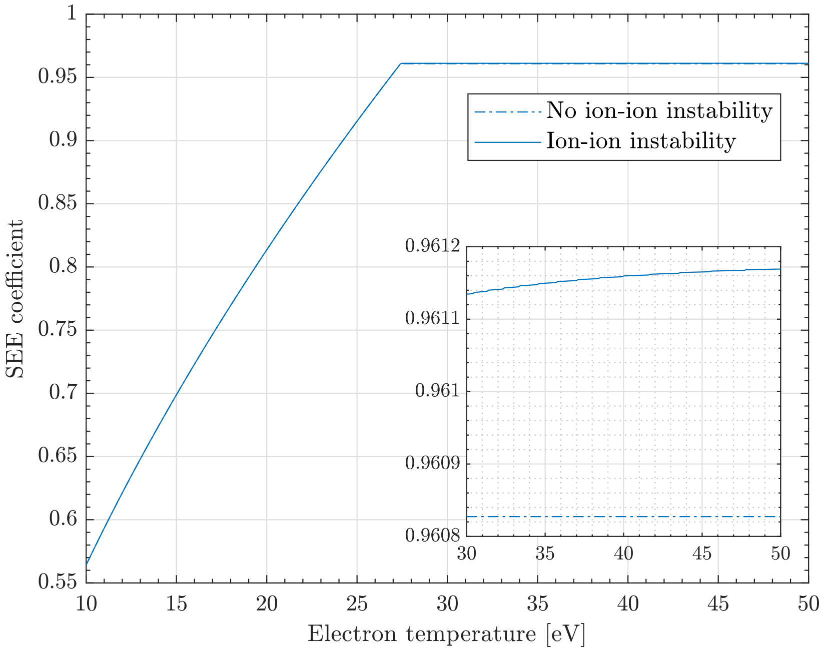

Figure 3.31: Comparison between the SEE coefficient $\sigma = \min(1.36 \cdot 0.123\, T_{eV}^{0.528}, \sigma_{SCS})$ obtained when ion-ion streaming instability is considered (solid lines) and when it is not (dash-dot lines) as a function of T_{eV}. In the panel is shown a magnification of the sheath saturation regime. The plasma characteristics are: 1.27N$_2$+O$_2$ mixture with $\bar{n}_3 = 2\bar{n}_1$ and $\bar{n}_4 = 2\bar{n}_2$, $T_{iV} = 0.2\,$eV.

σ reduces the sheath potential drop by emitting more electrons, in this temperature range σ_{SCS} is higher with respect to the no-instability case (Figure 3.31), and so also $\bar{n}_s$ (Figure 3.32).

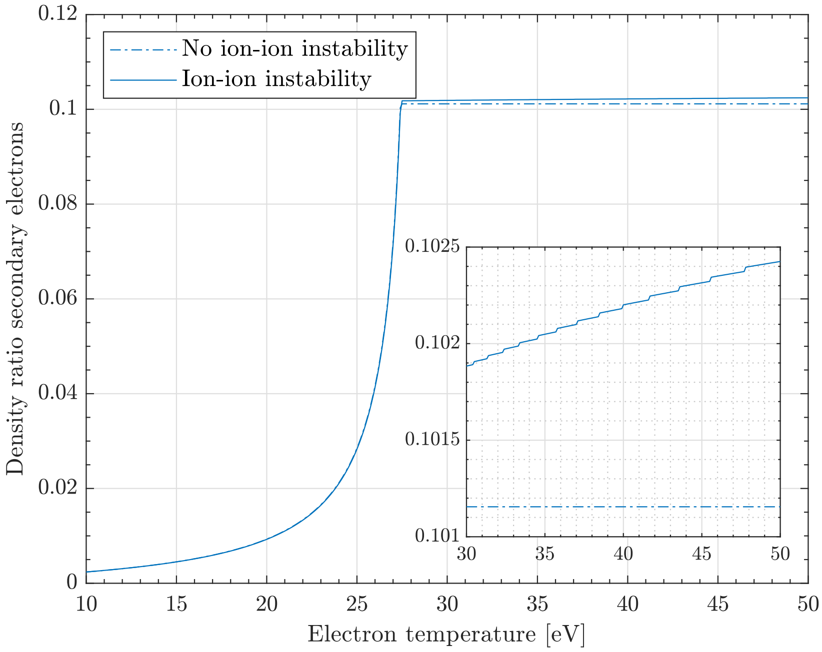

Figure 3.32: Comparison in case of SEE between the secondary electron density $\bar{n}_s$ obtained when ion-ion streaming instability is considered (solid lines) and when it is not (dash-dot lines) as a function of T_{eV}. In the panel is shown a magnification of the sheath saturation regime. SEE coefficient is $\sigma = \min(1.36 \cdot 0.123\ T_{eV}^{0.528}, \sigma_{SCS})$. The plasma characteristics are: 1.27N_2+O_2 mixture with $\bar{n}_3 = 2\bar{n}_1$ and $\bar{n}_4 = 2\bar{n}_2$, $T_{iV} = 0.2\,\text{eV}$.

Overall, while the onset of ion-ion streaming instabilities is not affected by SEE (as confirmed by Figures 3.25 and 3.27), the just analyzed results show that these instabilities also have a very small impact on SEE. Therefore, it can be safely concluded that the two phenomena are practically independent.

3.3.3. Model Limitations

Before proceeding with the discussion, it is worth mentioning that the presented plasma description involving ion-ion streaming instability presents some limitations, whose extent and nature however are still not clear at the time of writing. In particular, while the study of two-species plasmas with this approach has led to numerical results well in agreement with experimental evidence (see the work of Yip et al. [4]), the same could not be achieved with three species [91, 92]. Indeed, in these works, regardless of the missing measurement of the third species velocity at the sheath edge, the other two showed significant differences with the model. As a consequence, the approach was deemed by the authors as only qualitatively representative of the plasma behaviour. Even though similar measurements are not available for the air plasma here considered, it is expected that the same limitations will affect even more so this more complex case.

The main assumption used in the model that could be causing this inaccurate behaviour is that the differential flow between all ion species is considered blocked upon instability onset. Indeed, while it is true that instability-enhanced friction effectively keep the differential flow constant between two species, the reality could be much more complex in case of more ions. Also, this multispecies interaction could be highly depended on *which* ion species are considered or it could require different assumptions regarding their temperatures or even the presheath free fall itself. In general, at the time of writing, a satisfactory answer about this complex interaction is yet to be found. Nevertheless, even though the model predictions do not quantitatively reflect the real particles behaviour, they still result far more accurate than assuming individual ion sound speeds or a common system sound speed at the sheath edge under any condition.

3.3.4. Sensitivity Analysis

It is now presented a sensitivity analysis exploring the effects of ion temperatures T_i and plasma composition on the model results. Due to its more complete formulation, the case including SEE is always considered, unless differently indicated. Moreover, the electron temperature is fixed at $T_{eV} = 30\,\text{eV}$, which always causes BNSiO$_2$ secondary electron emission to saturate. Indeed, from Eq. 3.51 it results

$$\sigma = \min(1.0078, \sigma_{SCS}) = \sigma_{SCS} \tag{3.54}$$

as the space-charge saturation prevents $\sigma \geq 1$. In this way, it is excluded from the analysis the influence of the material-dependent expression of σ, in favour of σ_{SCS} which is self-consistently obtained in the model.

Ion Temperature

Among the model assumptions, by following the work of Hara and Mikellides [6], a reference common ion temperature $T_{iV} = 0.2\,\text{eV}$ was considered. In the following, the effects of its variation are presented. At first, these are analyzed while keeping all the ion temperatures equal each other. Then, this assumption is relaxed and also the effects produced by different values are investigated.

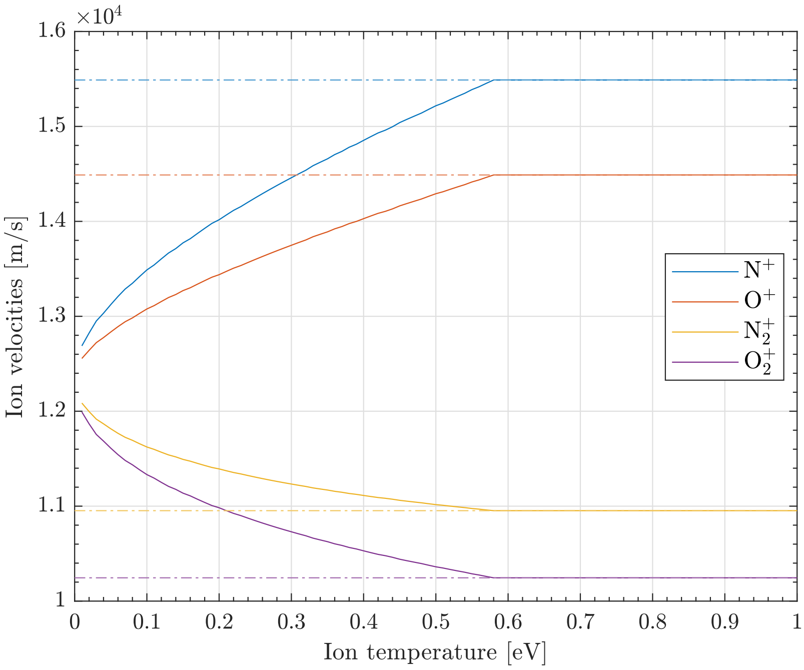

Figure 3.33: Individual ion velocities $u_{i,0}$ in case of ion-ion streaming instability (solid lines) as a function of T_{iV}. The dash-dot lines indicate the values corresponding to absence of instability. The plasma characteristics are: 1.27N$_2$+O$_2$ mixture with $\bar{n}_3 = 2\bar{n}_1$ and $\bar{n}_4 = 2\bar{n}_2$, $\sigma = \sigma_{SCS}$, $T_{eV} = 30\,\text{eV}$.

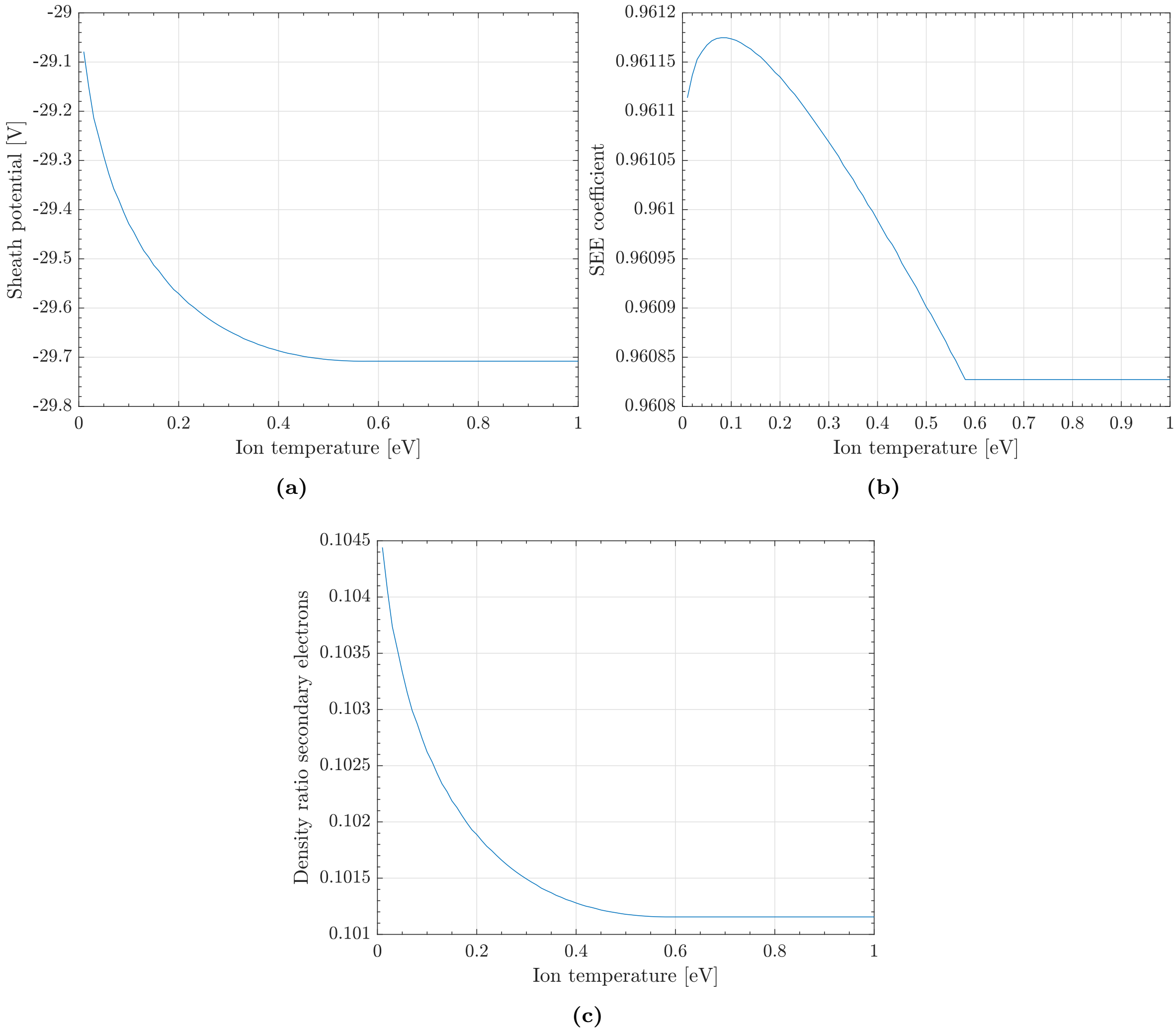

Figure 3.34: (a) Sheath potential ϕ_w, (b) space-charge saturation SEE coefficient σ_{SCS} and (c) secondary electron density $\bar{n}_s$ in case of ion-ion streaming instability as a function of T_{iV}. The plasma characteristics are: $1.27\text{N}_2\text{+O}_2$ mixture with $\bar{n}_3 = 2\bar{n}_1$ and $\bar{n}_4 = 2\bar{n}_2$, $\sigma = \sigma_{SCS}$, $T_{eV} = 30\,\text{eV}$.

The ion-ion streaming instability is highly dependent on T_i as this modifies the temperature ratio and thus the point of instability onset. Indeed, as already discussed in Section 2.2, $T_i = 0$, for instance, implies $\Delta u_c = 0$ and consequently the common ion velocity c_s. On the other hand, as T_i increases, $(T_e/T_i)_c$ decreases and so instability requires increasingly higher electron temperatures to appear. Therefore, in case a certain T_i value is not available, it is impossible to select a best guess, as each value carries its own legitimate effects to the model. In this view, the results proposed here are only presented for completeness. In particular, Figure 3.33 reports the just discussed variation between a common c_s and the individual $u_{i,0}$ in case of no instability for T_i between 0 and a certain value dependent on T_e (here $T_{iV} = 0.58\,\text{eV}$).

Regarding ϕ_w, σ_{SCS} and $\bar{n}_s$, these are reported in Figure 3.34. Note that even here after $T_{iV} = 0.58\,\text{eV}$ the variables remain constant, as the instability is off and T_{iV} loses any influence on the presheath/sheath model. Also, it is worth mentioning that, while the curves behaviour at $T_{iV} = 0$ may appear asymptotic, these instead terminate at real values. Indeed, even though $u_{i,0} = c_s$ for each ion species, the plasma sheath remains perfectly defined and so its potential and the wall electron emission.

Successively it is investigated the case in which ions possess different temperatures. Note that this scenario appears particularly plausible, being the ions poorly collisional and thus not effectively thermalized in general. However, the lack of any information about possible ion temperature differences did not allow to make substantiated assumptions other than a common T_{iV}. For the same reason, the results proposed here cannot be exhaustive and are only presented for completeness, so as to provide a general idea about the effects of these variations.

Figure 3.35 reports the ion velocities reached at the sheath edge in case each ion temperature is individually varied while keeping the other all equal to 0.2 eV. Interestingly, the results show that each one determines a unique effect on the instability onset, sharing however some similarities. Specifically, the two lightest species determine monotonically increasing profiles, which are similar to the behaviour reported in Figure 3.33. Note that the O^+ temperature variation affects the instability minimally, while the impact of N^+ temperature appears more significant. It is believed that this result is due to the fact that O^+ velocity in the presheath is just slightly lower than the N^+ one, thus limitedly contributing in establishing a differential velocity regime sufficient for the instability to arise.

On the other hand, temperature variations of the two heaviest species apparently produce

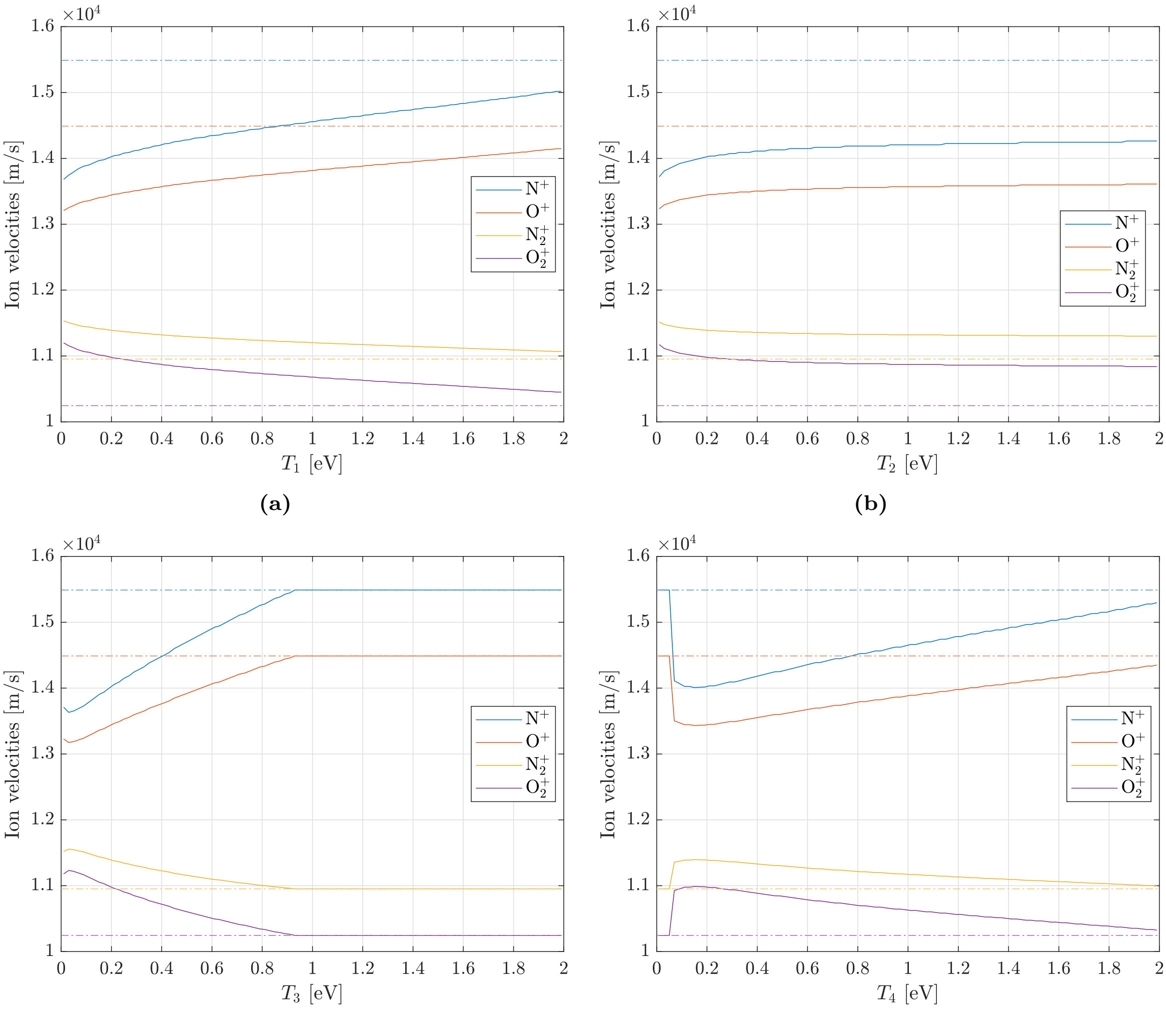

(a) **(b)**

(c) **(d)**

Figure 3.35: Individual ion velocities $u_{i,0}$ in case of ion-ion streaming instability (solid lines) as a function of (a) T_1, (b) T_2, (c) T_3 and (d) T_4. The dash-dot lines indicate the values corresponding to absence of instability. The plasma characteristics are: $1.27N_2$+O_2 mixture with $\bar{n}_3 = 2\bar{n}_1$ and $\bar{n}_4 = 2\bar{n}_2$, $\sigma = \sigma_{SCS}$, $T_{eV} = 30$ eV, $T_{iV} = 0.2$ eV for the three ion temperatures not varied.

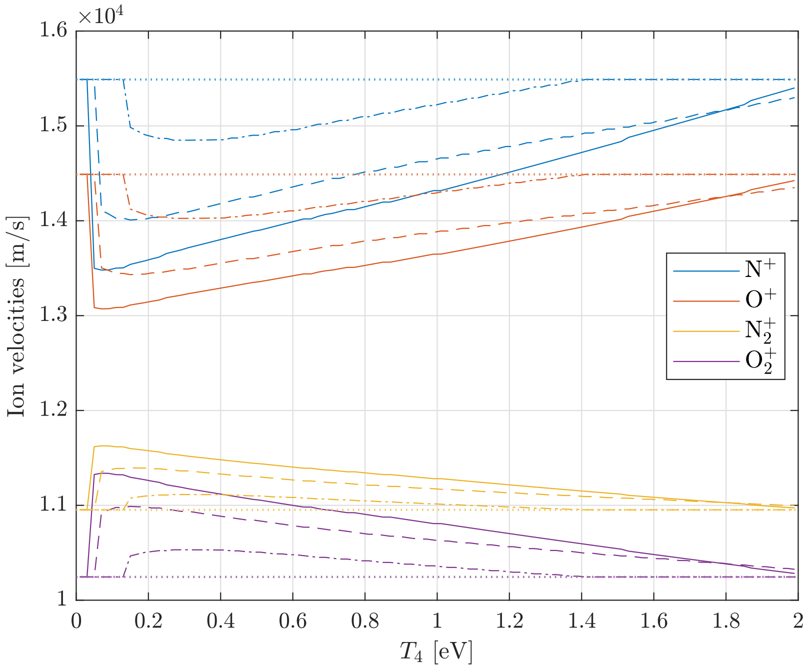

Figure 3.36: Individual ion velocities $u_{i,0}$ in case of ion-ion streaming instability as a function of T_4 for $T_1 = T_2 = T_3$ equal to 0.1 eV (solid lines), 0.2 eV (dashed lines) and 0.4 eV (dash-dot lines). The dotted lines indicate the values corresponding to absence of instability. The plasma characteristics are: $1.27N_2$+O_2 mixture with $\bar{n}_3 = 2\bar{n}_1$ and $\bar{n}_4 = 2\bar{n}_2$, $\sigma = \sigma_{SCS}$, $T_{eV} = 30$ eV.

more complex effects. Indeed, in case these possess very low temperatures (i.e. approximately < 0.1 eV), the instability forms further downstream along the presheath as they decreases, thus resulting in higher velocities at the sheath edge. This behaviour appears especially clear for the case of O_2^+, which below 0.05 eV even causes the instability to turn off. It is worth mentioning that even the two lightest ion species determine similar effects, even if these cannot be clearly resolved due to high sensitivity of the instability threshold at the significantly low temperatures involved (i.e. < 0.01 eV). However, despite the uncertainties, these results (not shown) suggest that instability may not completely turn off as in case of N_2^+ and O_2^+.

Overall, it can be concluded that, although variations in the temperatures of different ion species produce different effects on ion-ion streaming instability, significant disparities among them cause the instability to develop further downstream along the presheath, or even turn off. While this was expected in case of a single ion species having a higher temperature than the others, a similar behaviour is also observed in the opposite scenario.

Finally, it is noted that the behaviour of the profiles obtained is not dependent on the 0.2 eV temperature assumed for the other three ions, but is characteristic of the specific species whose temperature is varied. This is confirmed by Figure 3.36, which reports the $u_{i,0}$ obtained varying T_4 at different temperatures of the other ions, namely 0.1 eV, 0.2 eV and 0.4 eV. Here it is shown that the profile behaviours are maintained in the three cases while, as expected, higher temperatures push the instability threshold more towards the sheath edge. Interestingly, this also increases the T_4 range in which instability is off, thus confirming the aforementioned effect of significant disparities among ion temperatures.

Plasma Composition

Another important assumption that has been considered in the model concerns plasma composition. In particular, it has been assumed a uniformly ionizing $1.27N_2$+O_2 plasma mixture

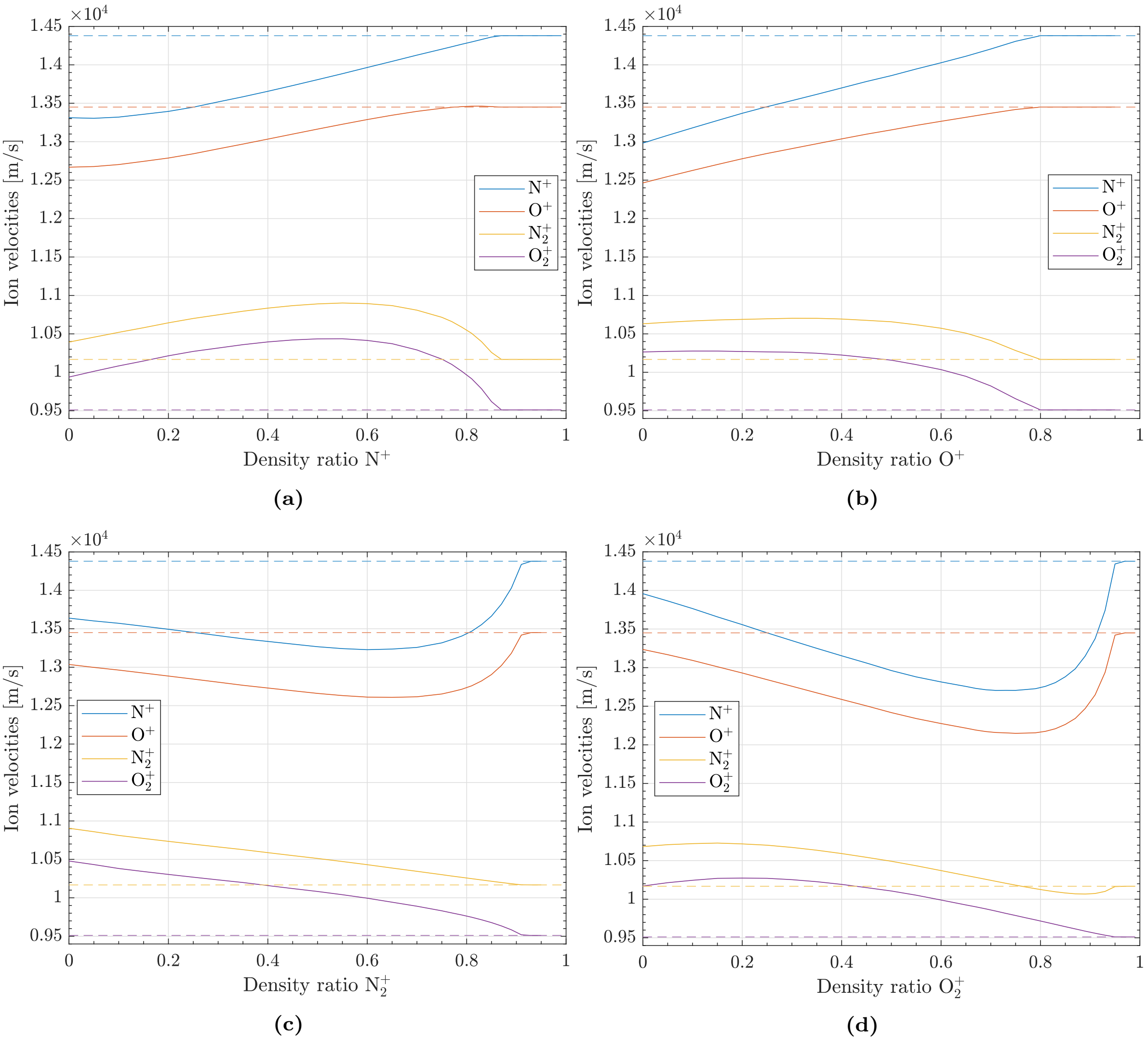

Figure 3.37: Comparison between the individual ion velocities $u_{i,0}$ reached in case of ion-ion streaming instability (solid lines) and the corresponding sound speeds $c_{s,i}$ (dashed lines) as a function of the (a) N^+, (b) O^+, (c) N_2^+ and (d) O_2^+ density ratios. This case does not include SEE. The plasma characteristics are: equal density ratios of the non-varying species, $T_{eV} = 30\,\text{eV}$, $T_{iV} = 0.2\,\text{eV}$.

in which N_2^+ and O_2^+ densities are double than those of N^+ and O^+, respectively. By doing so, a unique set of density ratios has been obtained (see System 3.35). However, all these assumptions are mainly arbitrarily and especially limited, as plasma composition varies greatly in an electric thruster. Therefore, to generalize the results of this presheath/sheath model, in the following are investigated the effects of varying one species at a time while keeping the others equal (e.g. $\bar{n}_1$ is varied and $\bar{n}_2 = \bar{n}_3 = \bar{n}_4$).

Starting from the ion velocities at the sheath edge, in Figure 3.37 is firstly presented a reference case in absence of SEE. In the four plots reported, as each ion density ratio is varied between 0 and 1, the ion velocities $u_{i,0}$ follow different behaviours. These depend on both the critical flow velocity Δu_c and the Bohm sheath criterion (Eq. 3.44). The former defines the distance between them, while the latter governs their general trends.

By recalling the discussion of Section 2.2, the critical flow velocity $\Delta u_c \equiv \Delta u_{14,c}$ was defined as a quantity dependent on the plasma characteristics, composition included. This dependence can be here readily inferred from the results, which show significant variations

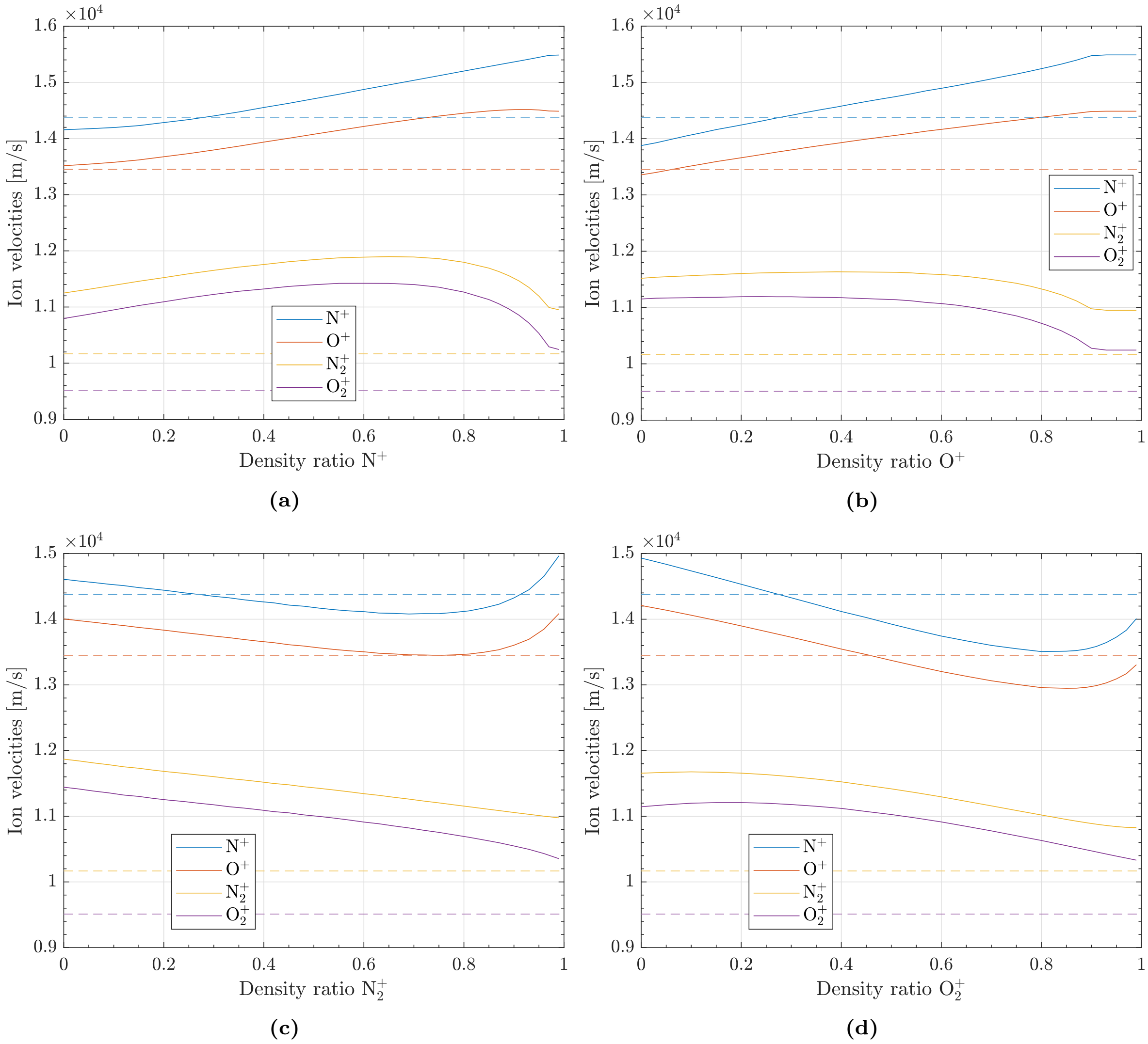

(a) **(b)** **(c)** **(d)**

Figure 3.38: Comparison between the individual ion velocities $u_{i,0}$ reached in case of SEE when ion-ion streaming instability is considered (solid lines) and the corresponding sound speeds $c_{s,i}$ (dashed lines) as a function of the (a) N^+, (b) O^+, (c) N_2^+ and (d) O_2^+ density ratios. The plasma characteristics are: equal density ratios of the non-varying species, $\sigma = \sigma_{SCS}$, $T_{eV} = 30\,\text{eV}$, $T_{iV} = 0.2\,\text{eV}$.

as the presence of different species is modified.[14] For instance, in case N^+ is varied, Δu_c at first slightly decreases up to $\bar{n}_1 \approx 0.2$ and then starts increasing ceaselessly until $\bar{n}_1 \approx 0.86$, where the maximum (indicating ions entering the sheath with their sound speeds) is reached. This absence of instability at high density ratios is common to all plots because, as the varied species increasingly dominates the plasma, the Δu_c needed becomes generally too high to be achieved before entering the sheath. In a two-species plasma this also happens toward low density ratios, as it would only remain the other ion species [4].

Another feature observed in the figures is that the O^+ variation is characterized by the lowest density ratio threshold for instability turning off, while the two heaviest species require significantly higher densities. This is related to the fact that the O^+ case is also the only one with a monotonically increasing Δu_c behaviour, thus rapidly shifting the point of instability onset toward the sheath edge upon concentration increments. Although this behaviour is mostly coincidental, it is noted that the percent increase of species with intermediate masses

---

[14] For more clarity the various Δu_c are also explicitly reported in Figure 3.39a.

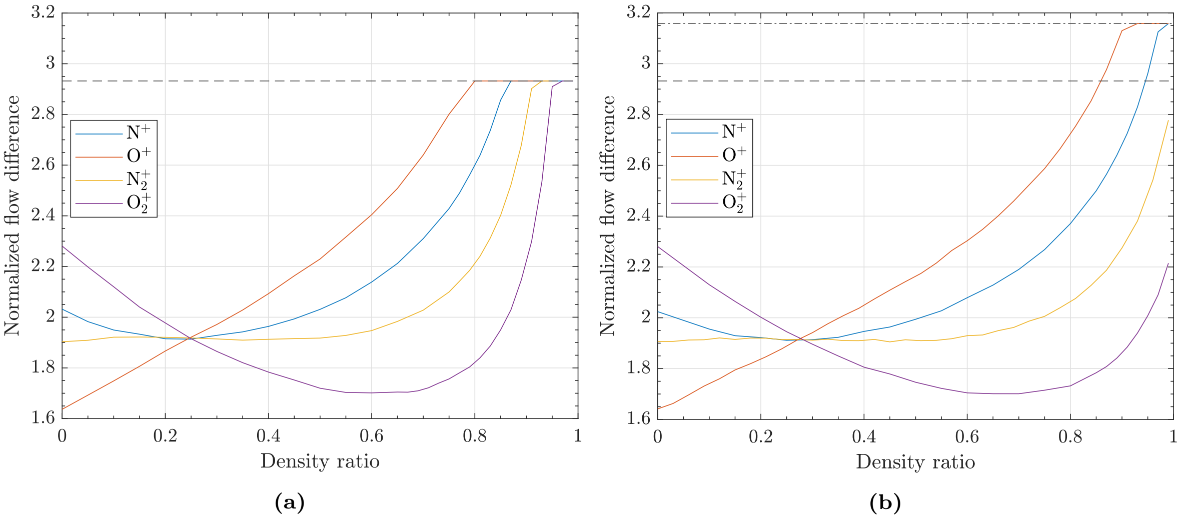

Figure 3.39: Critical flow difference Δu_c for ion-ion streaming instability (solid lines) (a) in case of no SEE and (b) in case it is considered, as a function of the density ratio of each species. The black lines represent the two possible maximum flow differences: $\Delta u_{14,max}$ (dash-dot) and $c_{s,1} - c_{s,4}$ (dashed). The plasma characteristics are: equal density ratios of the non-varying species, (a) $\sigma = 0$ or (b) $\sigma = \sigma_{SCS}$, $T_{eV} = 30\,\mathrm{eV}$, $T_{iV} = 0.2\,\mathrm{eV}$.

(i.e. O^+ and N_2^+) produces milder effects on the sheath criterion than that of the ones with extreme masses (i.e. N^+ and O_2^+). In particular, as the added species is lighter, it accelerates the others more strongly and, as it is heavier, it slows them down with increasing intensity. This phenomenon is due to the more intrusive action exerted by species with masses farther from the average plasma mass and it is implicitly governed by the Bohm criterion.

Regarding the case including SEE, the corresponding ion velocities are reported in Figure 3.38. In comparison with the reference case, all the curves are generally shifted upwards due to the velocity enhancement caused by the presence of secondary electrons. However, the general trends remain essentially unvaried, with the only difference that the curves result extended toward higher density ratios. This also appears very clearly in Figure 3.39, where Δu_c is shown for both cases. In general, the reason is that, as these ratios are expressed with respect to the primary electron population, by introducing a second one, due to quasi-neutrality a ion density ratio of 1 cannot correspond any more to a single-species plasma. Rather, in this case it results

$$\begin{cases} n_1 = n_e \\ n_2 + n_3 + n_4 = n_s \end{cases} \tag{3.55}$$

where N^+ is assumed to be varying.

The secondary electron density ratio $\bar{n}_s$ is shown in Figure 3.40a for all four ion variations. Here, regardless of the particular curve behaviours, its value remains practically constant at 0.10, suggesting that SEE and plasma composition are basically independent. This was indeed expected as the emission of secondary electrons is only a function of the electron density and σ. The former is not affected by the individual ion ratios but only by their sum. The latter, especially in case on emission saturation, which is shown in Figure 3.40b, is instead affected by the plasma composition, but the variation is so slight to only produce minor modifications to $\bar{n}_s$. Still regarding σ_{SCS}, from the figure it can be inferred a very useful rule: the lighter the plasma (on average), the smaller the SEE coefficient in saturation. Indeed, in absence of SEE a lighter plasma enters the sheath faster than a heavier one (see the general trends of the curve in Figure 3.37). This determines a lower potential drop $|\phi_w|$, as confirmed by Figure

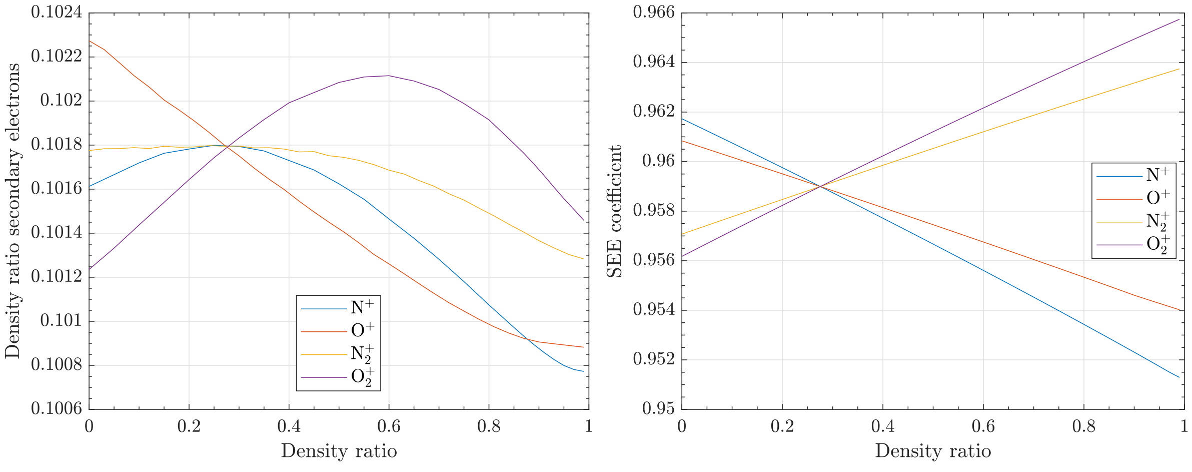

(a) **(b)**

Figure 3.40: (a) Secondary electron density $\bar{n}_s$ and (b) space-charge saturation SEE coefficient σ_{SCS} in case of ion-ion streaming instability as a function of the density ratio of each species. The plasma characteristics are: equal density ratios of the non-varying species, $\sigma = \sigma_{SCS}$, $T_{eV} = 30\,\mathrm{eV}$, $T_{iV} = 0.2\,\mathrm{eV}$.

3.41a, and consequently also a lower electric field at the wall. Therefore, in case of SEE, a lighter plasma requires a smaller emission coefficient to reach saturation than a heavier one. For completeness, an expression for the electric field at the wall is obtained by integrating Poisson's equation (Eq. 2.37) with $\bar{n}_s = 0$ over the potential ϕ, so as

$$\frac{1}{2}\left(\frac{d\varphi}{d\xi}\right)^2\bigg|_{\varphi=\varphi_w} = \sum_{i=1}^{N} 2\frac{m_i}{m_1}\frac{\bar{n}_{i,0}\bar{u}_{i,0}^2}{\theta}\left(\sqrt{1-\theta\frac{m_1}{m_i}\frac{Z_i\varphi_w}{\bar{u}_{i,0}^2}}-1\right) + \exp(\varphi_w) - 1 \tag{3.56}$$

where the electric field at the sheath edge has been put equal to 0. This equation confirms the correlation between a light plasma and a low electric field at the wall.

Finally, regarding the values of ϕ_w in case of SEE (Figure 3.41b) these show much more limited variations about lower average magnitudes with respect to the case in absence of SEE. Apart from the lower magnitude, which is an clear consequence of the added electron emission, the reason for a smaller variation over the density ranges is that σ_{SCS} acts contrarily to the trends of ϕ_w in absence of SEE (compare Figures 3.40b and 3.41a). Therefore, the sheath potential variations result effectively compensated in emission saturation regime. Moreover, it is noted that, due to the combined effects of the other plasma variables, each sheath potential curve varies considerably from the linear trends seen in absence of SEE, thus making it quite complex to be predicted.

3.4. Summary

To conclude the discussion about air plasma, it is here presented a brief summary.

Through the chapter, by means of an atmospheric model it was firstly defined air as a nitrogen/oxygen mixture. Then, this was investigated chemically, so as to determine the most significant plasma species to be considered in the thruster numerical model of Chapter 4. These are four neutral species (N_2, N, O_2, O), four positive ion species (N_2^+, N^+, O_2^+, O^+) and electrons.

Successively, the knowledge of number and type of ion species considered was used to solve for a representative air plasma the general sheath model presented in Section 2.3, also including the kinetic description of instability-enhanced friction in the presheath. The model solutions

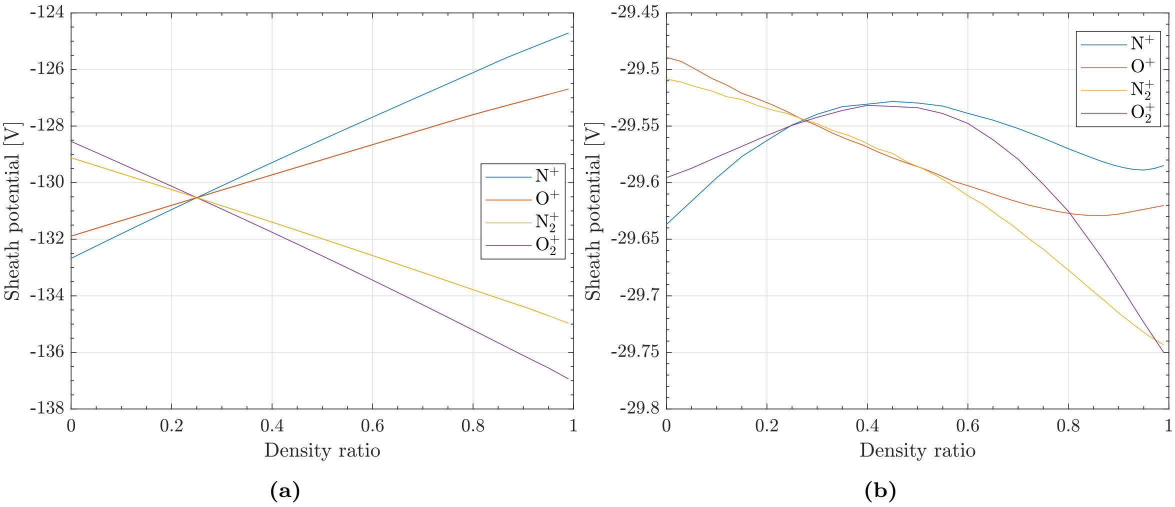

(a) **(b)**

Figure 3.41: Sheath potential ϕ_w for ion-ion streaming instability (solid lines) (a) in case of no SEE and (b) in case it is considered, as a function of the density ratio of each species. The plasma characteristics are: equal density ratios of the non-varying species, (a) $\sigma = 0$ or (b) $\sigma = \sigma_{SCS}$, $T_{eV} = 30\,\mathrm{eV}$, $T_{iV} = 0.2\,\mathrm{eV}$.

allowed to thoroughly investigate the effects of ion-ion streaming instabilities in the presheath, concluding that they may produce variations in the ion velocities at the sheath edge up to 20% of the corresponding sound speeds for the electron temperature range 10-50 eV. In particular, different combinations of instabilities and SEE were studied, showing comparable variations which become increasingly significant going toward higher T_e.

Another aspect evaluated was the solution sensitivity to the two main assumptions considered: ion temperature and plasma composition. The former appeared to significantly affect the instability threshold, which generally shifts toward the sheath edge as T_i increases. The latter highlighted the species-specific role of each ion considered, coherently with the general rule that lighter particles accelerate the others more strongly and heavier ones slow them down with increasing intensity.

Overall, these results provide a first-ever look at the behaviour of a representative sheath in a nitrogen/oxygen plasma. This sheath model will be then implemented in the thruster numerical model developed in Chapter 4, as explained in Section 4.4. In this way, it will be possible to consistently solve the plasma-wall interactions in the thruster channel depending on the local temperature and density conditions, also including the effect of ion-ion streaming instabilities.

4

HET Numerical Model

In this chapter it is described the numerical model employed for simulating the PFG air plasma, with particular focus on the steps performed to adapt it to this particular propellant and to the thruster characteristics. The model, characterized by a modular structure which allows great flexibility in the propellant choice, is being actively developed by a research group of the University of Pisa (in collaboration with SITAEL) and it is under continuous improvement [10].

By incorporating a fully fluid, time-dependent and axial one-dimensional description of the plasma discharge dynamics, the numerical model has been primarily developed with the aim of studying plasma oscillations in HETs (e.g. breathing mode) with minimum computational effort. It their last effort, Giannetti et al. [10] demonstrated that the proposed description contains all the necessary physics needed to reproduce such oscillations in a xenon plasma. In this work, this description is adapted to the more complicated case of a nitrogen/oxygen plasma which, as it is shown in Chapter 6, effectively shows a subtle breathing mode under some particular experimental conditions.

As briefly mentioned above, one of the main model features is modularity, which consists in having a main core part surrounded by many modules which independently define all the specific aspects of the simulation. This core part, which is also the major component of the model as it is responsible for defining and solving all the governing equations, is completely parametrized and thus independent from the particular case study considered (e.g. thruster geometry, propellant composition, particle reactions). This is defined by means of several modules which can be easily modified and provide to the core all the information and values required to numerically solve the equations. Among these modules, the main one is that responsible for the complete definition of the propellant used, which has been updated to comprise all the information and data presented in Chapter 3.

In Figure 4.1 it is reported a schematic representation of the model domain, highlighting the major features of a HET and representing the particular geometry of the thruster employed which, differently from the one used in the work of Giannetti et al. [10], implements a magnetic shielding configuration and a centrally mounted cathode. However, as the one-dimensional nature of the model does not allow to resolve these features, their effects can only be approximately accounted by a proper tuning of the calibration parameters (discussed in Section 4.5).

In general, all the equations and quantities are radially averaged over z-sections of the drawn domain, which extends from the thruster anode plate ($z = 0$) down to a virtual boundary at $z = z_f$. This corresponds either to the hallow cathode axial location or, for this geometry, to the intersection between the magnetic field line passing through it and the channel

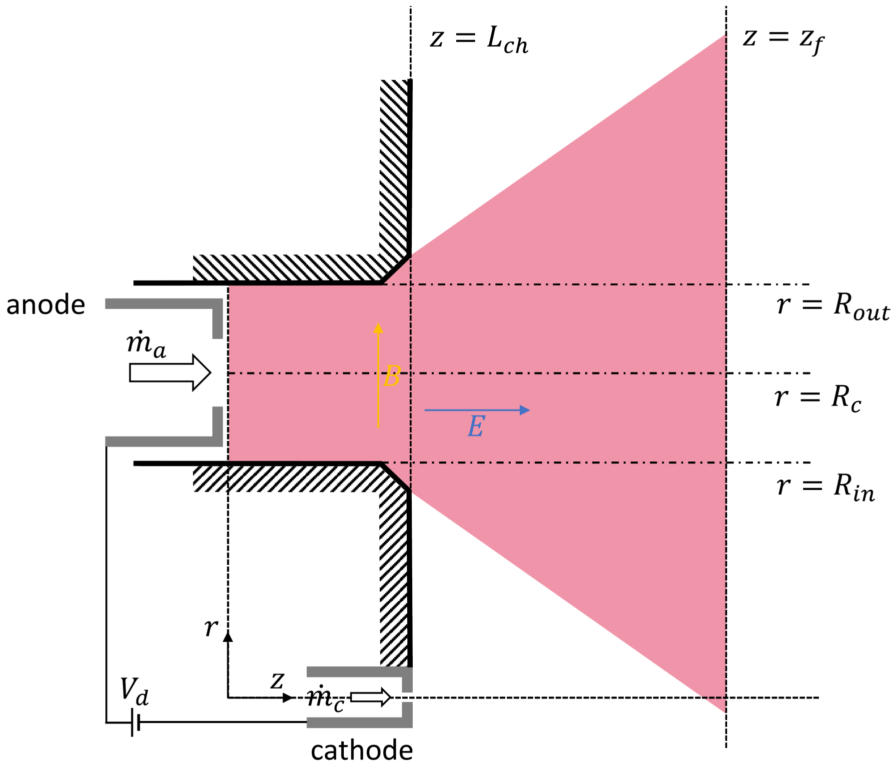

Figure 4.1: Schematic representation (not to scale) of the model domain on which the radially averaged quantities are defined. Also, the main features and components of a HET are shown.

centerline. Note that, although both options represent approximations dictated by the model one-dimensionality, they are nearly equivalent in practice as magnetic near field lines can be assumed isothermal and equipotential [93]. Consequently, the cathode boundary conditions (i.e. potential and electron temperature) can be considered at $z = z_f$ regardless of its position. In particular, in this work it is taken $z_f = 3L_{ch}$, where L_{ch} is the channel length. This choice has been made trying to balance the domain extension, which plays an important role for the plasma behaviour (see the model results in Chapter 6), and the computational time required.

Regarding the plasma radial thickness, while inside the channel it is fixed to $\Delta R = R_{out} - R_{in}$, thus resulting in a constant cross-sectional area $A = \pi \left(R_{out}^2 - R_{in}^2 \right)$, in the plume it may vary depending on the species, as each one follows its own expansion. Therefore, the cross-sectional area relative to each plasma species s results

$$A_s(z) = \begin{cases} A & \text{for} \quad z < L_{ch} \\ \pi \left(R_{out,s}^2(z) - R_{in,s}^2(z) \right) & \text{for} \quad z \geq L_{ch} \end{cases} \tag{4.1}$$

Note that the channel wall chamfering at the exit plane is not explicitly taken into account in the expression of $A_s(z)$, as it is indirectly included in the code by smoothing its discontinuity at the channel exit.

The inclusion of plume expansion represents one of the main novelties of this model description with respect to the xenon reference one of Giannetti et al. [10], which has been deemed necessary in the case under study as the high-temperature plasma region extends further downstream in the channel. This is due to both its composition and to the thruster magnetic shielding configuration, as it is discussed in detail in Chapter 6.

4.1. Assumptions

The main simplifying assumptions considered in the model are here reported.

Basic assumptions:

- **Axial one-dimensional model**
  Scalar equations with radially averaged plasma quantities.
- **Purely radial magnetic field B**
  The magnetic field is symmetric with respect to the channel centerline and purely radial, i.e.

  $$\mathbf{B}(z) = B_r(z)\hat{e}_r \tag{4.2}$$

  While this assumption can be considered reasonably valid in unshielded thrusters due to the almost radial behaviour near the field peak (as it has been also postulated by several authors [6, 10, 94]), this is not really the case in magnetic shielding configurations. Indeed, in order to protect the channel walls, the field topology is designed to have lines grazing them and reaching the near-anode region, characterized by a high potential and a low electron temperature. As such, the magnetic field results still symmetric but significantly curved toward the anode. However, the one-dimensional nature of the model does not allow to consider planar topologies for **B**. This leads to two viable options: define an arbitrary effective profile or use the real one at the channel centerline, as it usually done in literature. Due to the arbitrariness of the former, the latter option has been preferred in this work. Among the advantages of this uniquely defined choice, it is noted that a successful model calibration would confirm the feasibility of using the real centerline profile even in shielded configurations, provided that an appropriate parametric tuning is achieved (see Section 4.5).
- **Fluid plasma species**
  The plasma species (i.e. electrons, ions and neutrals) are treated as fluids.
- **Quasi-neutral plasma**
  Ion and electron densities are equal, which for the multispecies plasma considered means

  $$\sum_{i=1}^{4} n_i = n_e \tag{4.3}$$

  where the subscript numbering is the same used in Chapter 3. As a consequence all the plasma sheaths are excluded from the domain.
- **No facility effects**
  The plasma is modelled as the thruster would be firing in space. As such, the processes resulting from the presence of a vacuum chamber are not taken into account by any means. These mainly consist in neutral ingestion upon wall reflections and carbon sputtering from the wall panels lining the chamber.
- **Plume particle interactions independent of species expansion**
  Although different species expands differently outside the channel (as it is discussed in the following), particle interactions are modelled based on plasma quantities (e.g. densities, velocities) radially averaged over the entire respective domains. In other words, the presence of outer plume areas with only some plasma species population is not considered.

Neutrals assumptions:

- **Axial and constant neutral velocity**
  Each neutral species is assumed to have its own axial constant velocity. This has been determined by following the work of Reid [95], which numerically demonstrated a good correlation with the mean thermal velocity

$$\mathbf{u_n} = u_n \hat{e}_z = \sqrt{AF \frac{8 k_B T_a}{\pi m_i}} \hat{e}_z \tag{4.4}$$

  where T_a is the anode temperature and AF is an accommodation factor. Specifically, the neutral velocity at the channel centerline is obtained by using $AF = 1$, while that averaged over the anode plane (which is the one needed in this work) results from $AF = 0.25$. However, differently from the work of Reid, the HT5k thruster tested in this work deals with a N_2/O_2 mixture and it is not certain whether or not the same AF dependency would be obtained also in this case. Therefore, it is considered AF as a parameter to be defined during calibration. At the same time, even the anode temperature is not known in general and thus, for reasons that will become apparent in the following, also T_a is taken as a calibration parameter.

- **Constant neutral temperature**
  The temperature T_n of all neutral species is considered constant throughout the domain. In particular, by assuming a complete thermalization of the propellant inside the anode block, it results

$$T_n = T_a \tag{4.5}$$

Ions assumptions:

- **Axial ion velocity**

$$\mathbf{u_i}(z) = u_i(z) \hat{e}_z \tag{4.6}$$

- **Unmagnetized ions**
  Being the ion Larmor radius $r_{L,i}$ (i.e. the ion cyclotron radius due to the magnetic field interaction) much greater than the channel length L_{ch}, the ion motion is considered not affected by the magnetic field B_r.[1]

- **Non-collisional ions**
  Due to the low collisionality of ions during their motion along the channel, their interaction with the other species is here neglected. This is also in accordance with the assumptions considered in deriving the chemical model of Section 3.2.

- **Cold ions**
  Being the ion temperature T_i usually much smaller than the electron temperature T_e, the former can be safely neglected, i.e.

$$T_e \gg T_i \qquad \rightarrow \qquad T_i \approx 0 \tag{4.7}$$

  In this way, as it is explained in the following, the pressure term in the ion momentum equation can be eliminated and it is not necessary to solve an energy conservation equation for the ions. Note that this simplification has been postulated by several authors without jeopardizing the solution [6, 10, 96]. In particular, Ahedo et al. [96] highlighted the marginal effects on the model solution resulting from a finite ion temperature.

---

[1] More information can be found in Ref. [19].

Note that this assumption does not exclude from the model the effects of ion-ion streaming instabilities in the presheath. While it is has been stressed that a finite T_i is needed for generating them, this requirement holds from a local kinetic viewpoint. However, globally this temperature does not cause any other particular variation to the plasma behaviour in comparison with T_e. As a consequence it can be safely neglected in this fully fluid model, while still separately including its kinetic effects on the sheath description.

Electrons assumptions:

- **Axial and azimuthal electron velocity**
  Being the azimuthal component of the electron velocity fundamental for the thruster functioning, it has to be considered, i.e.

$$\mathbf{u_e}(z,\theta) = u_e(z)\hat{e}_z + u_{e,\theta}(\theta)\hat{e}_\theta \tag{4.8}$$

- **Negligible electron inertia**
  Being the electron mass m_e much smaller than any ion mass m_i, the inertial term in the electron momentum equation can be neglected. This also implies that electrons can be effectively considered in steady state with respect to the time scale relative to ions evolution.

- **Maxwellian distribution**
  It is considered a Maxwellian distribution function for the electrons. This assumption implies that the electron pressure can be expressed as

$$\mathcal{P}_e = n_e k_B T_e \tag{4.9}$$

  which should be more rigorously written as a stress tensor since $\mathcal{P}_e$ can, in general, be anisotropic. In addition, this assumption allows to write the electron internal energy (in eV) as

$$\epsilon = \frac{3}{2}\frac{k_B T_e}{e} \tag{4.10}$$

  which is the same used in Section 3.2.

- **Single electron population**
  Although the presheath/sheath model of Section 3.3 considers a secondary electron population to model the sheath and to define the generalized Bohm criterion, the thruster numerical model only includes a single electron population. Indeed, once these secondary electrons, which are characterized by very low energies (i.e. few eV [53, 54]), reach the plasma bulk, they rapidly thermalize with the primary population. Nevertheless, this assumption does not affect the plasma sheaths, where their effects on the particle and current balances play an important role.

4.2. Plasma Fluid Equations

Following from the model assumptions considered, the plasma fluid equations relative to each species are now illustrated.

4.2.1. Neutrals

Due to the constant velocity and temperature assumed for neutrals, only mass conservation is needed. Therefore, for each neutral species it is written

$$\frac{\partial n_n}{\partial t} A_n + \frac{\partial \Gamma_{n,z}}{\partial z} = S_{c,n} A_n + \dot{n}_{i,w} A_n \tag{4.11}$$

where $\Gamma_{n,z} = A_n n_n u_n$ is the axial flux of neutral species n, A_n is the relative plasma cross-sectional area and on the right-hand side are indicated the source/sink terms due to particle collisions and wall interaction, respectively. In particular, $S_{c,n}$ comprises all neutral losses and gains relative to the chemical model presented in Section 3.2. Depending on the species considered, this contribution assumes different expressions which are detailed in Table 4.1. These are written in terms of the various reaction frequencies $\nu_{n,r}$ that, for a neutral species n subjected to a reaction r, are defined as

$$\nu_{n,r} = n_n k_{n,r} \tag{4.12}$$

where $k_{n,r}$ is the reaction rate (see Table 3.8).

Table 4.1: Neutral atoms sink/source term $S_{c,n}$.

Neutron	$S_{c,n}$
N	$-n_e(\nu_{N,ion} - 2\nu_{N_2,diss} - \nu_{N_2,DI})$
O	$-n_e(\nu_{O,ion} - 2\nu_{O_2,diss} - \nu_{O_2,DI})$
N_2	$-n_e(\nu_{N_2,ion} + \nu_{N_2,diss} + \nu_{N_2,DI})$
O_2	$-n_e(\nu_{O_2,ion} + \nu_{O_2,diss} + \nu_{O_2,DI})$

Regarding $\dot{n}_{i,w}$, this source term represents the positive neutral density rate of change due to ion recombination at the walls. This is defined as

$$\dot{n}_{i,w} = n_i \nu_{i,w} \tag{4.13}$$

where $\nu_{i,w}$ is the ion-wall collision frequency, whose expression is presented in detail in Section 4.4.

Finally, Eq. 4.11 can be rearranged to highlight the effect of area expansion in the near-plume, so as to obtain the final expression

$$\frac{\partial n_n}{\partial t} + \frac{\partial}{\partial z}(n_n u_n) = S_{c,n} + \dot{n}_{i,w} - \underbrace{\frac{1}{A_n}\frac{\partial A_n}{\partial z} n_n u_n}_{\dot{n}_{n,pl}} \tag{4.14}$$

where the sink term $\dot{n}_{n,pl}$ represents the plume flux density loss. To determine it, the (plume) area variation contribution is firstly rearranged as

$$\frac{1}{A_n}\frac{\partial A_n}{\partial z} = \frac{1}{\pi\left(R_{out,n}^2 - R_{in,n}^2\right)} 2\pi\left(R_{out,n} + R_{in,n}\right)\tan(\lambda_n) = \frac{2}{\Delta R_n}\tan(\lambda_n) \tag{4.15}$$

where λ_n is the neutral plume half-divergence angle and ΔR_n is the neutral plasma radial thickness, i.e.

$$\Delta R_n = \frac{A_n}{2\pi R_c} \tag{4.16}$$

in which R_c represents the radial coordinate of the channel centerline (see Figure 4.1). Then, it is possible to define $\dot{n}_{n,pl}$ as

$$\dot{n}_{n,pl} = \begin{cases} 0 & \text{for} \quad z < L_{ch} \\ \dfrac{2\Gamma_{n,r}}{\Delta R_n} & \text{for} \quad z \geq L_{ch} \end{cases} \tag{4.17}$$

where $\Gamma_{n,r} = 1/2\ n_n v_{n,th} = n_n \sqrt{k_B T_n/(2\pi m_i)}$ is the radial random particle flux of neutrals. Note that this flux is calculated by assuming a radial expansion of the neutral fluid with the thermal velocity

$$v_{n,th} = \sqrt{\frac{2k_B T_n}{\pi m_i}} \tag{4.18}$$

which is defined (for the 1-D case) as the mean magnitude of the velocity in any single direction. Although not included in the work of Giannetti et al. [10], this plume expansion term has been specifically added in this work to improve the near-plume representativeness.

In general, the neutral area variation over the entire domain can be written as

$$\frac{\partial A_n}{\partial z} = \begin{cases} 0 & \text{for} \quad z < L_{ch} \\ 4\pi R_c \dfrac{v_{n,th}}{u_n} & \text{for} \quad z \geq L_{ch} \end{cases} \tag{4.19}$$

Note that this expression only depends on $T_n = T_a$ and AF, thus resulting equal for all neutral species. In order to calibrate neutral expansion independently from u_n, both T_n and AF are used as calibration parameters.

4.2.2. Ions

For ions, due to the assumption of constant temperature T_i, only mass and momentum conservation are needed. Specifically, similarly to the case of neutrals, for each ion species the continuity equation is written as

$$\frac{\partial n_i}{\partial t} A_i + \frac{\partial \Gamma_{i,z}}{\partial z} = S_{c,i} A_i - \dot{n}_{i,w} A_i \tag{4.20}$$

where $\Gamma_{i,z} = A_i n_i u_i$ is the ion axial flux and $S_{c,i}$ includes all ion source terms relative to the chemical model of Section 3.2. This is detailed, for each species, in Table 4.2.

Table 4.2: Sink/source terms for ion particles ($S_{c,i}$) and momentum ($S_{m,i}$).

Ion	$S_{c,i}$	$S_{m,i}$
N^+	$n_e(\nu_{N,ion} + \nu_{N_2,DI})$	$n_e(u_N \nu_{N,ion} + u_{N_2} \nu_{N_2,DI})$
O^+	$n_e(\nu_{O,ion} + \nu_{O_2,DI})$	$n_e(u_O \nu_{O,ion} + u_{O_2} \nu_{O_2,DI})$
N_2^+	$n_e \nu_{N_2,ion}$	$n_e u_{N_2} \nu_{N_2,ion}$
O_2^+	$n_e \nu_{O_2,ion}$	$n_e u_{O_2} \nu_{O_2,ion}$

As it has been done for neutrals, by rearranging Eq. 4.21, it can be highlighted the sink term $\dot{n}_{i,pl}$ representing ion losses due to plume expansion, so as to obtain

$$\frac{\partial n_i}{\partial t} + \frac{\partial}{\partial z}\left(n_i u_i\right) = S_{c,i} - \dot{n}_{i,w} - \underbrace{\frac{1}{A_i}\frac{\partial A_i}{\partial z} n_i u_i}_{\dot{n}_{i,pl}} \tag{4.21}$$

By applying Eqs. 4.15 and 4.16 to the ion case, $\dot{n}_{i,pl}$ can be defined as

$$\dot{n}_{i,pl} = \begin{cases} 0 & \text{for} \quad z < L_{ch} \\ \dfrac{2 n_i c_{s,i}\big|_{z=L_{ch}}}{\Delta R_i} & \text{for} \quad z \geq L_{ch} \end{cases} \tag{4.22}$$

where ions are assumed to radially leave the domain with their sound speeds at the channel exit [6, 94].

In general, similarly to the neutrals, the ion area variation over the entire domain can be written as

$$\frac{\partial A_i}{\partial z} = \begin{cases} 0 & \text{for} \quad z < L_{ch} \\ 4\pi R_c \dfrac{c_{s,i}\big|_{z=L_{ch}}}{u_i} & \text{for} \quad z \geq L \end{cases} \tag{4.23}$$

Regarding momentum conservation in the axial direction, for unmagnetized, singly charged and non-collisional ions, it results

$$\frac{\partial}{\partial t}\left(n_i u_i\right) + \frac{\partial}{\partial z}\left(n_i u_i^2 + \frac{\mathcal{P}_i}{m_i}\right) = -\frac{e n_i}{m_i}\frac{\partial \phi}{\partial z} + S_{m,i} - u_i(\dot{n}_{i,w} + \dot{n}_{i,pl}) \tag{4.24}$$

where $\mathcal{P}_i = n_i k_B T_i$ is the ion pressure and ϕ is plasma potential which defines the axial electric field as

$$E_z = -\frac{d\phi}{dz} \tag{4.25}$$

Consequently, the first term on the right-hand side of Eq. 4.24 represents the ion momentum increase in the positive axial direction under the effect of E_z.

The other mechanisms enhancing ion momentum in the model are ion-producing reactions, which are grouped within the source term $S_{m,i}$. This is strictly related to $S_{c,i}$ and detailed in Table 4.2.

Finally, the last two terms on the right-hand side model the ion momentum losses due to wall recombination and plume expansion, respectively. Note that the latter is the same appearing in Eq. 4.21.

4.2.3. Electrons

Electrons are the particles truly governing the plasma dynamics and therefore a complete modelling by means of all three conservation equations is essential. In particular, due to plasma quasi-neutrality (Eq. 4.3) and due to the fact that singly charged ions (i.e. the only ones considered) and electrons are created in pairs, the continuity equation combines the source terms relative to all ion species (i.e. N^+, O^+, N_2^+ and O_2^+, here indicated with a summation for brevity), such that

$$\frac{\partial n_e}{\partial t} A_e + \frac{\partial \Gamma_{e,z}}{\partial z} = \sum_{i=1}^{4}\left(S_{c,i} A_i - \dot{n}_{i,w} A_i\right) \tag{4.26}$$

where $\Gamma_{e,z} = A_e n_e u_e$ is the electron axial flux and A_e represents the electron plasma cross-sectional area, here approximated as

$$A_e = \frac{\sum_{i=1}^{4} n_i A_i}{n_e} \tag{4.27}$$

Consequently, by subtracting Eq. 4.26 from the sum of all ion continuity equations (Eq. 4.20) it is then obtained the current conservation equation

$$\frac{\partial}{\partial z}\left(\sum_{i=1}^{4} eA_i n_i u_i - eA_e n_e u_e\right) = \frac{\partial I_d}{\partial z} = 0 \tag{4.28}$$

which states that the total discharge current I_d is only time-dependent.

Regarding momentum conservation, which is characterized by a negligible electron inertia (see Section 4.1), both the axial and azimuthal directions are considered, thus respectively resulting in

$$m_e n_e \nu_e u_e = -\frac{\partial \mathcal{P}_e}{\partial z} + en_e\frac{\partial \phi}{\partial z} + en_e u_{e,\theta} B_r \tag{4.29}$$

$$m_e n_e \nu_e u_{e,\theta} = -en_e u_e B_r \tag{4.30}$$

where ν_e is the momentum transfer collision frequency, which drives electron diffusion across the magnetic field. In particular, this parameter is composed of several contributions, i.e.

$$\nu_e = \nu_{en} + \nu_{e,w} + \nu_{anom} \tag{4.31}$$

The first one takes into account the collisions between electrons and heavy particles (only neutrals here, as ions have been assumed non-collisional). Consequently, all reactions presented in the chemical model of Section 3.2 contribute to this term by means of their reactions rates $k_{n,r}$ (see Table 3.8) multiplied by the corresponding n_n. By recalling Eq. 4.12, it results

$$\nu_{en} = \sum_{n,r} \nu_{n,r} \tag{4.32}$$

Regarding $\nu_{e,w}$, this term represents the momentum losses due to electron collisions with the channel wall and it is detailed in Section 4.4.

Finally, ν_{anom} is the anomalous collision frequency term, which is an artificial contribution included to account for the fact that classical electron transport alone is known to under-predict the measured electron mobility across the magnetic field. The reasons at the basis of this long-standing problem are several, mainly the difficulties in both assessing which is/are the main transport driving mechanism/s involved and accurately sensing the plasma behaviour [97]. One of the most promising mechanisms consists in the turbulent electron transport by fluctuating azimuthal electric fields [98, 99, 100] which generates several plasma oscillations. However, also due to the inherent complexities related to these phenomena, a fully self-consistent model of electron transport in HETs has not been achieved yet. Rather, in this model ν_{anom} is assumed proportional to the electron gyro-frequency $\omega_e = eB_r/m_e$ following the classical expression

$$\nu_{anom} = \beta\frac{eB_r}{16m_e} = \frac{\beta}{16}\omega_e \tag{4.33}$$

in which β is a free calibration parameter generally dependent on both time and space. Its tuning is crucial for the model behaviour and it is discussed in detail in Section 4.5.

By putting together Eqs. 4.29 and 4.30 it is possible to delete the $u_{e,\theta}$ dependence, thus obtaining

$$n_e u_e = -\mu_\perp n_e \left(\frac{1}{e n_e} \frac{\partial \mathcal{P}_e}{\partial z} - \frac{\partial \phi}{\partial z} \right) \tag{4.34}$$

where $\mu_\perp$ is the electron mobility across the magnetic field, i.e.

$$\mu_\perp = \frac{\mu_\parallel}{1 + \Omega^2} \tag{4.35}$$

which is defined in terms of the along-field (or unmagnetized) mobility $\mu_\parallel = e/(\nu_e m_e)$ and the Hall parameter $\Omega = \omega_e/\nu_e$.

Finally, for a Maxwellian distribution of electrons, the (internal) energy conservation equation can be expressed as

$$\begin{aligned} &\frac{\partial}{\partial t}\left(\frac{3}{2} n_e k_B T_e\right) + \underbrace{\frac{\partial}{\partial z}\left(\frac{5}{2} n_e k_B T_e u_e\right)}_{A} = \\ &\qquad = \underbrace{\frac{\partial}{\partial z}\left(\frac{5}{2}\frac{\mu_\perp n_e k_B T_e}{e}\frac{\partial k_B T_e}{\partial z}\right)}_{Q} + u_e \frac{\partial \mathcal{P}_e}{\partial z} + \frac{e n_e u_e^2}{\mu_\perp} + S_e + S_w + S_{pl} \end{aligned} \tag{4.36}$$

where A and Q respectively indicate advection and conduction heat flows. Also, the sink term S_e represents the energy losses due to particle interactions and it is then defined as

$$S_e = -n_e (n_N K_{N,tot} + n_O K_{O,tot} + n_{N_2} K_{N_2,tot} + n_{O_2} K_{O_2,tot}) \tag{4.37}$$

where each $K_{n,tot}$ is the sum of all energy loss coefficients K relative to the reactions between electrons and the neutral species n (see Table 3.8).

Regarding S_w, this sink term models the electron thermal losses at the channel wall and it is defined as

$$S_w = -n_e W \tag{4.38}$$

where W is the electron power lost, which expression is presented in detail in Section 4.4.

Finally, S_{pl} represents the balance between energy advection and conduction in the expanding plume, thus resulting

$$S_{pl} = \frac{1}{A_e}\frac{\partial A_e}{\partial z}\frac{5}{2} n_e k_B T_e \left(\frac{\mu_\perp}{e}\frac{\partial k_B T_e}{\partial z} - u_e \right) \tag{4.39}$$

where $\partial A_e/\partial z$ is computed numerically once A_e is determined.

4.3. Model Formulation and Solution Procedure

Starting from the general plasma equations of the previous section, the relations used in the model are now derived.

At first, the electric field dependence from the ion momentum conservation equation (Eq. 4.24) is eliminated by means of Eq. 4.34, which can be rearranged as

$$E_z = -\frac{\partial \phi}{\partial z} = -\left(\frac{1}{e n_e}\frac{\partial \mathcal{P}_e}{\partial z} + \frac{u_e}{\mu_\perp} \right) \tag{4.40}$$

thus resulting in

$$\frac{\partial}{\partial t}(n_i u_i) + \frac{\partial}{\partial z}\left(n_i u_i^2 + \frac{\mathcal{P}_i}{m_i} \right) = -\frac{e n_i}{m_i}\left(\frac{1}{e n_e}\frac{\partial \mathcal{P}_e}{\partial z} + \frac{u_e}{\mu_\perp} \right) + S_{m,i} - u_i(\dot{n}_{i,w} + \dot{n}_{i,pl}) \tag{4.41}$$

Then, by noticing that

$$\frac{n_i}{n_e}\frac{\partial \mathcal{P}_e}{\partial z} = \frac{\partial \left(n_i k_B T_e\right)}{\partial z} - \mathcal{P}_e \frac{\partial \left(\frac{n_i}{n_e}\right)}{\partial z} \tag{4.42}$$

the final equation for ion momentum conservation becomes

$$\frac{\partial}{\partial t}\left(n_i u_i\right) + \frac{\partial}{\partial z}\left(n_i u_i^2 + \frac{\mathcal{P}_i + n_i k_B T_e}{m_i}\right) = \frac{\mathcal{P}_e}{m_i}\frac{\partial \left(\frac{n_i}{n_e}\right)}{\partial z} - \frac{e n_i u_e}{m_i \mu_\perp} + S_{m,i} - u_i(\dot{n}_{i,w} + \dot{n}_{i,pl}) \tag{4.43}$$

The reason for this manipulation, referred as electron-pressure coupling scheme, is a greatly improved numerical stability of the solution, as widely demonstrated in literature [101].

The second manipulation consists in inserting Eq. 4.34 into the current conservation equation (Eq. 4.28), thus obtaining

$$\sum_{i=1}^{4} e A_i n_i u_i + e A_e \mu_\perp n_e \left(\frac{1}{e n_e}\frac{\partial \mathcal{P}_e}{\partial z} - \frac{\partial \phi}{\partial z}\right) = I_d \tag{4.44}$$

After integration over the whole domain, this produces a new expression for the total discharge current I_d, i.e.

$$I_d = \frac{\Delta\phi + \displaystyle\int_0^{z_f}\left(\sum_{i=1}^{4}\frac{A_i n_i u_i}{A_e \mu_\perp n_e} + \frac{1}{e n_e}\frac{\partial \mathcal{P}_e}{\partial z}\right) dz}{\displaystyle\int_0^{z_f}\frac{1}{e A_e \mu_\perp n_e} dz} \tag{4.45}$$

where $\Delta\phi$ is the potential difference between the anode sheath edge ($z = 0$, i.e. the first domain point) and the cathode virtual line ($z_f = 0$). Note that this quantity is different from the discharge potential ϕ_d (which is calculated between anode and cathode) since $\Delta\phi$ also includes the potential drop $\phi_a \geq 0$ through the anode sheath, such that

$$\Delta\phi = \phi_d + \phi_a \tag{4.46}$$

Being sheaths excluded from the domain, ϕ_a must be separately modelled. Specifically, following the classical description of a charged electrode immersed in a plasma [6], ϕ_a is defined as

$$\phi_a = -\frac{k_B T_e}{e}\ln\left[\min\left(1, \frac{j_{e,a}}{j_{e,th}}\right)\right] \tag{4.47}$$

where $j_{e,a} = I_d/A - j_{i,a}$ is the electron current density at the anode and $j_{i,a}$ is that of ions there. Also, for a Maxwellian distribution of electrons, $j_{e,th} = e\Gamma_{e,th} = e n_e \sqrt{k_B T_e/(2\pi m_e)}$ is the current density due to their (random) thermal flux $\Gamma_{e,th}$. Note that the lower limit $\phi_a = 0$ is imposed to preserve the electron-repelling nature of this sheath, which is generally valid as the diffusion thermal flow is dominant [6]. Consequently, because only neutrals are emitted from the anode, the ions in its vicinity are attracted toward this sheath, where they will then recombine with the electrons so as to be re-emitted as neutrals. This determines the formation of a region of inverse ion flow adjacent to the anode sheath.

Once I_d is determined, the local electron velocity u_e is obtained from the current conservation equation (Eq. 4.28), such that

$$u_e = \sum_{i=1}^{4}\frac{A_i n_i u_i}{A_e n_e} - \frac{I_d}{e A_e n_e} \tag{4.48}$$

In conclusion, the final system of equations for this numerical model is given by

$$
\begin{cases}
\dfrac{\partial n_n}{\partial t} + \dfrac{\partial}{\partial z}\left(n_n u_n\right) = S_{c,n} + \dot{n}_{i,w} - \dot{n}_{n,pl} \\[2ex]
\dfrac{\partial A_n}{\partial z} = \begin{cases} 0 & \text{for} \quad z < L \\ 4\pi R_c \dfrac{v_{n,th}}{u_n} & \text{for} \quad z \geq L \end{cases} \\[2ex]
\dfrac{\partial n_i}{\partial t} + \dfrac{\partial}{\partial z}\left(n_i u_i\right) = S_{c,i} - \dot{n}_{i,w} - \dot{n}_{i,pl} \\[2ex]
\dfrac{\partial}{\partial t}\left(n_i u_i\right) + \dfrac{\partial}{\partial z}\left(n_i u_i^2 + \dfrac{\mathcal{P}_i + n_i k_B T_e}{m_i}\right) = \dfrac{\mathcal{P}_e}{m_i}\dfrac{\partial\left(\frac{n_i}{n_e}\right)}{\partial z} - \dfrac{e n_i u_e}{m_i \mu_\perp} + S_{m,i} - u_i(\dot{n}_{i,w} + \dot{n}_{i,pl}) \\[2ex]
\dfrac{\partial A_i}{\partial z} = \begin{cases} 0 & \text{for} \quad z < L \\ 4\pi R_c \dfrac{c_{s,i}\big|_{z=L_{ch}}}{u_i} & \text{for} \quad z \geq L \end{cases} \\[2ex]
n_e = \displaystyle\sum_{i=1}^{4} n_i \\[2ex]
A_e = \dfrac{\displaystyle\sum_{i=1}^{4} n_i A_i}{n_e} \\[2ex]
\dfrac{\partial}{\partial t}\left(\dfrac{3}{2} n_e k_B T_e\right) + \dfrac{\partial}{\partial z}\left(\dfrac{5}{2} n_e k_B T_e u_e\right) = \\
\qquad = \dfrac{\partial}{\partial z}\left(\dfrac{5}{2}\dfrac{\mu_\perp n_e k_B T_e}{e}\dfrac{\partial k_B T_e}{\partial z}\right) + u_e \dfrac{\partial \mathcal{P}_e}{\partial z} + \dfrac{e n_e u_e^2}{\mu_\perp} + S_e + S_w + S_{pl} \\[2ex]
I_d = \dfrac{\Delta\phi + \displaystyle\int_0^{z_f}\left(\sum_{i=1}^{4}\dfrac{A_i n_i u_i}{A_e \mu_\perp n_e} + \dfrac{1}{e n_e}\dfrac{\partial \mathcal{P}_e}{\partial z}\right) dz}{\displaystyle\int_0^{z_f}\dfrac{1}{e A_e \mu_\perp n_e} dz} \\[2ex]
u_e = \displaystyle\sum_{i=1}^{4}\dfrac{A_i n_i u_i}{A_e n_e} - \dfrac{I_d}{e A_e n_e}
\end{cases}
$$

where the unknowns to be solved for are (n_n, A_n, n_i, u_i, A_i, n_e, A_e, T_e, I_d, u_e). Clearly, it is implicitly considered that, dealing with a multispecies case with four neutrals and four ions, neutral continuity equation and ion continuity and momentum conservation equations have to be solved for each species individually. Therefore, the effective unknowns are (n_N, n_O, n_{N_2}, n_{O_2}, A_n, n_1, n_2, n_3, n_4, u_1, u_2, u_3, u_4, A_1, A_2, A_3, A_4, n_e, A_e, T_e, I_d, u_e), where the numbering is the same used in Chapter 3. While the system does not solve for the electric potential ϕ (because of the electron-pressure coupling exploited to obtain Eq. 4.43), this can be computed afterwards from the electron momentum equation (Eq. 4.34).

Although not explicitly derived, all the model equations are used in adimensional form in the code. In particular, the fundamental reference quantities employed are: $n^* = 1 \times 10^{18}\,\mathrm{m}^{-3}$, $L^* = L_{ch}$, $T^* = 12\,\mathrm{eV} \cdot e/k_B$, $m^* = m_1$, $u^* = \sqrt{k_B T^*/m^*}$. Then, all other variables and parameters are adimensionalized by using combinations of these.

Having defined the final system of equations, the solution procedure is now presented. The approach used exploits the fact that, although the system results highly non-linear and coupled, once discretized in time the equations can be sequentially advanced through successive time instants. In particular, starting from an initial condition at time t^k in which all plasma variables are known, the equations are solved in sequence to individually determine each variable at time $t^{k+1} = t^k + \Delta t$.

Regarding the spatial dimension, the entire axial domain is discretized and solved together at each time instant. Note that the time step Δt cannot be chosen independently from the distance between mesh elements Δz. Indeed, the fluid nature of problem involving transport of information in time and space is subjected to the CFL condition, which states that the distance travelled by any information in a time step must be lower than the mesh resolution. This condition ensures that information only propagate to the neighbouring cells of the domain and it represents a necessary condition for stability (not sufficient though). Therefore, the time step value results effectively limited by the spatial resolution employed. For a one-dimensional case the CFL conditions writes

$$\Delta t \leq \frac{C_{max} \Delta z}{u^*} \tag{4.49}$$

where C_{max} is the maximum Courant number, which depends on the discretization methods used.

The steps followed for the model solution are:

1. The neutral continuity equation (Eq. 4.14) is solved for all neutral species independently so as to determine the four respective n_n^{k+1}.

   This first subproblem is a simple scalar transport PDE with constant convective term due to the assumed fixed neutral velocity u_n. As such, it only requires a boundary condition on n_n, which can be obtained from the known injection conditions at the anode plate. Indeed, it is known that nitrogen and oxygen at ambient conditions (i.e. N_2 and O_2 only) are mixed in a ratio 1.27:1 and then injected in the thruster channel with a total mass flow rate $\dot{m}_a$ (which varies depending on the operative point). Consequently, the neutral injection mass flow rate $\dot{m}_n$ for each species results

   $$\dot{m}_N = 0 \qquad \dot{m}_O = 0 \qquad \dot{m}_{N_2} = \frac{1.27}{1.27+1}\dot{m}_a \qquad \dot{m}_{O_2} = \frac{1}{1.27+1}\dot{m}_a \tag{4.50}$$

   Then, for each equation the respective boundary condition can be written as

   $$n_n(0) = \frac{\dot{m}_n}{m_i u_n A} - \frac{j_{i,a}}{e u_n} \tag{4.51}$$

   where the first term takes into account the positive contribution of the injected neutrals, while the second one models ion recombination at the anode.

   Regarding the numerical discretization, Eq. 4.14 is advanced in time by means of a first-order explicit Euler scheme and in space following a finite-volume formulation (as it is also the case of all the other equations of the system). In particular, a first-order upwind scheme is employed.

2. The neutral plasma area A_n^{k+1} is obtained by solving Eq. 4.19.

3. The ion continuity (Eq. 4.21) and momentum conservation (Eq. 4.43) equations are solved together for each ion species so as to obtain the four respective couples of n_i^{k+1} and u_i^{k+1}.

This subproblem is a reduced Euler problem (i.e. ion energy conservation equation is neglected) and so also a hyperbolic system of two PDEs. As such, its wave-like behaviour requires a varying number of boundary conditions depending on the local (at the boundaries) characteristic velocities. In particular, at the cathode location ($z = z_f$) the ions outflow is generally supersonic and so no boundary condition is required. Regarding the anode boundary, in order for the sheath to form, the Bohm condition is imposed, i.e.

$$u_i(0) \leq -c_{s,i} \tag{4.52}$$

Note that, in view of the ion-ion streaming instabilities discussion carried out in this work also the anode sheath edge conditions could be affected. However, the different nature of this surface (i.e. charged and neutrals emitting) requires a separate detailed analysis which goes beyond the scope of this work.

Regarding the numerical discretization, the system is advanced in time by means of a first-order explicit Euler scheme and in space following a Rusanov finite-volume method [102, 103]. This scheme has been introduced in place of the Steger–Warming flux vector splitting (FVS) method [104] previously used, as the latter was prone to produce (in the xenon case) a discontinuity of the density derivative at the axial location where ions become sonic. In the multispecies case here analyzed, the presence of an additional source term in the momentum conservation equation (i.e. $\mathcal{P}_e/m_i \partial(n_i/n_e)/\partial z$) greatly decreased the method robustness which ultimately failed. Conversely, the more robust Rusanov approach artificially flatten the sonic discontinuity point, thus allowing a correct solution of the system.

4. The ion plasma areas A_i^{k+1} are obtained by solving Eq. 4.23.

5. The charge neutrality equation (Eq. 4.3) is solved proving n_e^{k+1}.

6. The electron plasma area A_e^{k+1} is obtained by solving Eq. 4.27.

7. The electron energy conservation equation (Eq. 4.36) is solved so as to obtain T_e^{k+1}.

   This subproblem is a one-dimensional elliptic PDE, which thus requires a condition imposed on each boundary. Specifically, at the anode side it is used the known outflow electron energy flux

   $$\Gamma_{e,a} = \frac{j_{e,a}}{e}(2k_B T_e + e\phi_a) \tag{4.53}$$

   while at the cathode axial location it is assumed a constant electron temperature of 2 eV [105].

   Regarding the numerical discretization, the system is advanced in time by means of a first-order implicit Euler scheme and in space following a second-order finite-volume method, which centrally evaluates the gradients at the cell interfaces.

8. The total discharge current I_d^{k+1} is retrieved from Eq. 4.45.

   This integral equation is discretized in space by using a first-order centered finite-volume approach.

9. The electron flow velocity u_e^{k+1} is obtained by solving Eq. 4.48.

All these steps are executed in this order at each time instant, so as to model the plasma evolution.

4.4. Plasma-wall Interaction

While the reactions between particles depend on fixed experimental (or numerical) cross-sections, the plasma-wall interaction phenomena, which comprehend ion recombination, electron momentum and energy losses, are instead based on a sheath model. In this work, this is exactly the one which is presented and used in Sections 2.3 and 3.3.

Starting from ion recombination (neutralization) at the channel walls, this process is governed by the ion-wall collision frequency $\nu_{i,w}$ which, by recalling Eq. 2.61, for each ion species results

$$\nu_{i,w} = \alpha \frac{2}{\Delta R} \frac{n_i}{n_e} u_{i,0} \tag{4.54}$$

where the coefficient α is a calibration parameter (constant) employed in the model to tune the wall interaction phenomena. Its calibration is discussed in detail in the next section. Note that ion neutralization does not exchange any energy between electrons and ions, thus not contributing to the electron energy balance. Also, note that the ion velocity at the sheath edge, in the radial direction, is indicated with $u_{i,0}$ (coherently with the notation used in the previous chapters), which should not be confused with the axial ion velocity u_i.

Regarding electron momentum losses at the wall, these are modelled by means of the collision frequency $\nu_{e,w}$, which contributes to the total momentum transfer collision frequency ν_e (Eq. 4.31). In particular, for the plasma considered and a dielectric wall emitting secondary electrons, the balance between ion and electron fluxes at the wall (Eq. 2.59) leads to

$$\nu_{e,w} = \frac{\sum_{i=1}^{4} \nu_{i,w}}{1-\sigma} \tag{4.55}$$

which, using Eq. 4.54, becomes

$$\nu_{e,w} = \frac{\alpha}{1-\sigma} \frac{2}{\Delta R} \sum_{i=1}^{4} \left(\frac{n_i}{n_e} u_{i,0} \right) \tag{4.56}$$

Electrons impacting walls with the collision frequency $\nu_{e,w}$ do not only contribute to momentum transfer, but also lose their energy. Precisely, by recalling Eq. 2.55, the average power lost is defined as

$$W = \nu_{e,w} \left[2k_B T_e + (1-\sigma) e |\phi_w| \right] \tag{4.57}$$

where the sheath potential ϕ_w is obtained from the zero current condition at the wall (Eq. 3.49) and it reads as

$$\phi_w = -\frac{k_B T_e}{e} \ln \left[\frac{(1-\sigma)\sqrt{\dfrac{k_B T_e}{2\pi m_e}}}{\sum_{i=1}^{4} \dfrac{n_i}{n_e} u_{i,0}} \right] \tag{4.58}$$

Here $\sigma = \min(1.36 \cdot 0.123\ T_{eV}^{0.528}, \sigma_{SCS})$ due to the BNSiO$_2$ channel walls. Regarding σ_{SCS}, as it is shown in Section 3.3, its value is subjected to variations depending on T_e and especially on the plasma composition. As these vary locally in the channel, it would be required to solve also the sheath model at each point to determine the precise σ_{SCS}, substantially increasing the computational time. However, unless it results that doing so would beneficially affect the solution representativeness, this is not generally done. Therefore, an average value of 0.961 is selected from Figure 3.31, which considers the reference 1.27N$_2$+O$_2$ mixture with $\bar{n}_3 = 2\bar{n}_1$ and $\bar{n}_4 = 2\bar{n}_2$.

In the above equations, depending on the values used for the velocities $u_{i,0}$, two cases are distinguished. Indeed, the numerical model is solved for both the common case in which these are assumed equal to the corresponding individual sound speeds and for the novel case involving ion-ion streaming instabilities. In this way, it is possible to compare the two approaches and evaluate the impact of such kinetic instability description on the fluid thruster model employed. The results of this comparison are presented in detail in Chapter 6. It is stressed that, as discussed in Subsection 3.3.4, the commonly used case does not include the effect of SEE on $u_{i,0}$ (thus reflecting the general approach found in literature), while the case with ion-ion instabilities does, being it self-consistently resolved by the presheath/sheath model.

While the case $u_{i,0} = c_{s,i}$ is self-explanatory, the other requires further discussion regarding the model implementation adopted. Indeed, in order to determine the ion velocities resulting from the instability-enhanced friction onset in the presheath, it is required to solve inside the thruster model the entire presheath/sheath model of Section 3.3. As this process need to be repeated for every channel location at each simulation time step, the computational time needed would be excessively long, thus making the model unusable.

In order to avoid this issue, the presheath/sheath model is separately solved for a uniformly spaced set of plasma conditions in terms of electron temperature and composition. Then, all these resolved points are grouped together and interpolated, so as to create a complete mapping covering all possible combinations of these variables (within the respective ranges, see below). The resulting interpolant is successively passed to the thruster model, thus avoiding the need of repeatedly solving the presheath/sheath model at each channel location.

As it may be expected, this solution comes at the expenses of some accuracy loss, even though this is highly dependent on the mapping resolution. Precisely, in this work it is considered an electron temperature resolution of 1 eV in the range 1-40 eV and normalized ion densities in steps of 0.97/14. The range of the latter is clearly not fixed as it depends on all the others based on the plasma quasi-neutrality condition (Eq. 4.3). As such, starting from a common minimum normalized density of 0.01, the first density ranges up to 0.97 (i.e. $1 - 3 \cdot 0.01$) in 14 steps, for a total of 15 values over the entire range. The second one however can only reach the maximum 0.97 in case the first is 0.01, thus also forcing the two remaining to be 0.01, ans so on. These ranges are summarized as

$$
\begin{aligned}
&\bar{n}_1 = [0.01,\ 1 - 3 \cdot 0.01] \\
&\quad \Rightarrow \bar{n}_2 = [0.01,\ 1 - 2 \cdot 0.01 - \bar{n}_1] \\
&\quad\quad \Rightarrow \bar{n}_3 = [0.01,\ 1 - 0.01 - \bar{n}_1 - \bar{n}_2] \\
&\quad\quad\quad \Rightarrow \bar{n}_4 = 1 - \bar{n}_1 - \bar{n}_2 - \bar{n}_3
\end{aligned}
$$

where the step size is always fixed.

Once the mapping resolution is set, the presheath/sheath model is solved at each of these points, associating to it the required set of solution variables. For the present case these specifically are $u_{1,0}$, $u_{2,0}$, $u_{3,0}$, $u_{4,0}$, ϕ_w and σ_{SCS}. Note that, in addition to the velocities $u_{i,0}$, also ϕ_w and σ_{SCS} are considered, since these are self-consistently determined by the presheath/sheath model.

Regardless of the solution variables considered, the discrete mapping results a 5-D function associating a fixed value of $(u_{1,0}, u_{2,0}, u_{3,0}, u_{4,0}, \phi_w, \sigma_{SCS})$ to a unique combination of the four parameters $(\bar{n}_1, \bar{n}_2, \bar{n}_3, T_{eV})$. In order to interpolate this discrete mapping, so as to create an interpolant to load in the thruster model, it is used N-dimensional gridded linear interpolation.

Finally, it is briefly discussed the mapping accuracy by comparing the respective solutions with the numerically exact ones presented in Section 3.3. In particular, it is considered the same reference plasma composition used in the presheath/sheath model, since this does not correspond to any resolved point of the mapping. The results are displayed in Figure 4.2.

Overall, all quantities show a quite accurate agreement over the electron temperature range considered, with the only exception of the neighbourhood of the discontinuity point caused by emission saturation. While the ability to precisely resolve this point is clearly related to the T_{eV} resolution used, the 1 eV step appears sufficiently precise in following the discontinuity for both $u_{i,0}$ and σ, with a maximum variation of 0.9% and 0.4%, respectively.

On the other hand, the case of ϕ_w highlights a maximum variation of 12.8% due to the much steeper discontinuity. Although this is not ideal, it does not even justify the additional time required to increase the T_{eV} resolution, which would not just involve a local refinement as the discontinuity point is not fixed. This can be surely mentioned as the main (and possibly only) limitation of using this mapping to model the effects of ion-ion streaming instability.

Apart from the discontinuity point, the very close agreement in the other regions does not require particular comments.

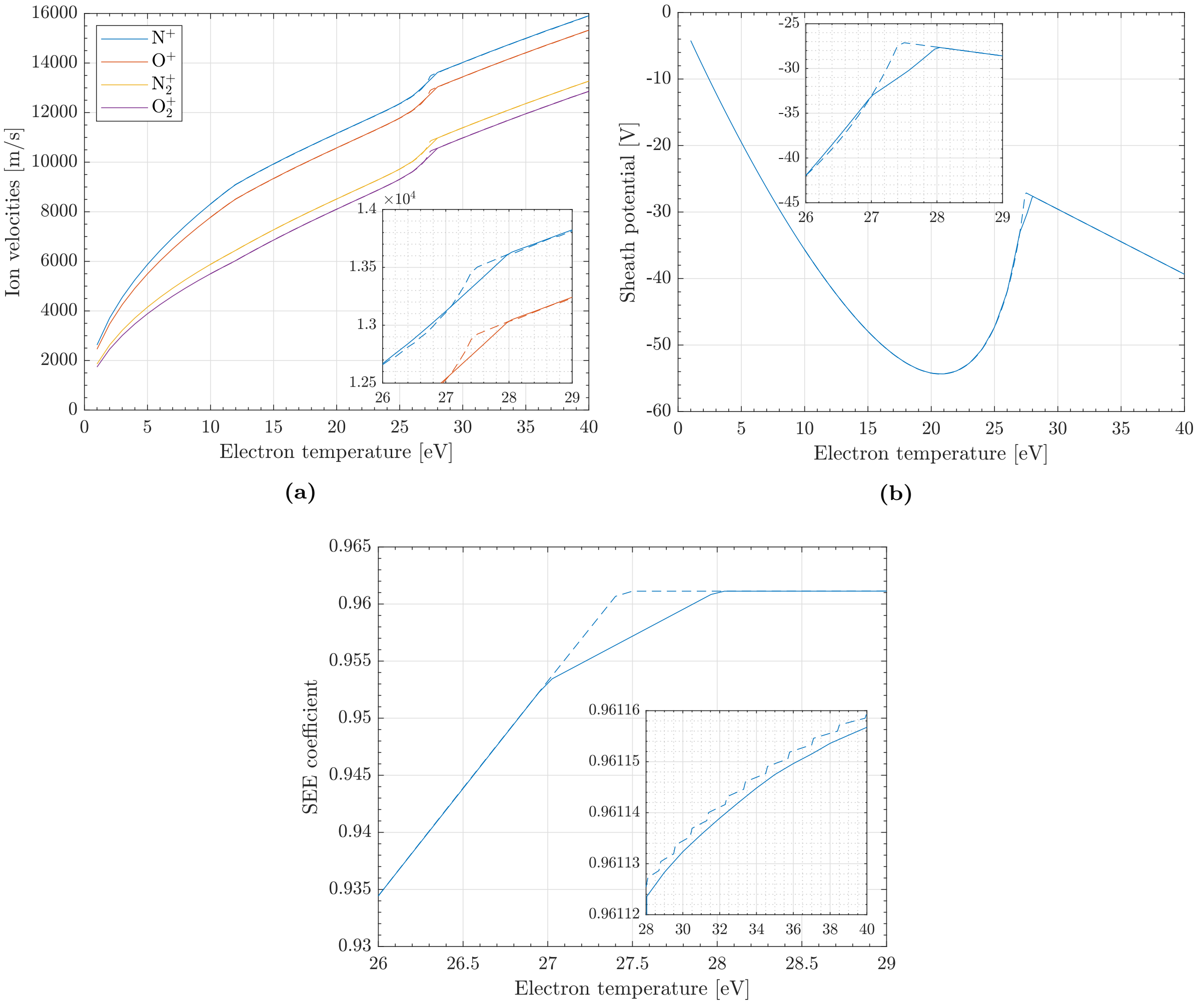

(a) **(b)**

(c)

Figure 4.2: Comparison between the results obtained with the mapping (solid lines) and the exact ones obtained with the presheath/sheath model of Section 3.3 (dashed lines) for (a) the individual ion velocities $u_{i,0}$, (b) the sheath potential ϕ_w and (c) the SEE coefficient σ in case of ion-ion instability as a function of T_{eV}. The plasma characteristics are: $1.27N_2$+O_2 mixture with $\bar{n}_3 = 2\bar{n}_1$ and $\bar{n}_4 = 2\bar{n}_2$, $\sigma = \min(1.36 \cdot 0.123\ T_{eV}^{0.528}, \sigma_{SCS})$, $T_{iV} = 0.2\,\text{eV}$.

4.5. Model Calibration

In order to obtain a representative model validated on experimental data, this has to be calibrated. Indeed, apart from its overall simplified nature, some processes in particular result either unknown, uncertain or too complex to be modelled in detail, thus relying on approximated descriptions. Consequently, a proper tuning of these phenomena is crucial to compensate (where possible) for their uncertainties or simplifications, in the effort of matching the experimental results. To do so, in the model are introduced some calibration parameters: the anode/neutral temperature T_a, the neutral velocity accommodation factor AF, the wall-interaction parameter α and the anomalous diffusion coefficient β.

The anode/neutral temperature T_a is a parameter dependent on several factors, mainly the anode thermal exchange characteristics and the electron power dissipated on it. The former are a consequence of the anode material, geometry and mounting, while the latter varies in relation to the operational point and power of the thruster, as well as the plasma behaviour in general. As a consequence, even making a prediction for an average T_a is generally quite difficult in absence of experimental measurements or a dedicated model. However, for a thruster of this size and power it is approximately expected a temperature range of 700-1100 K [95].

In the thruster model, the anode/neutral temperature is key for determining the axial velocity at which all neutral species move through the channel and in the plume (Eq. 4.4). In particular, this is among the main parameters governing propellant ionization since faster neutrals have a shorter channel residence time and thus are less likely subjected to electron impacts. Therefore, in order to faithfully simulate the particle interactions, a careful tuning of this parameter is essential. Moreover, this temperature is also directly responsible for the thermal neutral loss rate due to plume expansion (Eq. 4.17), which allows to significantly improve the model representativeness in this region.

In order to independently tune neutral axial velocities u_n and neutral radial expansion velocities $v_{n,th}$ in the plume, it is necessary to also add the accommodation factor AF among the calibration parameters. This indeed only affects u_n (Eq. 4.4), representing a parameter used to *accommodate* the injection velocity to the numerical description employed (e.g. radially averaged variables). Even though Reid [95] theorized $AF = 0.25$ for xenon neutral velocities averaged over the anode plane, the N_2/O_2 mixture used in this work may be characterized by a different dependency.

Regarding the wall interaction parameter α, this is an arbitrary factor scaling the physical phenomena related to the sheath/wall description, namely: ion recombination and electron momentum and energy losses. However, this parameter has not been artificially introduced in this work, but rather it appears in the general sheath theory as a constant with value $\exp(-1/2) \approx 0.6$. Specifically it represents the density decrement factor between plasma bulk and sheath edge predicted by the Boltzmann relationship for electrons (Eq. 2.27). As the numerical model here employed considers radially averaged quantities, and thus approximates $n_{i,0} \equiv n_i$ in Eq. 4.54, it is expected $\alpha < 0.6$. In addition, by considering that the general sheath theory is known to overestimate electron losses (and so all other related quantities) with respect to a real sheath [106, 107], an even lower value of α is foreseen.

Note that the tuning of α also allows to take into account the reduced plasma interactions with the channel walls resulting from the thruster magnetic shielding configuration, which cannot be resolved by the model.

Due to its direct action on several physical mechanisms characterizing the plasma behaviour and composition, even small variations of α may greatly modify the model solution. In general, as α is increased the discharge current decreases due to the lower density of ions and electrons, eventually reaching a point in which the plasma cannot be sustained any more. This effect is also enhanced by the corresponding lower electron temperature (due to thermal losses to the wall) which reduces the ionization efficiency. As the electron momentum is concerned, a higher α also contributes to its decrement because of the increased electron flux toward the walls, which is governed by $\nu_{e,w}$. At the same time, this higher collision frequency facilitates the electron transport across the channel.

Finally, the anomalous diffusion coefficient β is an arbitrary parameter used to model the artificial anomalous collision frequency ν_{anom}, which represents the effects of plasma turbulence and azimuthal oscillatory modes [108]. These very complex phenomena are not completely understood yet and thus cannot be self-consistently resolved in numerical models. Therefore, approximate expressions such as Eq. 4.33 (based on Bohm diffusion) are employed to model their impact on plasma collisionality. In such simplified descriptions, the parameter β is in general a function of both time and space, even though in this work only the axial dependence is considered, i.e. $\beta(z)$. In particular, following the experimental and numerical results found in literature [6, 101, 109], β is essentially defined as a step function with a variably smooth transition at the channel exit. Indeed, there is general agreement about the fact that outside the channel ν_{anom} is much greater than inside (i.e. about two orders of magnitude) even though its local behaviour, especially near the anode where measurements cannot be accurately performed, remains partially uncertain. As such, the tuning of β reduces to a complex trial and error process in which the electron mobility throughout the domain is varied in order to match experimental data.

Note that, in order to avoid tuning β while also modelling anomalous collision more precisely, a self-consistent description suggested by Lafleur et al. [110] has been initially implemented. This proposes, by means of a kinetic approach, an effective cross-field electron mobility μ_{eff}, enhanced by azimuthal instability, i.e.[2]

$$\mu_{eff} = \frac{\dfrac{|q|}{m_e \nu_e}}{1 + \dfrac{\omega_e^2}{\nu_e^2}} \left(1 + \frac{\omega_e}{\nu_e} \frac{R_{ei}}{|q| n_e E_z} \right) \tag{4.59}$$

In this expression, R_{ei} is the (instability-enhanced) electron-ion frictional force, which is the result of both electron density and azimuthal electric field fluctuations associated with the instability. Although this description is in good agreement with experiments [110], in this work it could not be coupled properly with the numerical scheme employed. Therefore, Eq. 4.33 has been used.

In conclusion, the four calibration parameters employed appear significantly coupled with effects often competing. This characteristic, together with the strongly non-linear nature of the model, results in parameter variations generally difficult to predict, making the tuning process even more arduous.

---

[2] Clearly, the electron collision frequency ν_e appearing in this expression does not include the ν_{anom} contribution.

5

Experimental Campaign

In this chapter it is presented the PFG experimental campaign conducted at SITAEL in the Ospedaletto (Pisa) facility. As the test has been planned and managed independently from this work,[1] this chapter is not meant to describe a proposed test plan. Rather, in the following are mainly discussed the various diagnostics employed, with special focus on data acquisition and analysis. It is shown that the particular multispecies plasma probed significantly complicates the data analysis task, as the majority of the diagnostics employed is unable to distinguish between different ion species. Therefore, it has been often necessary to combine together the measurements of different instruments in order to solve these uncertainties. Note that, although it has been ultimately possible to only process the triple Langmuir probe data due to time limitations, in the following it is still proposed an overall data analysis approach covering all diagnostics.

5.1. Test Description

In this section are briefly presented, for reference, the test objectives, items and facility.

5.1.1. Test Objectives

The objectives of the PFG experimental campaign can be summarized as:

1. **Verify whether or not the PFG can withstand operation with the selected atmospheric propellant.**
   This objective is an essential condition for any successive activity in experimental campaign and refers to at least one operating point. Specifically, to verify it, the coupling between the thruster operated with N_2/O_2 and the cathode operated with N_2 has to be proven possible, i.e. able to sustain the discharge, for at least one operating point.
2. **Verify the stability of PFG operation with the selected atmospheric propellant.**
   Assuming that the PFG can be operated in at least one operating point, it is necessary to assess the stability of its performance. Stability here refers to thermal steady-state, which is considered reached when the measured temperature variation at the anode backplate is less than $\pm 1\,^{\circ}\mathrm{C}$ over a time span of 30 minutes.
3. **Characterize the PFG performance at thermal equilibrium for a group of operating points.**

---

[1] This experimental campaign is part of the AETHER project, aiming at the early design of a ram-EP thruster, funded by the European Union's Horizon 2020 research and innovation programme.

A complete characterization of the thruster requires performance acquisition and evaluation over several operating points. However, to meet this objective it is sufficient to characterize at least one.

4. **Assess the PFG plume representativeness with respect to the reference VLEO orbit conditions.**
   By analyzing the data collected during the PFG characterization, it can be investigated the existence of an operating point effectively reflecting the Particle Flow Generator capability expected from this thruster.

5.1.2. Test Items

For the test it is employed a SITAEL HT5k (DM3) Hall thruster (Figure 5.1), which implements a magnetic shielding field topology and is coupled with a centrally mounted SITAEL HC20h hollow cathode (Figure 5.2). The specifications of these two test items are reported in Table 5.1 for nominal operations with xenon. Note that operation with an N_2/O_2 mixture at the anode and N_2 at the cathode (more details in Section 5.3) is expected to greatly degrade the thruster performance and to also modify its stable operating range. However, as this novel configuration of the HT5k is only intended as a PFG and not as a feasible thruster alternative, these changes are of little practical concern.

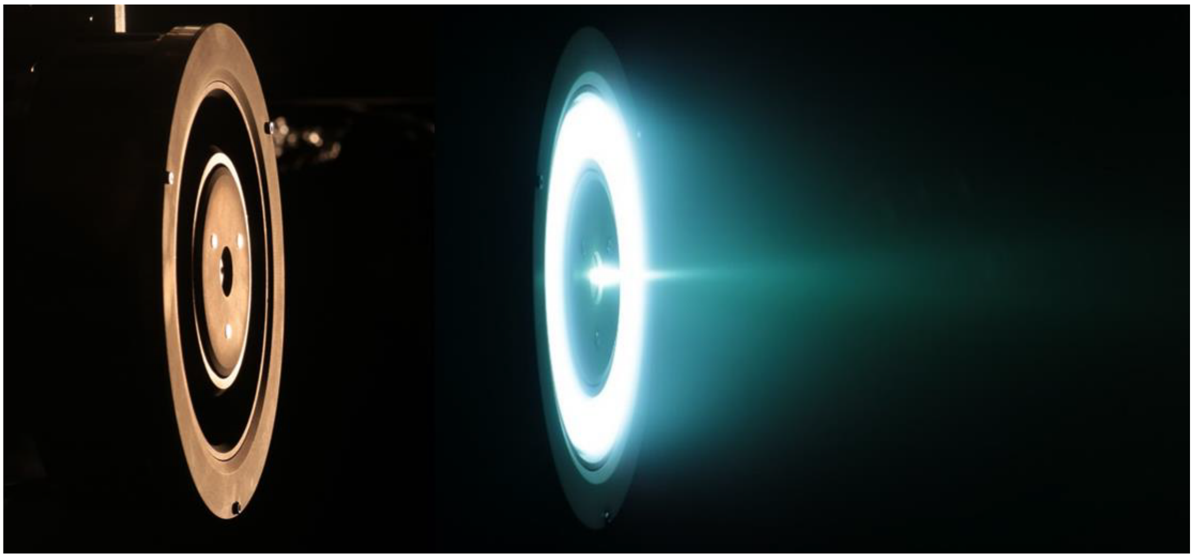

Figure 5.1: SITAEL HT5k turned off (left) and firing with Xe (right). (Source: Ref. [1])

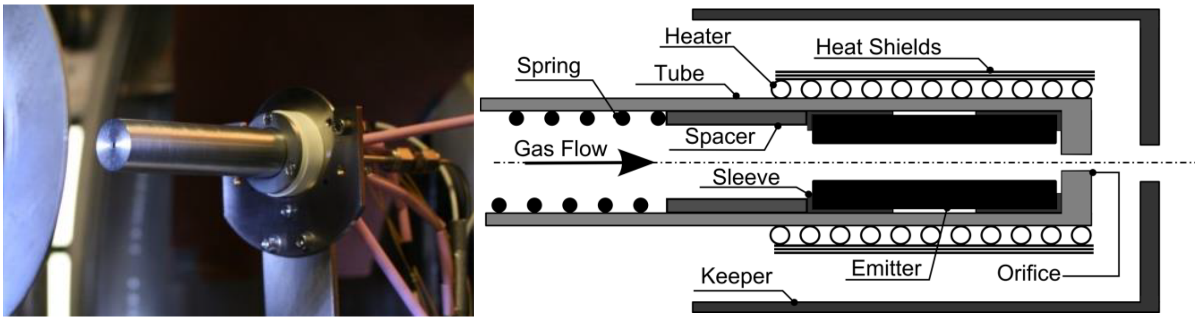

(a) (b)

Figure 5.2: (a) SITAEL HC20h cathode during a stand-alone test campaign. (b) Hollow cathode general schematic. (Source: Ref. [105])

Table 5.1: SITAEL HT5k (DM3) and HC20h specifications for Xe operation. (Reproduced with permission of SITAEL)

HT5k (DM3)		HC20h	
Mass flow rate	5-20 mg/s	Mass flow rate	0.5-2 mg/s
Discharge power	2.5-7.5 kW	Heater power	<180 W
Voltage	250-500 V	Ignition voltage	<200 V
Thrust	120-350 mN	Emission current	8-20 A
Specific impulse	1600-2400 s	Keeper current	0-5 A
Mass	12 kg	Heater current	<10 A
Lifetime	>15 MN s	Lifetime	>10 000 h
		Number of ignitions	>8000

5.1.3. Test Facility

The test is performed in SITAEL main vacuum chamber: IV10 (Figure 5.3). This is the largest one currently available in Europe for testing of electric propulsion devices and among the largest in the world. Its dimensions and technical specifications are presented in Table 5.2. With respect to smaller chambers, such massive size alone generally allows to maintain a lower density of background neutral atoms produced upon collisions between the thruster plume and the chamber walls, thus resulting better representative of the real space environment. Moreover, to reduce further these back-sputtering effects, the chamber is internally lined up with Grafoil (purity > 99.9%). Additionally, a liquid N_2 cooled bi-conical beam target is placed on the opening cap of the chamber, in front of the thruster, so as to reduce even further back-sputtering contamination of the device. Indeed, this target diverts the impacting particles toward the chamber walls rather than reflecting them back to the thruster. There are located 8 He-cooled copper cold panels with a Xe pumping speed of 60 000 L/s each, which add to the 2 chamber turbomolecular pumps (2000 L/s each) and 2 cryogenic pumps (6000 L/s each). Overall, all these characteristics allows this facility to maintain (with xenon HETs) an operating pressure $<3 \times 10^{-5}$ mbar and to achieve an ultimate pressure $<8 \times 10^{-8}$ mbar.

Figure 5.3: SITAEL IV10 vacuum chamber. (Source: Ref [111])

Table 5.2: SITAEL IV10 vacuum chamber dimensions and specifications. (Reproduced with permission of SITAEL)

Dimensions		Specifications	
Inner diameter	5.74 m	Total leak rate	$<1 \times 10^{-4}$ mbar · L/s
Inner free diameter	5.40 m	Ultimate vacuum	$<8 \times 10^{-8}$ mbar
Length of cylindrical section	6.00 m	Operating vacuum	$<3 \times 10^{-5}$ mbar
Vacuum vessel total length	9.40 m	Pump-down time	72 h
Free length for beam expansion	6.90 m		
Internal free volume	$>160\,\mathrm{m}^3$		

5.2. Test Equipment: Diagnostics

In this section are discussed all the diagnostic devices employed in this campaign together with the relative data acquisition and analysis approaches, tailored on the particular multispecies plasma investigated. Great emphasis is posed on the cross-interactions between different probe outputs, in order to reconstruct at best the plasma characteristics (e.g. density and velocity distributions in the plume and potential, temperature and species densities in the channel).

5.2.1. Thrust Stand

For the test is employed a single axis thrust balance characterized by a double-pendulum configuration. This allows to sustain the thruster weight while leaving a free degree of freedom in the axial direction. The sensing element is based on high precision load cells measuring the strain on the flexural elements. The balance is mounted on a tilting platform actuated by a stepper motor, which allows to level the system during calibration and before operations. Indeed, during the pump-down procedure the chamber warping determines a slight drift of the assembly, which needs to be compensated. Also, the stand is equipped with an electromagnetic calibrator which exerts a variable force upon request. This is used at the beginning of each test day to calibrate the sensing element.

Regarding its main specifications, this system is able to measure a thrust in the range 5-500 mN with a resolution of 1 mN and a 1% accuracy.

5.2.2. Oscilloscope

During the PFG test the discharge current transient and steady state signals are acquired by means of an oscilloscope. The device used is a Tektronix DPO 4104 with 1 GHz bandwidth, a maximum sample rate of 5 GS/s and a memory depth of 20 MB. In this campaign the discharge current is sampled at 10 MHz.

5.2.3. Faraday Probes

A Faraday probe is a plasma diagnostic device used to measure the ion current density in the plume of EP devices. In its simplest configuration it is composed of a planar metallic disk collecting the impinging ions. This is called collector and it is biased to a sufficiently negative potential to repel electrons (which could alter the ion charge flux measurement) and reach ion saturation operation. Note that the probe is not selective on the species or charge of the impacting ions and thus measures the total ion current at its plume location.

The simplest probe design just described is referred to as nude Faraday probe and has several shortcomings. These are now briefly illustrated to also introduce the more advanced probe designs addressing them.

The first and major problem is the probe measurement dependence to facility effects, resulting from operating the thruster in a vacuum chamber of particular size and background pressure. These are driven by CEX collisions between the fast ions generated in the thruster and the random distribution of slow background neutrals, and thus result increasingly strong as the chamber pressure is higher. Also, the background neutrals can be ingested in the thruster, there ionized and then accelerated as another population of low-energy ions. Because the probe cannot distinguish between fast ions produced in the discharge chamber and slow ones generated by these processes, artificially high current densities are measured at high half-divergence angles ($> 60°$) in the plume [112]. In order to solve this problem, it has been developed a new design called Magnetically Filtered Faraday Probe (MFFP), which implements a magnetic field in front of the collector to filter away these ions. However, by simply eliminating all low-energy ions this solution is not particularly accurate in reflecting on-orbit plume conditions.

Another problem is represented by stray ions impacting the collector plate laterally. To prevent them from contributing to the measured current, the collector is generally inserted in an external metallic shield.

A third shortcoming of nude Faraday probes is the influence of sheath edge effects at the collector plate borders. These can increase its effective area, thus leading to incorrect measurements. However, by adding guard rings at the side of the plate or an annular disk (called collimator) or even a grid in front of it, it is possible to maintain a uniform planar sheath on the negatively biased collector.

Finally, depending on the materials used for its components, the current measurement can be negatively affected by SEE. Note that, the electron emission interesting the internal surfaces of these devices is from ion bombardment and not from electron impacts as it is the case of thruster channel walls. This phenomenon, which leads to SEE yields much lower than the electron-impact SEE, is generally neglected in the thruster [53]. However, the almost complete absence of primary electrons impinging on the collector disk makes it more relevant in Faraday probes. Without going into great details, which would go beyond the scope of this work, ion-impact SEE in molybdenum/tungsten (the metals generally used) are associated with an Auger-type electron emission, which interests the inner shells of the material particles [113, 114]. This quite complex mechanism is different from electron-impact SEE happening on insulators such as $BNSiO_2$ and it is discussed in detail in Ref. [115]. Therefore, unless otherwise stated, SEE in Faraday probes always refers to ion impacts only.

As an additional remark note that, although Faraday probes are invasive diagnostics, their size is both much larger than local Debye lengths and smaller than the local electron mean free path. As such, the probe disturbance to the plasma is generally low [112].

SITAEL Design

The design used at SITAEL includes collector, external shield and a frontal grid. The purpose of the grid, apart from promoting the formation of a uniform planar sheath on the collector, is that of filtering out plasma electrostatic disturbances and impinging electrons, and it is achieved by left it floating or slightly negatively biased. A schematic of the device, also including the electric circuitry placed outside the chamber, is shown in Figure 5.4. Note that both collector and grid are biased to a potential of -20 V, which is typical for such devices [116].

Regarding the material employed, all three components are made of molybdenum, which is characterized by a very low emissivity, so as to reduce secondary electron contamination.

Installation and Measurement

The IV10 vacuum chamber is equipped with a semicircular movable rack on which are installed 18 Faraday probes. Their disposition on the rack is defined by the angle φ, where at $\varphi = 0°$ stands the central probe and the other distribute between $-90° < \varphi < 90°$ (see Figure 5.5). All probes are at the same distance $R = 1\,\text{m}$ from the thruster center. As the rack moves from

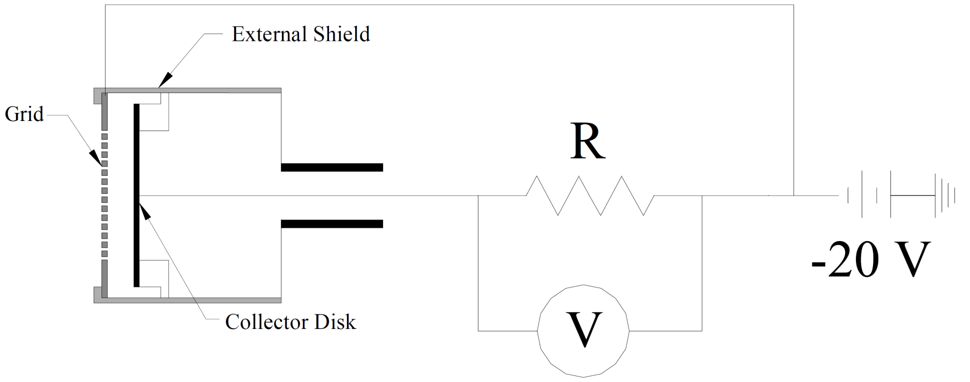

Figure 5.4: SITAEL Faraday probe schematic and electrical circuit. (Modified from source: Ref. [112])

its rest position (the one in Figure 5.5) back and forth through the plume, the probes span with an angle $-90° < \theta < 90°$, where at $\theta = 0°$ the rack is aligned with the vertical plane containing the thruster centerline.

Regarding the ion current measurement, this is obtained by reading the voltage drop V across the resistor R (see Figure 5.4). Note that, depending on their location on the rack, the probes are connected to different resistors R. This is done to keep the voltage V within the voltmeter measurement range, regardless of the lower local current expected at higher divergence angles. Then, the local total ion current density $j(\theta, \varphi)$ results

$$j(\theta, \varphi) = \sum_i \Gamma_i Z_i e = \frac{I}{A_{c,eff}} \tag{5.1}$$

where Γ_i and Z_i are respectively the flux and charge number of the i-th ion species, I is the probe current and $A_{c,eff}$ is its effective collector area.

Note that the quantity $A_{c,eff}$ is an empirical value defined during the probe calibration with a known discharge of xenon. From a theoretical point of view, this term takes into account all the uncertainties related to the probe design and internal particle interactions and can be written as

$$A_{c,eff} = T_g \; \kappa_P \; \kappa_{SEE} \; (A_c + \kappa_G) \tag{5.2}$$

where T_g is the grid transmissivity, κ_P and κ_{SEE} are factors respectively accounting for internal particle interactions and SEE, A_c is the collector geometric area and κ_G is a factor accounting for ions collected at the collector sidewalls. Apart from A_c, which is measurable, the other contributions cannot be generally distinguished or predicted accurately. While this is not a problem for the xenon case, a nitrogen/oxygen plasma can potentially lead to significant variations in these parameters.

In particular, it is expected a different plasma interaction with the probe internal surfaces, thus leading to variations in κ_{SEE}. Note that, in general, despite the low electron emissivity of the probe material, ion impacts on the molybdenum collector can still produce secondary electrons which, accelerating away from the plate, artificially increase the measured current. Following the definition used by Brown et al. [116], κ_{SEE} can be defined as

$$\kappa_{SEE} = \frac{1}{1 + \sum_i \frac{\Omega_i \gamma_i}{Z_i}} \tag{5.3}$$

where Ω_i and γ_i are respectively the ion current fraction and the ion-impact SEE yield for the i-th ion species. The former is generally unknown in this campaign, as the $E \times B$ probe could

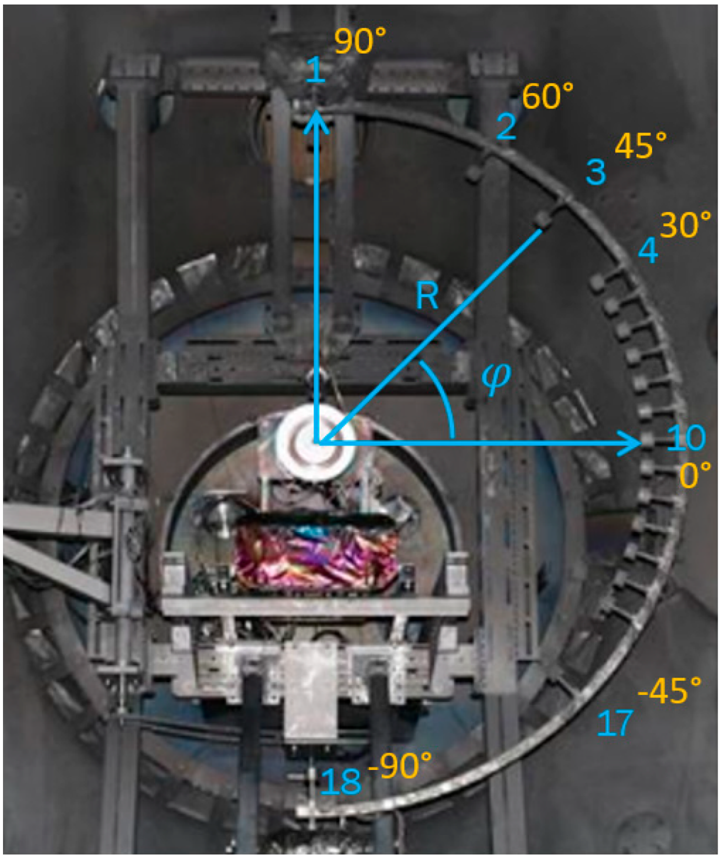

Figure 5.5: The Faraday probes arrangement on the movable rack (in rest position) inside the IV10 chamber. (Source: Ref. [117])

not be installed (see Subsection 5.2.6) and the only remaining species-selective diagnostics employed are the spectrometers, located at the thruster exit though. Therefore, a certain experimentally determined value of Ω_i can only be obtained there, while the plume remains excluded.

As γ_i is concerned, this parameter can be estimated from the experimental results of Mahadevan et al. [114], which measured the SEE yield of molybdenum referring to impacts of atmospheric gases ions. In particular, for the four ion species identified in Section 3.2 (i.e. N^+, N_2^+, O_2 and O_2^+), these are reported in Figure 5.6. Note that, contrarily to the case of noble gases [113], these yields experience wide variations for different bombarding ion kinetic energies. Therefore, it results difficult to provide some representative average values, as done instead by Brown et al. [116] for xenon. To avoid this issue it would be necessary to resolve the energy distributions of each ion species by means of the RPA measurements, for instance. However, as discussed in Subsection 5.2.4, also these would require the local ion density ratios. In any case, by assuming that the corrected κ_{SEE} can be ultimately computed, it would be then possible to correct the effective probe area $A_{c,eff}$ with a simple scaling.

In general, what can be immediately noticed by comparing Figure 5.6 and the representative γ_i reported by Brown et al. for xenon is that for these atmospheric gases the yields are all significantly higher, thus producing lower κ_{SEE} regardless of Ω_i. As a consequence, the uncorrected ion current density measured is expected to underestimate the real one.

Once the local total current density $j(\theta, \varphi)$ is determined, it is possible to derive by integration the ion beam current I_{beam} and the half-divergence angle λ. In particular, by combining the measurements of all the Faraday probes through a complete horizontal sweep, the former

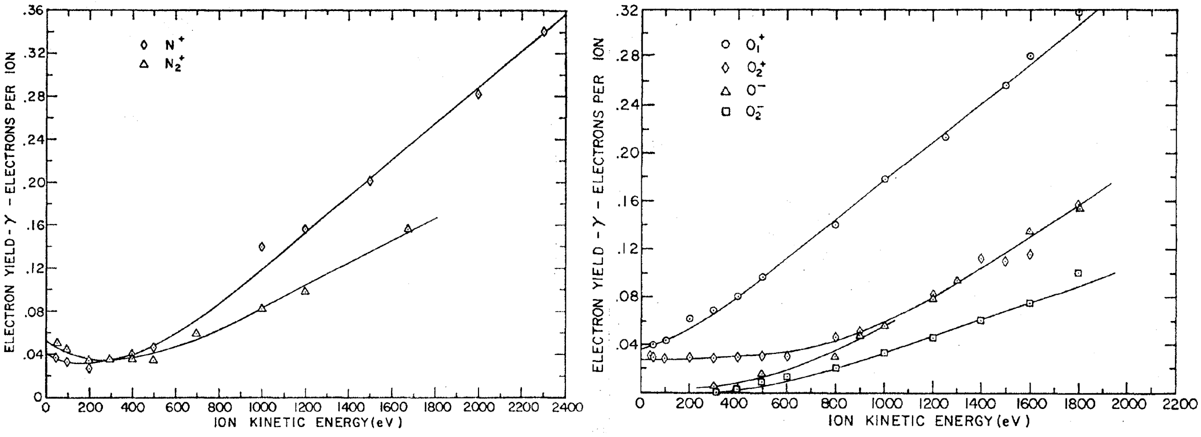

(a) (b)

Figure 5.6: SEE yields γ_i of clean molybdenum for impacts of (a) nitrogen ions and (b) oxygen ions. (Source: Ref. [114])

results

$$I_{beam} = R^2 \int_{-\frac{\pi}{2}}^{\frac{\pi}{2}} \int_{-\frac{\pi}{2}}^{\frac{\pi}{2}} j(\theta,\varphi)\frac{\kappa_D}{\kappa_A}\cos^2(\varphi)\frac{l_D}{l_A}d\theta d\varphi \tag{5.4}$$

Here κ_D and κ_A are respectively the distance and angular correction factors on the θ-plane, introduced to account for the systematic error resulting from the hemispheric reference system. Similarly, l_D and l_A are the correction factors accounting for the position of each probe on the φ-plane. These geometric corrections are necessary since the measurements are taken with respect to a single point at the thruster center, rather than considering its real geometry. In particular, these approximate the ion flow as it would be coming from two point sources (for each angular coordinate) located at the channel centerlines (see Figure 5.7). In this way the effect of the annular channel geometry on the plume current distribution can be better taken into account. While this correction still represents an approximation, it manages to reduce the measurement error [116].

The problem symmetry with respect to both angular coordinates allows to define the geometric correction factors relative to θ- and φ- planes in the same way. In particular, referring to Figure 5.7, the distance correction factors κ_D and l_D result

$$\kappa_D = \left[\frac{1}{2}\left(\frac{R_N(\theta)}{R}+\frac{R_F(\theta)}{R}\right)\right]^2 \qquad l_D = \left[\frac{1}{2}\left(\frac{R_N(\varphi)}{R}+\frac{R_F(\varphi)}{R}\right)\right]^2 \tag{5.5}$$

where, relatively to a generic angle $\delta = [\theta, \varphi]$,

$$\frac{R_{N,F}(\delta)}{R} = \sqrt{\cos^2(\delta) + \left(\sin(\delta) \mp \frac{D_T - w}{2R}\right)^2} \tag{5.6}$$

Regarding the angular correction factors κ_A and l_A, these result

$$\kappa_A = \cos\left(\frac{\alpha_N+\alpha_F}{2}\right) \qquad l_A = \cos\left(\frac{\beta_N+\beta_F}{2}\right) \tag{5.7}$$

where

$$[\alpha_{N,F}, \beta_{N,F}] = \pm\left[\delta - \arctan\left(\frac{\sin(\delta) \mp \dfrac{D_T - w}{2R}}{\cos(\delta)}\right)\right] \tag{5.8}$$

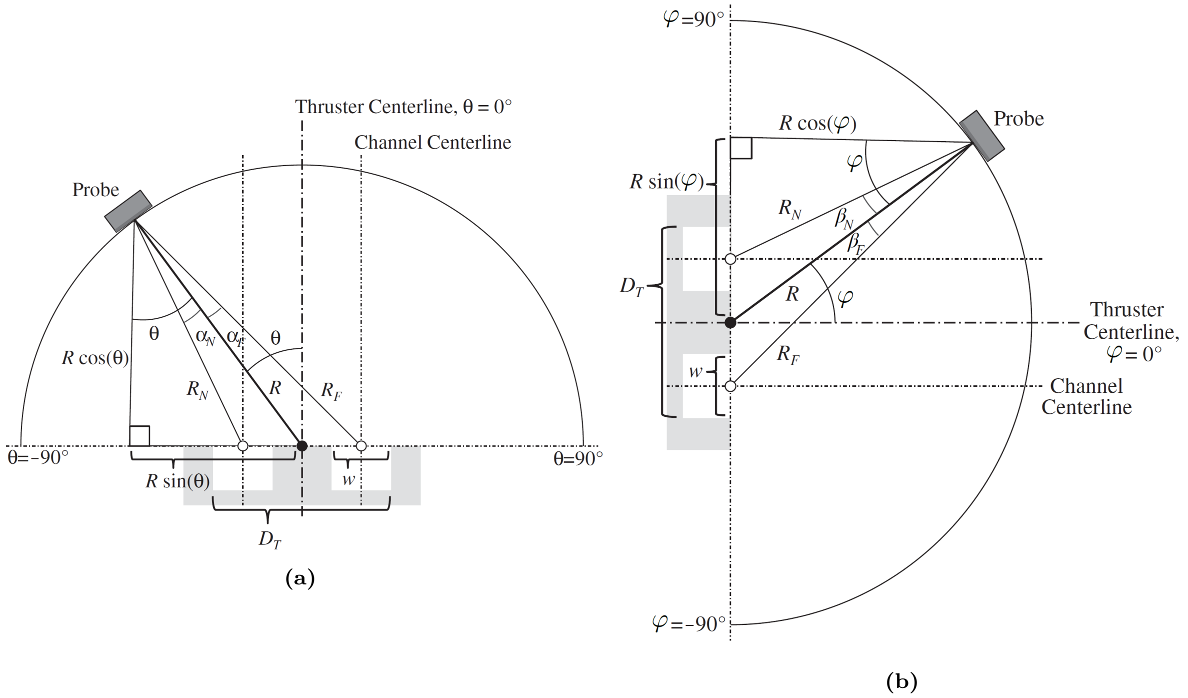

(a)

(b)

Figure 5.7: Schematics of the two-point source coordinate system used for Faraday probe measurements relative to the (a) θ-plane and (b) φ-plane. (Modified from source: Ref. [116])

Finally, the half-diverge angle λ is obtained from

$$\lambda = \arccos\left(\frac{I_{axial}}{I_{beam}}\right) \tag{5.9}$$

where I_{axial} is the axial component of the beam current, i.e.

$$I_{axial} = R^2 \int_{-\frac{\pi}{2}}^{\frac{\pi}{2}} \int_{-\frac{\pi}{2}}^{\frac{\pi}{2}} j(\theta,\varphi)\frac{\kappa_D}{\kappa_A}\cos(\alpha_A)\frac{l_D}{l_A}\cos(\beta_A)\cos^2(\varphi)d\theta d\varphi \tag{5.10}$$

Here α_A and β_A are angular factors accounting for the projections on the channel centerlines and are defined as

$$[\alpha_A, \beta_A] = \begin{cases} \delta - [\alpha_N, \beta_N] & \text{for} \quad \arcsin\left(\dfrac{D_T - w}{2R}\right) \leq |\delta| \leq 90^\circ \\ 0 & \text{for} \quad 0^\circ \leq |\delta| \leq \arcsin\left(\dfrac{D_T - w}{2R}\right) \end{cases} \tag{5.11}$$

5.2.4. Retarding Potential Analyzer (RPA) Probe

A Retarding Potential Analyzer (RPA) probe is a plasma diagnostic device used to measure the ion energy distribution in the plume. Its design is very similar to a gridded Faraday probe, with the only difference that between the front grid and the collector are placed other biased grids with the function of particle filters. In particular, the probe generally filters out plume electrons (as the gridded Faraday probe), ions with energies lower than a given threshold and secondary emitted electrons. Consequently, only sufficiently energetic ions can reach the collector. By sweeping the positive potential of the ion-filtering grid (IRE) the threshold is varied and the entire ion energy distribution can be sensed. As for Faraday probes, also the RPA is not selective on the ion species or charge.

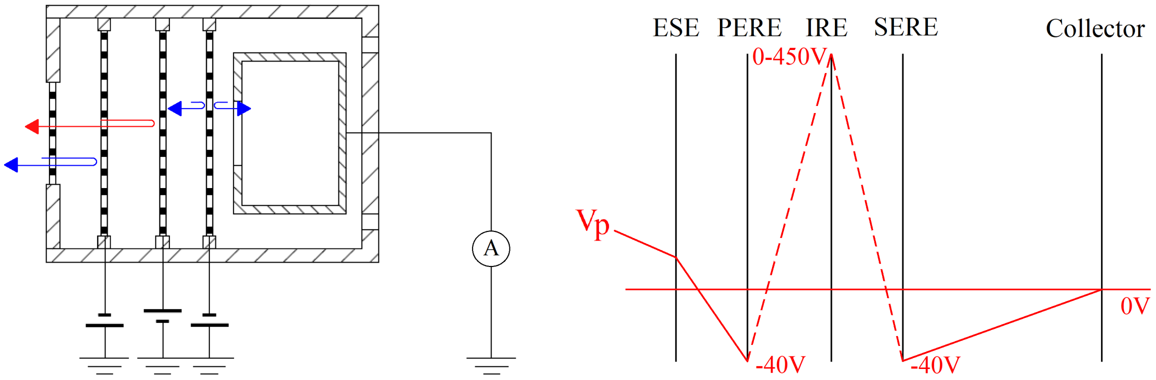

Figure 5.8: SITAEL RPA probe schematic (left) and voltage scheme (right).

The functioning of this device overcomes all the limitations of common Faraday probes without introducing additional ones. Indeed, the grids prevent secondary electrons from leaving the collector and allow to distinguish fast beam ions from the slow ones produced by CEX collisions or background neutral ingestion. Also, having dimensions comparable to that of Faraday probes, the plasma disturbance results low as well.

However, the RPA can be also used as a Faraday probe by short-circuiting the electron-repelling grids (i.e. PERE and SERE, see Figure 5.8) and collector and by leaving the IRE grid floating. In this way the probe can collect the total ion current density, in contrast to the RPA mode in which only a fraction of the current is allowed to reach the collector.

SITAEL design

The RPA probe developed by SITAEL is composed of four grids (see Figure 5.8), which are:

- **External Shielding Electrode (ESE)**
  This grid is generally left floating or slightly negatively biased with respect to the surrounding plasma and it acts as a filter for plasma electrostatic disturbances, which could interfere with current collection. In this design it is left floating.
- **Primary Electron Retarding Electrode (PERE)**
  This grid is negatively biased ($-40\,\text{V}$) to repel primary electrons from the plume flow.
- **Ion Retarding Electrode (IRE)**
  The positive potential sweep on this grid allows to filter ions based on their energy. Only ions which have been accelerated in the channel by a voltage greater than that of this grid can pass through it and reach the collector. In this design the voltage is swept in range 0-450 V.
- **Secondary Electron Suppressor Electrode (SERE)**
  This last grid is adjacent to the collector and it is negatively biased with respect to it so as to suppress SEE from its surface. In this design it is biased at $-40\,\text{V}$ as the PERE, while the collector is grounded.

Regarding the material choice, both grids and collector are made of molybdenum, which is characterized by a very low emissivity so as to reduce secondary electron contamination.

Installation and Measurement

A single RPA probe is installed on the IV10 movable rack next to the central Faraday probe (Figure 5.9). However, the measurement is only done at a single location (i.e. generally on

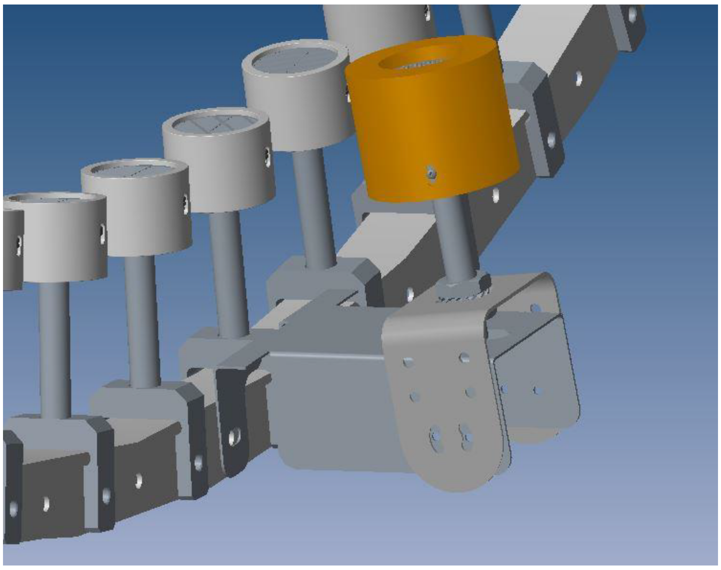

Figure 5.9: Integration of the RPA probe (orange) on the movable rack inside the IV10 chamber. In grey are shown some of the Faraday probes. The one adjacent to the RPA is the central one, at $\varphi = 0$. (Reproduced with permission of SITAEL)

the thruster centerline) as it involves a large voltage sweep, which is not compatible with continuous operations as the rack moves.

The data obtained from this diagnostic device are in the form of an I-V curve, where the collected current is measured as the IRE voltage V_{grid} is swept. For a single ion species i in a one-dimensional case, by indicating as $u_{i,min}$ the minimum ion velocity necessary to overcome the IRE grid, the collected current may be defined [118, 119]

$$I_i(u_i) = q_i A_{c,eff} \int_{u_{i,min}}^{\infty} u_i f(u_i) du_i \tag{5.12}$$

where $A_{c,eff}$ is the effective collector area[2] (see Eq. 5.2) and $f(u_i)$ is the ion velocity distribution function (IVDF) at the probe entrance grid. This distribution function is correlated with the ion energy distribution function (IEDF) $g(E)$ by the definition

$$\int_{0}^{\infty} f(u_i) du_i = n_i \tag{5.13}$$

which implies

$$f(u_i) du_i = dn_i = g(E) dE \tag{5.14}$$

For the case under study, it is assumed that the ion energy E completely results from an electrostatic acceleration in the thruster channel, thus allowing to express the IEDF as $g(V_{acc})$, where V_{acc} is the ion acceleration voltage for species i. Since

$$dV_{acc} = d\left(\frac{1}{2}\frac{m_i}{q_i}u_i^2\right) = \frac{m_i}{q_i} u_i du_i \tag{5.15}$$

it results

$$f(u_i) = \frac{m_i}{q_i} u_i g(V_{acc}) \tag{5.16}$$

---

[2] Note that differently from the Faraday probes, the SITAEL RPA probe used is a newly designed device and as such it has never been calibrated or tested with xenon. Consequently, it is not possible to follow the same $A_{c,eff}$ scaling procedure proposed for them in Subsection 5.2.3.

Consequently, Eq. 5.12 can be then rewritten as

$$I_i(V_{grid}) = \frac{q_i^2 A_{c,eff}}{m_i} \int_{V_{grid}}^{+\infty} f\left(\sqrt{\frac{2q_i V_{acc}}{m_i}}\right) dV_{acc} \tag{5.17}$$

or alternatively

$$I_i(V_{grid}) = q_i A_{c,eff} \sqrt{\frac{2q_i}{m_i}} \int_{V_{grid}}^{+\infty} \sqrt{V_{acc}}\; g(V_{acc}) dV_{acc} \tag{5.18}$$

Finally differentiation yields both $f(u_i)$ and $g(V_{acc})$ as a function of the probe I-V curve derivative, i.e.

$$f(u_i) = -\frac{m_i}{q_i^2 A_{c,eff}} \frac{dI(V_{grid})}{dV_{grid}} \tag{5.19}$$

$$g(V_{acc}) = -\frac{1}{q_i A_{c,eff}} \sqrt{\frac{m_i}{2q_i V_{grid}}} \frac{dI(V_{grid})}{dV_{grid}} \tag{5.20}$$

It is important to note that both these distribution functions refer to the plasma at the probe entrance only. Indeed, the presence of a grid determines the formation of a sheath accelerating the ions. Therefore, the ion velocity u_i should be more precisely written as

$$u_i = \sqrt{u_{i,bulk} + \frac{2q_i \phi_w}{m_i}} \tag{5.21}$$

where ϕ_w is the sheath potential drop in front of the probe grid. In the same way, the equivalent acceleration voltage V_{acc} is given by the sum of the effective potential difference ϕ_{acc} accelerating the ions plus the sheath potential drop ϕ_w, i.e.

$$V_{acc} = \phi_{acc} + \phi_w \tag{5.22}$$

As a consequence, the real distribution functions in the plasma bulk, assuming no collisions and flux conservation through the probe sheath, result

$$f_{bulk}(u_{i,bulk}) = f(u_i) \tag{5.23}$$

$$g_{bulk}(\phi_{acc}) = g(V_{acc}) \tag{5.24}$$

While it becomes easy to determine g_{bulk} in the plasma once the sheath potential drop is known, the same does not hold for f_{bulk}, which results very sensitive to ϕ_w due to the required inversion of Eq. 5.21. Therefore, IVDFs are generally presented as relative distributions rather than absolute.

In the plasma under analysis, the presence of multiple ion species complicates the analysis of the probe measurements. Indeed, unless they are characterized by sufficiently different energies, the overall collected current I_{tot} cannot be decomposed in a sum of individual contributions, i.e.

$$\frac{dI_{tot}(V_{grid})}{dV_{grid}} = \sum_{i=1}^{4} \frac{dI_i(V_{grid})}{dV_{grid}} = -e^2 A_{c,eff}\left(\frac{f_1(u_1)}{m_1} + \frac{f_2(u_2)}{m_2} + \frac{f_3(u_3)}{m_3} + \frac{f_4(u_4)}{m_4}\right) \tag{5.25}$$

$$\begin{aligned} &= -eA_{c,eff}\sqrt{2eV_{grid}}\left(\frac{g_1(V_{acc,1})}{\sqrt{m_1}} + \frac{g_2(V_{acc,2})}{\sqrt{m_2}}\right. \\ &\quad \left. + \frac{g_3(V_{acc,3})}{\sqrt{m_3}} + \frac{g_4(V_{acc,4})}{\sqrt{m_4}}\right) \end{aligned} \tag{5.26}$$

However, dissociation phenomena are expected to produce the majority of atomic ions (i.e. N^+ and O^+) more downstream in the thruster channel with respect to N_2^+ and O_2^+, since a higher overall threshold energy and number of collisions are required. This implies that the two groups of ions may be subjected to potentially different acceleration voltages. In case this difference is not compensated by the diverse ion masses (very similar within each group), in principle it should be possible to distinguish at least two separate peaks on the measured distribution functions. Then, by exploiting the relative ion density ratios at the probe location (in case these are available from a numerical model or from $E \times B$ probe data, for instance) it would be possible to fit the sum of the four individual distributions to the total measured one.

5.2.5. Fast-diving Triple Langmuir Probe

A triple Langmuir probe is a plasma diagnostic device used to instantaneously measure electron temperature T_e, plasma potential V_{gp} and ion density n_i. It is composed of three tiny electrodes which are commonly called *float* (F), *common* (C) and *bias* (B). The F electrode is left floating, while a potential V_{BC} is applied between the other two (see Figure 5.11a). By measuring the current I_{BC} flowing between B and C, the voltage V_{FC} and that between the ground and C (i.e. V_{gC}), it is possible to derive the local plasma parameters. Note that, to obtain accurate measurements with this design, it has to be ensured that plasma properties are homogeneous between the electrodes. To do so, these have to be mounted sufficiently close to each other while still keeping them enough separated to avoid interactions between their respective sheaths.

With respect to the common design with a single electrode, which can only determine the three plasma properties by sweeping the probe voltage, the triple configuration allows instantaneous readings. In this way, by rapidly inserting and extracting the probe (fast-diving technique), such design allows measurements inside the thruster channel. Indeed, the high plasma temperature encountered there poses strong limitations to the probe residence time, not compatible with a voltage sweep.

The capability of instantaneously measuring the plasma makes this probe a very suitable tool for studying plasma oscillations in Hall thrusters. Indeed, even in case of breathing mode (10-30 kHz), which is among the lowest-frequency oscillations generally investigated in these devices, the characteristic time of the probe motion (i.e. $\mathcal{O}(1)$ Hz) results orders of magnitude longer than that of the oscillations [120]. This allows to capture them locally, undisturbed from the motion of the probe, which can be considered steady in comparison.

The harsh environment encountered, as well as the high accelerations upon insertion and extraction, results in strict constraints on the probe materials and design, which need to be made sufficiently durable and resistant. At the same time, this device is a highly intrusive diagnostics, which is known to significantly perturb the plasma, especially inside the channel [120]. Therefore, developing this instrument requires a complex trade-off between size, geometry, material characteristics (e.g. ablation) and induced plasma perturbation. Generally, a smaller probe results less invasive at the expenses, however, of a higher manufacturing complexity and a lower electrode durability.

SITAEL Design

The triple Langmuir probe used at SITAEL [10, 120, 121] (shown in Figure 5.11b) is composed of three electrodes obtained from 75% tungsten and 25% rhenium alloy wires with a diameter of 0.178 mm. These are then covered by a 1/8” alumina insulating tube (characterized by a high dielectric strength and melting temperature) which leaves exposed the three electrodes of length 2.6 mm. As this dimension is much greater than the electrode diameter, tip effects can be neglected in the sheath theory governing current collection. Moreover, these are placed at a minimum distance of 2 mm, thus minimizing their mutual interactions. Indeed, this is much longer than the typical sheath length expected, which is in the order of the Debye length (see

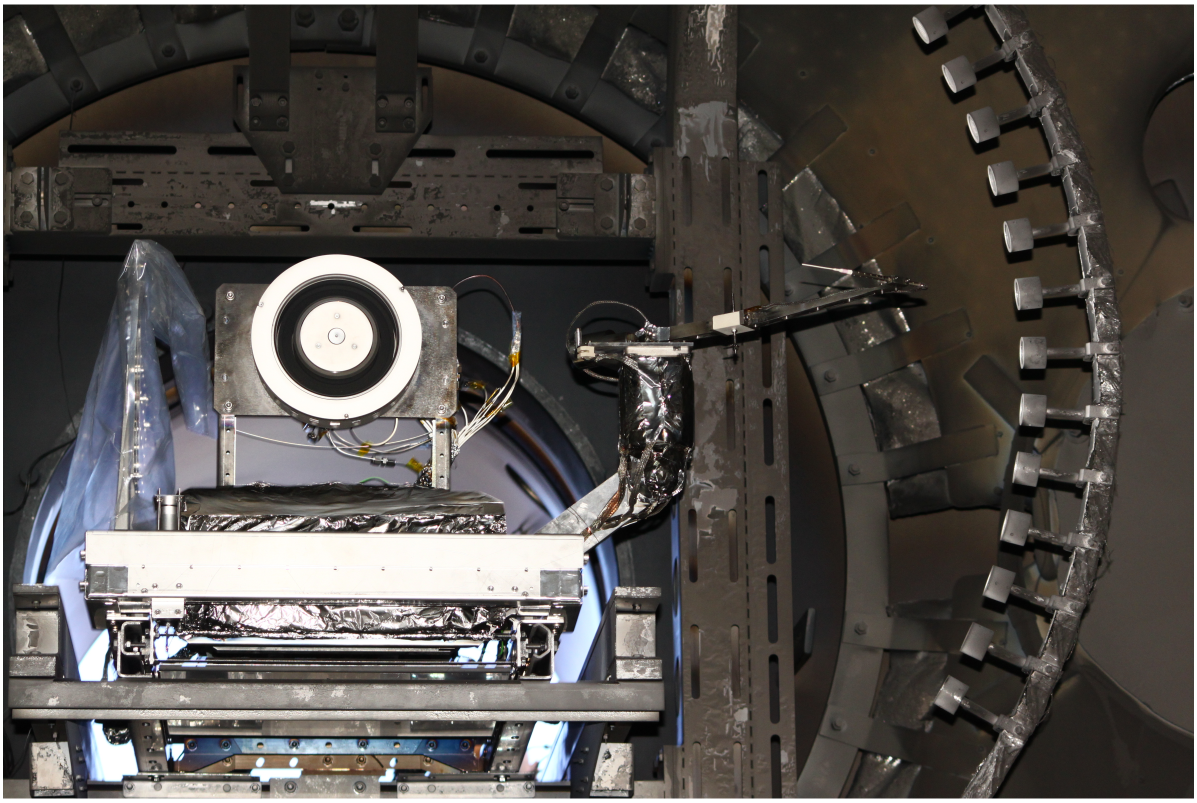

Figure 5.10: Experimental setup showing the PFG, the spectrometer tube lens on the linear rail (just below the thruster), the triple Langmuir probe mounted on the robotic arm and part of the movable rack with the central group of Faraday probes. Note that, once the picture was taken, the RPA probe had not been integrated on the rack yet. (Reproduced with permission of SITAEL)

Eq. 2.20).

Regarding the applied potential V_{BC}, this is fixed at 36 V, which brings V_C above the floating potential V_F and V_B below (see Figure 5.11a).

Installation and Measurement

In order to perform the fast-diving, the probe is mounted on a small robotic arm installed next to the thruster, as shown in Figures 5.10 and 5.11c. As this arm rotates, the probe tip follows a circular trajectory with radius 350 mm. However, the acquisition happens only in the final 0.27 rad arc (indicated in blue in Figure 5.11c), which limits the maximum radial deviation from the channel centerline to 9.5 mm in the near-plume and 0.2 mm inside the channel. To minimize the probe exposure to the harsh environment in front of the thruster, while not in use the arm is placed in a rest position far from the plume. In total, the acquisition is performed in 200 ms by using high-speed magnetic actuators to move the arm. The probe position is recorded by an encoder which ensured a spatial resolution of 0.3 mm.

From the probe configuration in Figure 5.11a, the currents passing through each electrode readily result

$$\begin{cases} I_C &= I_{BC} \\ I_B &= -I_{BC} \\ I_F &= 0 \end{cases} \tag{5.27}$$

In general, as it is the case of any surface in contact with a plasma, this current is represented

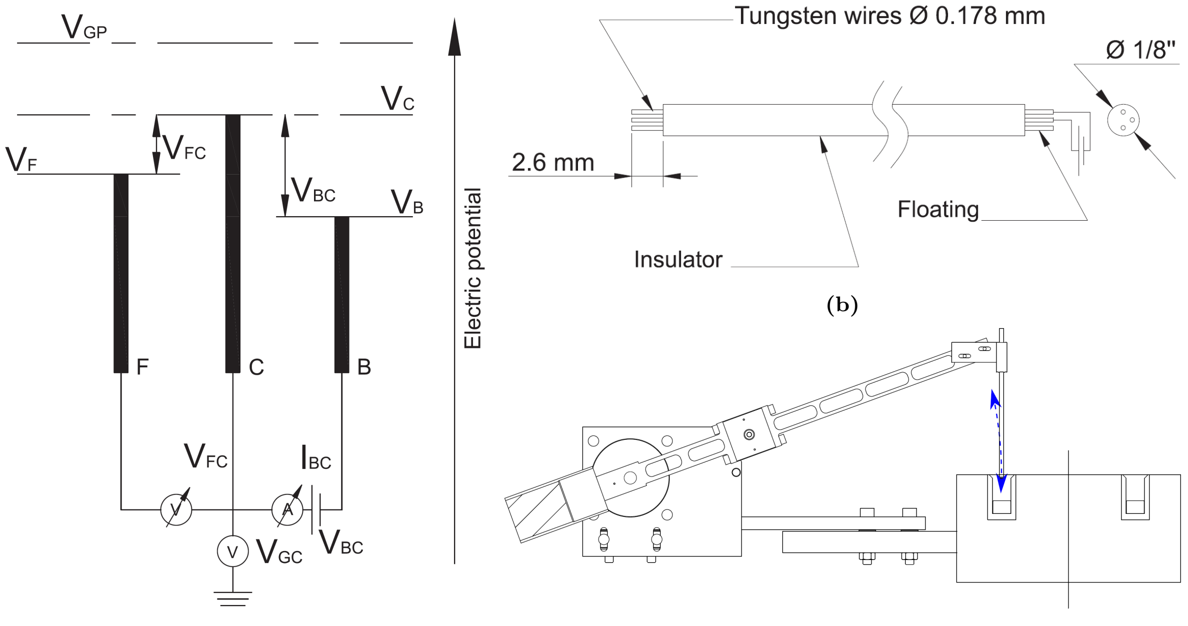

(a) (b) (c)

Figure 5.11: SITAEL triple Langmuir probe schematics: (a) electrical configuration, (b) construction and dimensions, (c) thruster channel insertion system (robotic arm) with indicated in blue the measurement arc. (Source: Ref. [121])

as a sum of an electron contribution and an ion one, i.e.

$$I = I_e - \sum_{i=1}^{4} I_i \tag{5.28}$$

Note that in the following this definition is restricted to the case in which the electrode (i.e. a single Langmuir probe) works in the ion saturation region (or a least the transition region) of the probe I-V_{pr} characteristics (Figure 5.12). Indeed, as in a triple Langmuir probe it is not necessary to sweep the electrodes voltages V_{pr} to determine the plasma properties, these are kept constant at values below the plasma potential V_{gp} (see Figure 5.11a), where their I-V_{pr} characteristics are less dependent on geometry.

Consequently, by defining the normalized probe potential

$$\chi = -\frac{e\left(V_{gp} - V_{pr}\right)}{k_B T_e} \tag{5.29}$$

which is thus always negative, the electron current contribution can be written as

$$I_e(V_{pr}, T_e, n_e, V_{gp}) = I_{e,th}\exp\left(\chi\right) = e n_e A_{pr}\sqrt{\frac{k_B T_e}{2\pi m_e}}\exp\left(-\frac{e\left(V_{gp} - V_{pr}\right)}{k_B T_e}\right) \tag{5.30}$$

This expression, although approximate, is generally used in sheath theory since provides a good representativeness.

On the other hand, depending on the probe geometry and secondary sheath phenomena eventually addressed, the ion current I_i may assume different forms. The simplest considers the ions arriving at the sheath edge with their unmodified Bohm velocities following the thin sheath theory, which assumes an infinite, steady and collisionless planar sheath. This is precisely the

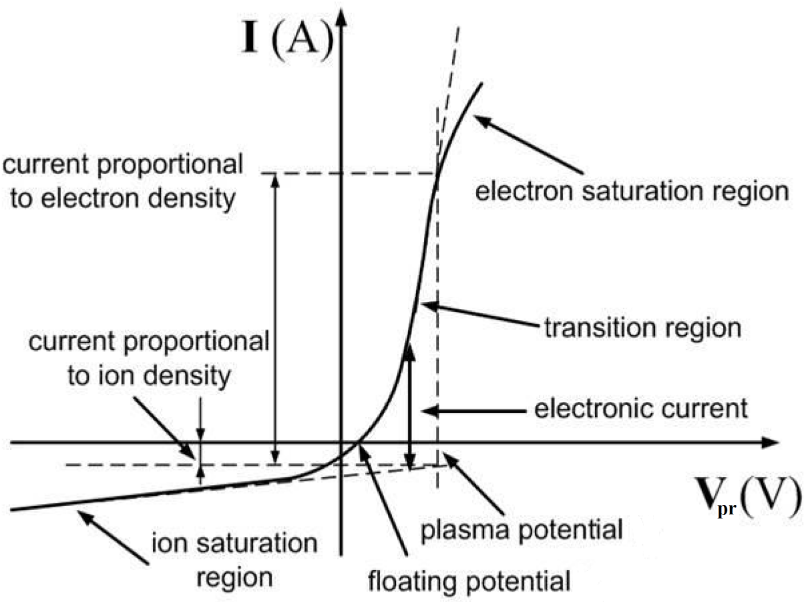

Figure 5.12: Typical single Langmuir probe I-V_{pr} characteristics. The curve steepness in both saturation regions (especially the electron one) is highly dependent on the probe geometry. (Modified from source: Ref. [122])

theory used in the previous chapters. As a consequence, Eq. 5.28 becomes

$$\begin{aligned} I_{TS}(V_{pr}, T_e, n_i, V_{gp}) = \sum_{i=1}^{4} eA_{pr}n_i \Bigg[&\sqrt{\frac{k_B T_e}{2\pi m_e}} \exp\left(-\frac{e\,(V_{gp}-V_{pr})}{k_B T_e}\right) \\ &- \exp\left(-\frac{1}{2}\right) \sum_{i=1}^{4} \sqrt{\frac{k_B T_e}{m_i}} \Bigg] \end{aligned} \tag{5.31}$$

A natural evolution of this basic theory would be that of accounting for ion-ion streaming instabilities in the presheath in multispecies plasma. In this way, by including the results obtained with the air presheath/sheath model presented in Section 3.3, it would be possible to draw a better picture of the probe current collection. However, due to time limitations it has not been possible to extend such results also to the analysis of experimental data.

Nevertheless, the major limitation faced in defining a representative sheath model for Langmuir probes is the electrode geometry itself. Indeed, the sheath forming around the tiny cylindrical electrodes cannot be generally approximated by a planar sheath, especially in case of probe radius R_{pr} in the order of the plasma Debye length λ_{De}. This particular problem was addressed by Laframboise [123], which numerically calculated the functional relationship between the normalized probe potential χ and the normalized probe current $f(\chi)$ both in ion and electron saturation regions of a Maxwellian plasma characterized by $R_{pr}/\lambda_{De} = 0 - 100$. Also, Laframboise did this analysis for both cylindrical and spherical Langmuir probes distinguishing between the cases of cold and hot ions, i.e. $T_i/T_e = 0$ and $T_i/T_e = 1$, respectively. In particular, the Laframboise sheath solution takes into account the electrode sheath expansion with temperature, which results particularly useful in plasma regions with high T_e, possibly outside the range of application of the thin sheath theory [121].

While Laframboise only calculated few cases involving R_{pr}/λ_{De}, over the years other authors proposed parametrizations of his results, aiming at a complete functional solution for an arbitrary R_{pr}/λ_{De}. For cylindrical probes, the parametrization proposed by Mausbach [124] is the most accurate and it represents a generalization of that of Peterson and Talbot [125]. In particular, Mausbach's normalized probe current $f(\chi)$ is defined as

$$f(\chi) = a\,(b+\chi)^c \tag{5.32}$$

where a, b and c are the fitting coefficients that depend on R_{pr}/λ_{De} and T_i/T_e. Then, in the ion saturation region, the electrode current results

$$I = I_{e,th}\exp(\chi) - \sum_{i=1}^{4} I_{i,0} f(-\chi) \tag{5.33}$$

where, for cold ions,

$$I_{i,0} = en_i A_{pr} u_i = en_i A_{pr}\sqrt{\frac{k_B T_e}{2\pi m_i}} \tag{5.34}$$

As a consequence, Eq. 5.28 becomes

$$\begin{aligned} I_{MA}(V_{pr}, T_e, n_i, V_{gp}) = \sum_{i=1}^{4} eA_{pr}n_i \Bigg[& \sqrt{\frac{k_B T_e}{2\pi m_e}} \exp\left(-\frac{e\,(V_{gp}-V_{pr})}{k_B T_e}\right) \\ & -\sqrt{\frac{k_B T_e}{2\pi m_i}} a\left(b + \frac{e\,(V_{gp}-V_{pr})}{k_B T_e}\right)^c \Bigg] \end{aligned} \tag{5.35}$$

Having defined the probe current, by knowing V_{BC} and the four normalized ion densities $\bar{n}_i = n_i/n_e$, it is possible to solve the System 5.27 along the probe trajectory using the instantaneous measured quantities I_{BC}, V_{FC} and V_{gC}. In this way, T_e, V_{gp} and the four n_i can be retrieved.

Note that the normalized ion densities are not generally known a priori but they can be experimentally retrieved, only 60 mm downstream the thruster exit, from the spectrometers scans (see Subsection 5.2.7). Although these are expected to vary in the Langmuir probe measurement domain, it is not possible to collect spatial-dependent variations. It is worth mentioning that, due to delays in the experimental campaign, the results of the spectral acquisitions are not yet available at the time of writing. Therefore, in the analysis of the triple Langmuir probe measurements, carried out in Subsection 6.1.1, are employed the ion density ratios retrieved from the calibrated thruster model.

Regardless of the probe physical model adopted, the so obtained results do not consider the uncertainties related to the probe measurements in such a harsh environment as the plasma of a HET. In particular, both the plasma disturbance caused by the probe itself and the plasma inhomogeneities between the electrodes in the high-T_e region (due to the strong azimuthal electron current) make them particularly significant. In order to properly estimate these uncertainties, the probe data may be analyzed by means of a Bayesian approach, as detailed by Saravia et al. [121].

Bayesian Analysis This type of data analysis allows to combine measured data with physical models, so as to perform inferences about the system state while consistently keeping track of the uncertainties. In other words, Bayesian analysis allows to update the knowledge of a certain system in presence of new evidence with the respective uncertainties.

Mathematically, the Bayesian Probability Theory (BPT) associates the "state of knowledge" of one or more parameters to their probability distributions by means of the Bayes theorem[3]

$$p(\mathbf{\Theta}|\mathbf{D}, I) = \frac{p(\mathbf{D}|\mathbf{\Theta}, I)\cdot p(\mathbf{\Theta}|I)}{p(\mathbf{D}|I)} \tag{5.36}$$

---

[3] The symbol $|$ means *given*, so that $p(A|B,C)$ is the distribution probability of A given B and C.

where $\mathbf{\Theta}$ represents the parameters, $\mathbf{D}$ is the measured data and I represents all the previous knowledge about the variables, which consists for instance in their nature or in how they relate to each other. Note that in case of more than one parameter, the knowledge is represented by the joint probability of all them. Specifically, the probability distribution of the parameter of interest can be then obtained by means of the *marginalization rule*, i.e.

$$p(\theta_1|D,I) = \int_{-\infty}^{+\infty} p(\theta_1,\theta_2|D,I)d\theta_2 \tag{5.37}$$

where $\mathbf{\Theta} = \begin{bmatrix}\theta_1 & \theta_2\end{bmatrix}$ are the parameters here. This rule tells that by integrating over the full range of one parameter it is obtained the distribution probability of the remaining ones.

The probability terms appearing in Eq. 5.36 are now briefly defined for the case under study. A more detailed discussion about the principles and applications of this approach to triple Langmuir probes data analysis can be found in the work of Saravia et al. [121].

At first, it is defined the vector $\mathbf{\Theta}$, which contains the investigated plasma properties, i.e.

$$\mathbf{\Theta} = \begin{bmatrix} T_e \\ n_1 \\ n_2 \\ n_3 \\ n_4 \\ V_{gp} \\ \delta V_1 \\ \delta V_2 \end{bmatrix} \tag{5.38}$$

Note that here have been also included two correction parameters δV_1 and δV_2, accounting for mutual interactions between the probe electrodes in presence of plasma inhomogeneities. As for the previous chapters, the density subscripts refer to the four considered ions in order of growing mass.

Regarding the vector $\mathbf{D}$, this contain the average values of the probe measurements at a given time instant, i.e.

$$\mathbf{D} = \begin{bmatrix} I_{BC} \\ V_{FC} \\ V_{gC} \end{bmatrix} \tag{5.39}$$

Then, the term $p(\mathbf{\Theta}|I)$ represents the distribution probability of the parameters given only what it is known a priori about them. This term is also called *previous knowledge* of the parameters and it is the analysis starting point. In order to express the initial lack of knowledge about $\mathbf{\Theta}$, the parameters are only represented by approximate numeric ranges: ≈ 116 to $\approx 1.16 \times 10^6\,\mathrm{K}$ (corresponding the 0.01-100 eV range) for T_e, 10^{15} to $10^{20}\mathrm{m}^{-3}$ for n_i and 25 to 330 V for V_{gp} [120, 121].

Regarding $p(\mathbf{D}|\mathbf{\Theta},I)$, this term represents the probability that measurements $\mathbf{D}$ are true given a certain value of $\mathbf{\Theta}$. This is also called *likelihood* of the measurements and it is expressed through a multivariate Gaussian distribution

$$p(\mathbf{D}|\mathbf{\Theta},I) = \frac{\exp\left(-\frac{1}{2}(\mathbf{D}-\mathbf{Y})^T\Sigma^{-1}(\mathbf{D}-\mathbf{Y})\right)}{\sqrt{(2\pi)^N|\Sigma|}} \tag{5.40}$$

where $N = 8$ in the number of variables, Σ is the covariance matrix of the experimental data and $\mathbf{Y}$ is a simple forward model of the expected $\mathbf{D}$ given a certain $\mathbf{\Theta}$, i.e.

$$\mathbf{Y} = \begin{bmatrix} I_{BC} \\ V_{FC} \\ V_{gC} \end{bmatrix} = f \left(\begin{bmatrix} T_e \\ n_1 \\ n_2 \\ n_3 \\ n_4 \\ V_{gp} \\ \delta V_1 \\ \delta V_2 \end{bmatrix} \right) = f(\mathbf{\Theta}) \tag{5.41}$$

This physical model is given by the aforementioned System 5.27, which results

$$\begin{cases} I_C = I(V_{gC}, T_e, n_i, V_{gp} + \delta V_j) = I_{BC} \\ I_B = I(V_{gC} - V_{BC}, T_e, n_i, V_{gp}) = -I_{BC} \\ I_F = I(V_{gC} - V_{FC}, T_e, n_i, V_{gp} + \delta V_k) = 0 \end{cases} \tag{5.42}$$

Note that, depending on the electrodes arrangement on the probe, the subscripts j and k may take the value 1 in case the corresponding electrode is screened from the azimuthal electron current or 2 otherwise.

The last term on the right-end side of Eq. 5.36 is $p(\mathbf{D}|I)$, which represents the probability of observing the measured data. This is also called *evidence* and for such parameters estimation problems it consists of a simple normalization constant.

Finally, the result of Eq. 5.36 is $p(\mathbf{\Theta}|\mathbf{D}, I)$, or the *posterior knowledge*, which represents the updated knowledge about $\mathbf{\Theta}$ given the measurements $\mathbf{D}$ and the theoretical model I.

The details about the actual solution procedure of this nested inference process go beyond the scope of this work and can be found explained in detail in the work of Saravia et al. [121].

5.2.6. $\mathbf{E} \times \mathbf{B}$ Probe

The $E \times B$ probe, also known as Wien Filter, is a plasma diagnostic device used to measure local ion density and current fractions in the plume of EP devices. It acts as an ion velocity filter which exploits Lorentz's force on the incoming ions to selectively distinguish species. However, as ion velocity is a function of the charge over mass ratio, this device cannot distinguish doubly charged molecular ions (e.g. N_2^{2+}) and singly charged atomic ions (e.g. N^+).

While the installation of this device had been initially envisioned, it was later discarded due to bad material compatibility between some pure iron probe components and atomic oxygen in the plume. The resulting strong oxidation is particularly relevant for the common fixed setup in which the probe is aligned with the channel certerline. To overcome this problem, as an alternative it was also investigated the possibility of installing the probe on the movable rack. However, the excessive weight of the device did not allow to pursue this option, thus definitely excluding it from this experimental campaign.

5.2.7. Spectrometers

In the current experimental campaign are also included three emission spectrometers to determine the relative plume composition from the plasma emission spectrum. Two of these devices are provide by the Von Karman Institute for Fluid Dynamics (VKI) and the last one comes from the Italian National Research Council (CNR). The three devices are placed outside the

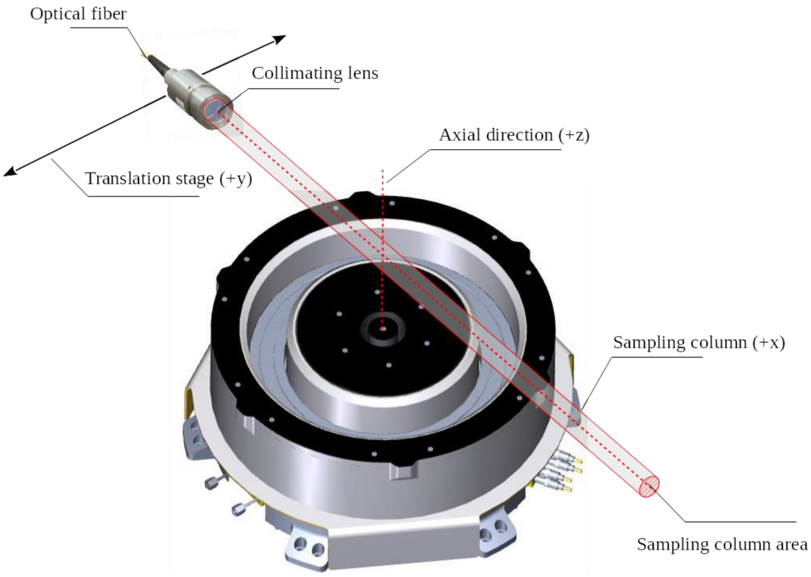

Figure 5.13: Schematic of the spectrometer acquisition system. (Reproduced with permission of SITAEL)

vacuum chamber and interfaced, one by one through an optical fiber, with a tube lens responsible for the spectral acquisition. This tube is driven by an adjustable stepper motor and mounted on a linear rail (see Figure 5.10) that allows scanning the plume perpendicularly to the thruster axis (see Figure 5.13). The rail is placed 60 mm downstream the thruster channel exit.

The spectra collected by these devices allow to compute the absolute and relative densities of the plasma species (excited states included) at the acquisition plane, thus providing a unique and fundamental information for the numerical and experimental characterization of this air plasma. In particular, by recalling the discussion of Subsection 5.2.5 about the triple Langmuir probe, the knowledge of these densities allows to translate the probe measurements in potential, density and electron temperature profiles. Moreover, it is worth mentioning that accurate spectral readings may also indicate the local electron temperature, without relying on the triple Langmuir probe.

In order to determine the plasma species densities from an emission spectrum, is necessary a collisional-radiative model of the mixture analysed. This kinetic model allows to identify the radiative transitions useful for the reconstruction of the plasma parameters. While for xenon such transitions range approximately between wavelengths of 750 nm and 1000 nm, the more complex nitrogen/oxygen plasma under study would require a much wider spectral range, thus negatively affecting the spectral resolution. Indeed, the equipment used for the spectral acquisition (i.e. the collimating lens over the rail) requires all spectral lines to be acquired at the same time to allow continuous characterization of the thruster plume. For this reason, an optimal spectral window between 200 nm and 1150 nm has been selected to balance spectral resolution and range.

5.2.8. Summary

To conclude the discussion about plasma diagnostics, Table 5.3 reports the main features of those employed. In particular, are highlighted the plasma quantities required by each one for a complete analysis of the multispecies air plasma under study.

Table 5.3: Summary of the plasma diagnostics employed in the PFG experimental campaign and their main features.

Diagnostics	Measured quantities	Location	Required quantities	Plasma perturbation
Faraday probes	• Current density • Beam current • Plume divergence	Rack	• Ion density ratios • Ion energies	Low
RPA	• EVDF • IVDF	Rack	• Ion density ratios	Low
Fast-diving triple Langmuir probe	• Electron temperature • Plasma potential • Ion densities	Near-plume/ channel	• Ion density ratios	High
Spectrometers	• Electron density • Ion densities • Electron temperature • Density of excited states	Near-plume (60 mm downstream channel exit)	None	None

5.3. Test Plan

The test activities can be divided in five main phases:

1. **Test Unit (TU) pre-test verifications and outgassing with Xe**
   In this phase it is verified the electrical setup and it is fired the thruster with Xe to accelerate material outgassing, which is the gradual release of trapped, frozen or absorbed gas or vapour from any material placed in vacuum. This mainly concerns the thruster ceramics and the possible moisture that these may have absorbed at atmospheric condition is storage. By heating the TU (i.e. firing), this process is speeded up, thus preventing any chemical contamination from affecting the experimental campaign.

Topic	Description
Test items	• HT5k Hall thruster • HC20h hollow cathode
Test type	Electrical setup verification and subsequent ignition and outgassing with Xe: • Anode line: Xe • Cathode line: Xe
Test objective	• Verify electrical setup. • Outgassing of the TU with Xe.
Test duration	1 day
Pass/Fail criteria	• TU electrical setup is compliant with the reference configuration. • TU outgassing is completed according to the applicable procedures.

2. **Diagnostic validation with Xe**
   During this phase, all the diagnostics are tested firing the TU with Xe in order to confirm their nominal behaviour and eventually adjust calibration.

Topic	Description
Test items	• HT5k Hall thruster • HC20h hollow cathode
Test type	Diagnostic validation with Xe: • Anode line: Xe • Cathode line: Xe
Test objective	• Verify nominal diagnostics functioning. • Calibrate diagnostics, if needed.
Test duration	3 days
Pass/Fail criteria	All the diagnostics employed operate nominally and data are correctly collected.

3. **Reference Performance Test (RPT) with Xe**
   During this phase, it is tested the PFG with Xe before the characterization with atmospheric propellant in order to confirm its nominal behaviour. To account for measurement errors, three acquisitions are performed with each plasma diagnostics.

Topic	Description
Test items	• HT5k Hall thruster • HC20h hollow cathode
Test type	RPT with Xe: • Anode line: Xe • Cathode line: Xe
Test objective	Verify the PFG reference performance with Xe **before** the characterization with atmospheric propellant.
Test duration	1 day
Pass/Fail criteria	• The thruster is capable of reaching thermal steady-state condition at the RPT point ($\phi_d = 300\,\mathrm{V}$, $\dot{m}_a = 10\,\mathrm{mg/s}$, $\dot{m}_c = 1\,\mathrm{mg/s}$). Thermal steady-state is considered reached when the temperature variation is less than ±3 °C over a time span of 30 minutes.

4. **PFG characterization with atmospheric propellant**
   This phase is the main activity of the experimental campaign in which the PFG is characterized with atmospheric propellant. To account for measurement errors, three acquisitions are performed with each plasma diagnostics at each operating point tested.

<table>
<tr><th>Topic</th><th>Description</th></tr>
<tr><td>Test items</td><td>• HT5k Hall thruster
• HC20h hollow cathode</td></tr>
<tr><td>Test type</td><td>PFG characterization with atmospheric propellant
• Anode line: Xe (ignition), 1.27N_2+O_2 (operation)
• Cathode line: Xe (ignition), N_2 (operation)</td></tr>
<tr><td>Test objective</td><td>Characterize PFG performance and stability envelope with atmospheric propellant 1.27N_2+O_2 according to the characterization matrix below. The cathode mass flow rate is fixed at 0.63 mg/s (N_2) for all points.
<table>
<tr><th>$\dot{m}_a \setminus \phi_d$</th><th>225 V</th><th>300 V</th><th>375 V</th><th>450 V</th></tr>
<tr><td>2 mg/s</td><td></td><td></td><td></td><td>X</td></tr>
<tr><td>2.5 mg/s</td><td></td><td></td><td>X</td><td>X</td></tr>
<tr><td>3 mg/s</td><td></td><td>X</td><td>X</td><td>X</td></tr>
<tr><td>3.5 mg/s</td><td></td><td>X</td><td>X</td><td></td></tr>
<tr><td>4 mg/s</td><td>X</td><td>X</td><td></td><td></td></tr>
<tr><td>4.5 mg/s</td><td>X</td><td></td><td></td><td></td></tr>
<tr><td>5 mg/s</td><td>X</td><td></td><td></td><td></td></tr>
</table>
Note that this characterization matrix may be subjected to changes during the campaign if required by the testing conditions.</td></tr>
<tr><td>Test duration</td><td>5-10 days</td></tr>
<tr><td>Pass/Fail criteria</td><td>• The thruster is capable of reaching thermal steady-state condition in at least No. 1 N_2/O_2 operating point. Thermal steady-state is considered reached when the temperature variation is less than ±1 °C over a time span of 30 minutes.
• PFG performance (in terms of thrust, voltage/current characteristics and diagnostic acquisition) is measured at thermal steady state in at least No. 1 N_2/O_2 operating point.</td></tr>
</table>

5. **Reference Performance Test (RPT) with Xe**
   During this phase, it is tested the PFG with Xe after the characterization with atmospheric propellant in order to asses whether its nominal behaviour has been affected. To account for measurement errors, three acquisitions are performed with each plasma diagnostics.

Topic	Description
Test items	• HT5k Hall thruster • HC20h hollow cathode
Test type	RPT with Xe: • Anode line: Xe • Cathode line: Xe
Test objective	Verify the PFG reference performance with Xe **after** the characterization with atmospheric propellant.
Test duration	1 day
Pass/Fail criteria	• The thruster is capable of reaching thermal steady-state condition at the RPT point ($\phi_d = 300\,\mathrm{V}$, $\dot{m}_a = 10\,\mathrm{mg/s}$, $\dot{m}_c = 1\,\mathrm{mg/s}$). Thermal steady-state is considered reached when the temperature variation is less than ±3 °C over a time span of 30 minutes. • The thruster shows comparable performance (±10% in terms of thrust and mass flow rate) with respect to the RPT done before characterization with atmospheric propellant.

6

Results

In this chapter are presented the results obtained from both the experimental campaign and the calibrated numerical model. The former are not presented in their entirety as the thruster plume characterization could not be achieved due to project time limitations. Rather, only the diagnostic results directly involved in the model validation (i.e. discharge current measurements and triple Langmuir probe data) are reported and analysed in detail.

Concerning the thruster model, two cases are distinguished, depending on whether or not ion-ion streaming instabilities are included in the sheath description. Model calibration is then discussed, with particular attention on the physical significance of the selected parameters, also in comparison with the ones used by Giannetti et al. [10] in their work with xenon. Finally, the predicted plasma behaviour is thoroughly investigated and ultimately compared with the experimental data retrieved from the triple Langmuir probe, so as to asses model validation.

6.1. Experimental Campaign

The thruster experimental campaign was successfully completed as prescribed in the test plan of Section 5.3. However, a complete PFG performance and stability envelope characterization could be only performed in a single operating point, outside the characterization matrix initially proposed. This point, which in the following will be referred to as the *reference operational point*, is characterized by: $\phi_d = 225\,\mathrm{V}$, $\dot{m}_a = 6\,\mathrm{mg/s}$, $\dot{m}_c = 0.63\,\mathrm{mg/s}$.

Regarding the ones tabulated in the characterization matrix, most of them were effectively tested, even though the actuated rail on which the spectrometer tube lens was mounted consistently failed upon transitioning from Xe to N_2/O_2 at the anode. The cause of such failure was identified in the excessively high plume divergence observed during air operation. Indeed, the rail and its stepper motor resulted greatly exposed to the plume plasma, which ultimately caused components overheating. As a consequence, several critical failures of the rail subsystem (e.g. expansion of the rail blocking the tube lens, burned stepper motor cables) occurred during the testing, forcing the entire TU (which comprehends thruster, rail, thrust balance and Langmuir probe) to be repeatedly brought out of the chamber for fixing. This inconvenience significantly slowed down the campaign and especially prevented the spectrometer from being used during most of the thruster characterization activity. However, a more robust rail configuration was eventually found, which allowed to completely characterize the reference operating point even with emission spectra acquisition.

Still regarding the points on the original characterization matrix, it was observed that when operated at high voltages (i.e. $\phi_d \geq 375\,\mathrm{V}$) the thruster temperature (measured at the back of the anode injection plate) dangerously increased, even up to 420 °C at some point. To better

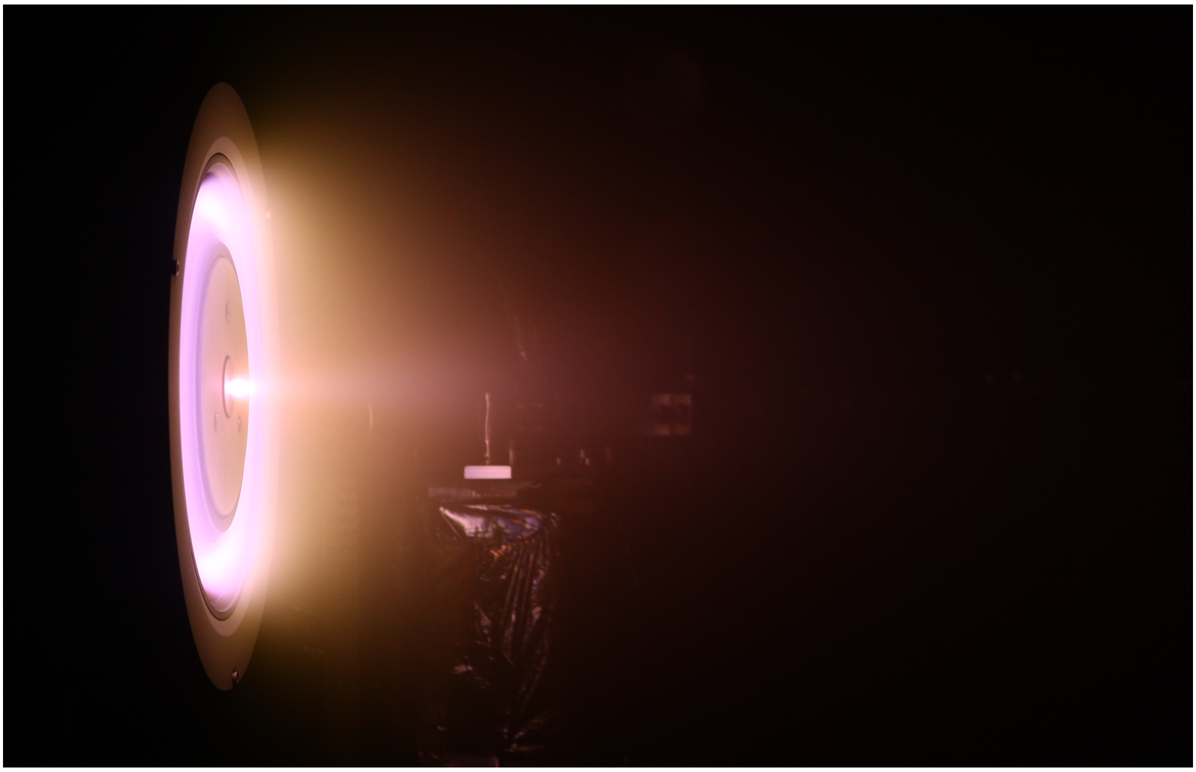

Figure 6.1: SITAEL HT5k firing with N_2/O_2 at the anode and N_2 at the cathode. (Reproduced with permission of SITAEL)

understand the significance of this temperature, continued operations at this operating point caused the steel anode to melt. This extreme heating, whose effects were also observed on other components, is currently under investigation. However, it is speculated that the root cause is the low ionization efficiency of the thruster, which maintained high the electron energy, and thus the electron power deposition on the anode.

Regarding the choice of using an $\dot{m}_a$ higher than what initially planned in the characterization matrix at $\phi_d = 225\,\mathrm{V}$, it should be firstly mentioned that the matrix values were just guesses, as the thruster had never been tested before with air. Then, during the campaign were observed discharge currents lower than expected for the employed anode mass flow rates. As a consequence, to maintain the thruster operative envelope within the nominal 2-6 kW range, higher $\dot{m}_a$ were adopted.

As it is shown in the following, the reference operating point is characterized by a stable behaviour. During the campaign, this significant stability, probably caused by the ionization efficiency of the thruster, appeared as a feature common to all the operating points tested. However, in order to perform a meaningful calibration of the numerical model, which could potentially reproduce breathing mode oscillations also using N_2/O_2, it was necessary to force the thruster plasma to oscillate. Indeed, by having an oscillating discharge current to match, it is possible to calibrate the model without even comparing experimental and simulated plasma parameters profiles, as the amplitude, frequency and mean value of the current are sufficiently unique data, in general. On the other hand, a constant discharge current can be obtained with many sets of calibration parameters, even significantly different from each other. As a consequence, by realizing that it is generally unlikely for the plasma parameters profiles to show an accurate match between experimental data and simulated results, the solution may not result univocal.

Then, in order to promote breathing mode oscillations, the maximum magnetic field magnitude B_{max} was gradually decreased from the nominal B^* employed in the stable reference operating point. Once at $B_{max} = 0.57B^*$, some irregular current oscillations were observed from the oscilloscope reading, which could indicate the entrance in an oscillatory regime. However, by decreasing B_{max} even further, the plasma suddenly became too unstable to safely proceed with the characterization. Therefore, it was kept $B_{max} = 0.57B^*$ for the oscillating reference operating point. In this condition, the current showed a controlled oscillation that, although not constantly sustained, was characterized by a well-defined and relatively noise-free behaviour due to the moderate signal amplitude. These features appeared very promising in view of a satisfactory and univocal model calibration.

The raw current signals relative to both operating points are reported in Figure 6.2c and their main features are listed in Table 6.1. Also, Figures 6.2a and 6.2b present their power spectral densities (PSD).

As mentioned above, the operating point with the highest magnetic field shows a substantially stable, although noisy, behaviour, with a maximum amplitude < 2.5 A. Even though a main oscillatory component can be recognized, due to its low amplitude it results hardly

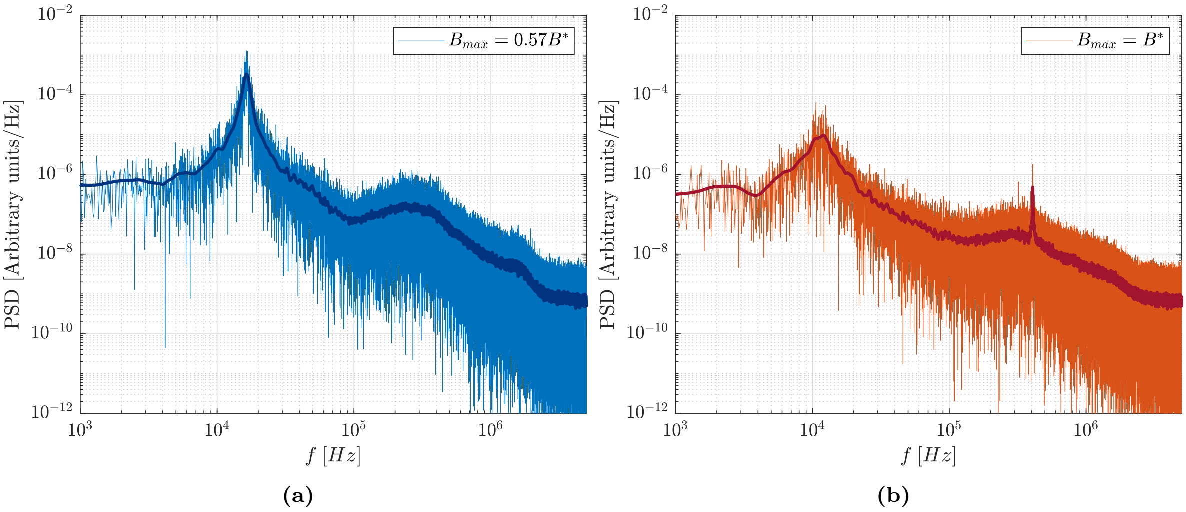

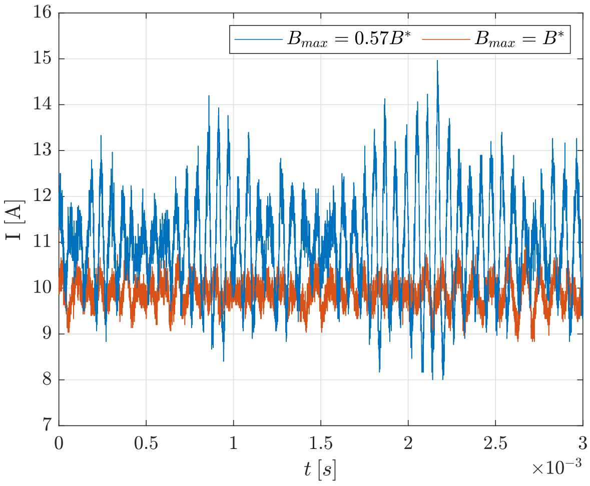

(c)

Figure 6.2: Experimental discharge current. Comparison between the reference operating points with $B_{max} = 0.57B^*$ (blue) and with $B_{max} = B^*$ (orange). (a)-(b) Power spectral density (PSD) of the signals. (c) Raw signals.

Table 6.1: Comparison between experimental discharge current parameters.

Quantity	Unit	$B_{max} = 0.57B^*$	$B_{max} = B^*$
I_{avg}	[A]	10.95	9.92
I_{max}	[A]	14.97	11.13
I_{min}	[A]	8.00	8.70

distinguishable from the background noise. Specifically, the PSD in Figure 6.2b shows a slightly-spread dominant peak between 10.4-12.3 kHz and a prominent spike at high frequencies caused by noise. Note that these appear of comparable intensity, with roughly an order of magnitude difference, thus confirming the high influence of noise on the main signal content. Overall, these characteristics make this operating point not suitable for a reliable model calibration.

On the other hand, the operating point with $B_{max} = 0.57B^*$ exhibits a much more defined oscillatory behaviour regarding both amplitude and dominant frequency. Specifically, the PSD in Figure 6.2a depicts a sharp peak at 16.4 kHz, which is characterized by an intensity several orders of magnitude higher than any high-frequency component (i.e. approximately $f > 100$ kHz). Note also that this range does not present any prominent peak, as it was instead the case of Figure 6.2b.

Regarding the raw current signal, Figure 6.2c shows a non-periodic pattern in which the wave amplitude varies from minima similar to the case $B_{max} = B^*$ up to maxima two to three times bigger. This behaviour allows to hypothesize that this operating point locates at the transition between stable and oscillating regimes. This would be also coherent with the unstable response observed at lower magnetic fields. Probably, an operating point characterized by a sustained oscillation exists for $0.52B^* < B_{max} < 0.57B^*$, even though steps lower than $0.05B^*$ could not be explored. Referring to the work of Sekerak [126], this regime may be referred as a transition between local and global modes, which generally occurs lowering the magnetic field intensity. The former mode is characterized by the presence of azimuthal perturbations (spokes) that does not substantially affect the discharge current, thus remaining generally stable. The latter instead shows negligible spokes with the entire discharge oscillating in unison: a behaviour characteristics of breathing mode. In view of these considerations, only the high-amplitude signal portions were used as a reference for calibrating the model (see Section 6.2).

As a final remark regarding the current comparison, the stable signal exhibits an average value lower than the oscillating one. It is speculated that this is due to the higher confinement exerted by B, which reduces the electron mobility, and thus the discharge current.

6.1.1. Triple Langmuir Probe

The measurements acquired with the fast-diving triple Langmuir probe are now presented and analyzed. Note that these solely refer to the oscillating reference operating point. Indeed, as it may be recalled from Subsection 5.2.5, the analysis of the probe data in a multispecies plasma necessarily requires the ion density ratios, which are not generally known. While it was initially planned to employ the results obtained from the spectrometer data analysis (performed by VKI and CNR), at the moment of writing they are not available yet. Therefore, it has been decided to use the ion density ratios predicted by the numerical model, whose results are presented in the next section (Section 6.2). In particular, the quantities are calculated at the thruster channel exit and they result

$$\bar{n}_1 = 0.22 \qquad \bar{n}_2 = 0.24 \qquad \bar{n}_3 = 0.37 \qquad \bar{n}_4 = 0.17 \tag{6.1}$$

for N^+, O^+, N_2^+ and O_2^+, respectively.

To perform the analysis, at first the raw probe parameters (I_{BC}, V_{FC} and V_{gC}), which are acquired at 5 MHz, are downsampled to 250 kHz by averaging series of 20 measurements. This is done to smooth the data dispersion caused by noise and consequently facilitate the successive analytical process. In this regard, it is mentioned that a low pass filter cutting the signal at 120 kHz is located before the oscilloscope responsible for the acquisition. Therefore, all the parameter oscillations above this threshold are ascribable to line and measurement noises, and can be partially removed with the downsampling.

A small time interval of the raw measurements in comparison with the downsampled data is shown in Figure 6.3. In all three plots it can be clearly observed the oscillatory behaviour of the probe parameters in response to plasma oscillations. Recall from Subsection 5.2.5 that these develop over characteristic times much shorter than that of the probe motion, which thus does not affect their measurement.

Then, by using the resulting time series of I_{BC}, V_{FC} and V_{gC} together with the aforemen-

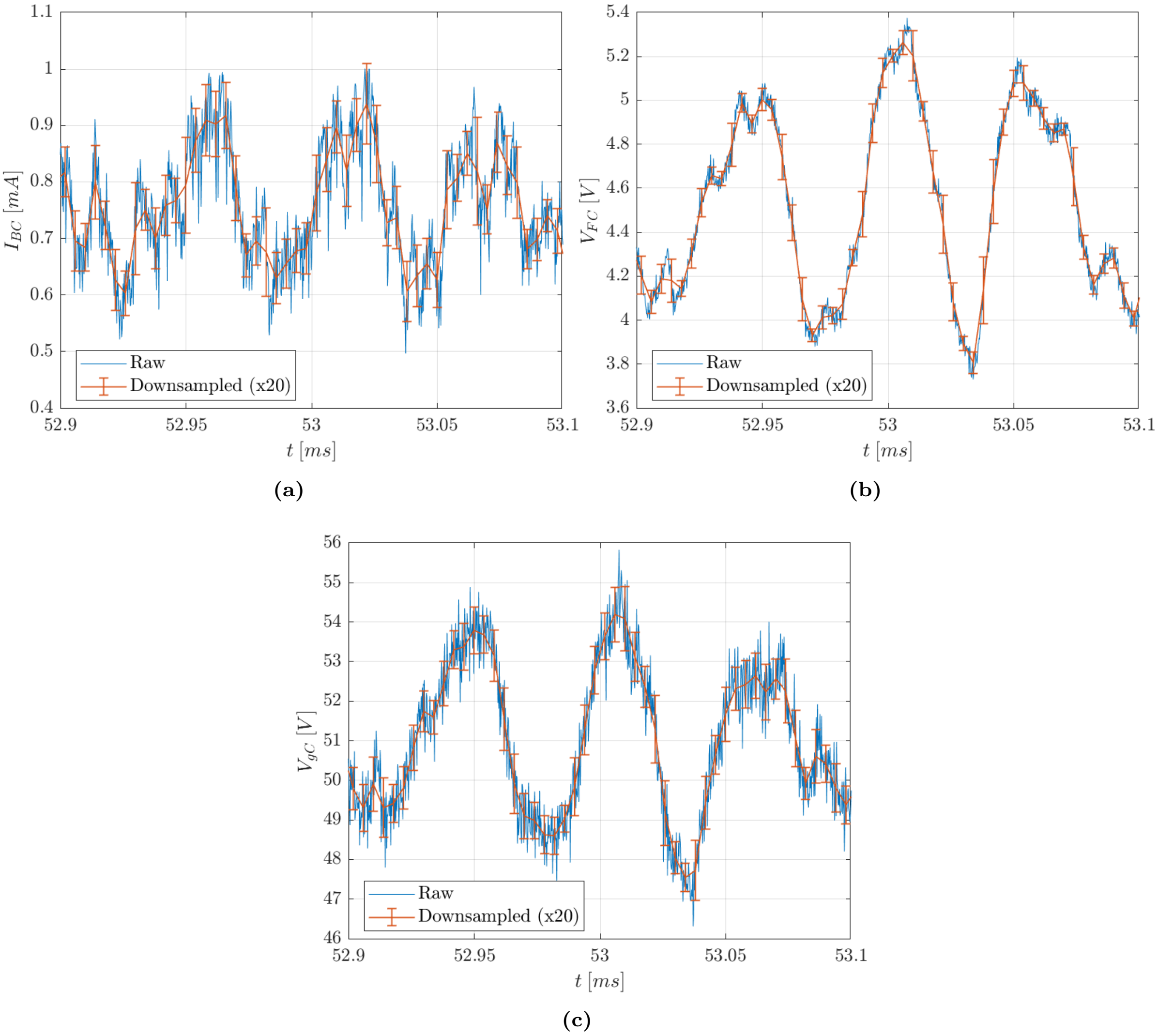

Figure 6.3: Raw parameters measured by the fast-diving triple Langmuir probe and corresponding downsampled data (x20) with 1σ standard deviation error bars. (a) Bias-common current I_{BC}. (b) Float-common voltage V_{FC}. (c) Ground-common voltage V_{gC}.

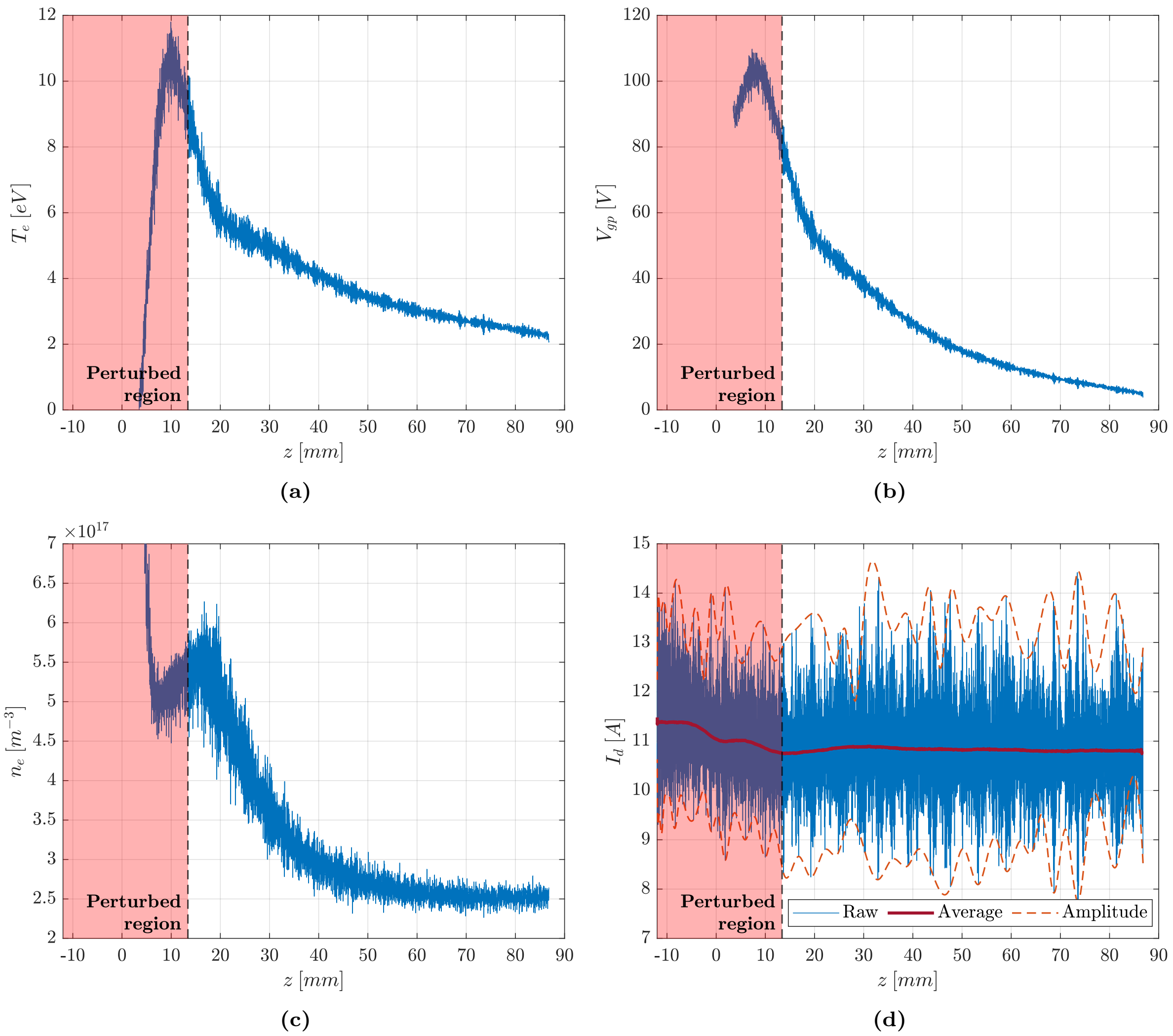

(a) **(b)**

(c) **(d)**

Figure 6.4: Plasma parameters obtained from the fast-diving triple Langmuir probe measurements. (a) Electron temperature T_e. (b) Plasma potential V_{gp}. (c) Electron density n_e. (d) Thruster discharge current I_d during fast-diving.

tioned ion density ratios $\bar{n}_i$, it is solved the System 5.27 at each time instant. Specifically, the formulation employed for the electrode currents description is the one of Mausbach [124], given in Eq. 5.35. The obtained plasma parameters (T_e, V_{gp} and n_e) are then shown in Figures 6.4a to 6.4c as a function of the axial location on the channel centerline (with respect to the exit plane).

The results appear significantly disturbed in the region just outside the channel, where the magnetic shielding configuration is known to shift the high-temperature electron plasma. Note also that inside the channel they could not be even obtained by solving System 5.27 because of great discontinuities in the probe parameters I_{BC}, V_{FC} and V_{gC}. The main causes attributed to this disturbed behaviour are the flow perturbations induced by the probe presence and plasma inhomogeneities between the probe electrodes, especially relevant in regions characterized by a strong azimuthal electron current (recall the discussion in Subsection 5.2.5). While the former are inevitable and represent the main limitation of plasma insertion probes, the latter can be partially accounted for with the correction parameters δV_1 and δV_2 that, by using a Bayesian inference approach, could be then marginalized from the results. However, this technique cannot be exploited in solving the direct problem here addressed (i.e. System 5.27), which would just become underdetermined by including these corrections. Even if using two sets of results acquired with different probe configurations (e.g. switch and non-switch arrangements[1]) would theoretically resolve the indetermination, in practice this process makes the results not univocal. As a consequence, in this work the plasma parameters in the perturbed region cannot be reliably reconstructed, not even qualitatively.

While the plasma parameters do not provide a clear indication of where the perturbed region begins, this information can be effectively retrieved by observing the discharge current measured during probe acquisition (Figure 6.4d). In particular, the average current remains constant until the probe tip reaches about $z = 13.4\,\mathrm{mm}$. Then, it noticeably starts increasing, thus clearly indicating that past that location the probe is perturbing the plasma. In addition, it is also observed a reduction in the raw current oscillations amplitude upon entering in the perturbed region. Note that these same characteristics were also identified by Giannetti et al. [120] in their experimental work with a xenon HT5k, although they appeared more well-defined and located further upstream.

Regarding the plasma parameters in the unperturbed region, they all exhibit a very distinct behaviour, monotonically increasing from the far plume to the channel. Their values appear reasonable and in line with the expectations. In particular, with respect to the xenon case investigated by Giannetti et al. [120], all profiles are effectively shifted downstream due to the magnetic shielding configuration of the thruster and, as expected from the lower ionization efficiency, the electron density results significantly reduced. Additionally, they present relatively small oscillations, with the maximum values concentrated in the high magnetic field region of the thruster. Even the electron density, which in the xenon case was characterized by severe oscillations, here shows a very moderate behaviour. As a final remark about this last profile, it is noticed a peak near the edge of the perturbed region. While this appears to be related to the disturbed plasma, from the available data its nature cannot be assessed.

In conclusion, the data show that unperturbed plasma can be quantitatively probed only starting from 13.4 mm downstream the thruster exit. Therefore, only the plasma parameters determined there can be used for the numerical model validation, discussed in Section 6.2.

6.2. Numerical Model

This section discusses the results obtained with the model calibrated on the oscillating reference operating point. These are presented for both the case in which ion-ion streaming instabilities in the plasma presheath are considered and in case they are not. In this way, the effects resulting from the inclusion of this novel kinetic description can be readily identified and evaluated in comparison with experimental evidence.

6.2.1. Ion-ion Streaming Instabilities Neglected

As mentioned in the previous section, the model has been calibrated on the high-amplitude oscillations observed in the measured current. In particular, due to the substantial amplitude variations observed, only a small signal portion has been used as a reference. This is characterized by some of the highest-amplitude oscillations, as it has been observed that these correspond to more developed and sustained oscillatory regimes (see Figure 6.2). Figure 6.5 shows the direct comparison between this portion of the raw experimental signal and the current predicted by the model. At a first sight the agreement appears very tight, with only minor differences possibly attributable to high-frequency noise of the experimental data. However, in the detailed view of Figure 6.5b are highlighted high-frequency components predicted by the simulation superimposed to the main harmonics. In view of their similar amplitudes, these

---

[1] More details can be found in Ref. [121].

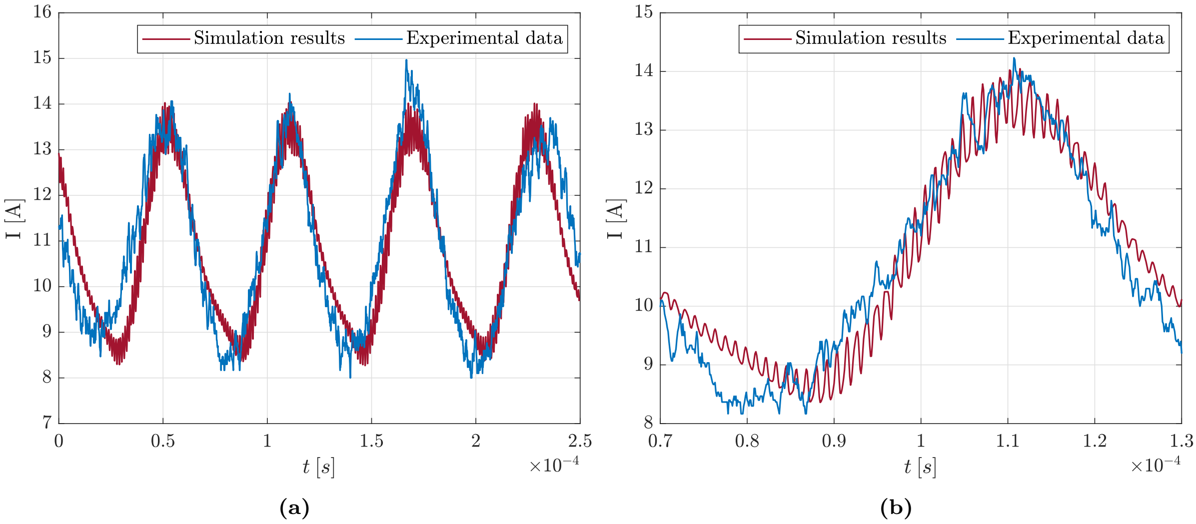

Figure 6.5: Discharge current comparison between experimental measurements and simulation results. (a) Signal profiles over a 0.25 ms time interval. (b) Detail of the signal profiles highlighting the high-frequency components of the waves.

Table 6.2: Comparison between the discharge current control parameters used to match the experimental discharge current with the one predicted by the model. The experimental values only refers to the signal portion considered for calibration (Figure 6.5a).

Quantity	Unit	Experimental	Simulation	Variation
I_{avg}	[A]	10.95	10.85	-0.91%
I_{max}	[A]	13.70 – 14.97	14.05	$+2.55\%$ to -6.15%
I_{min}	[A]	8.00 – 8.47	8.27	$+3.37\%$ to -2.36%
f_{BM}	[kHz]	16.36	16.67	$+1.89\%$

could then suggest a physical nature of the high-frequency irregular oscillations measured, although not correctly reconstructed because of electrical noise.

In order to match the experimental current with the one predicted by the model, several control parameters have been monitored during calibration. These are compared in Table 6.2 and confirm the high similarity of the signals, which show very slight variations both regarding signal amplitude and frequency. In particular, note that the latter only refers to the main harmonics with frequency f_{BM}, which is the one characterizing breathing mode oscillations.

A more detailed analysis of the frequency components of the signals is proposed in Figure 6.6, which reports their power spectral densities (PSD). In the detailed view of Figure 6.6a it can be appreciated an almost perfect match between the signals traces, with the only exception of two distinct harmonics appearing in the simulated current at frequencies of $f_2 = 34.46\,\text{kHz} \approx 2f_{BM}$ and $f_3 = 51.14\,\text{kHz} \approx 3f_{BM}$. Note that the experimental low-frequency peak appears slightly lower in intensity than the predicted one. This is indeed expected as the measured discharge current oscillation is not continuously sustained in time (see Figure 6.2c), and thus the lower-amplitude portions of the signal reduce the intensity of these frequency components in the PSD graph.

Then, by showing the complete frequency range (Figure 6.6b),[2] in the MHz region appear

---

[2] Note that, as mentioned in Section 5.2, the oscilloscope used for acquiring the discharge current samples

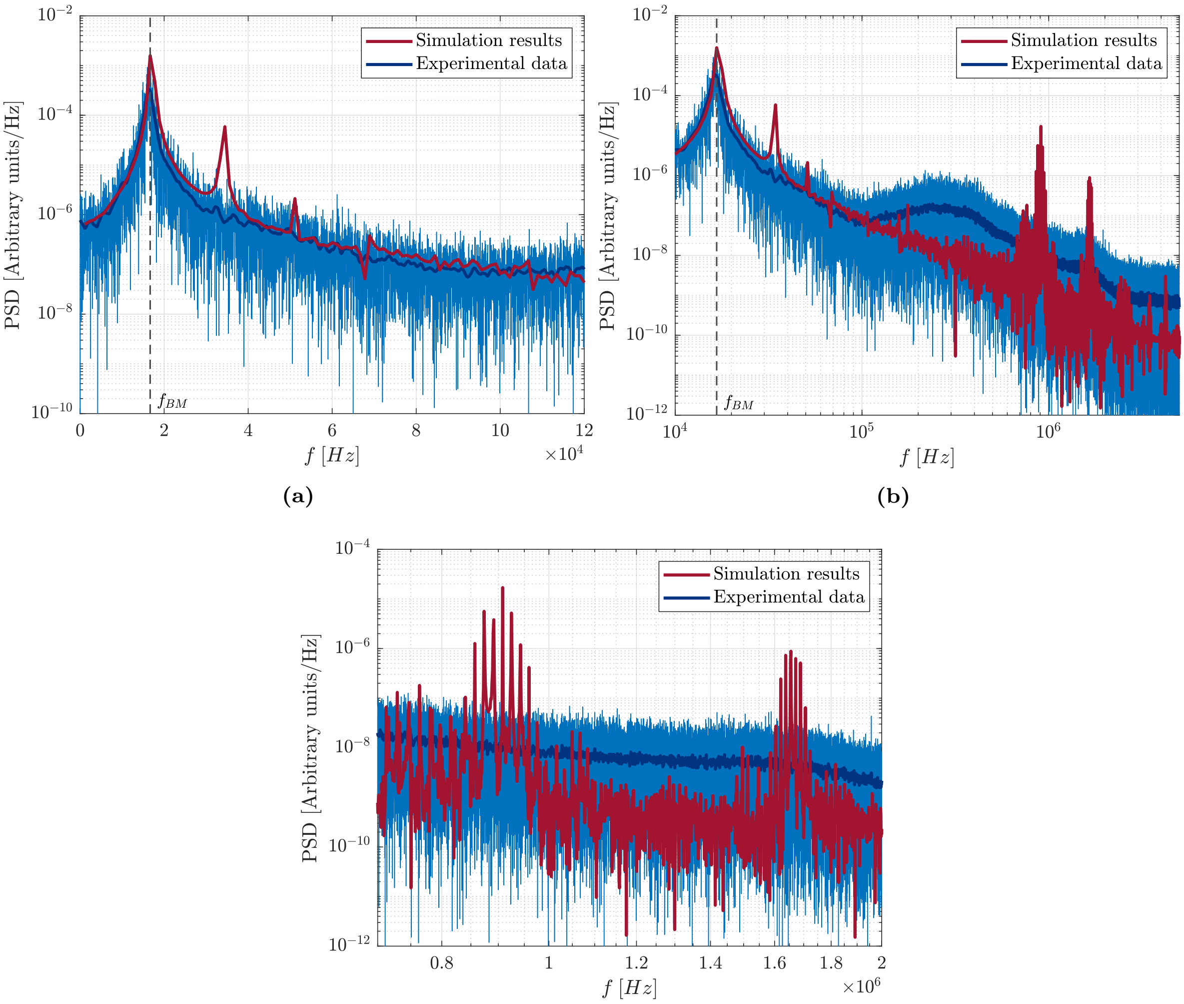

(a) **(b)**

(c)

Figure 6.6: Discharge current comparison between experimental measurements and simulation results. Power spectral density (PSD) (a) in the 0-120 kHz frequency range and (b) over the complete frequency range highlighting the high-frequency components of the signals. (c) Detail of the high-frequency peaks predicted by the simulation.

two prominent peaks, which are characteristic of the high-frequency oscillations predicted by the model. Specifically, these are at about 908.18 kHz and 1.65 MHz, and are shown in greater detail in Figure 6.6c. In support to their physical nature, it is mentioned that Barral and Ahedo [13] also predicted very similar oscillations. Indeed, as it is shown in the following, these frequency components are the result of plasma density oscillations characterized by propagation velocities very close to the respective ion velocities. This behaviour suggests clearly that they may be tightly related to the so-called *ion transit instability*, which has been observed both numerically and experimentally [11, 12].

Calibration Parameters

The best match between simulation results and experimental data, shown in Figure 6.5, has been achieved for $AF = 0.12$, $T_a = 723\,\mathrm{K}$, $\alpha = 0.1$, $\beta = 0.048$ inside the channel and $\beta = 4.5$ in the plume.

---

at 10 MHz. Therefore, for the Nyquist-Shannon sampling criterion, a maximum frequency of 5 MHz can be captured.

Before exploring the parameters used, it is reported a general difficulty, arisen during the calibration process, in defining their effects on the plasma behaviour. Indeed, it is believed that the high number of plasma species considered, each characterized by several chemical interactions with the others, makes the model extremely non-linear and sensible to general calibration parameters as the ones used. In addition, the inclusion of a plume expansion description for both neutrals and ions complicates further the model physics, especially in the axial region around the channel exit, which results characterized by major variations (i.e. magnetic field peak, end of wall interaction effects, beginning of plume). Nevertheless, it also emerged that, for this multispecies plasma, the plume expansion significantly affects the oscillatory plasma behaviour, thus requiring an accurate description. This important result highlights the causal relationship between plume and ionization instabilities (i.e. breathing mode), in clear contrast with what assumed by Giannetti et al. [10] for the xenon case. It is thought that the main reason for this difference is a combination of two effects: the propellant and the magnetic-shielding configuration. The former, composed by light molecular particles, is subjected to dissociation, whose products naturally ionize further downstream in the channel and partially also in the near-plume. The latter enhances this behaviour even more, by shifting the thruster acceleration region outside the channel. In these conditions, it appears clearly that the plume description becomes relevant also for phenomena generally explained by the internal channel physics alone.

As explained in Section 4.5, both AF and T_a contribute toward the definition of the neutral velocities, while only the latter determines their expansion in the plume (equal for all neutrals since T_a is the same). During the calibration process it was observed that independent variations of these two quantities generally result in competing effects, even though a precise characterization could not be clearly defined, especially for T_a.

In general, variations of AF at constant T_a appears to affect both oscillation frequency and amplitude. This behaviour, which is similarly to the one also identified by Giannetti et al., is coherent with a simple understanding of these instabilities: faster neutrals arrive sooner in the high electron temperature region where they are ionized, thus increasing the frequency of the oscillations. At the same time, ionization becomes less intense and abrupt variations are prevented due to the lower neutral densities, with the result of reducing the instability amplitude. By further increasing AF, the plasma tends toward a stable condition, even though, before reaching it, the oscillation may exhibit a lower frequency. A possible explanation is that after a certain velocity threshold the neutral densities drop to levels too low for causing a ionization surge. However, also in combination with wall neutralization of ions, after a certain time neutrals may still build up in the channel to a sufficient level, thus resulting in a lower-frequency instability.

Regarding variations of T_a at constant AF, as anticipated above it could not be defined a clear cause-effect relation. Starting from a particular oscillating solution, it was observed that both positive and negative variations of T_a may eventually damp the oscillations, even though this happens more often by decreasing it. In general, a higher T_a, and thus a higher neutral expansion, appears to increasingly perturb the current signal with high-frequency components, eventually up to a point in which the plasma results completely disturbed.

Overall, the value of 0.12 used for AF is in line with the 0.25 proposed by Reid [95], while $T_a = 723\,\mathrm{K}$ appears to underestimate the real anode temperatures observed during the experimental campaign, probably in between $800\,\mathrm{K}$ and $1000\,\mathrm{K}$ due to the dull red glow visible at thruster shutdown.

Resulting from these calibration parameters, the following neutral velocities are used: $u_N = 361\,\mathrm{m/s}$, $u_O = 338\,\mathrm{m/s}$, $u_{N_2} = 255\,\mathrm{m/s}$ and $u_{O_2} = 239\,\mathrm{m/s}$. It is expected that, by introducing variable velocities through the solution of the respective neutral momentum con-

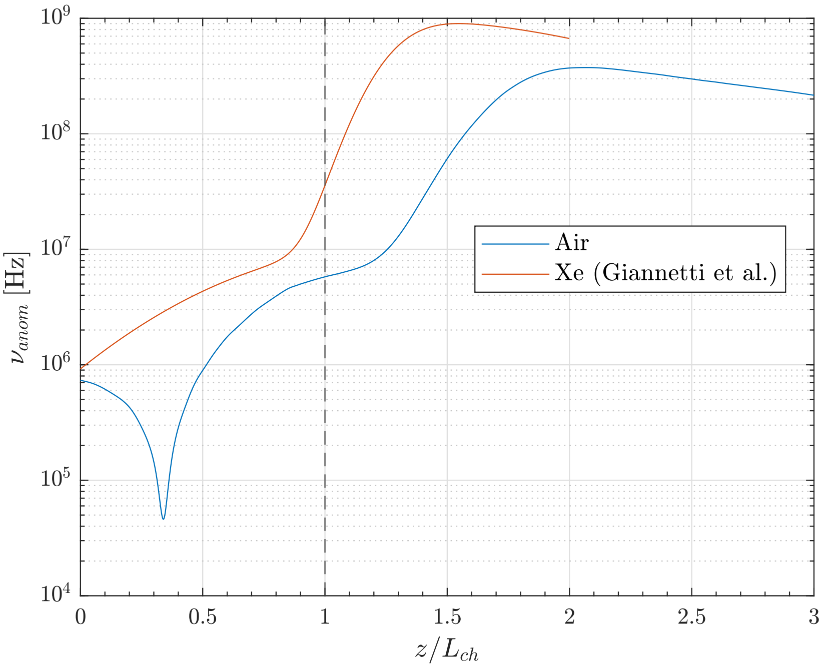

Figure 6.7: Comparison between the anomalous collision frequency ν_{anom} profiles used in this work for calibrating the model for air operation (blue) and in the work of Giannetti et al. [10] with xenon (orange).

servation equations, more accurate results may be obtained and possibly even a more robust model.

As the wall interaction parameter α is concerned, the value of 0.1 used is basically the same employed in the xenon case [10], even though in this case the thruster is magnetically shielded. By looking at the PFG channel exit during firing in Figure 6.1, it can be clearly seen that the plasma results separated from the channel walls, thus confirming the effectiveness of the magnetic shielding configuration to a very first approximation. Hence, the low value of α appears particularly reasonable. However, it is recalled the general tendency of the classical sheath description to overestimate wall losses [106, 107]. This characteristics, in addition to the impossibility of radially resolving the ions density gradients due to the one-dimensional description, does not allow to make reliable considerations about the representativeness of α.

During calibration, it was observed that the effects of variations in α are strictly related to the amplitude of current oscillations, both at high and low frequencies. In general, it appears that α acts as a damping coefficient for oscillations, promoting higher amplitudes in response to smaller values. From the several tries attempted during this process, this tendency seems to affect more strongly the high-frequency components which, in case of a reduced α, eventually completely disturb the signal. On the other hand, increasing α enhances wall losses which reduce the electron temperature. Also, wall neutralization of ions results boosted, with the overall effect of smoothing down density variations and thus damping current oscillations.

Finally, regarding β, it is firstly noted that the internal and external values employed reflect quite accurately the two orders of magnitude difference used in the xenon case. This quite interesting result confirms, also for an nitrogen/oxygen plasma, the presence of a very distinct separation in the ν_{anom} profile. In particular, its plot is reported in Figure 6.7 together with the one used by Giannetti et al. for xenon.

At first, it is observed the significant profile difference inside the channel. By recalling the definition of ν_{anom} (Eq. 4.33), the severe trough observed in the air case is due to the specific magnetic field (B) profile implemented in the thruster. Indeed, its magnetic shielding configuration is characterized by a 0 mT point in the near-anode region and approximately on the channel centerline. Consequently, as the real B profile on this axis is employed, this feature also appears in ν_{anom}. Physically, the trough implies an almost null electron confinement, which however has been observed to not strongly affect the plasma behaviour, as artificial manipulations of B have highlighted.

Secondly, the ν_{anom} profile for air shows a global downward shift with respect to the xenon one. In general, variations in the ν_{anom} value are related to the mean discharge current level, as a lower collisionality in regions of high B, for instance, decreases the electron perpendicular mobility (see Eq. 4.35), and thus the current. At the same time, these also greatly affect the oscillation amplitude, as demonstrated in the work of Hara and Mikellides [6] by modifying the value of ν_{anom} only inside the channel. Also in this work, a similar behaviour of the discharge current has been observed, with the breathing mode oscillation shifting upwards with reduced amplitude for higher values of β inside. In addition, as expected, variations of the outside value produced less noticeable effects, being further from the thruster core.

Other differences with the profile proposed by Giannetti et al. consist in the position and inclination of the transition between internal and external values of ν_{anom}. The former appears well outside the channel as a consequence of the magnetic shielding configuration, which brings downstream the thruster acceleration region. What was observed during calibration is the current tendency of reducing the oscillation amplitude in response to more internal transitions. Regarding the transition steepness, the air case exhibits a less inclined profile, probably because of a smoother variation of the physical phenomena due to the high number of species considered, still interacting with each others along the entire domain. Note that the calibration highlighted a consistent difficulty in sustaining the discharge in case of steeper transitions.

Moreover, by looking at Figure 6.7 it can be clearly understood the importance of having extended the model domain, which otherwise, with such downstream inclined transition, would have completely excluded the outer part of ν_{anom}.

Overall, the profile of β represents the most important calibration parameter for reproducing plasma oscillations, but also the most challenging due to the many degrees of freedom available. In addition to the cause-effects relations outlined above, each variation also affects the oscillation frequency components, in ways often very difficult to predict. It is expected that the implementation of a time-varying profile for ν_{anom} would allow better representativeness and calibration ease.

Plasma Evolution

Having calibrated the model on the experimental discharge current, it is now possible to investigate the nitrogen/oxygen plasma behaviour, as predicted by the simulation. In particular, Figure 6.8 shows the time-varying profiles of the most relevant quantities discussed in the following (a complete overview of all of them is reported in Appendix D). The plots reproduce their evolution over the entire domain, extending in the plume up to three times the channel length, for a time interval of 0.5 ms.

By looking at the figures, the high-frequency oscillations identified in the current signal (Figure 6.5b) can be immediately recognized. Interestingly, these appear to not appreciably affect the neutral densities, even though during calibration both T_a and AF have been observed to affect these oscillations. It is believed that the lack of ion neutralization mechanisms in the plume does not allow for these instabilities to reflect back on neutrals, which thus continue their expansion while only being ionized. In this view, it is supposed that the inclusion of CEX collisions, for instance, could act as a feedback mechanism for these plume instabilities. Note that a very similar behaviour was also identified by Barral and Ahedo [13], which concluded that the ion transit instability responsible for the high-frequency oscillations propagates too

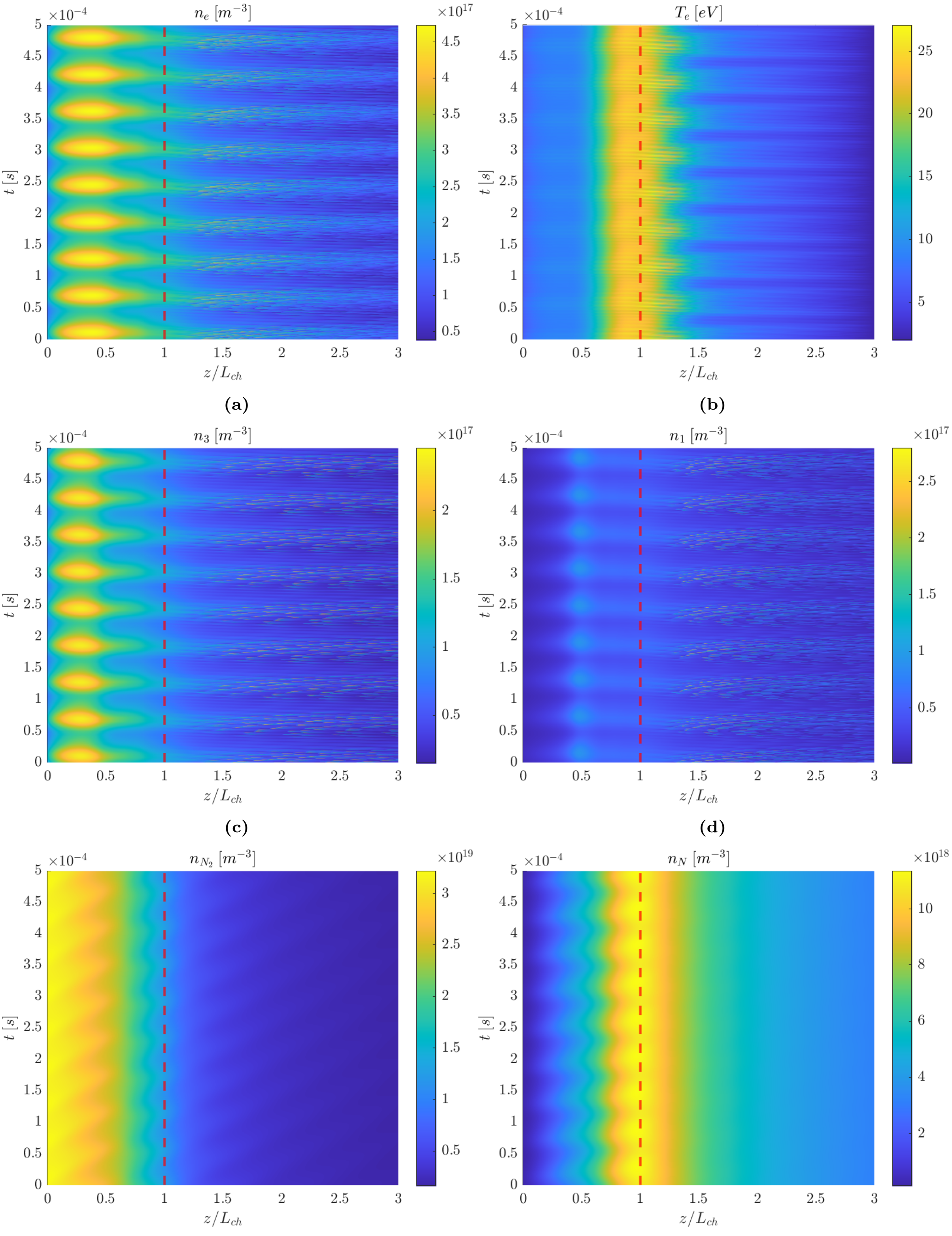

(a) (b) (c) (d) (e) (f)

Figure 6.8: Unfiltered simulated plasma behaviour in space and time. (a) Electron density n_e. (b) Electron temperature T_e. (c) N_2^+ density n_3. (d) N^+ density n_1. (e) N_2 density n_{N_2}. (f) N density n_N. The red dashed line indicates the channel exit.

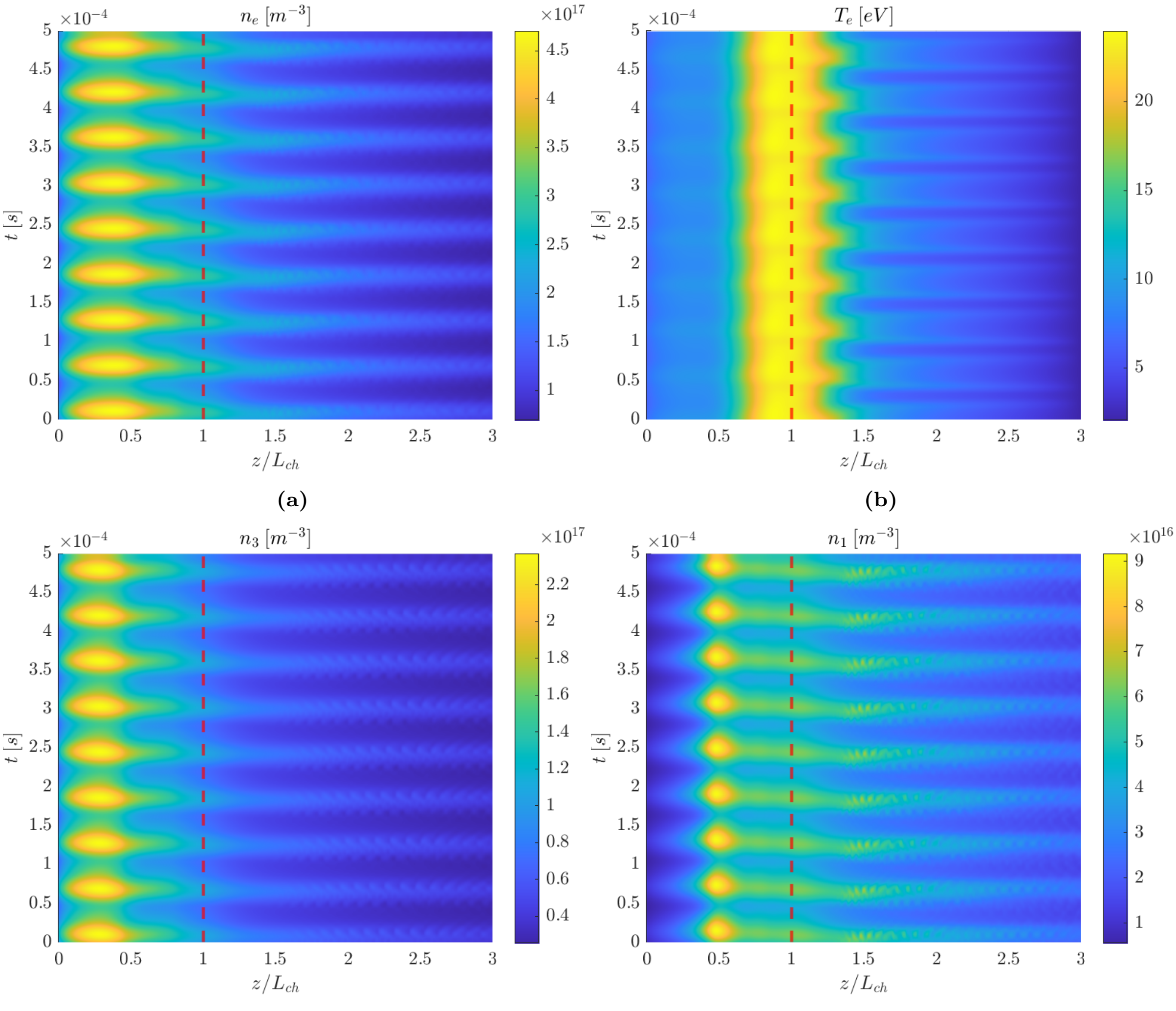

(a) **(b)** **(c)** **(d)**

Figure 6.9: Filtered simulated plasma behaviour in space and time. Frequencies above 120 kHz are removed. (a) Electron density n_e. (b) Electron temperature T_e. (c) N_2^+ density n_3. (d) N^+ density n_1. The red dashed line indicates the channel exit.

fast to induce observable variations in the neutral densities. Probably both reasons contribute to the predicted behaviour.

In order to isolate the breathing mode oscillations from the high-frequency components, the results have been filtered, removing oscillations above 120 kHz.[3] Then, the same plots presented in Figure 6.8 (neutral densities excluded) are reported filtered in Figure 6.9, while a complete overview can be found in Appendix D. Note how the filtering allows to better identify the characteristics of some plasma quantities, such as the electron temperature and the atomic ions densities, which previously resulted partially masked.

The figures clearly illustrate the plasma dynamics characterizing low-frequency longitudinal oscillations which, contrarily to what can be generally found in literature, in this case interest several molecular and atomic species which evolves in unison. This result is rather unique and alone confirms that the model includes all the physics necessary to reproduce breathing mode

---

[3] Recall from Subsection 6.1.1 that this value corresponds to the maximum frequency resolvable by the triple Langmuir probe. Consequently, during model validation (discussed in the following), it can be presented a more accurate comparison between these filtered results and the probe ones.

oscillations even in complex multispecies plasmas. Specifically, molecular neutrals are injected into the channel at the anode plate with their constant velocities. As they move away from the anode, they almost immediately start interacting with the surrounding electrons that, with temperatures of $\approx 10\,\text{eV}$, are already sufficiently energetic to dissociate both O_2 and N_2, as well as partially ionize them (recall Table 3.8). Due to the similar ionization energies, this condition causes two coincident surges of the N_2^+ and O_2^+ densities, which are represented by the periodic peaks in the corresponding plots (Figures 6.9c and D.2j). These occupy almost completely the first half of the channel, showing maximum density peaks about two orders of magnitude lower than the respective molecular neutrals (Figures 6.8e and D.2c). In comparison, note that, in the work of Giannetti et al. with xenon, this ratio remains within an order of magnitude lower. This is a clear indicator of the lower ionization efficiency achieved during air operation.

At the same time, about halfway along the channel, two additional density surges occur, corresponding to N^+ and O^+ (Figures 6.9d and D.2h). These, in comparison to the N_2^+ and O_2^+ ones, appear more localized but with similar density levels. All the newly generated ions then split in two groups. The majority move downstream, where they get accelerated outside of the thruster by the main electric field. The other group instead moves upstream under the action of a weak reverse electric field generated to compensate the electron pressure and to verify the conditions at the anode sheath. In this way, these ions recombine at the anode plate and, by increasing the respective neutral densities, further fuel the successive breathing mode oscillation.

Note that, due to their low densities, the four synchronous surges, appearing almost in phase opposition with respect to the corresponding neutral oscillations, do not significantly affect dissociation phenomena, which result in high N and O densities around the channel exit (Figures 6.8f and D.2b), where the electron temperature is maximum. Interestingly, these quantities exhibit an oscillatory behaviour mostly limited to the channel region, while in the plume little or no signs of instability are observed. This characteristic is coherent with the density profiles of N_2 and O_2 and the lack of neutralization mechanisms in the plume.

As a final remark about the neutral density distributions, nitrogen neutrals appear to develop further downstream with respect to the oxygen ones. This behaviour is due to two effects combined: the anode boundary conditions and their dissociation cross-sections. The former results in more N_2 injected than O_2 (due to the $1.27 N_2/O_2$ mixture) at a higher speed (due to the constant T_n). The latter determines a dissociation rate of O_2 two times higher than N_2. Note that, as a consequence of this characteristic, the density of O_2^+ (Figure D.2j) appears noticeably lower than that of N_2^+, even becoming the lowest one in the plume.

As the electron temperature is concerned, Figure 6.9b shows a wide peak centered on the channel exit, which is coherent with the magnetic-shielding configuration simulated. It is interesting to observe that, in response to the surges, the electron temperature peak shrinks and steepens in the plume. This causes the plasma potential drop to slightly deepen there (Figure D.2l), thus boosting the ions to their highest velocities. Specifically, the model predicts that all ions are accelerated to almost the same velocity (compare Figures D.2m to D.2p). This can be explained by observing that heavier ions are produced further upstream with respect to N^+ and O^+, and are then accelerated by a higher potential drop. Therefore, even if lighter ions would naturally reach higher velocities if subjected to the same potential drop, this is instead lower on average, levelling them out. In the context of evaluating the PFG plume representativeness as a uniform atmospheric flow, this result appears very promising. However, it is also recalled that, if this would be the case, the total IVDF obtained from the RPA probe would not provide any information about the individual ion contributions (see Subsection 5.2.4), thus complicating the plume characterization.

Regarding the ion densities characterizing the thermosphere (see Figure 3.1) the model cannot provide any comparable information due to the limited domain considered. Indeed, the absolute densities predicted are orders of magnitude higher, clearly indicating that the flow needs to further expand downstream before reaching a location in which it possibly matches the target composition. The same also holds for the relative ion density ratios.

To better visualize the plasma dynamics related to breathing mode and high-frequency oscillations individually, in Figures 6.10 and 6.11 are proposed two additional spatiotemporal analyses. These cover few representative time stamps along a breathing mode oscillation (i.e. filtered model results) and a high-frequency one (i.e. unfiltered model results), respectively.

Starting from breathing mode, the time stamps are indicated over the filtered current signal in Figure 6.10a. Then, Figure 6.10b shows the electron temperature behaviour in response to such low-frequency oscillations which, as highlighted above, exhibits a shrinkage in the plume during the descending portion of the current wave. Correspondingly, the ion velocities reach their maximum values (Figures 6.10e and 6.10f). Inside the channel these quantities show very slight or null variations, due to the limited fluctuation of the density surges. Specifically these

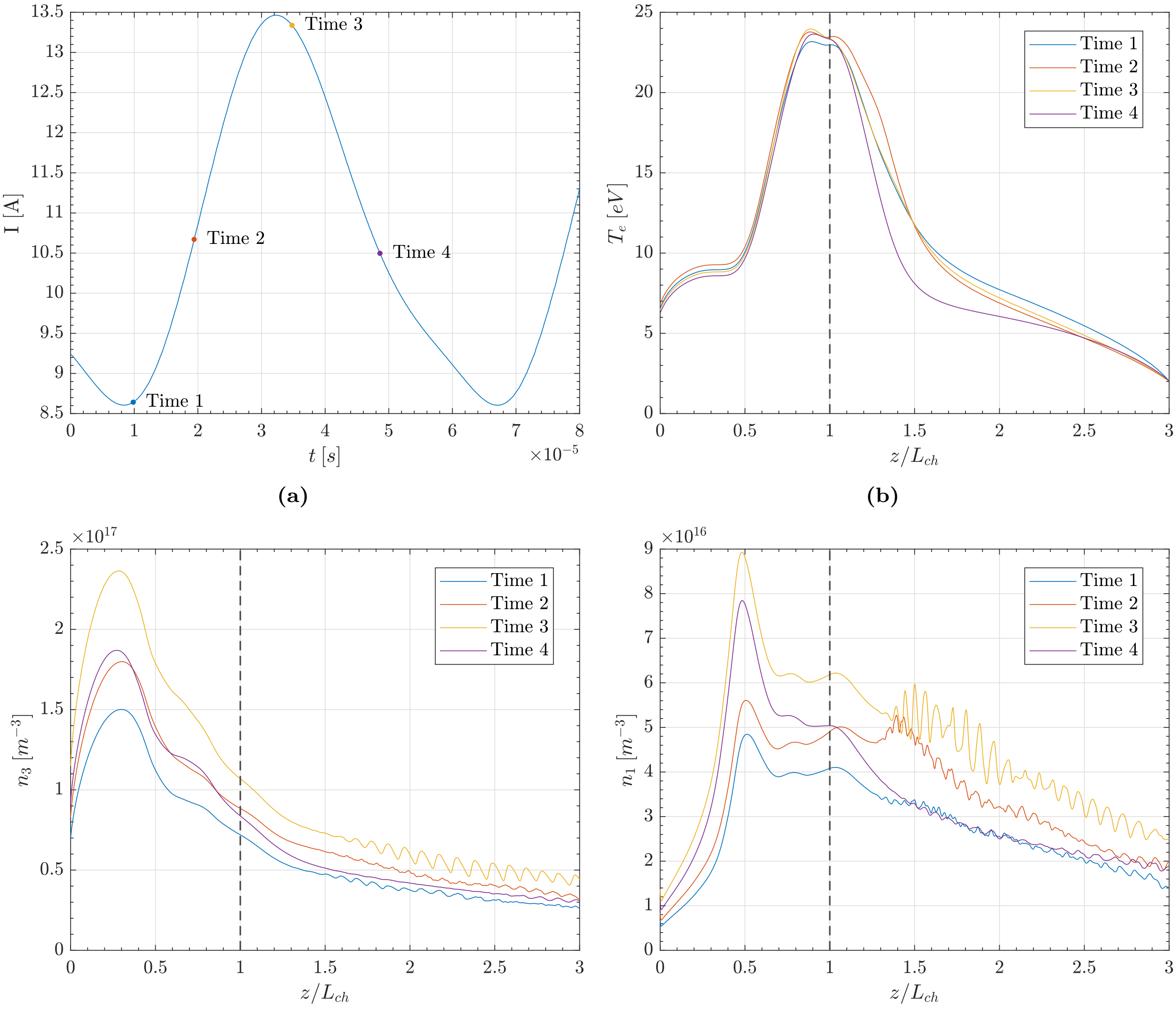

(a) **(b)**

(c) **(d)**

Figure 6.10: Simulated plasma behaviour at 4 time stamps along a single breathing mode oscillation. Frequencies above 120 kHz are removed. (a) Discharge current with the selected time stamps indicated. (b) Electron temperature T_e. (c) N_2^+ density n_3. (d) N^+ density n_1. The black dashed line indicates the channel exit.

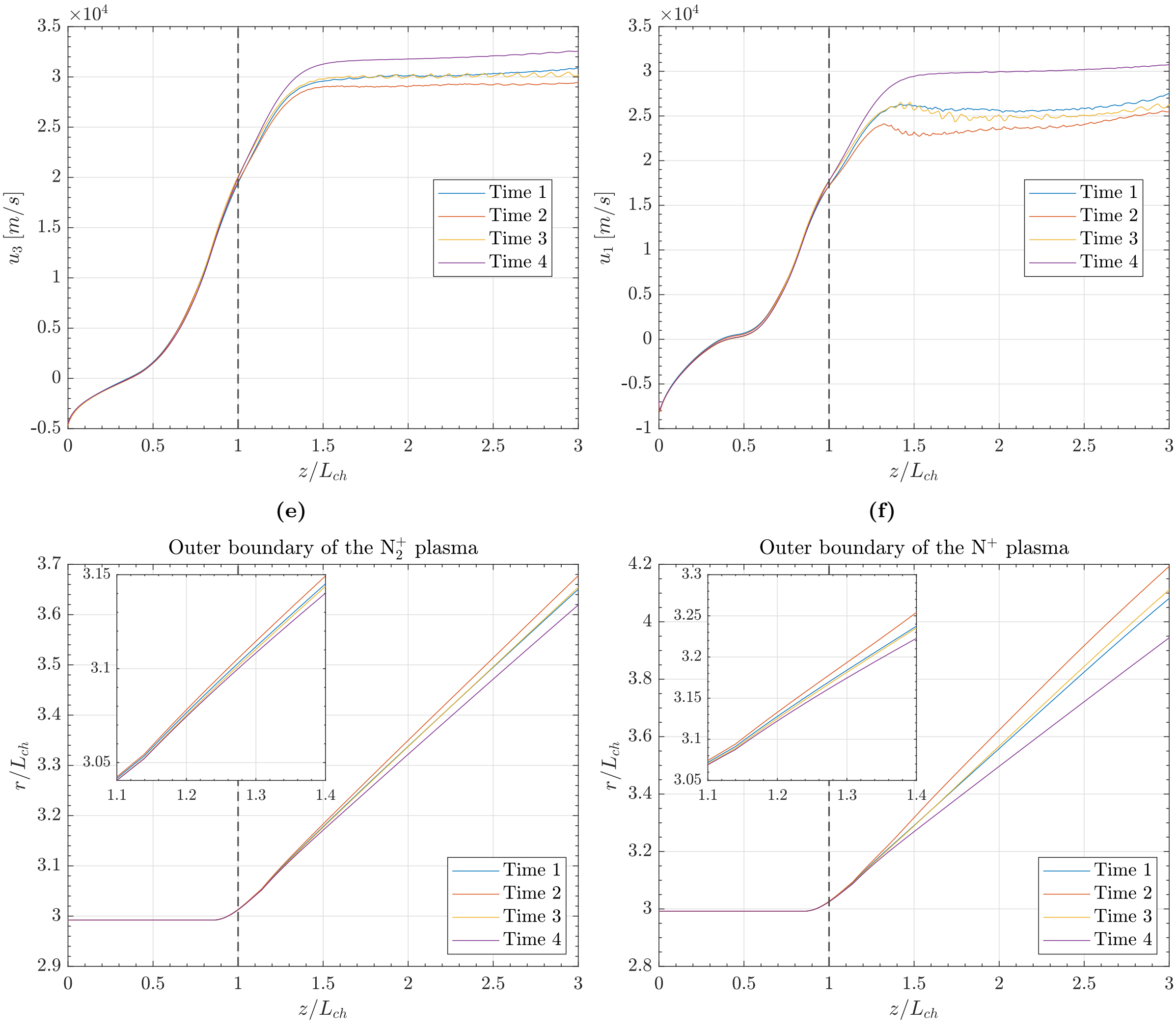

(e) (f)

(g) (h)

Figure 6.10 (cont.): (e) N_2^+ velocity u_3. (f) N^+ velocity u_1. (g) Two-dimensional plot (axial-radial) of the N_2^+ plasma outer boundary. (h) Two-dimensional plot (axial-radial) of the N^+ plasma outer boundary.

are reported in Figures 6.10c and 6.10d for N_2^+ and N^+, respectively. Note the presence in the plume of unfiltered oscillations at very high-frequency, which most probably leaked from the filter.

Finally, Figures 6.10g and 6.10h show the outer boundaries of the N_2^+ and N^+ plasmas, respectively, and their two-dimensional variations (axial and radial). The inner boundaries are not shown since they are identical due to the channel symmetry. Note that both plumes expand and contract rigidly in response to oscillations, as the ion velocities rapidly reach a stable value once outside of the channel. In particular, higher velocities correspond to more focused plumes and vice versa. Also, lighter species are characterized by a wider divergence due to the higher sound velocity at the channel exit (see Eq. 4.22).

Relatively to the filtered results here investigated, the model predicts the following half-divergence angles for the ion species: $\lambda_1 = 24°$-$34°$ for N^+, $\lambda_2 = 23°$-$31°$ for O^+ (not shown), $\lambda_3 = 17°$-$23°$ for N_2^+ and $\lambda_1 = 15°$-$21°$ for O_2^+ (not shown). Note that these values significantly underestimate the experimental data obtained from the Faraday probes measurements (not presented in this work), which indicate very high half-divergence angles, in excess of 60°.

This result was largely expected due to the intrinsic limits of the plume expansion description employed. Indeed, with a one-dimensional model it is simply not possible to resolve the complex physical interactions that characterize the near-plume region. Specifically, a two-dimensional magnetic field topology is fundamental, as its curvature determines radial components of the electric field that directly affect the ion beam focusing or defocusing (i.e. plasma lens [127]). This characteristic results particularly relevant in magnetic shielding configurations where the curvature significantly alternates between convex and concave, with the effect of directing the local electric field vector either away from the channel centerline or toward it, respectively [128, 129].

As the analysis of high-frequency oscillations is concerned, the respective time stamps are indicated in Figure 6.11a. Note that the plasma quantities shown in Figure 6.11 are the same just presented for the filtered case.

By looking at the density plots of N_2^+ and N^+ (Figures 6.11c and 6.11d), it can be immediately inferred the nature of these high-frequency oscillations, which are due to ion density

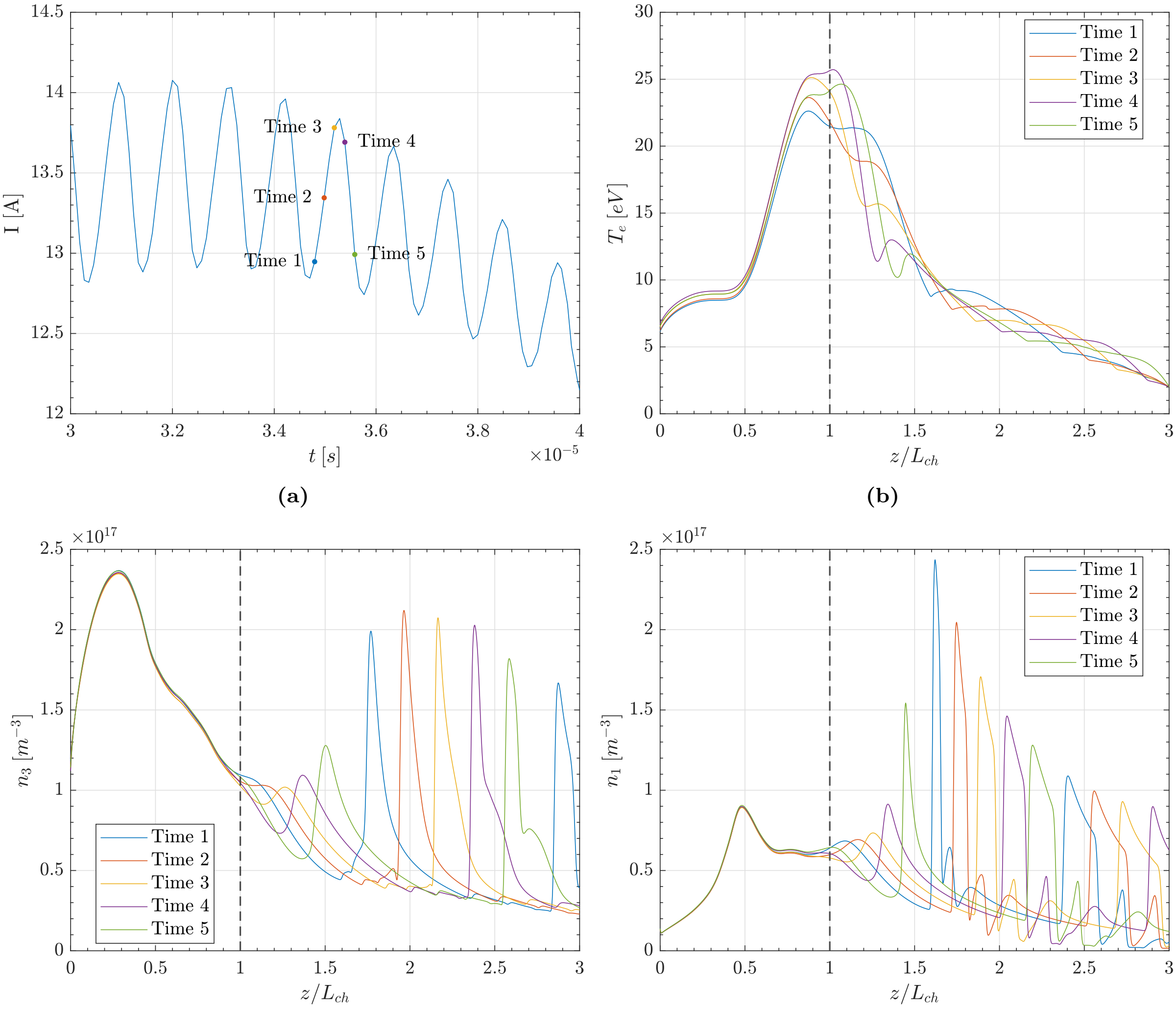

(a) **(b)**

(c) **(d)**

Figure 6.11: Simulated plasma behaviour at 5 time stamps along a single high-frequency oscillation. (a) Discharge current with the selected time stamps indicated. (b) Electron temperature T_e. (c) N_2^+ density n_3. (d) N^+ density n_1. The black dashed line indicates the channel exit.

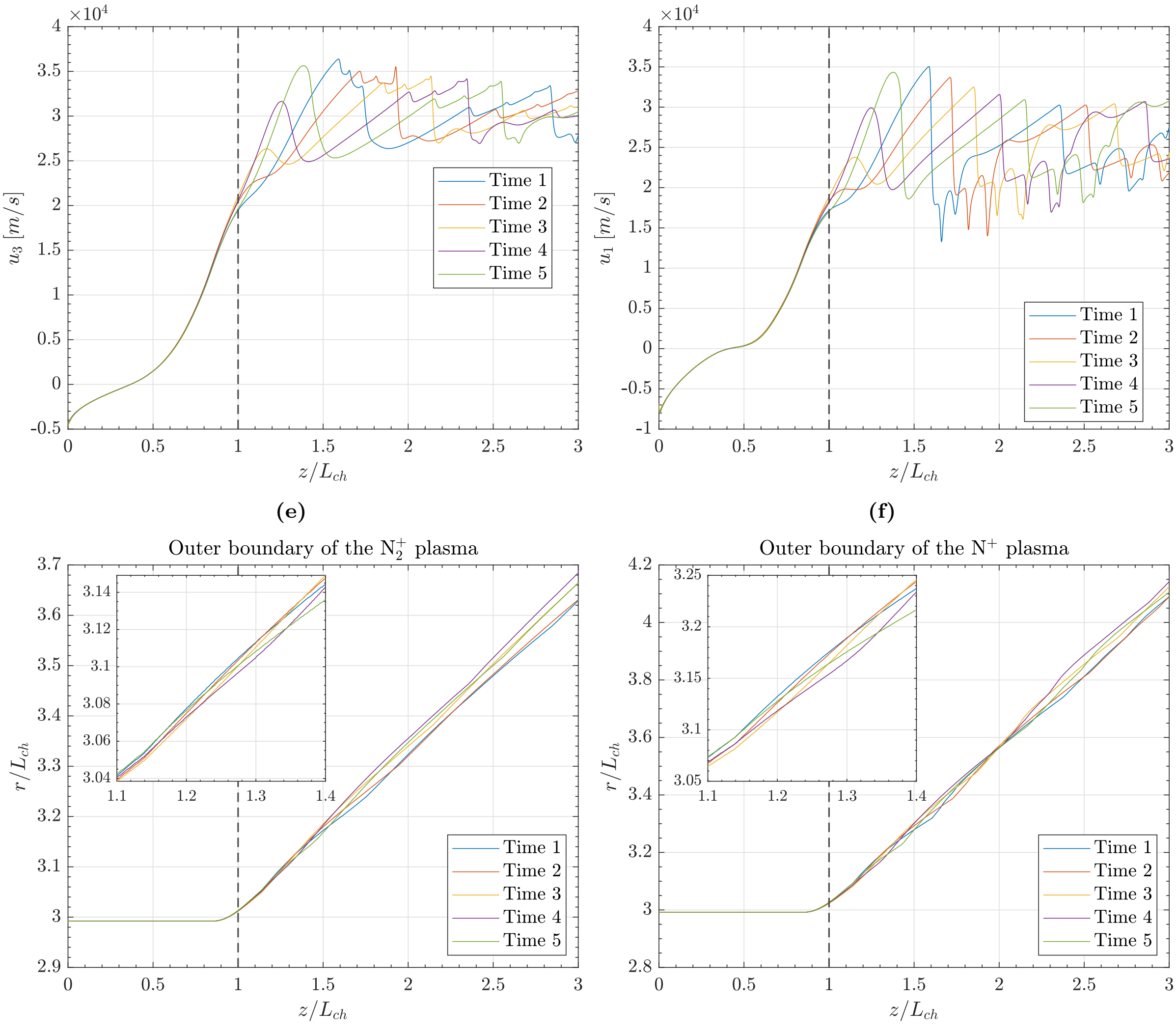

(e) **(f)**

(g) **(h)**

Figure 6.11 (cont.): (e) N_2^+ velocity u_3. (f) N^+ velocity u_1. (g) Two-dimensional plot (axial-radial) of the N_2^+ plasma outer boundary. (h) Two-dimensional plot (axial-radial) of the N^+ plasma outer boundary.

waves that develop at the channel exit and then propagate in the plume. Depending on the ion species, these waves show different characteristics in terms of propagation speed, amplitude and shape. In general, the lighter the species, the slower the propagation speed and the higher the amplitude reached relatively to the density peak inside the channel. Also, lighter species appear more prone to oscillation, showing stronger initial responses which then rapidly decrease, resulting in more disturbed wave profiles.

The effects of the density waves reflect on all other plasma quantities either individually, as in the case of the ion velocities (Figures 6.11e and 6.11f), or all summed together, as for the electron temperature (Figure 6.11b) and density (not shown). Regarding the velocities, due to ion momentum conservation in the plume, these sharply decrease at the corresponding density peak location, thus creating a higher velocity wavefront right behind it. As expected, lighter species determine higher and more disturbed wavefronts.

As the electron temperature is concerned, the profiles of Figure 6.11b highlight the formation of a slight peak right outside the channel, which periodically collapses in the plume. In this process, the profile widens and the former peak becomes a temperature bulge propagating in the plume while rapidly losing amplitude. Note that the propagation speed of this bulge is higher than any of the ion density waves.

As introduced above, these oscillations appear to propagate with speeds very similar to the corresponding ion velocities, thus suggesting a tight relationship with the ion transit instability observed by many authors [11, 12, 13]. Clearly, this behaviour is mainly recognizable in those plasma quantities individually related to each ion species (i.e. ion density and velocity), while a mixed response is produced in collective quantities as the electron temperature. Indeed, the presence of several ions produces oscillations with different velocities and amplitudes, which contribute together to their evolution.

In conclusion, the outer boundaries of the N_2^+ and N^+ plasmas are presented in Figures 6.11g and 6.11h, respectively. In both cases, even though the oscillations develop strongly in the plume, the effects on divergence remain limited. Some oscillatory trends can be indeed recognized during the expansion but they do not cause significant variations.

Validation

The model results are now compared with the experimental data in order to understand their accuracy. As mentioned in the discussion above, the filtered dataset is employed rather than the original one, so as to align the obtained plasma properties with the triple Langmuir probe data. In any case, the high-frequency oscillations predicted by the model could not have been experimentally investigated by any of the testing apparatuses employed in the campaign, and therefore not even validated.

The comparison of electron temperature, plasma potential and the four ion densities (obtained from the probe electron density by using the constant ratios in Eq. 6.1) is reported in Figure 6.12. It is noted that the plasma potential measured by the probe refers to the system ground, while the simulated one is relative to the cathode plasma potential. By neglecting the small potential drop across the cathode (i.e. cathode coupling potential), a quantitative comparison between the two is achieved by rescaling the measured one with the known cathode reference potential of $-19.2\,\mathrm{V}$.

By looking at the plots, it immediately appears how much the impossibility of resolving probe measurements inside the perturbed region affects the comparison. However, important considerations about the results can still be made. In particular, starting from the electron temperature (Figure 6.12a), the agreement between the data is remarkable, with the simulated profile matching the knee point of the experimental data and then following it very closely. Note that the very final decrease in the simulated value is a feature of the model, also visible in the work of Giannetti et al. [10]. This is not affected by the particular plume description implemented, if any, as it solely depends on the fact that the computational domain is limited and a boundary conditions has to be placed there (i.e. $T_{eV} = 2\,\mathrm{eV}$, in this case). By extending the domain up to 5 channel length, for instance, the simulated profile would most likely show a closer resemblance to the final slope of the measured Te profile.

Regarding the plasma potential (Figure 6.12b), the model predicts a very alike profile with respect to the probe result, even though the drop locates too upstream. Specifically, the model appears to struggle in reproducing the typical downstream shift of the acceleration region seen in magnetically shielded thrusters and here confirmed by the probe data. This is believed to be mainly due to the simplified (one-dimensional) description of the electric field, which prevents it from extending in the near-plume.

As the ion densities are concerned (Figures 6.12c to 6.12f), the simulated ones appear all underestimated with respect to the experimental evidence. However, it is worth mentioning that the model results are radially averaged, while the probe ones are measured on the channel centerline. Therefore, the relatively limited difference observed in the plots (approximately between two to four times) could be well in agreement with this fact. Nevertheless, as for

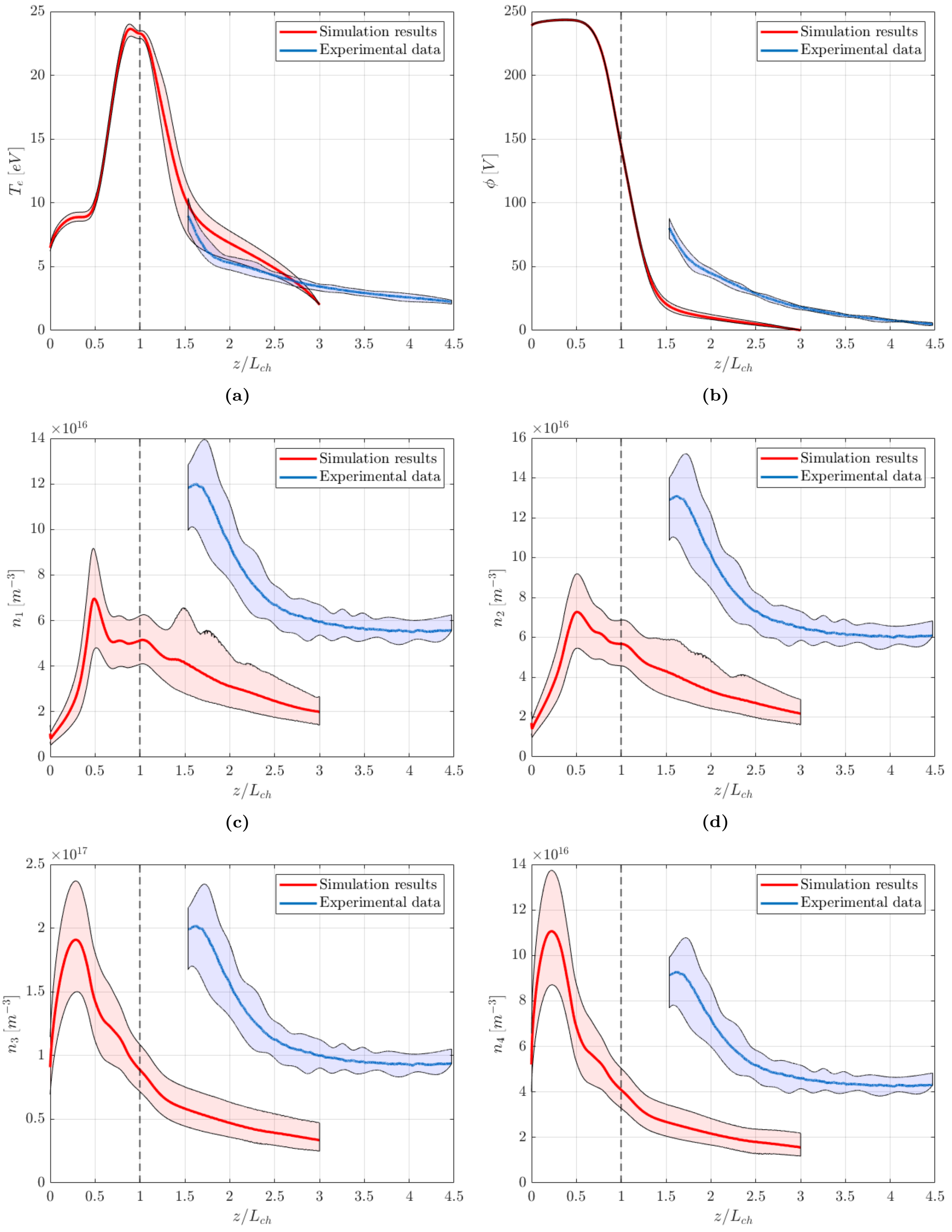

(a)

(b)

(c)

(d)

(e)

(f)

Figure 6.12: Comparison between the simulation results and the experimental data obtained from the triple Langmuir probe. (a) Electron temperature T_e. (b) Plasma potential ϕ. (c) N^+ density n_1. (d) O^+ density n_2. (e) N_2^+ density n_3. (f) O_2^+ density n_4. Solid lines represent the time-averaged values, while the shaded areas envelope the local oscillations of the various properties. The black dashed line indicates the channel exit.

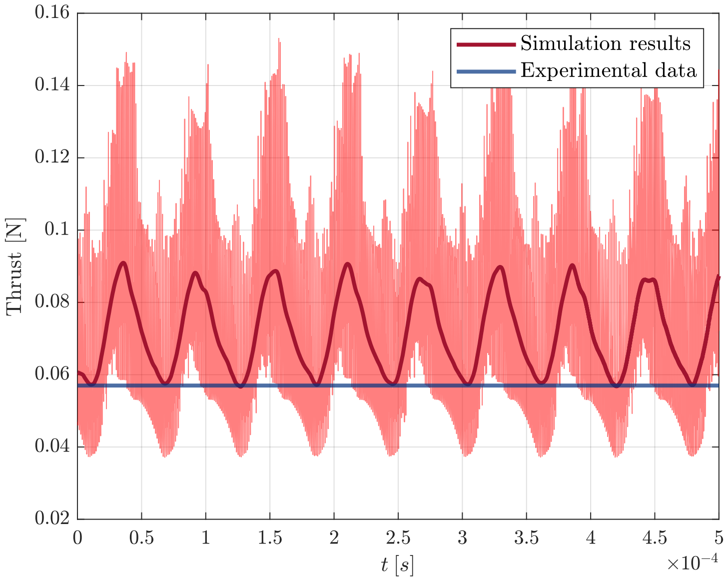

Figure 6.13: Thrust comparison between experimental measurements and simulation results. The red solid line represents the time-averaged value of the unfiltered thrust signal (shaded in light red) predicted by the model. The blue solid line represents the experimentally measured thrust of 57 mN.

the case of the potential, the simulated density profiles also appear excessively upstream with respect to experimental ones, as also observed by Giannetti et al. in the xenon case. Finally, note that the implementation of plume expansion determines curves qualitatively very similar to the probe profiles, further confirming the importance of this phenomenon.

Then, it is also presented a brief comparison about the device thrust. Theoretically, the thrust generated (in vacuum) can be written as a sum of the contributions of each ion species produced, i.e.

$$F = \sum_{i=1}^{4} m_i A_i n_i u_i^2 \bigg|_{z=z_f} \tag{6.2}$$

Note that the computation is carried out at the plume domain boundary (i.e. $z = z_f$), where the electron pressure can be safely neglected and thus the thrust only depends on the momentum flux.

By using Eq. 6.2, the predicted total thrust is compared with the experimentally measured value of 57 mN in Figure 6.13. It is mentioned that although even in reality the thrust should oscillate as a consequence of breathing mode, the thrust stand employed (see Subsection 5.2.1) provides accurate measurements only during transients, i.e. upon shutting off the thruster. Therefore, only an average value could be retrieved.

By looking at the time-averaged value of the simulated thrust, the model appears to generally overestimate this quantity, which reaches the experimental value exactly at the bottom of the oscillation. Then, it increases up to about 90 mN, which corresponds to a $\approx 58\%$ increment. Overall, this result appears quite promising and, due to the moderate difference, possibly even more accurate than what a constant value for the experimental thrust could suggest.

6.2.2. Ion-ion Streaming Instabilities Considered

It is now presented the case study in which ion-ion streaming instabilities in the plasma presheath are implemented in the model formulation, following the approach outlined in Section 4.4.

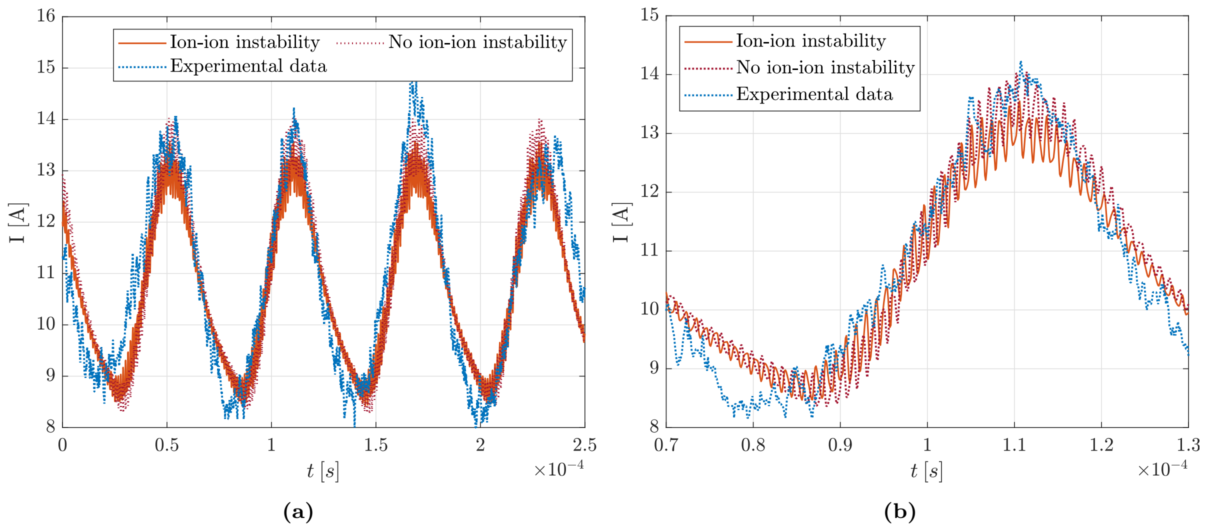

Figure 6.14: Discharge current comparison between experimental measurements (blue) and simulation results in case ion-ion streaming instability is considered (orange) or not (red). (a) Signal profiles over a 0.25 ms time interval. (b) Detail of the signal profiles highlighting the high-frequency components of the waves.

By just accounting for the instabilities without calibrating again the model, the discharge current predicted is reported in Figure 6.14, in comparison with the previous one and the experimental signal. The agreement with the description neglecting these phenomena is striking, with only a minimal reduction in amplitude observed (i.e. 0.2 A at the bottom and 0.5 A at the top). Also, the oscillatory behaviour appears unchanged, showing very similar frequencies for both breathing mode and high-frequency oscillations. Note that the amplitude of the latter appears also unaltered.

Although it was initially planned to calibrate again the model implementing the new description, these results safely confirm that it is not necessary. Moreover, recall that the reference portion of the experimental current has been selected arbitrarily over a significantly disturbed signal (Figure 6.2). Therefore, a small amplitude reduction, as the one here observed, results negligible in comparison. Rather, by keeping the same set of calibration parameters it is possible to isolate the effect of these instabilities on the modelled physics. Note however that the small value assigned to α during calibration strongly reduces the effects of wall interaction phenomena with respect to what predicted by the general theory discussed in Section 3.3, regardless of the presheath description. Consequently, the already limited differences brought by the inclusion of these instabilities in the classical sheath model are expected to be further reduced.

This prediction is confirmed by Figure 6.15, which reports a comparison between the model results (filtered case) obtained with the two descriptions. Note that only the electron temperature and density are presented, being the plasma parameters exhibiting the greatest variations. To better highlight them, are also proposed two plots showing their percent variations (Figures 6.15c and 6.15d). Overall, the differences appear barely distinguishable, with only a minor reduction in the peak values of both quantities (and also in those of the ion densities, as a consequence) observed in case ion-ion instability is taken into account. These are due to a slightly higher electron power loss caused by the modified Bohm criterion and to the consequent reduced ionization. The major effect observed is however a variation in the oscillation frequency, which appears increased to a small extent.

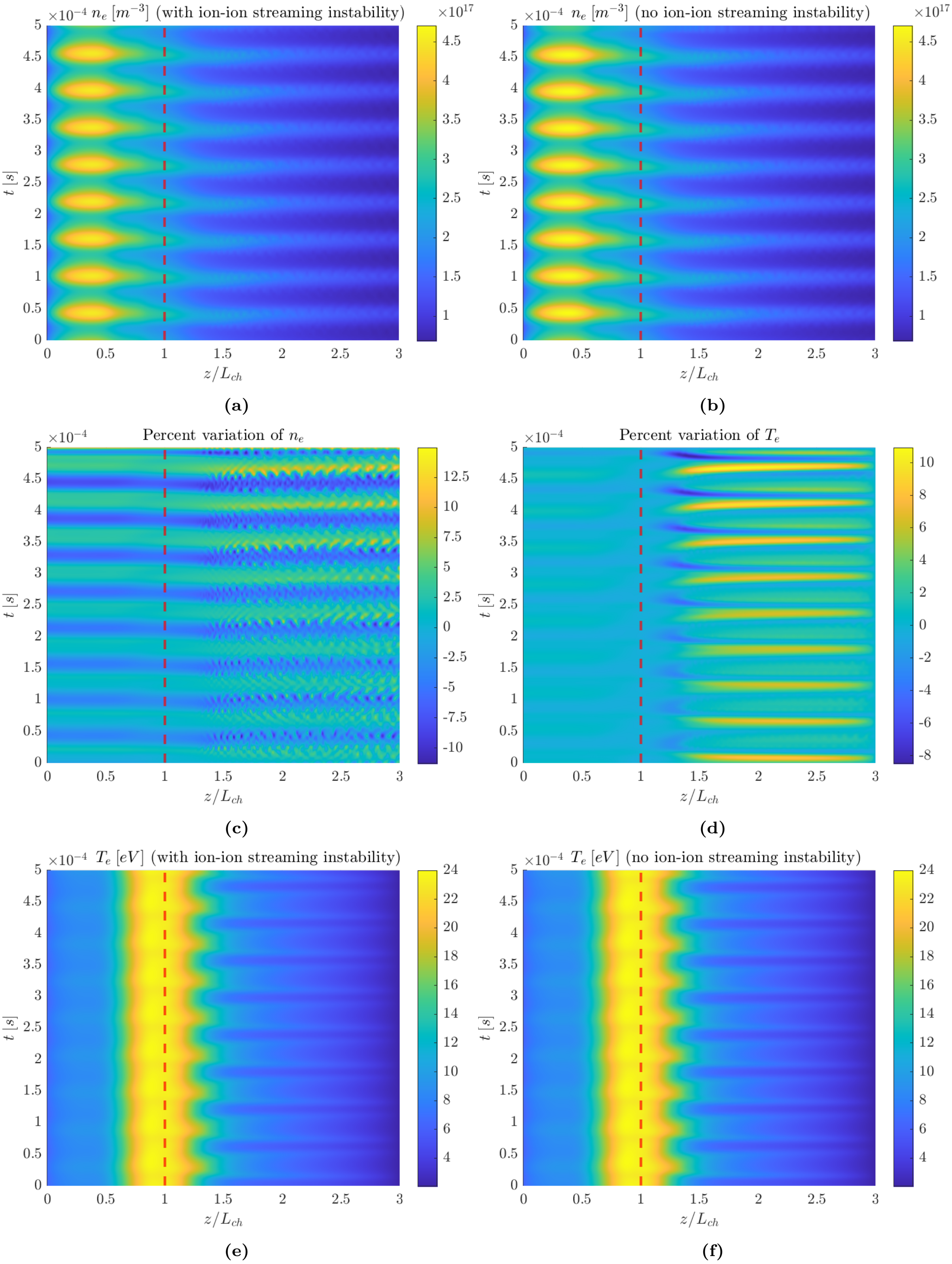

Figure 6.15: Comparison between model results in case ion-ion streaming instability are considered or not. All results are filtered, i.e. frequencies above 120 kHz are removed. (a)-(b) Electron density n_e. (c) Percent variation of n_e caused by the inclusion of instability. (d) Percent variation of T_e caused by the inclusion of instability. (e)-(f) Electron temperature T_e. The red dashed line indicates the channel exit.

6.3. Summary

To conclude the discussion about numerical and experimental results, it is here presented a brief summary.

Firstly, the most suitable experimental point to be used as a reference for model calibration and validation (i.e. that with $B_{max} = 0.57B^*$) was defined. This was selected based on the discharge current signal, which exhibited a well-defined and relatively noise-free behaviour, although not constantly sustained in time.

Then, the triple Langmuir probe measurements were presented and analysed, so as to retrieve the probed plasma parameters. These however showed strong perturbations even outside the channel due to the thruster magnetic shielding configuration and the strong azimuthal electron current present. As a consequence, it was concluded that the probe measurements could be considered reliable only from 13.4 mm downstream the channel exit, thus preventing the experimental validation of the model results in the most critical regions.

Successively, the results of model calibration in absence of ion-ion streaming instability were presented, showing a predicted discharge current accurately reproducing the major features of the reference experimental signal. Specifically, breathing mode low-frequency oscillations at $f_{BM} = 16.36\,\text{kHz}$ appeared to be reliably replicated, while high-frequency components predicted in the 0.9-1.7 MHz frequency range could not be experimentally resolved due to background noise. However, the spatiotemporal analysis of the model results suggested a very tight relationship of the latter with the ion transit instability observed in literature [11, 12, 13].

After having assessed the successful model calibration, the predicted space-time plasma properties were thoroughly investigated. These allowed to identify all the dynamic mechanisms responsible for breathing mode ionization instability, thus confirming the physical validity of the current formulation in reproducing these oscillations, even in complex multispecies plasmas.

Then, the predicted plasma properties were compared with the results obtained from the triple Langmuir probe measurements. Apart from the high-frequency oscillations, which could not be experimentally validated due to the probe signal filtering, the comparison resulted satisfactory, even if significantly limited due to the probe perturbation to the plasma. In particular, all the properties compared (i.e. species densities, electron temperature and plasma potential) were reproduced at the correct order of magnitude, although the model failed in shifting outside the channel the thruster acceleration region, as it typically happens in magnetically shielded devices. As a consequence, both the plasma potential and the density profiles were predicted too upstream. In addition, the latter also appeared underestimated by 2-4 times with respect to the probe results. Regarding the electron temperature, the agreement was remarkable, with both magnitude and inclination tightly matching.

Overall, the (limited) comparison did not allow a complete experimental validation of the model, as the conditions inside the channel could not be even explored with the triple Langmuir probe. However, the remarkable agreement with the discharge current signal undoubtedly confirmed the physical validity of the numerical description implemented.

Regarding the model results obtained while accounting for ion-ion streaming instability, these appeared barely distinguishable from the ones neglecting it. This result was indeed expected as the magnetic-shielding configuration of the thruster has required a significantly low value of α to achieve a successful calibration, thus limiting the plasma-wall interactions. Even though in the particular case studied this kinetic instability does not play a significant role, simulations of non-shielded thrusters are expected to show a higher sensitivity to it, in line with the variations observed in Section 3.3.

7

Conclusions

7.1. Summary

The main objective of the research presented in this work was to investigate the plasma behaviour in an air-propelled Hall thruster by means of numerical modelling and experimental measurements. Starting from exploration of both the internal chemical interactions and sheath description appropriate for a multispecies nitrogen/oxygen plasma, a numerical model of the thruster has been developed and calibrated. Then, its results have been thoroughly investigated and compared with the experimental measurements of the device, achieving a satisfactory (partial) validation. Therefore, the main objective of this work can be considered accomplished.

As an added note, in view of the results accomplished, this research will lead to the publication of a journal article in the following months.

The specific research questions driving the activities and the investigation presented in this work are now answered.

- **Q1**: *Which are the characteristics of a multispecies nitrogen/oxygen plasma in terms of internal particle interactions and how can these be modelled?*

  Simulating the internal particle interactions in a nitrogen/oxygen plasma represents a very challenging task due to the presence of a multitude of plasma species mutually affecting each other while exchanging energy and momentum.

  Chemically, the high reactivity of both nitrogen and oxygen determines a continuous interplay between reagents and products. In order to correctly model these interactions in the thruster model, at first these were thoroughly investigated from experimental and numerical data collected from literature. In this way it was possible to identify the dominant processes and also the main ion products to be accounted for in the model, namely N_2^+, N^+, O_2^+ and O^+. Then, by means of the Boltzmann equation solver Bolsig+ [25] the reaction rates required by the thruster model were computed.

  Physically, these interactions may get involved in several kinetic instabilities, with different effects on either the microscopic or the macroscopic scale of investigation. In particular, the growth of an instability-enhanced friction among positive ion species in the plasma presheath was identified as a major kinetic phenomenon for the simulation of an air-propelled Hall thruster. Therefore, a numerical model originally developed by Baalrud et al. [3] was extended to the four-ions case needed. The numerical scheme identifies the onset of unstable plasma modes, as the ions move toward the sheath edge, by solving the plasma dielectric function for the dispersion relation. Once this instability arises, the differential flow between the ion species freezes and new conditions are reached at the sheath edge. In this work, the development of this kinetic instability in a nitrogen/oxygen plasma was thoroughly investigated, assessing the relevant conditions necessary for its onset and the effects produced on the sheath formulation.

- **Q1.1**: *How does the Bohm sheath criterion modify in a nitrogen/oxygen plasma?*

  The underdetermined nature of the Bohm sheath criterion in presence of multiple ion species was solved by modelling ion-ion streaming instabilities in the presheath. The so obtained ion velocities at the sheath edge showed to be noticeably different from the respective sound speeds, especially at high electron temperatures. Specifically, while accounting for secondary electron emission (SEE) from the channel walls, these showed an overall shift toward the common system sound speed, which ranged from a 4-6% decrement for N^+ and O^+ to an increment of well over 10% for N_2^+ and O_2^+ in the space-charge saturated (SCS) regime.

- **Q1.2**: *Which chemical reactions should be considered for accurately describing the nitrogen/oxygen plasma of a Hall thruster?*

  From the analysis of the chemical interactions relative to a nitrogen/oxygen plasma investigated in literature, it was preliminary concluded that only electron-impact reactions must be necessarily accounted for, due to their dominant cross-sections. This fact then allowed to safely neglect collisions between heavy species in the model, and thus reactions between nitrogen and oxygen products. Also, resonant charge-exchange (CEX) collisions were neglected, but mainly because of the lack of sufficient data rather than their limited influence on the plasma. Among the electron-impact collisions, these were all thoroughly explored apart from recombination, which is believed to become significant in a time scale longer than the ion residence time in the thruster. The investigation concluded that for each neutral particle present in the plasma (i.e. N_2, N, O_2 and O), the reactions to be included in the thruster model are: single ionization, excitation, elastic momentum transfer and dissociation/dissociative ionization (when applicable). The only unimportant electron-impact reactions identified were those producing multiply charged positive ions or negative ions, namely electron attachment and dissociative attachment.

- **Q2**: *How can the existing time-dependent 1D model be modified to simulate the SITAEL HT5k thruster operating with air?*

In order to modify the numerical model developed by Giannetti et al. [10] for simulating an air-propelled HT5k Hall thruster, several modelling options were evaluated. Indeed, the multispecies sheath description and the physical characteristics of this device have introduced elements of novelty with respect to the original model, thus requiring a dedicated modelling effort. In particular, regarding the sheath description, the presheath/sheath model developed for the air plasma case, which numerically computes the effects of ion-ion streaming instabilities on the Bohm criterion, could not be coupled with the thruster model directly due to the great computational power required. Consequently, the results were firstly computed separately for a dense range of electron temperatures and ion density ratios, and then used to create a five-dimensional mapping. This was then interpolated and the resulting interpolant implemented in the model.

Regarding the magnetic shielding configuration of the thruster, although this feature is not resolvable by a one-dimensional model, it was still employed the real magnetic field profile measured on the channel centerline, so as to keep a general approach. In addition, in view of the expected downstream shift of the plasma properties caused by the magnetic field profile, a plume expansion description for both ions and neutrals was implemented. Ions were assumed to radially expand with their sound speeds at the channel exit, while neutrals expansion was described based on their thermal agitation. For the same reason, the domain was also extended further downstream in the plume to two channel lengths from the thruster exit plane. This allowed to provide enough space for the plasma to develop outside the channel.

Finally, regarding the centrally mounted cathode position, the cathode boundary conditions in the plume were kept unchanged. Indeed, although even this feature cannot be resolved in 1D, it was assumed that the equipotentialization and isothermalization of the magnetic field lines allow to retrieve them at the channel centerline.

  - **Q2.1**: *Which are the model calibration parameters needed in the new formulation?*

    The new formulation of the model implementing air operation essentially necessitates the same calibration parameters used in the original setting, namely the anode temperature T_a, the wall interaction coefficient α and the space-dependent profile of ν_{anom}, i.e. the anomalous electron collision frequency. However, the implementation of neutral expansion in the plume required to add among the free parameters also the accommodation factor AF, defining the scaling between injection velocity and effective radially averaged velocity. Indeed, even if also $T_a = T_n$ defines the neutral velocities, it also governs their plume expansion and these two features required to be independently described.

  - **Q2.2**: *Can the originally employed numerical scheme effectively describe the behaviour of a multispecies nitrogen/oxygen plasma?*

    Apart from the inclusion of a plume expansion description, the original numerical scheme employed by Giannetti et al. [10] for simulating xenon operation proved partially suitable also for describing the behaviour of a multispecies nitrogen/oxygen plasma. However, the presence of an additional source term in the ion momentum conservation equation, dependent on the density ratio derivative, caused the flux vector splitting (FVS) method, employed for spatial discretization, to fail in solving the respective Euler problems. As a solution, a more robust Rusanov finite-volume method was employed.

- **Q3**: *How can the data collected during the PFG experimental campaign be analysed and merged to completely characterize the thruster functioning?*

In order to process all the data collected during the experimental campaign, apart from the emission spectra which are processed by the RAM-EP project partners (i.e. VKI and CNR), a specific analysis methodology extending to the case of a nitrogen/oxygen plasma was outlined. This revealed the limits of the currently employed analysis approaches in dealing with multiple ion species, which cannot not be often distinguished by the instrument. As a consequence the employment of species-selective devices, able to provide the relative ion concentrations in the plasma, was identified as a fundamental requisite for analysing the data.

Regarding Faraday probes, the presence of multiple ion species is believed to only affect the effective probe collection area, by specifically varying the ion-impact SEE yield of the molybdenum internal surfaces. This influences the computation of the total current density collected, and thus of the thruster beam current. In order to solve this uncertainty, both the ion density ratios at the probe locations and the individual ion kinetic energies would be needed. The latter specifically are required to estimate the individual ion-impact SSE yields from experimental material relationships. These can be theoretically obtained from the RPA measurements.

As the RPA probe is concerned, its measurements suffer from the same uncertainties on the effective collection area characterizing the Faraday probes. However, its filtering action allows to distinguish the current contributions relative to ion populations with different energies. Upon very clean measurement, this feature would then theoretically allow to distinguish the ion energy distribution functions (IEDF) of atomic and molecular ions, as the former are believed to be generated further downstream in the plasma, thus experiencing a lower accelerating potential.

Lastly, regarding the triple Langmuir probe, it was presented a simple analysis approach using the direct model of the current collected by a charged electrode immersed in a plasma. This consisted in extending the parametrization of Mausbach [124] to four ion species, without however applying the considerations about presheath instabilities treated in this work. In order to be solved, this model would require the ion density ratios along the probe trajectory. While these could not be experimentally measured, a trade-off was identified in the employment of the local ones resulting from the spectrometers results. Finally, in order to carry out a more accurate analysis, the theoretical structure of a more advanced Bayesian inference approach was outlined, which allows to compensate for plasma inhomogeneities between the probe electrodes while consistently keeping track of the uncertainties. However, this could not be later applied to the results due to time limitations.

  - **Q3.1**: *Which are the limits encountered in the testing phase and how do they affect the thruster experimental characterization?*

    The major limitation encountered in the preliminary testing phase was the impossibility of including the $E \times B$ probe (i.e. a device filtering the ions based on their charge over mass ratio) in the test setup. In particular, a fixed installation was excluded due to bad material compatibility between some pure iron probe components and atomic oxygen, and the installation of the vacuum chamber movable rack could not be pursued because of weight constraints. The consequences on the thruster experimental characterization have been severe, precluding the possibility to experimentally define the ion density ratios in the far plume. Therefore, the only option remaining for analyzing Faraday probes and RPA results is that of simulating them.

    In addition, another limit encountered in the testing phase was the recurrent failure of the actuated rail system responsible for the spectrometer tube lens translation. The cause were identified in the excessive plume divergence during air operation, which thus invested the system with detrimental effects. As a consequence, most of the characterized operating points lack the emission spectral acquisitions.

- **Q4**: *Can the developed model successfully reproduce the plasma dynamics experimentally captured in an HT5k Hall thruster operating with air?*

During model calibration, it was possible to accurately reproduce the major features of the discharge current signal measured in an oscillating operating point. The agreement was remarkable concerning both the oscillation amplitude and mean value, and the characteristic frequency components. Specifically, breathing mode low-frequency oscillations at $f_{BM} = 16.36\,\text{kHz}$ appeared to be reliably reproduced, even though only a limited signal portion could be used as a reference, since this ionization instability was not completely sustained yet in the plasma at the operating point investigated. Also, the simulated current presented high-frequency components in the 0.9-1.7 MHz frequency range superimposed to the main breathing mode instability that could not be experimentally resolved due to background noise.

The analysis of the space-time plasma properties predicted by the model allowed to identify all the dynamic mechanisms responsible for breathing mode. This result alone can be considered a partial physical validation of the model, which confirms to include all the physics necessary to reproduce breathing mode oscillations even in complex multispecies plasmas.

Then, the predicted plasma properties were compared with the results obtained from the fast-diving triple Langmuir probe measurements. Apart from the high-frequency oscillations predicted, which could not be experimentally validated due to the probe signal filtering, the comparison resulted satisfactory, even if significantly limited due to the probe perturbation to the plasma. In particular, all the properties compared (i.e. species densities, electron temperature and plasma potential) were reproduced at the correct order of magnitude, although the model failed in shifting outside the channel the thruster acceleration region as it typically happens in magnetically shielded devices. As a consequence, both the plasma potential and the density profiles were predicted too upstream. In addition, the latter also appeared underestimated by 2-4 times with respect to the probe results. Regarding the electron temperature, the agreement appeared remarkable, with both magnitude and inclination tightly matching.

Overall, the (limited) comparison did not allow a complete experimental validation of the model, as the conditions inside the channel could not be even explored with the triple Langmuir probe. However, the remarkable agreement with the discharge current signal undoubtedly confirmed the physical validity of the numerical description implemented.

- **Q4.1**: *Which are the model limits in reproducing the thruster behaviour?*

  The main limitations of the model in reproducing the real thruster behaviour are all essentially related with its one-dimensional description. In particular, starting from the radially averaged plasma quantities, this necessary approximation strongly simplifies the predicted results which, in a real thruster, possibly show even significant radial variations, especially in the plume. This feature also prevented a completely quantitative comparison with the triple Langmuir probe results, which are measured at the channel centerline.

  Another model limitation, which become particularly apparent by dealing with the experimental results of a magnetically shielded thruster, is the radial magnetic field profile assumed. Indeed, based on the difficulties encountered in reproducing the downstream shift of the high-temperature region typical of these configurations, a two-dimensional description of the field topology appears fundamental. Contextually, the lack of a radial component of the electric field in the model near-plume region significantly affects the plasma expansion behaviour, which also led to predicted divergences strongly underestimated with respect to the experimental evidence.

7.2. Recommendations for Future Work

The research carried out in this work represents an initial point for the numerical and experimental investigation of Hall thrusters operating with air. In the following are presented the main aspects which should be addressed in future works willing to continue on this path.

7.2.1. 2D Numerical Model in Magnetic Coordinates

The main follow-on work probably concerns the extension of the numerical model employed to a two-dimensional description. Especially for the case study investigated in this work, the magnetic shielding configuration of the real thruster and the need of modelling a representative plume have significantly exposed the limitations of a one-dimensional description with radially averaged plasma quantities. Extending the domain in two dimensions will allow to incorporate the real topology of the magnetic field, and thus consistently resolve the plasma behaviour also in the radial direction. To do so, the domain has to be discretized in magnetic coordinates (i.e. on a Magnetic Field Aligned Mesh (MFAM)), which is the general approach also followed in literature by many research groups [8].

7.2.2. Time-varying Anomalous Electron Collision Frequency

Another general aspect related to the numerical model that should be improved is the description of the anomalous electron collision frequency ν_{anom}. The high sensitivity of this parameter observed during model calibration confirmed the key role played by this quantity in governing the plasma dynamics. It is worth mentioning that in literature are present several studies supporting this observation, both numerical [110] and experimental [130]. Hence, by adopting a time-varying description of the effects of plasma turbulence on electron transport, it is expected to considerably improve the model representativeness. Note that the development of a self-consistent description of these effects is a long-standing problem interesting the modelling of Hall thrusters in general, and not only the specific scheme employed in this work.

7.2.3. Neutral Momentum Conservation Equation and CEX collisions

Model calibration highlighted the great influence of neutrals on the plasma behaviour. However, the adopted description was limited under many aspects, especially regarding the constant neutral velocities assumed. It is then recommended to expand the modelling of these species, which are many in the air plasma case investigated in this work, by solving the respective momentum conservation equations. This would then allow not only to better track their evolution, but also to meaningfully introduce other important phenomena as CEX collisions. Indeed, while discussing the model results, it was observed that the neutrals behaviour appeared partially uncoupled from the other species in the plume due to the lack of neutralization mechanisms there. In reality this coupling is partially maintained by these resonant processes, which elastically exchange ion and neutral charges. Therefore, it is believed that their implementation would shed new light on plume ionization instabilities.

7.2.4. PFG Experimental Characterization

A main research question initially foreseen for this work ultimately remained unanswered: "*Are the PFG plume composition and velocity representative of the atmospheric flow expected in the thermosphere?*". Due to the limited representativeness shown by the numerical model results, especially in the plume, in order to precisely answer this query, it will be necessary to experimentally characterize the plasma by means of the measurements collected. However, as highlighted in Chapter 5, the multispecies nature of this plasma greatly complicates the data analysis and, due to the lack of species-selective diagnostics apart from the spectrometers, will also require modelling some plume properties, such as the densities. In general, it is recommended the implementation of a global Bayesian inference approach incorporating all the diagnostic measurements. In this way, it will be then possible to consistently track their combined uncertainties while marginalizing the unknown quantities.

7.2.5. Ion-ion Streaming Instability on Langmuir Probes

In this work, the current collected by the triple Langmuir probe electrodes was modelled as a sum of individual contributions from the ion species (Subsection 5.2.5). However, the study of presheath instabilities in Chapter 2 highlighted that ion-ion interactions may happen, thus possibly modifying the general assumptions of both thin sheath theory and Laframboise sheath solution [123]. It is then recommended to extend the theory of instability-enhanced friction also to the analysis of these probes, in order to determine the influence on results.

A

Error Function

The (Gauss) error function [131] is a special entire function, widely used in probability and statistics, defined as the integral of a normal distribution from 0 to ζ, which is in general a complex number, scaled such that $\mathrm{erf}(\pm\infty) = \pm 1$, i.e.

$$\mathrm{erf}(\zeta) = \frac{2}{\sqrt{\pi}} \int_0^{\zeta} e^{-t^2} dt \tag{A.1}$$

Figure A.1 shows its real and imaginary components, as well as its magnitude, for a complex argument ζ.

The main properties of erf are

$$\begin{aligned} \mathrm{erf}(-\infty) &= -1 \qquad & \mathrm{erf}(+\infty) &= 1 \\ \mathrm{erf}(-\zeta) &= -\mathrm{erf}(\zeta) \qquad & \mathrm{erf}(\zeta^*) &= [\mathrm{erf}(\zeta)]^* \end{aligned}$$

where * here means complex conjugation.

Similarly to Eq. A.1, the complementary error function is defined as

$$\mathrm{erfc}(\zeta) = \frac{2}{\sqrt{\pi}} \int_{\zeta}^{\infty} e^{-t^2} dt = 1 - \mathrm{erf}(\zeta) \tag{A.2}$$

Finally, it can be also defined an imaginary error function erfi, such that

$$\mathrm{erfi}(\zeta) = -i \cdot \mathrm{erf}(i\zeta) = \frac{2}{\sqrt{\pi}} \int_0^{\zeta} e^{t^2} dt \tag{A.3}$$

which implies

$$\mathrm{erf}(i\zeta) = i \cdot \mathrm{erfi}(\zeta) = \frac{2i}{\sqrt{\pi}} \int_0^{\zeta} e^{t^2} dt \tag{A.4}$$

In this work, $\mathrm{erfi}(\zeta)$ is used to describe and solve in MATLAB the plasma dispersion function $Z(\zeta)$, as it is shown in Appendix B.

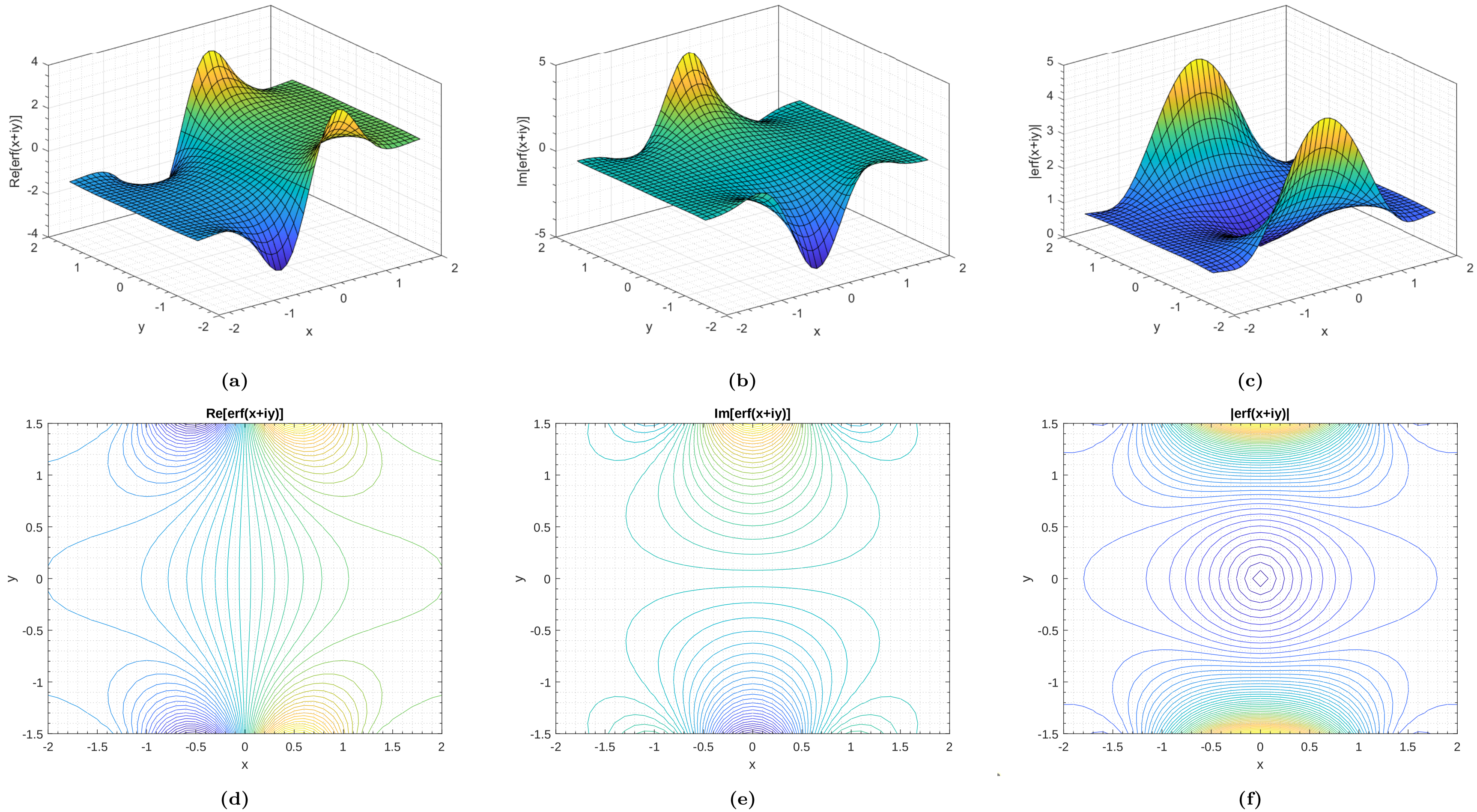

Figure A.1: Surface and contour plots of the error function erf(ζ) for a complex argument $\zeta = x + iy$. (a)/(d) Real component. (b)/(e) Imaginary component. (c)/(f) Magnitude.

B

Plasma Dispersion Function

The plasma dispersion function is a special function often recurring during the study of oscillations in hot plasmas once the particle velocities are assumed to follow a Maxwellian distribution [48]. In particular, it is defined as

$$Z(\zeta) = \frac{1}{\sqrt{\pi}} \int_{-\infty}^{\infty} \frac{e^{-t^2}}{t-\zeta} dt \tag{B.1}$$

for $\mathrm{Im}(\zeta) > 0$ and as the analytic continuation of this expression for $\mathrm{Im}(\zeta) \leq 0$. An alternative representation is

$$Z(\zeta) = 2ie^{-\zeta^2} \int_{-i\zeta}^{\infty} e^{-t^2} dt = i\sqrt{\pi} e^{-\zeta^2} \mathrm{erfc}(-i\zeta) \tag{B.2}$$

which has the advantage of being valid for every ζ. This expression also shows the close relationship between plasma dispersion function and error function (see Eq. A.2). Figure B.1 shows its real and imaginary components, as well as its magnitude, for a complex argument ζ.

It is worth noticing that the plasma dispersion function $Z(\zeta)$ is just a scaled form of the Faddeeva function $w(\zeta)$, i.e.

$$w(\zeta) = e^{-\zeta^2} \mathrm{erfc}(-i\zeta) \tag{B.3}$$

By exploiting Eqs. A.2 and A.3, $Z(\zeta)$ can be rewritten as

$$Z(\zeta) = i\sqrt{\pi} e^{-\zeta^2} \left(1 + \mathrm{erfi}(\zeta)\right) \tag{B.4}$$

which is the formulation used in this work for the MATLAB implementation.

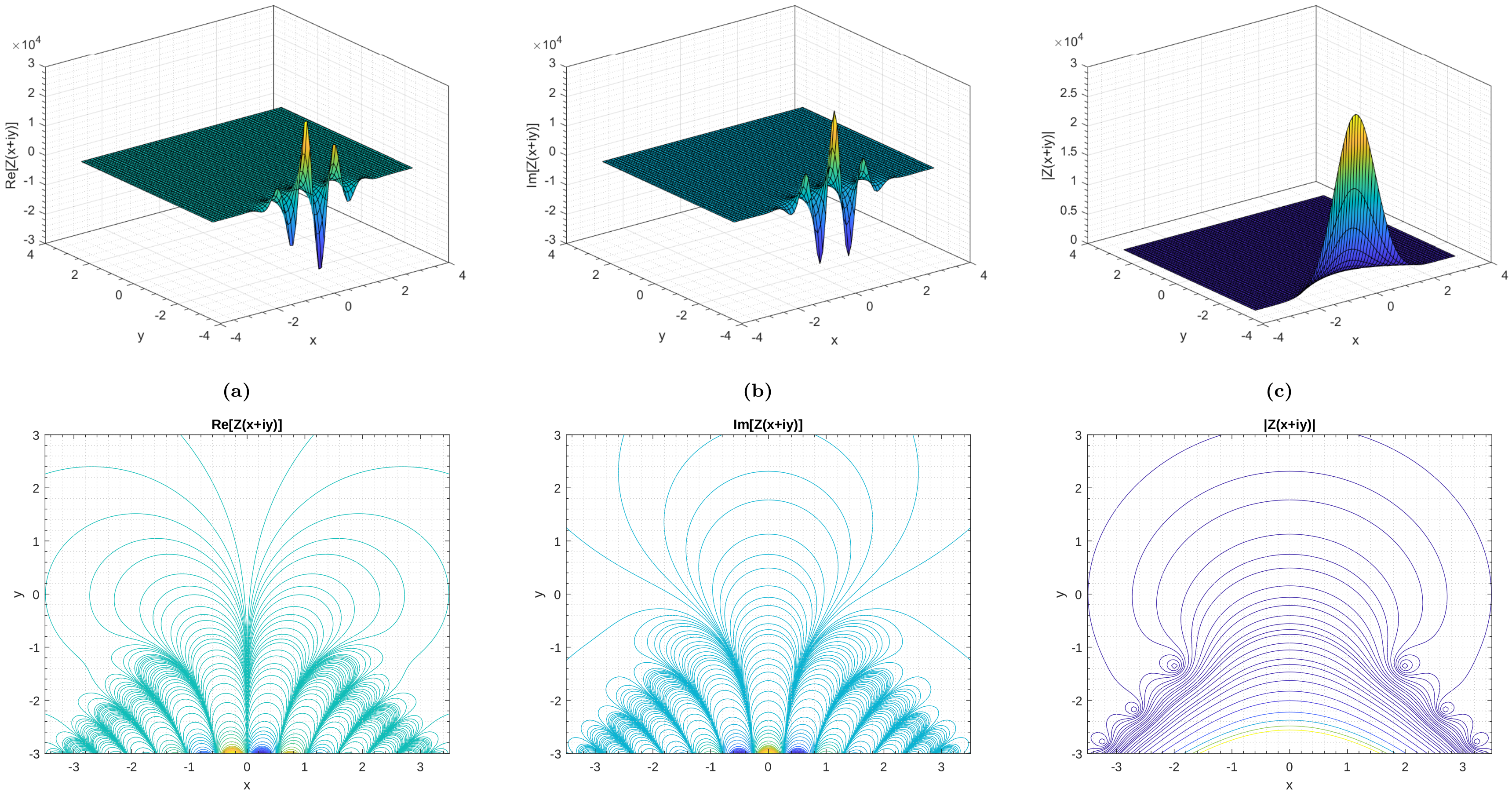

(a) (b) (c)

(d) (e) (f)

Figure B.1: Surface and contour plots of the plasma dispersion function $Z(\zeta)$ for a complex argument $\zeta = x + iy$. (a)/(d) Real component. (b)/(e) Imaginary component. (c)/(f) Magnitude. Note in plot (f) the zeroes of $|Z(\zeta)|$ diagonally aligned.

C

Electronic Terms for Atoms and Molecules

This Appendix provides a brief overview about electronic terms for both atoms and diatomic molecules. The discussion is expected to provide, in a concise manner, the basis needed to fully understand the topics addressed in Chapter 3.

C.1. Atoms [132]

Electron characteristics in atoms can be described based on four quantum numbers. The first is the principal number n, indicating its energy and consequently the electron shell as well as, on average, its distance from the nucleus. Then, there is the angular momentum quantum number l, which defines the type of orbital (e.g. s, p, d, f for respectively $l = 0, 1, 2, 3$) with a value ranging between 0 and $n - 1$. Thirdly, the magnetic quantum number m_l describes the specific orbital orientation. Different orbitals have different possible orientations and the value of m_l ranges between $-l$ and l with integer steps. Finally, the last quantum number is the spin number s, which describes the spin angular momentum of the electron within the orbital and it has only values $\pm 1/2$. For the Pauli exclusion principle, only electrons with different spin number can be located in the same orbital, thus limiting their maximum number to two.

In order to fully describe the energy level of an atom, it is not sufficient to determine its electron configuration. Indeed, this only describes how the electrons distribute in the orbitals (only taking into account the quantum numbers n and l), while no information is given about the orbital and spin angular momenta. To complete the description it is used the so called *term symbol*

$$^{2S+1}L_J \tag{C.1}$$

in which L is the total orbital quantum number (or total orbital angular momentum), S is the total spin quantum number (or total spin angular momentum) and J is the total angular momentum (quantum number). While a detailed discussion about quantum mechanics goes beyond the scope of this work, the way these quantities are calculated is based on the specific quantum numbers of all the atom electrons. In particular, in Table C.1 are shown the possible values assumed by L and S in case of atoms with 1, 2 or 3 electrons (the procedure can be extended indefinitely) in unfilled orbitals. Indeed, full orbitals do not contribute to the overall angular momentum and can be discarded in the process. Regarding J, its range of values is $L + S, L + S - 1 \ldots, |L - S|$ for each possible value of L and S. Note that, because of the possible ranges of these three quantities, their respective combinations may determine a variety of term symbols, even for the same electron configuration.

In general, in the therm symbol, instead of the numerical value of L it is placed a corresponding letter, which follows the same nomenclature used for orbitals. Therefore, for instance,

Table C.1: Calculation of the total quantum numbers L and S for atoms with 1, 2 or 3 electrons in unfilled orbitals. The procedure can be extended for more electrons by adding one at a time.

Term	No. of e$^-$	Notation	Range (integers)
L	1	L_1	l_1
	2	L_2	$l_1+l_2, l_1+l_2-1, \ldots, \|l_1-l_2\|$
	3	L_3	$L_2+l_3, L_2+l_3-1, \ldots, \|L_2-l_3\|$
S	1	S_1	s_1
	2	S_2	$s_1+s_2, s_1+s_2-1, \ldots, \|s_1-s_2\|$
	3	S_3	$S_2+s_3, S_2+s_3-1, \ldots, \|S_2-s_3\|$

the letters corresponding to $L = 0, 1, 2, 3, 4$ are respectively S, P, D, F, G. For higher values of L, the letters proceed in alphabetical order with all the remaining ones apart from J which is excluded.

Another characteristic of the term symbol, which is often included, is *parity*. This is calculated as

$$P = (-1)^{\sum_i l_i} \tag{C.2}$$

where the index i refers to all the electrons. Clearly, only an odd number of electrons in odd orbitals (e.g. p, f) can determine $P = -1$ (i.e. *odd parity*), while all other cases have $P = 1$ (i.e. *even parity*). Conventionally, there are two ways of indicating the parity of a term symbol. The first consists in adding an o superscript on the right only in case of odd parity, while omitting it otherwise. The second convention consists in adding a u or g subscript on the right in case of odd or even parity, respectively.

Finally, the superscript $2S + 1$ in the term symbol represents the spin multiplicity, which classifies the electronic states of atoms in *singlets* $(2S + 1 = 1)$, *doublets* $(2S + 1 = 2)$, *triplets* $(2S + 1 = 3)$, *quartets* $(2S + 1 = 4)$, and so on.

As a general comment, often in literature the term symbols are reported omitting the J subscript/s, so as to keep a brief notation.

C.2. Diatomic Molecules [132, 133]

As diatomic molecules (or even molecules in general) are concerned, while the discussion shares many similarities with that presented for atoms, it also substantially grows in complexity. Indeed, molecules have planar or even spatial geometries that allow rotational and vibrational movements of the bounds. These, together with various possible symmetries and transitions, require a high level of detail to accurately describe the molecule state.

In general, electronic terms for molecules are composed by a letter followed by the molecular term symbol

$$^{2S+1}\Lambda^{(+/-)}_{\Omega,(g/u)} \tag{C.3}$$

which shares some similarities with that for atoms. Its components are now described for the case of diatomic molecules.

Contrarily to atoms, the lack of a spherical symmetry in linear molecules results in a variable orbital angular momentum of the electrons, depending on the axis. In particular, this momentum remains constant only with respect to the internuclear axis of the molecule and thus the use of the total orbital quantum number L is discarded in favour of its projection on that axis: M_L. This quantity can take the values

$$M_L = L, L-1, L-2, \dots, -L \tag{C.4}$$

Molecule states which only differ in the sign of M_L have the same energy (as a reversed direction of the electron motion does not change the system energy) and are labelled *degenerate*. On the other hand, states with different $|M_L|$ have in general widely varying energies. Therefore, it is defined

$$\Lambda = |M_L| \tag{C.5}$$

which for the specific case of a diatomic molecule becomes

$$\Lambda = |M_{L_1} + M_{L_2}| \tag{C.6}$$

Consequently, it holds that

$$\Lambda = 0, 1, 2, \dots, L_1 + L_2 \tag{C.7}$$

As for the case of L in atomic term symbols, each value of Λ corresponds to a capital Greek letter. Specifically, molecular states with $\Lambda = 0, 1, 2, 3, \dots$ are respectively designated as $\Sigma, \Pi, \Delta, \Phi, \dots$ states. Note that all states with $\Lambda \neq 0$ (i.e. non-Σ states) are doubly degenerate as M_L can results in two values $\pm\Lambda$.

Regarding the spin angular momentum, as for the case of atoms, even in molecules the total quantum number S is calculated from the s of all the electrons in unfilled orbitals. Therefore, for diatomic molecules it results

$$S = S_1 + S_2, S_1 + S_2 - 1, \dots, |S_1 - S_2| \tag{C.8}$$

However, while in atoms and in molecular Σ states the total spin S is fixed in space, in degenerate states (i.e. $\Pi, \Delta, \Phi, \dots$) only its projection along the internuclear axis M_S remains constant. This is completely analogous to the case of L and its projection M_L. Then, the possible range for M_S is defined as

$$M_S = S, S-1, S-2, \dots, -S \tag{C.9}$$

Note that the value and sign of M_S extend the number of possible degenerate states as the pairs (M_L, M_S) and $(-M_L, -M_S)$ are degenerate but different from the degenerate pairs $(M_L, -M_S)$ and $(-M_L, M_S)$. All these pairs are grouped together by means of the quantum number Ω, which is defined as

$$\Omega = \Lambda + M_S \tag{C.10}$$

where different values of Ω generally correspond to states with different energies.

In addition to the quantum numbers just discussed, the molecular states are distinguished also based on to their symmetry properties, which depend on those of the field in which te electrons move. In this context are briefly discussed *reflection* (+/- superscript) and *parity* (g/u subscript).

As the (+/-) superscript is concerned, this is only used for non-degenerate states (i.e. Σ states) to indicate whether or not they are symmetric with respect to reflections about the infinite planes passing through the internuclear axis (i.e. + sign) or they are antisymmetric (i.e. - sign). Conversely, molecular terms with $\Lambda \neq 0$ always have a symmetric state and an antisymmetric one which, having the same energy, are considered together, thus omitting the (+/-) superscript.

On the other hand, parity is related to the symmetry with respect to the molecular center of mass which, in diatomic molecules, bisects the internuclear axis. Symmetric states are defined even (i.e. g) while antisymmetric ones are odd (i.e. u). In practice, the same expression used for parity in atoms (Eq. C.2) also hold for molecular states, where i refers to all the molecule electrons.

Finally, as for atoms, the term $2S + 1$ represents the state spin multiplicity, which defines singlets, doublets, triplets, etc...

In order to complete the description of molecular electronic terms, it is now briefly discussed the letter placed in front of the term symbol (e.g. $A\ ^3\Sigma_u^+$). Its purpose is that of labelling the different electronic states, mainly based on their energy level. In particular, X conventionally indicates the ground state and higher states with the same multiplicity are labelled $A, B, C, D, \ldots$ in order of increasing energy. In case of higher states with different multiplicity, the letters $a, b, c, d, \ldots$ are instead used. The only exception to this rule is N_2 which, even if its ground state is $X\ ^1\Sigma_g^+$, has singlets conventionally designated with $a, b, c, d, \ldots$ and triplets with $A, B, C, D, \ldots$.

D

Numerical Model Results

D.1. Unfiltered

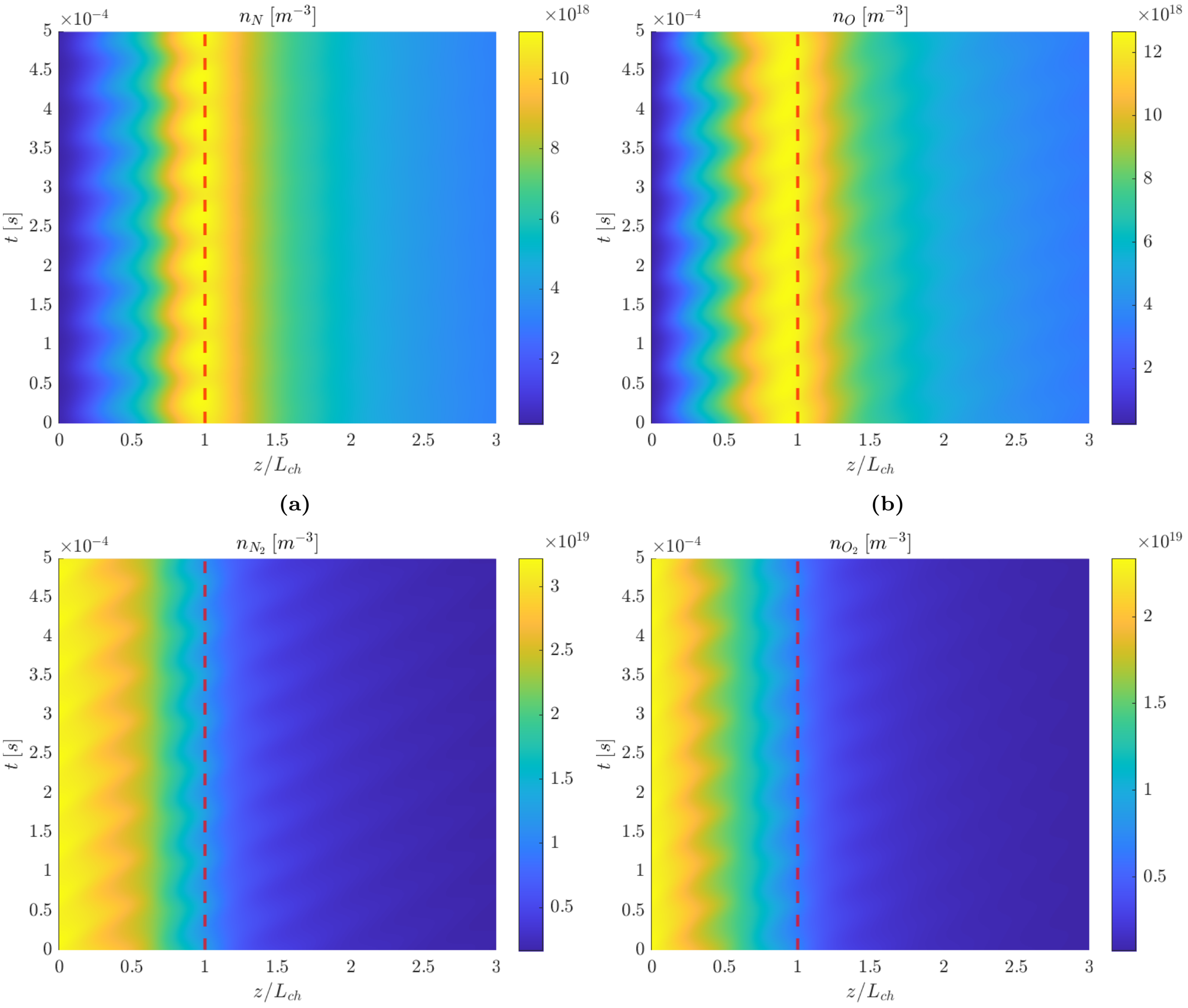

(a)

(b)

(c)

(d)

Figure D.1: Unfiltered simulated plasma behaviour in space and time. (a) N density n_N. (b) O density n_O. (c) N_2 density n_{N_2}. (d) O_2 density n_{O_2}. The red dashed line indicates the channel exit.

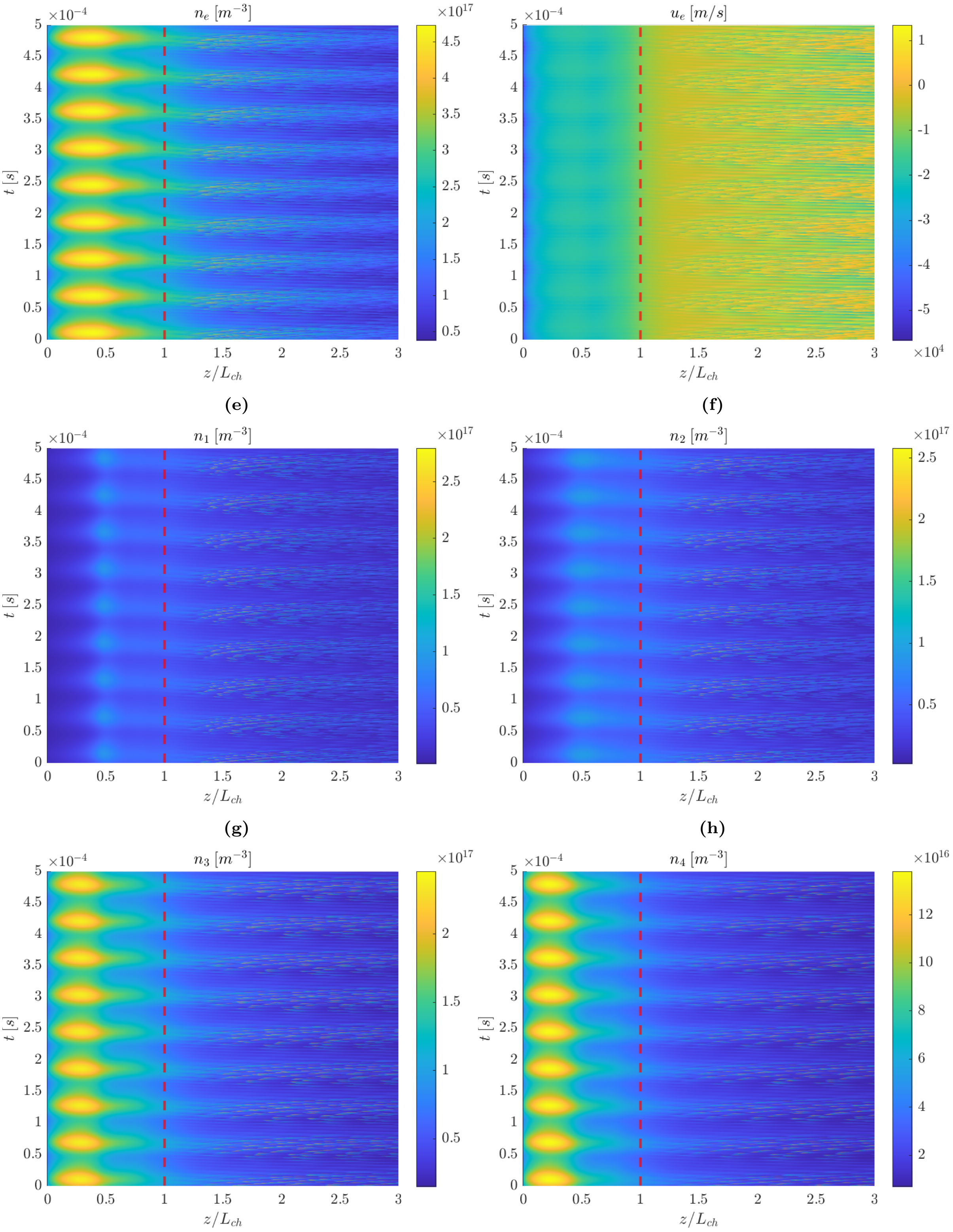

(e) **(f)** **(g)** **(h)** **(i)** **(j)**

Figure D.1 (cont.): (e) Electron density n_e. (f) Electron velocity u_e. (g) N^+ density n_1. (h) O^+ density n_2. (i) N_2^+ density n_3. (j) O_2^+ density n_4.

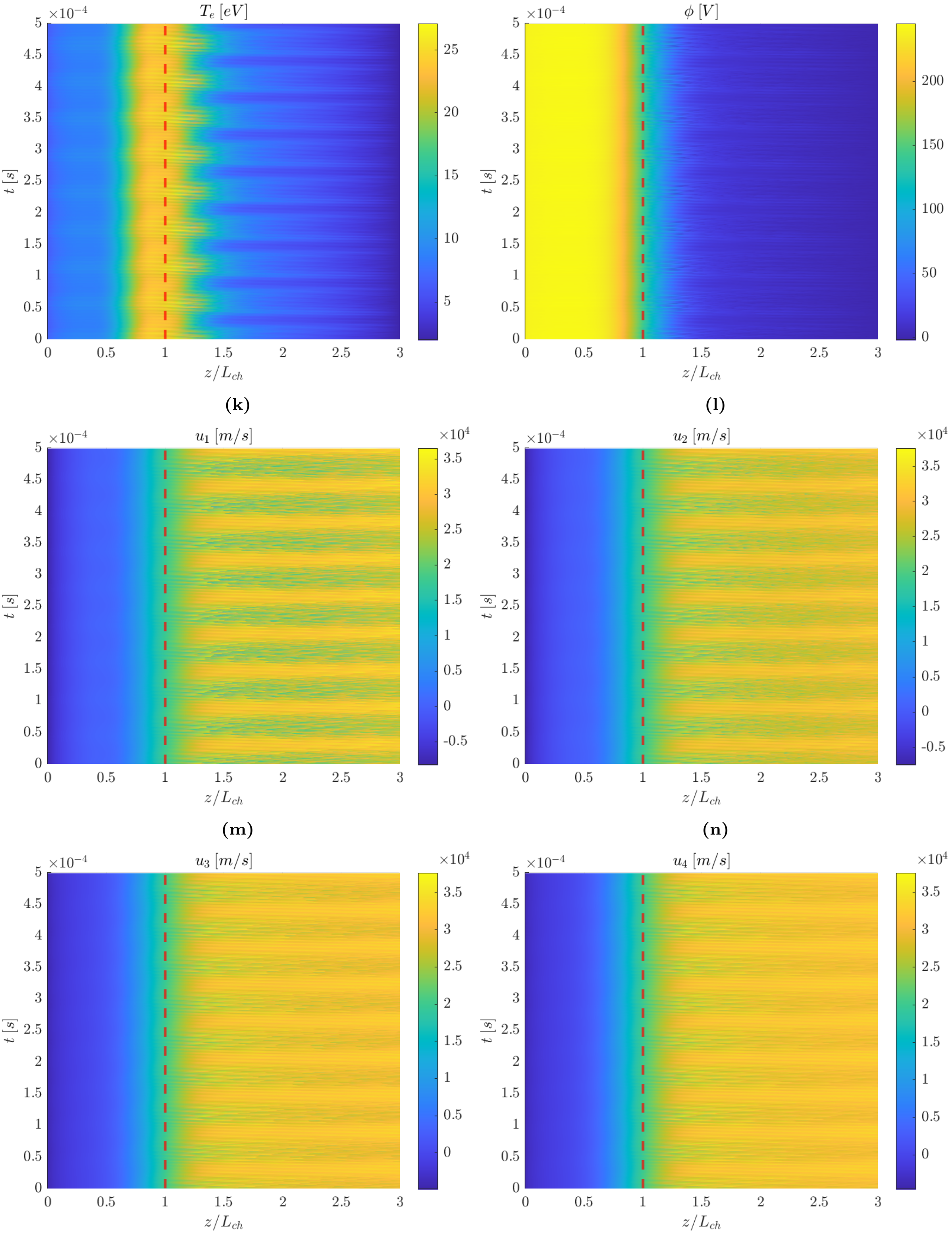

(k) (l)

(m) (n)

(o) (p)

Figure D.1 (cont.): (k) Electron temperature T_e. (l) Plasma potential ϕ. (m) N^+ velocity u_1. (n) O^+ velocity u_2. (o) N_2^+ velocity u_3. (p) O_2^+ velocity u_4.

D.2. Filtered (oscillations above 120 kHz removed)

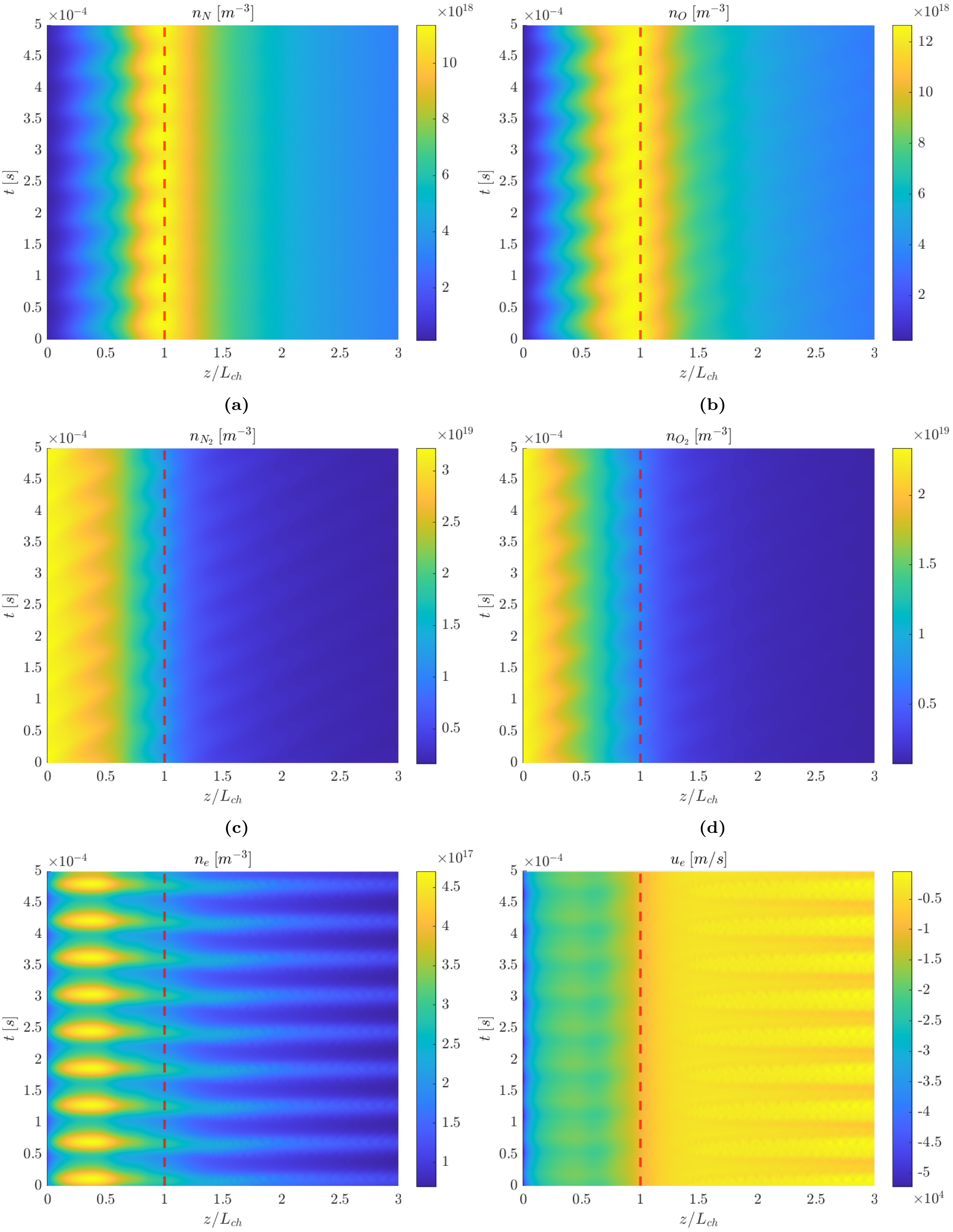

(a) **(b)** **(c)** **(d)** **(e)** **(f)**

Figure D.2: Filtered simulated plasma behaviour in space and time. Frequencies above 120 kHz are removed. (a) N density n_N. (b) O density n_O. (c) N_2 density n_{N_2}. (d) O_2 density n_{O_2}. (e) Electron density n_e. (f) Electron velocity u_e. The red dashed line indicates the channel exit.

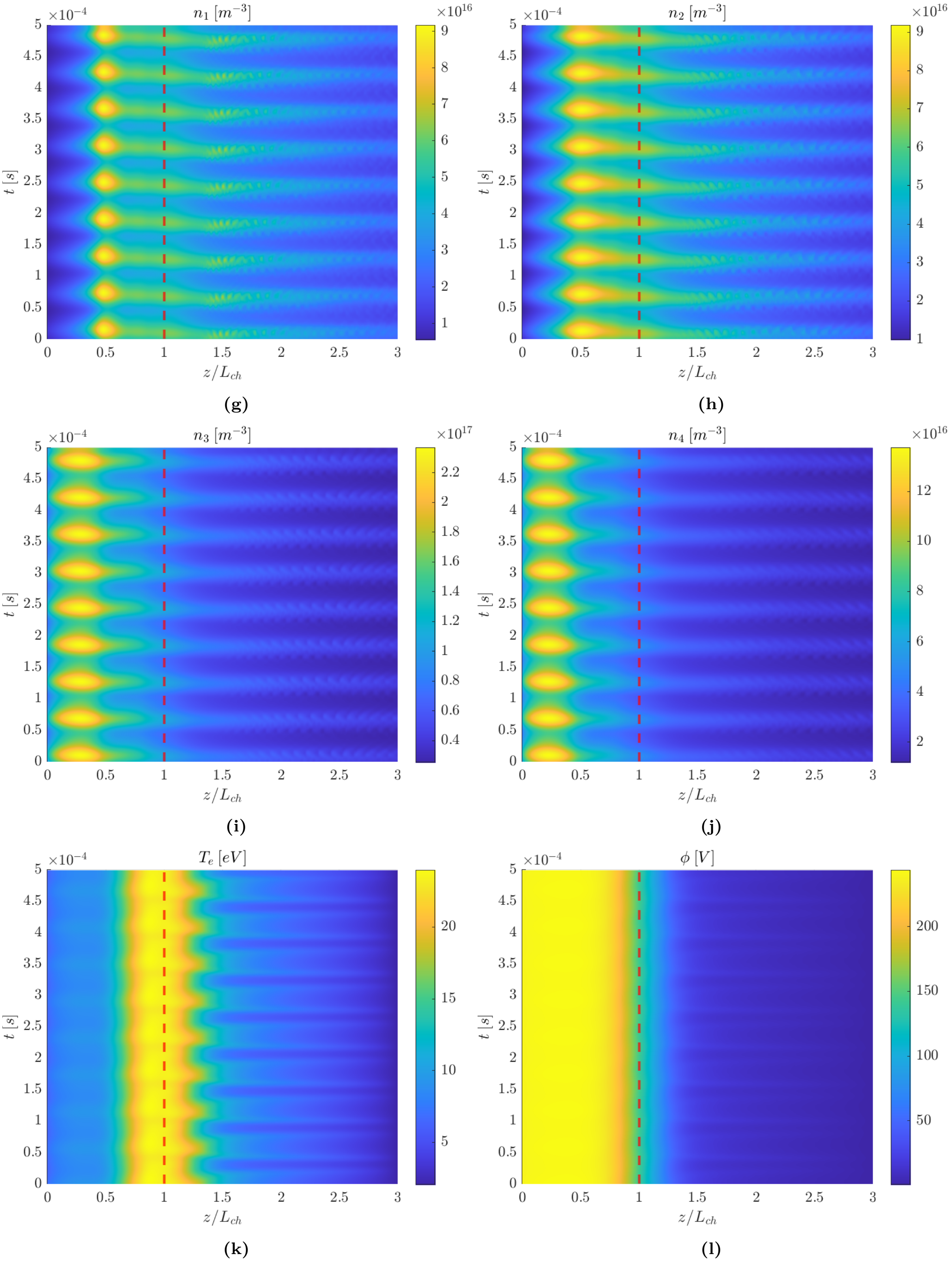

(g) **(h)** **(i)** **(j)** **(k)** **(l)**

Figure D.2 (cont.): (g) N^+ density n_1. (h) O^+ density n_2. (i) N_2^+ density n_3. (j) O_2^+ density n_4. (k) Electron temperature T_e. (l) Plasma potential ϕ.

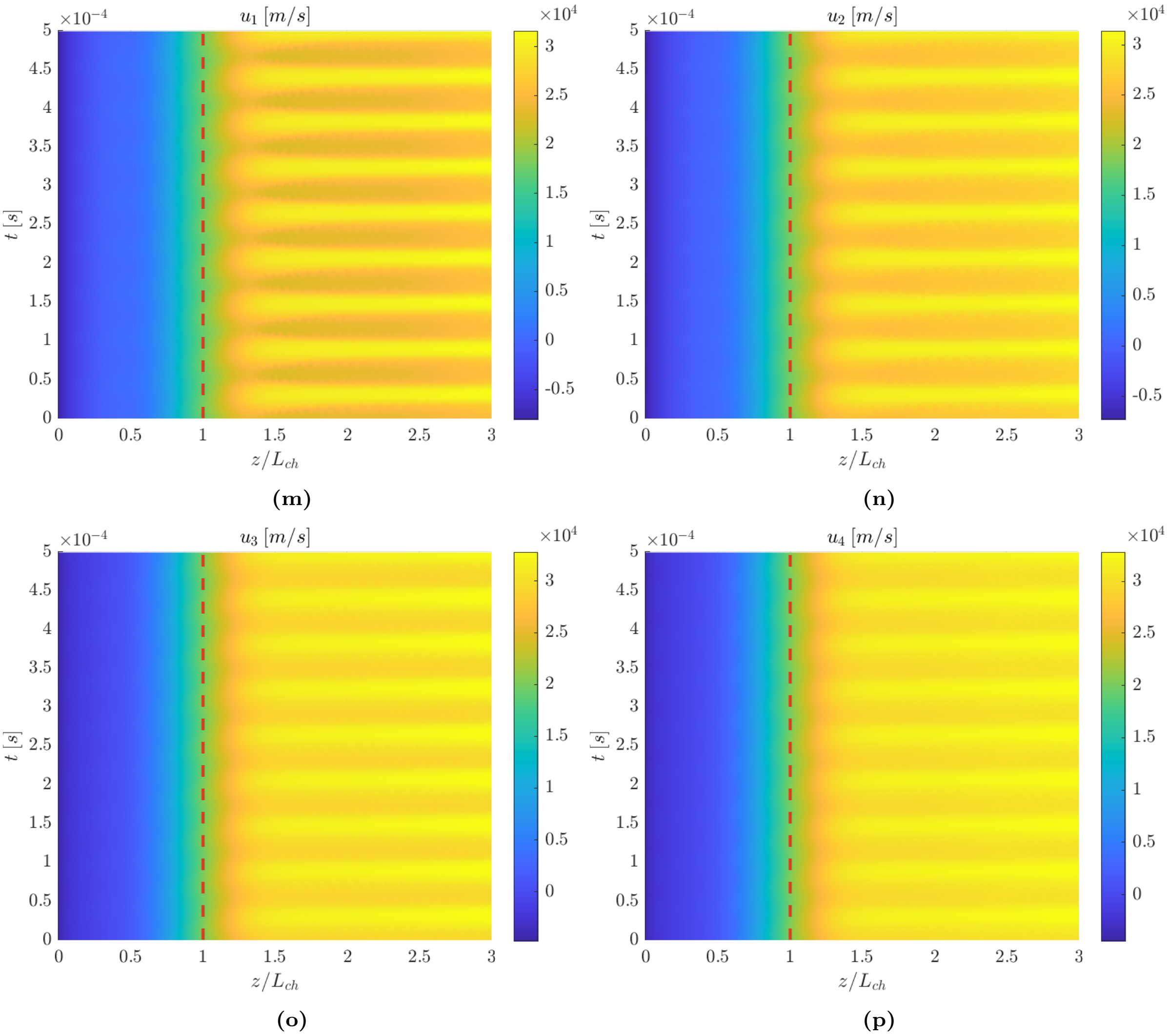

(m) **(n)** **(o)** **(p)**

Figure D.2 (cont.): (m) N$^+$ velocity u_1. (n) O$^+$ velocity u_2. (o) N$_2^+$ velocity u_3. (p) O$_2^+$ velocity u_4.

References

[1] V. Giannetti, E. Ferrato, A. Piragino, M. Reza, F. Faraji, M. Andrenucci, and T. Andreussi, "HT5k Thruster Unit Development History, Status and Way Forward," in *36th International Electric Propulsion Conference, Vienna, Austria*, 2019.

[2] E. Ferrato, V. Giannetti, A. Piragino, M. Andrenucci, T. Andreussi, and C. A. Paissoni, "Development Roadmap of SITAEL's RAM-EP System," in *36th International Electric Propulsion Conference, Vienna, Austria*, vol. 9, 2019.

[3] S. D. Baalrud, C. C. Hegna, and J. D. Callen, "Instability-enhanced collisional friction can determine the Bohm criterion in multiple-ion-species plasmas," *Physical review letters*, vol. 103, no. 20, p. 205002, 2009.

[4] C. S. Yip, N. Hershkowitz, and G. Severn, "Experimental test of instability-enhanced collisional friction for determining ion loss in two ion species plasmas," *Physical review letters*, vol. 104, no. 22, p. 225003, 2010.

[5] S. Barral, G. Cifali, R. Albertoni, M. Andrenucci, and L. Walpot, "Conceptual Design of an Air-Breathing Electric Propulsion System," in *Joint Conf. of 30th Int. Symp. on Space Technology and Science, 34th Int. Electric Propulsion Conf. and 6th Nano-Satellite Symp.*, 2015.

[6] K. Hara and I. G. Mikellides, "Characterization of low frequency ionization oscillations in Hall thrusters using a one-dimensional fluid model," in *2018 Joint Propulsion Conference*, 2018.

[7] D. Pérez Grande, *Fluid modeling and simulation of the electron population in Hall Effect Thrusters with complex magnetic topologies*. PhD thesis, Universidad Carlos III de Madrid (uc3m), 2018.

[8] F. Taccogna and L. Garrigues, "Latest progress in Hall thrusters plasma modelling," *Reviews of Modern Plasma Physics*, vol. 3, no. 1, pp. 1–63, 2019.

[9] H. C. Dragnea, A. L. Ortega, H. Kamhawi, and I. D. Boyd, "Simulation of a Hall Effect Thruster Using Krypton Propellant," *Journal of Propulsion and Power*, vol. 36, no. 3, pp. 335–345, 2020.

[10] V. Giannetti, M. M. Saravia, L. Leporini, S. Camarri, and T. Andreussi, "Numerical and Experimental Investigation of Longitudinal Oscillations in Hall Thrusters," *Aerospace*, vol. 8, no. 6, p. 148, 2021.

[11] S. Barral, K. Makowski, Z. Peradzyński, and M. Dudeck, "Transit-time instability in Hall thrusters," *Physics of Plasmas*, vol. 12, no. 7, p. 073504, 2005.

[12] E. Fernandez, M. K. Scharfe, C. A. Thomas, N. Gascon, and M. A. Cappelli, "Growth of resistive instabilities in E× B plasma discharge simulations," *Physics of Plasmas*, vol. 15, no. 1, p. 012102, 2008.

[13] S. Barral and E. Ahedo, "Low-frequency model of breathing oscillations in Hall discharges," *Physical Review E*, vol. 79, no. 4, p. 046401, 2009.

[14] T. Andreussi, E. Ferrato, V. Giannetti, A. Piragino, C. A. Paissoni, G. Cifali, and M. Andrenucci, "Development Status and Way Forward of SITAEL's Air-breathing Electric Propulsion," in *AIAA Propulsion and Energy 2019 Forum*, p. 3995, 2019.

[15] F. Romano, Y. A. Chan, G. Herdrich, C. Traub, S. Fasoulas, P. C. Roberts, K. Smith, S. Edmondson, S. Haigh, N. H. Crisp, V. T. Oiko, S. D. Worrall, S. Livadiotti, C. Huyton, L. A. Sinpetru, A. Straker, J. Becedas, R. M. Domínguez, D. González, V. Cañas, V. Sulliotti-Linner, V. Hanessian, A. Mølgaard, J. Nielsen, M. Bisgaard, D. Garcia-Almiñana, S. Rodriguez-Donaire, M. Sureda, D. Kataria, R. Outlaw, R. Villain, J. S. Perez, A. Conte, B. Belkouchi, A. Schwalber, and B. Heißerer, "RF helicon-based inductive plasma thruster (IPT) design for an atmosphere-breathing electric propulsion system (ABEP)," *Acta Astronautica*, vol. 176, pp. 476–483, 2020.

[16] ESA Express Procurement Plus - EXPRO+, "Technology Enhancement of ram-Electric Propulsion system for Very Low Earth Orbit mission," tech. rep., European Space Agency (ESA), 2020.

[17] T. Andreussi, G. Cifali, V. Giannetti, A. Piragino, E. Ferrato, A. Rossodivita, M. Andrenucci, J. Longo, and L. Walpot, "Development and Experimental Validation of a Hall Effect Thruster RAM-EP Concept," in *35th International Electric Propulsion Conference*, pp. 8–12, 2017.

[18] A. Gurciullo, A. L. Fabris, and M. A. Cappelli, "Ion plume investigation of a Hall effect thruster operating with Xe/N2 and Xe/air mixtures," *Journal of Physics D: Applied Physics*, vol. 52, no. 46, p. 464003, 2019.

[19] D. M. Goebel and I. Katz, *Fundamentals of electric propulsion: ion and Hall thrusters*, vol. 1. John Wiley & Sons, 2008.

[20] M. A. Lieberman and A. J. Lichtenberg, *Principles of plasma discharges and materials processing.* John Wiley & Sons, 2005.

[21] D. Bohm, "Minimum ionic kinetic energy for a stable sheath," in *The Characteristics Of Electrical Discharges In Magnetic Fields* (A. Guthrie and R. K. Wakerling, eds.), ch. 3, pp. 77–86, New York: McGraw-Hill Book Company Inc., 1949.

[22] F. F. Chen, *Introduction to Plasma Physics and Controlled Fusion (Volume 1: Plasma Physics).* Springer Science & Business Media, 2012.

[23] K. U. Riemann, "The Bohm criterion and boundary conditions for a multicomponent system," *IEEE Transactions on plasma science*, vol. 23, no. 4, pp. 709–716, 1995.

[24] S. Pancheshnyi, S. Biagi, M. C. Bordage, G. J. M. Hagelaar, W. L. Morgan, A. V. Phelps, and L. C. Pitchford, "The LXCat project: Electron scattering cross sections and swarm parameters for low temperature plasma modeling," *Chemical Physics*, vol. 398, pp. 148–153, 2012.

[25] G. Hagelaar and L. Pitchford, "Solving the Boltzmann equation to obtain electron transport coefficients and rate coefficients for fluid models," *Plasma Sources Science and Technology*, vol. 14, no. 4, p. 722, 2005.

[26] H. B. Valentini and F. Herrmann, “Boundary value problems for multi-component plasmas and a generalized Bohm criterion,” *Journal of Physics D: Applied Physics*, vol. 29, no. 5, p. 1175, 1996.

[27] M. S. Benilov, “Multifluid equations of a plasma with various species of positive ions and the Bohm criterion,” *Journal of Physics D: Applied Physics*, vol. 29, no. 2, p. 364, 1996.

[28] K. U. Riemann, “The Bohm criterion and sheath formation,” *Journal of Physics D: Applied Physics*, vol. 24, no. 4, p. 493, 1991.

[29] M. J. Goeckner, J. Goree, and T. E. Sheridan, “Measurements of ion velocity and density in the plasma sheath,” *Physics of Fluids B: Plasma Physics*, vol. 4, no. 6, pp. 1663–1670, 1992.

[30] L. Oksuz and N. Hershkowitz, “First experimental measurements of the plasma potential throughout the presheath and sheath at a boundary in a weakly collisional plasma,” *Physical review letters*, vol. 89, no. 14, p. 145001, 2002.

[31] S. D. Baalrud and C. C. Hegna, “Determining the Bohm criterion in plasmas with two ion species,” *Physics of Plasmas*, vol. 18, no. 2, p. 023505, 2011.

[32] R. N. Franklin, “Plasmas with more than one species of positive ion and the Bohm Criterion,” *Journal of Physics D: Applied Physics*, vol. 33, no. 24, p. 3186, 2000.

[33] R. N. Franklin, “The transition from collisionless to collisional in active low-temperature plasmas with more than one species of positive ion generated by electron impact and the Bohm criterion,” *Journal of Physics D: Applied Physics*, vol. 34, no. 13, p. 1959, 2001.

[34] R. N. Franklin, “Joining active plasma and sheath when the plasma contains two species of positive ions,” *Journal of Physics D: Applied Physics*, vol. 36, no. 1, p. 34, 2002.

[35] R. N. Franklin, “The plasma–sheath and its stability in a quiescent plasma containing two species of positive ion,” *Journal of Physics D: Applied Physics*, vol. 36, no. 15, p. 1806, 2003.

[36] G. D. Severn, X. Wang, E. Ko, and N. Hershkowitz, “Experimental studies of the Bohm criterion in a two-ion-species plasma using laser-induced fluorescence,” *Physical review letters*, vol. 90, no. 14, p. 145001, 2003.

[37] D. Lee, G. Severn, L. Oksuz, and N. Hershkowitz, “Laser-induced fluorescence measurements of argon ion velocities near the sheath boundary of an argon–xenon plasma,” *Journal of Physics D: Applied Physics*, vol. 39, no. 24, p. 5230, 2006.

[38] D. Lee, N. Hershkowitz, and G. D. Severn, “Measurements of Ar+ and Xe+ velocities near the sheath boundary of Ar–Xe plasma using two diode lasers,” *Applied Physics Letters*, vol. 91, no. 4, p. 041505, 2007.

[39] D. Lee, L. Oksuz, and N. Hershkowitz, “Exact solution for the generalized Bohm criterion in a two-ion-species plasma,” *Physical review letters*, vol. 99, no. 15, p. 155004, 2007.

[40] L. Oksuz, D. Lee, and N. Hershkowitz, “Ion acoustic wave studies near the presheath/sheath boundary in a weakly collisional argon/xenon plasma,” *Plasma Sources Science and Technology*, vol. 17, no. 1, p. 015012, 2007.

[41] A. Lenard, “On Bogoliubov’s kinetic equation for a spatially homogeneous plasma,” *Annals of Physics*, vol. 10, no. 3, pp. 390–400, 1960.

[42] R. Balescu, “Irreversible processes in ionized gases,” *The Physics of Fluids*, vol. 3, no. 1, pp. 52–63, 1960.

[43] S. D. Baalrud, J. D. Callen, and C. C. Hegna, “A kinetic equation for unstable plasmas in a finite space-time domain,” *Physics of Plasmas*, vol. 15, no. 9, p. 092111, 2008.

[44] L. D. Landau, “Die kinetische Gleichung für den Fall Coulombscher Wechselwirkung,” *Phys. Z. Sowjetunion*, vol. 10, no. 2, pp. 154–164, 1936. [English translation in *Collected Papers of L. D. Landau*, edited by D. Ter Harr (Pergamon, London, 1965)].

[45] D. G. Swanson, *Plasma waves.* CRC Press, 2003.

[46] X. Z. Tang and Z. Guo, “Kinetic model for the collisionless sheath of a collisional plasma,” *Physics of Plasmas*, vol. 23, no. 8, p. 083503, 2016.

[47] S. D. Baalrud, “Influence of ion streaming instabilities on transport near plasma boundaries,” *Plasma Sources Science and Technology*, vol. 25, no. 2, p. 025008, 2016.

[48] B. D. Fried and S. D. Conte, *The Plasma Dispersion Function: the Hilbert transform of the Gaussian.* New York: Academic Press Inc., 1961.

[49] S. D. Baalrud, J. D. Callen, and C. C. Hegna, “Kinetic theory of instability-enhanced collisional effects,” *Physics of Plasmas*, vol. 17, no. 5, p. 055704, 2010.

[50] S. D. Baalrud, T. Lafleur, W. Fox, and K. Germaschewski, “Instability-enhanced friction in the presheath of two-ion-species plasmas,” *Plasma Sources Science and Technology*, vol. 24, no. 1, p. 015034, 2015.

[51] N. Hershkowitz, “Sheaths: More complicated than you think,” *Physics of Plasmas*, vol. 12, no. 5, p. 055502, 2005.

[52] X. Y. Zhao, N. Xiang, J. Ou, D. H. Li, and B. B. Lin, “Sheath structure in plasma with two species of positive ions and secondary electrons,” *Chinese Physics B*, vol. 25, no. 2, p. 025202, 2015.

[53] A. J. Dekker, “Secondary electron emission,” in *Solid state physics*, ch. 17, pp. 418–445, Springer, 1981.

[54] A. Domínguez-Vázquez, F. Taccogna, and E. Ahedo, “Particle modeling of radial electron dynamics in a controlled discharge of a Hall thruster,” *Plasma Sources Science and Technology*, vol. 27, no. 6, p. 064006, 2018.

[55] T. Gyergyek, J. Kovačič, and M. Čerček, “A Fluid Model of the Sheath Formation in Front of an Electron Emitting Electrode with Space Charge Limited Emission Immersed in a Plasma that Contains a One-Dimensional Mono-Energetic Electron Beam,” *Contributions to Plasma Physics*, vol. 50, no. 2, pp. 121–134, 2010.

[56] G. D. Hobbs and J. A. Wesson, “Heat transmission through a langmuir sheath in the presence of electron emission,” Tech. Rep. CLM-R 61, Culham Laboratory, United Kingdom Atomic Energy Authority, Abingdon (England), 1966.

[57] J. M. Picone, A. E. Hedin, D. P. Drob, and A. C. Aikin, “NRLMSISE-00 empirical model of the atmosphere: Statistical comparisons and scientific issues,” *Journal of Geophysical Research: Space Physics*, vol. 107, no. A12, pp. SIA–15, 2002.

[58] ECSS Secretariat, “Space engineering – Space environment,” Standard ECSS-E-ST-10-04C Rev. 1, European Space Agency, Noordwijk, NL, June 2020.

[59] ISO Central Secretary, “Space environment (natural and artificial) – Earth upper atmosphere,” Standard ISO 14222:2013, International Organization for Standardization, Geneva, CH, Sept. 2013.

[60] A. V. Phelps, “Laboratory studies of electron attachment and detachment processes of aeronomic interest,” *Canadian Journal of Chemistry*, vol. 47, no. 10, pp. 1783–1793, 1969.

[61] P. C. Cosby, “Electron-impact dissociation of nitrogen,” *The Journal of Chemical Physics*, vol. 98, no. 12, pp. 9544–9553, 1993.

[62] Y. Itikawa, “Cross Sections for Electron Collisions with Nitrogen Molecules,” *Journal of Physical and Chemical Reference Data*, vol. 35, no. 1, pp. 31–53, 2006.

[63] H. F. Winters, “Ionic adsorption and dissociation cross section for nitrogen,” *The Journal of Chemical Physics*, vol. 44, no. 4, pp. 1472–1476, 1966.

[64] A. Lofthus and P. H. Krupenie, “The spectrum of molecular nitrogen,” *Journal of Physical and Chemical Reference Data*, vol. 6, no. 1, pp. 113–307, 1977.

[65] L. Campbell, D. C. Cartwright, M. J. Brunger, and P. J. O. Teubner, “Role of electronic excited N2 in vibrational excitation of the N2 ground state at high latitudes,” *Journal of Geophysical Research: Space Physics*, vol. 111, no. A09317, 2006.

[66] B. G. Lindsay and M. A. Mangan, “Cross sections for ion production by electron collisions with molecules,” in *Interactions of Photons and Electrons with Molecules* (Y. Itikawa, ed.), vol. 17C of *Landolt-Börnstein - Group I Elementary Particles, Nuclei and Atoms*, ch. 5, Springer-Verlag Berlin Heidelberg, 2003.

[67] H. C. Straub, P. Renault, B. G. Lindsay, K. A. Smith, and R. F. Stebbings, “Absolute partial cross sections for electron-impact ionization of H_2, N_2, and O_2 from threshold to 1000 eV,” *Physical Review A*, vol. 54, no. 3, p. 2146, 1996.

[68] D. Rapp and P. Englander-Golden, “Total cross sections for ionization and attachment in gases by electron impact. I. Positive ionization,” *The Journal of Chemical Physics*, vol. 43, no. 5, pp. 1464–1479, 1965.

[69] “IST-Lisbon database.” www.lxcat.net/IST-Lisbon. Retrieved on May 17, 2021.

[70] Y. Wang, O. Zatsarinny, and K. Bartschat, “B-spline R-matrix-with-pseudostates calculations for electron-impact excitation and ionization of nitrogen,” *Physical Review A*, vol. 89, no. 6, p. 062714, 2014.

[71] C. Tian and C. R. Vidal, “Electron impact ionization of N_2 and O_2: contributions from different dissociation channels of multiply ionized molecules,” *Journal of Physics B: Atomic, Molecular and Optical Physics*, vol. 31, no. 24, p. 5369, 1998.

[72] D. Rapp, P. Englander-Golden, and D. D. Briglia, “Cross sections for dissociative ionization of molecules by electron impact,” *The Journal of Chemical Physics*, vol. 42, no. 12, pp. 4081–4085, 1965.

[73] J. Mazeau, F. Gresteau, R. I. Hall, and A. Huetz, “Energy and width of $N^-(^3P)$ from observation of its formation by dissociative attachment to N_2 and NO,” *Journal of Physics B: Atomic and Molecular Physics*, vol. 11, no. 18, p. L557, 1978.

[74] “Biagi database.” www.lxcat.net/Biagi. Retrieved on May 17, 2021.

[75] Y. Itikawa, M. Hayashi, A. Ichimura, K. Onda, K. Sakimoto, K. Takayanagi, M. Nakamura, H. Nishimura, and T. Takayanagi, “Cross Sections for Collisions of Electrons and Photons with Nitrogen Molecules,” *Journal of Physical and Chemical Reference Data*, vol. 15, pp. 985–1010, July 1986.

[76] E. C. Zipf and R. W. McLaughlin, “On the dissociation of nitrogen by electron impact and by EUV photo-absorption,” *Planetary and Space Science*, vol. 26, no. 5, pp. 449–462, 1978.

[77] “BSR database.” www.lxcat.net/BSR. Retrieved on May 19, 2021.

[78] G. J. Schulz, “Resonances in electron impact on diatomic molecules,” *Reviews of Modern Physics*, vol. 45, no. 3, p. 423, 1973.

[79] Y. Itikawa, A. Ichimura, K. Onda, K. Sakimoto, K. Takayanagi, Y. Hatano, M. Hayashi, H. Nishimura, and S. Tsurubuchi, “Cross Sections for Collisions of Electrons and Photons with Oxygen Molecules,” *Journal of Physical and Chemical Reference Data*, vol. 18, no. 1, pp. 23–42, 1989.

[80] P. C. Cosby, “Electron-impact dissociation of oxygen,” *The Journal of Chemical Physics*, vol. 98, no. 12, pp. 9560–9569, 1993.

[81] Y. Itikawa, “Cross Sections for Electron Collisions with Oxygen Molecules,” *Journal of Physical and Chemical Reference Data*, vol. 38, no. 1, pp. 1–20, 2009.

[82] P. H. Krupenie, “The spectrum of molecular oxygen,” *Journal of Physical and Chemical Reference Data*, vol. 1, no. 2, pp. 423–534, 1972.

[83] R. R. Laher and F. R. Gilmore, “Updated excitation and ionization cross sections for electron impact on atomic oxygen,” *Journal of Physical and Chemical Reference Data*, vol. 19, no. 1, pp. 277–305, 1990.

[84] L. Sigaud, N. Ferreira, and E. C. Montenegro, “Absolute cross sections for O_2 dication production by electron impact,” *The Journal of Chemical Physics*, vol. 139, no. 2, p. 024302, 2013.

[85] “TRINITI database.” www.lxcat.net/TRINITI. Retrieved on May 19, 2021.

[86] “Phelps database.” www.lxcat.net/Phelps. Retrieved on May 20, 2021.

[87] D. Rapp and D. D. Briglia, “Total cross sections for ionization and attachment in gases by electron impact. II. Negative-ion formation,” *The Journal of Chemical Physics*, vol. 43, no. 5, pp. 1480–1489, 1965.

[88] L. L. Alves, P. Coche, M. A. Ridenti, and V. Guerra, “Electron scattering cross sections for the modelling of oxygen-containing plasmas,” *The European Physical Journal D*, vol. 70, no. 6, pp. 1–9, 2016.

[89] T. F. Gallagher, *Rydberg atoms.* No. 3 in Cambridge Monographs on Atomic, Molecular and Chemical Physics, Cambridge University Press, 1994.

[90] G. J. M. Hagelaar, *Brief documentation of BOLSIG+ version 03/2016.* Laboratoire Plasma et Conversion d'Energie (LAPLACE), Université Paul Sabatier, Mar. 2016.

[91] G. Severn, C.-S. Yip, N. Hershkowitz, and S. D. Baalrud, “Experimental studies of ion flow near the sheath edge in multiple ion species plasma including argon, xenon and neon,” *Plasma Sources Science and Technology*, vol. 26, no. 5, p. 055021, 2017.

[92] C.-S. Yip, N. Hershkowitz, G. Severn, and S. D. Baalrud, “Laser-induced fluorescence measurements of argon and xenon ion velocities near the sheath boundary in 3 ion species plasmas,” *Physics of Plasmas*, vol. 23, no. 5, p. 050703, 2016.

[93] A. I. Morozov and V. V. Savelyev, “Fundamentals of Stationary Plasma Thruster Theory,” in *Reviews of Plasma Physics* (S. V. Kadomtsev B. B., ed.), vol. 21, pp. 203–391, Boston, MA: Springer, 2000.

[94] E. Ahedo, J. M. Gallardo, and M. Martınez-Sánchez, “Effects of the radial plasma-wall interaction on the Hall thruster discharge,” *Physics of Plasmas*, vol. 10, no. 8, pp. 3397–3409, 2003.

[95] B. M. Reid, *The influence of neutral flow rate in the operation of Hall thrusters.* PhD thesis, University of Michigan, 2009.

[96] E. Ahedo, J. M. Gallardo, and M. Martınez-Sánchez, “Model of the plasma discharge in a Hall thruster with heat conduction,” *Physics of Plasmas*, vol. 9, no. 9, pp. 4061–4070, 2002.

[97] I. G. Mikellides and A. L. Ortega, “Challenges in the development and verification of first-principles models in Hall-effect thruster simulations that are based on anomalous resistivity and generalized Ohm's law,” *Plasma Sources Science and Technology*, vol. 28, no. 1, p. 014003, 2019.

[98] M. S. McDonald and A. D. Gallimore, “Rotating spoke instabilities in Hall thrusters,” *IEEE Transactions on Plasma Science*, vol. 39, no. 11, pp. 2952–2953, 2011.

[99] M. McDonald, C. Bellant, B. St. Pierre, and A. Gallimore, “Measurement of cross-field electroncurrent in a hall thruster due to rotating spoke instabilities,” in *47th AIAA/ASME/SAE/ASEE Joint Propulsion Conference & Exhibit*, p. 5810, 2011.

[100] C. L. Ellison, Y. Raitses, and N. J. Fisch, “Cross-field electron transport induced by a rotating spoke in a cylindrical Hall thruster,” *Physics of Plasmas*, vol. 19, no. 1, p. 013503, 2012.

[101] K. Hara, “Non-oscillatory quasineutral fluid model of cross-field discharge plasmas,” *Physics of Plasmas*, vol. 25, no. 12, p. 123508, 2018.

[102] V. V. Rusanov, “The calculation of the interaction of non-stationary shock waves and obstacles,” *USSR Computational Mathematics and Mathematical Physics*, vol. 1, no. 2, pp. 267–279, 1961.

[103] E. F. Toro, *Riemann solvers and numerical methods for fluid dynamics: a practical introduction.* Springer Science & Business Media, 2013.

[104] J. L. Steger and R. F. Warming, “Flux vector splitting of the inviscid gasdynamic equations with application to finite-difference methods,” *Journal of Computational Physics*, vol. 40, no. 2, pp. 263–293, 1981.

[105] D. Pedrini, F. Torrini, J. Grassi, F. Paganucci, T. Andreussi, T. Misuri, and M. Andrenucci, “Development of hollow cathodes for 5 to 20 kW hall thrusters,” in *35th International Electric Propulsion Conference*, 2017.

[106] D. Sydorenko, A. Smolyakov, I. Kaganovich, and Y. Raitses, “Kinetic simulation of secondary electron emission effects in Hall thrusters,” *Physics of Plasmas*, vol. 13, no. 1, p. 014501, 2006.

[107] I. D. Kaganovich, Y. Raitses, D. Sydorenko, and A. Smolyakov, “Kinetic effects in a Hall thruster discharge,” *Physics of Plasmas*, vol. 14, no. 5, p. 057104, 2007.

[108] J. P. Boeuf, “Tutorial: Physics and modeling of Hall thrusters,” *Journal of Applied Physics*, vol. 121, no. 1, p. 011101, 2017.

[109] I. G. Mikellides, B. Jorns, I. Katz, and A. Lopez Ortega, “Hall2De simulations with a first-principles electron transport model based on the electron cyclotron drift instability,” in *52nd AIAA/SAE/ASEE Joint Propulsion Conference*, p. 4618, 2016.

[110] T. Lafleur, S. D. Baalrud, and P. Chabert, “Theory for the anomalous electron transport in Hall effect thrusters. II. Kinetic model,” *Physics of Plasmas*, vol. 23, no. 5, p. 053503, 2016.

[111] T. Andreussi, A. Piragino, M. Reza, V. Giannetti, F. Faraji, E. Ferrato, D. Pedrini, A. Kitaeva, A. Rossodivita, M. Andrenucci, C. A. Paissoni, and G. Becatti, “Development status and way forward of SITAEL’s 20kW class Hall thruster, the HT20k,” in *36th International Electric Propulsion Conference, Vienna, Austria*, pp. 15–20, 2019.

[112] M. L. R. Walker, *Effects of Facility Backpressure on the Performance and Plume of a Hall Thruster.* University of Michigan, 2005.

[113] H. D. Hagstrum, “Auger Ejection of Electrons from Molybdenum by Noble Gas Ions,” *Physical Review*, vol. 104, no. 3, p. 672, 1956.

[114] P. Mahadevan, G. D. Magnuson, J. K. Layton, and C. E. Carlston, “Secondary-Electron Emission from Molybdenum Due to Positive and Negative Ions of Atmospheric Gases,” *Physical Review*, vol. 140, no. 4A, p. A1407, 1965.

[115] H. D. Hagstrum, “Theory of Auger Ejection of Electrons from Metals by Ions,” *Physical Review*, vol. 96, no. 2, p. 336, 1954.

[116] D. L. Brown, M. L. R. Walker, J. Szabo, W. Huang, and J. E. Foster, “Recommended practice for use of Faraday probes in electric propulsion testing,” *Journal of Propulsion and Power*, vol. 33, no. 3, pp. 582–613, 2017.

[117] A. Piragino, F. Faraji, M. Reza, E. Ferrato, A. Piraino, and T. Andreussi, “Background Pressure Effects on the Performance of a 20 kW Magnetically Shielded Hall Thruster Operating in Various Configurations,” *Aerospace*, vol. 8, no. 3, p. 69, 2021.

[118] C. Böhm and J. Perrin, "Retarding-field analyzer for measurements of ion energy distributions and secondary electron emission coefficients in low-pressure radio frequency discharges," *Review of scientific instruments*, vol. 64, no. 1, pp. 31–44, 1993.

[119] N. Gulbrandsen, Å. Fredriksen, J. Carr Jr, and E. Scime, "A comparison of ion beam measurements by retarding field energy analyzer and laser induced fluorescence in helicon plasma devices," *Physics of Plasmas*, vol. 22, no. 3, p. 033505, 2015.

[120] V. Giannetti, M. M. Saravia, and T. Andreussi, "Measurement of the breathing mode oscillations in Hall thruster plasmas with a fast-diving triple Langmuir probe," *Physics of Plasmas*, vol. 27, no. 12, p. 123502, 2020.

[121] M. M. Saravia, A. Giacobbe, and T. Andreussi, "Bayesian analysis of triple Langmuir probe measurements for the characterization of Hall thruster plasmas," *Review of Scientific Instruments*, vol. 90, no. 2, p. 023502, 2019.

[122] P. Diego, I. Bertello, M. Candidi, A. Mura, G. Vannaroni, and D. Badoni, "Plasma and fields evaluation at the Chinese seismo-electromagnetic satellite for electric field detector measurements," *IEEE Access*, vol. 5, pp. 3824–3833, 2017.

[123] J. G. Laframboise, "Theory of Spherical and Cylindrical Langmuir Probes in a Collisionless, Maxwellian Plasma at Rest," tech. rep., Institute for Aerospace Studies, University of Toronto (Ontario), 1966.

[124] M. Mausbach, "Parametrization of the Laframboise theory for cylindrical Langmuir probe analysis," *Journal of Vacuum Science & Technology A: Vacuum, Surfaces, and Films*, vol. 15, no. 6, pp. 2923–2929, 1997.

[125] E. W. Peterson and L. Talbot, "Collisionless electrostatic single-probe and double-probe measurements," *AIAA Journal*, vol. 8, no. 12, pp. 2215–2219, 1970.

[126] M. J. Sekerak, *Plasma Oscillations and Operational Modes in Hall Effect Thrusters*. PhD thesis, University of Michigan, 2014.

[127] A. Fruchtman and A. Cohen-Zur, "Plasma lens and plume divergence in the Hall thruster," *Applied physics letters*, vol. 89, no. 11, p. 111501, 2006.

[128] R. W. Conversano, D. M. Goebel, R. R. Hofer, I. G. Mikellides, and R. E. Wirz, "Performance analysis of a low-power magnetically shielded Hall thruster: experiments," *Journal of Propulsion and Power*, vol. 33, no. 4, pp. 975–983, 2017.

[129] R. W. Conversano, D. M. Goebel, I. G. Mikellides, R. R. Hofer, and R. E. Wirz, "Performance analysis of a low-power magnetically shielded Hall thruster: computational modeling," *Journal of Propulsion and Power*, vol. 33, no. 4, pp. 992–1001, 2017.

[130] E. T. Dale and B. A. Jorns, "Non-invasive time-resolved measurements of anomalous collision frequency in a Hall thruster," *Physics of Plasmas*, vol. 26, no. 1, p. 013516, 2019.

[131] L. C. Andrews, *Special functions of mathematics for engineers*, vol. 49. Spie Press, 1998.

[132] M. Capitelli, G. Colonna, and A. D'Angola, *Fundamental Aspects of Plasma Chemical Physics: Thermodynamics*, vol. 66 of *Atomic, Optical and Plasma Physics*. Springer New York, 2012.

[133] G. Herzberg, *Molecular Spectra and Molecular Structure. Vol. 1: Spectra of Diatomic Molecules*. New York: D. Van Nostrand Company, Inc., 2nd ed., Feb. 1963.